

Solution Processed Aluminium Oxide Film for Surface Passivation of p-type Crystalline Silicon Surfaces

Submitted in partial fulfilment of the requirements
of the degree of
Doctor of Philosophy

By

KALAIVANI S
(Roll No.124070001)

Supervisor

Prof. Anil Kottantharayil



Department of Electrical Engineering
INDIAN INSTITUTE OF TECHNOLOGY BOMBAY

2023

This Thesis is dedicated in the devotional service at the Lotus Feet of Lord Sri Sri RadhaKrishna and all my Spiritual Masters including His Divine Grace A. C. Bhaktivedanta Swami Prabhupada (Founder-Acharya of International Society for Krishna Consciousness (ISKCON)) and His Holiness Gopal Krishna Goswami Maharaja (Disciple of His Divine Grace A.C. Bhaktivedanta Swami Prabhupada)

Thesis Approval

This thesis entitled “**Solution Processed Aluminium Oxide Film for Surface Passivation of p-type Crystalline Silicon Surfaces**” by **KALAIVANI S** (Roll No: 124070001) is approved for the degree of **Doctor of Philosophy**

Examiners

Prof. Pradeep R. Nair

Digital Signature
Pradeep R. Nair (i11102)
04-May-23 10:55:56 AM

Prof. Sundar Kumar Iyer

S. Sundar Kumar Iyer

Supervisor (s)

Prof. Anil Kottantharayil

Digital Signature
Anil Kottantharayil (i06163)
03-May-23 12:14:10 PM

Chairperson

Prof. Mohamad Aslam

Digital Signature
Prof. Mohammed Aslam (i08003)
03-May-23 12:56:54 PM

Date : May 02, 2023

Place : IIT Bombay, Mumbai

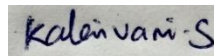
Declaration

I declare that this written submission represents my ideas in my own words and where other's ideas or words have been included, I have adequately cited and referenced the original sources. I also declare that this thesis contains the work from the Indian patent number: 391027. Parts of chapter 4 of this thesis include the work we have published in the proceedings of the 42th IEEE Photovoltaic Specialist Conference (PVSC), 2015. Parts of chapter 5 and chapter 6 include the work we have published in Solar Energy Materials and Solar Cells, vol. 197, pp. 93–98, 2019 and the Indian patent number: 391027.

I also declare that I have adhered to all principles of academic honesty and integrity and have not misrepresented or fabricated or falsified any ideas, data, facts or sources in my submission. I understand that any violation of the above will be cause of disciplinary action by the institute and evoke penal action from the sources which have thus not been properly cited or from whom proper permission has not been taken when needed.

Date: May 02, 2023

Place: IIT Bombay, Mumbai



KALAIVANI S

(Roll No. 124070001)

Abstract

Efficient and inexpensive photovoltaic systems are necessary to meet the increasing global electricity demand. In order to improve the efficiency of the crystalline silicon (c-Si) solar cells, the recombination losses of charge carriers must be reduced by the surface passivation techniques. Aluminium oxide (AlO_x) thin films are highly relevant for various high efficiency silicon solar cells. In literature, AlO_x layers are shown to be negatively charged dielectrics that provide an excellent passivation of lowly and highly doped p-type c-Si surfaces. It is also shown in literature that high efficiency c-Si solar cells are passivated by AlO_x films deposited using atomic layer deposition (ALD) and plasma-enhanced chemical vapour deposition (PECVD). Although several deposition techniques are mentioned in literature for AlO_x deposition, solution processed AlO_x thin film deposition technique is shown to be an inexpensive process. This thesis work aims to achieve excellent c-Si surface passivation by AlO_x film using low cost deposition techniques. Two simple, inexpensive and non-vacuum deposition techniques — spin coating and spray coating — are investigated for surface passivation of p-type c-Si.

Spin coating is one of the excellent thin film deposition techniques on laboratory scale and beneficial to the process development and research activities. In this work, AlO_x films are developed successfully for p-type c-Si surface passivation by spin coating process. The spin coated AlO_x film exhibits thickness and refractive index (RI) uniformity with standard deviation of 0.27 nm and less than measurement resolution for thickness and RI, respectively over 2-inch silicon wafer for five measurement points. The effective minority carrier lifetime (τ_{eff}) of spin coated AlO_x film is 1.9 μs at excess minority carrier density (Δn) of $1 \times 10^{15} \text{ cm}^{-3}$ after the annealing of AlO_x film at 800 °C for 10 s in nitrogen (N_2) ambient, whereas improved τ_{eff} of 160 μs and maximum effective surface recombination velocity ($S_{\text{eff,max}}$) of 94 $\text{cm}\cdot\text{s}^{-1}$ at an injection level of $1 \times 10^{15} \text{ cm}^{-3}$ are obtained after annealing at 780 °C for 130 min in oxygen (O_2) ambient. For spin coated AlO_x film, promising surface passivation is obtained only after prolonged high temperature annealing. Despite the ability to deposit good quality uniform thin film on a smooth flat surface with good reproducibility, it lacks some key aspects necessary for large-scale production. For commercial large-size solar cell fabrication, silicon wafers with textured surface/rough surface are typically used. To deposit thin AlO_x

film (e.g., sub-20-nm-thin) on large-size silicon wafer, the silicon substrate may require high spinning speed to allow the film to thin down which may leads to generation of defects in the deposited film and subsequently affect the surface passivation. Spin coating is limited to single wafer processing and has low throughput. Moreover, it has poor material usage.

Spray coating is one of very promising alternative deposition techniques. It is an attractive option for photovoltaic industry due to the possibility of high throughput, capability of reproducible film deposition on large size non-flat surfaces with low material wastage. In a major departure from the spray pyrolysis process reported in literature wherein the precursor solution is typically sprayed onto a preheated substrate, in this work the solution is sprayed onto the substrate at room temperature and then dried using a hot plate to obtain the film, a process sequence amenable to conveyer belt processing with high throughput. AlO_x thin film deposited by a spray coating process using hand-held sprayer is investigated for surface passivation of p-type c-Si. The spray coated AlO_x film shows excellent thermal stability. For float-zone (FZ) wafers passivated by spray coated AlO_x films, τ_{eff} of 502 μs and corresponding $S_{\text{eff,max}}$ of 28 $\text{cm}\cdot\text{s}^{-1}$ at Δn of $1 \times 10^{15} \text{ cm}^{-3}$ are obtained after annealing at 850 $^\circ\text{C}$ for 2 hours in O_2 . For spray coated AlO_x film, promising surface passivation is obtained only after a prolonged high temperature annealing. Besides, hand-held sprayers are not suitable for large area applications due to low throughput. It is difficult to achieve uniformity over large area substrates and reproducibility is also difficult to achieve with hand-held sprayer. Moreover, quality of the film deposited by hand-held sprayers depends on the skills of the operator.

In this work, for further process development and optimization studies of spray coated AlO_x films, spraying instrument is custom designed and built for solar cell applications with largest wafer size capacity of 200 mm \times 200 mm. The customized automated spraying instrument provides facility to precisely control the flow rate, duration of spray, spray ON/OFF and X-Y movements with control of speed. The control of entire spraying process can be achieved through a software program that enable spray processes to take place according to the parameters already set using the software program. The vacuum chuck design is optimized using photoluminescence (PL) imaging to minimize defect generation during spray coating. It is reported in literature that, hydrophilic silicon surfaces are more preferable for AlO_x film deposition. In this work, superhydrophilic silicon surfaces are obtained by ultraviolet (UV)-ozone (O_3) treatment. The ultrathin silicon oxide (SiO_x) film

grown by UV/O₃ treatment is incorporated prior to AlO_x deposition by spray coating process using spraying instrument as part of surface passivation scheme. Promising structural, electrical and passivation characteristics of spray coated AlO_x film deposited by spraying instrument are achieved for low thermal budget annealing with the incorporation of UV/O₃ grown ultrathin SiO_x film. The films also exhibit good thermal stability and are blister-free.

Excellent film thickness and RI uniformity is achieved for spray coated AlO_x film using spraying instrument. The mean value of AlO_x film thickness is 12.4 nm and the standard deviation is 0.3 nm before post deposition annealing (PDA) at 520 °C for 20 min in O₂ ambient. The mean of RI is 1.63 and the standard deviation is 0.01 before PDA. The mean values of film thickness and RI are found to be 10.3 nm and 1.64, respectively after PDA. The spray coated AlO_x film is found to be smooth with root mean square (RMS) roughness of 0.33 nm before and after PDA by atomic force microscope (AFM) measurements. It is reported in literature that, hydrogen incorporation during Al₂O₃ deposition by ALD and PECVD methods leads to blister formation during high temperature annealing processes for certain process conditions. In this work, hydrogen related bonds are not observed by Fourier transform infrared spectroscopy (FTIR) measurements for as-deposited, PDA and rapid thermal processing (RTP)-fired (860 °C) AlO_x films. 2D and 3D optical imaging confirms that there are no blisters in the film for annealing temperature up to 860 °C. The density of interface states (D_{it}) is found to be in the range of $(8.5-10) \times 10^{10} \text{ eV}^{-1} \cdot \text{cm}^{-2}$ whereas the fixed oxide charge density (Q_f) is in the range of $-(5.2-5.5) \times 10^{12} \text{ cm}^{-2}$ after PDA at 520 °C for 20 min in O₂ ambient. Moreover, the mean breakdown field is $4.7 \text{ MV} \cdot \text{cm}^{-1}$. The D_{it} and Q_f values are comparable to those reported for ALD and PECVD Al₂O₃ and are in the range of interest for high quality passivation of p-type silicon surface. For the sample after PDA at 520 °C for 20 min in O₂ ambient, τ_{eff} of 471 μs and S_{eff} of $8 \text{ cm} \cdot \text{s}^{-1}$ at Δn of $1 \times 10^{15} \text{ cm}^{-3}$ are obtained and it indicates that the silicon surface is well passivated. Thermal stability of spray coated AlO_x films is studied for different temperatures, as high temperature stability of AlO_x layers is necessary for majority of solar cell applications. It is observed that the S_{eff} is maintained at $8 \text{ cm} \cdot \text{s}^{-1}$ up to an annealing temperature of 700 °C and is $12 \text{ cm} \cdot \text{s}^{-1}$ for 750 °C and this is found to be comparable to literature reports. This is achieved without the use of a capping layer. For ALD and PECVD films, silicon nitride (SiN_x) capping layer may be necessary to stabilize the passivation as stated in literature.

In addition, surface passivation of highly boron doped p-type silicon by 10 nm AlO_x thin film deposited using spraying instrument is also investigated. An emitter saturation current density (J_{0e}) of $92 \text{ fA}\cdot\text{cm}^{-2}$ and $145 \text{ fA}\cdot\text{cm}^{-2}$ are obtained for p^+ emitter of $70 \text{ }\Omega/\square$ and $34 \text{ }\Omega/\square$ sheet resistance, respectively with nitric acid based boron-rich layer (BRL) removal process. UV/ O_3 oxidation is used as an alternative method for removing BRL and J_{0e} value of $120 \text{ fA}\cdot\text{cm}^{-2}$ is obtained for p^+ emitter with sheet resistance of $70 \text{ }\Omega/\square$. Further, two process technologies for rear contact are also explored. Patterning of spray coated AlO_x film is made by selectively removing the passivation layer using photolithography followed by wet etching. This process is suitable for fabrication at laboratory scale, but it is an expensive process for large volume industrial production. Laser firing of aluminium metal on the rear surface through the spray coated AlO_x passivation layer is attempted as an alternative method for rear contact. Laser fired contact hole with $\sim 2 \text{ }\mu\text{m}$ depth is obtained after laser firing.

In conclusion, the results show that the spray coated AlO_x thin film deposited by inexpensive spraying instrument is a practical option and may be used as a surface passivation layer for p-type c-Si surfaces in silicon solar cell structures such as passivated emitter and rear contact (PERC) solar cells.

Table of Contents

Abstract	v
Table of Contents	ix
List of Figures	xiii
List of Tables	xviii
List of Symbols	xix
List of Acronyms	xxvii
1 Introduction	1
1.1 Motivation	4
1.2 Thesis outline	5
2 Surface Passivation of Silicon - a Literature Review	7
2.1 Structure of PERC solar cell	7
2.2 Theory of recombination processes	9
2.2.1 Recombination in the c-Si bulk	9
2.2.2 Recombination at the c-Si surface	13
2.2.3 Methods to reduce surface recombination	14
2.2.4 Emitter recombination	15
2.3 Surface passivation materials	18
2.3.1 Silicon dioxide (SiO ₂)	18
2.3.2 Silicon nitride (SiN _x)	19
2.3.3 Hydrogenated amorphous silicon (a-Si:H)	20
2.3.4 Aluminum oxide (Al ₂ O ₃)	21
2.4 Methods for deposition of Al ₂ O ₃	22
2.4.1 Atomic layer deposition (ALD)	22
2.4.2 Plasma-enhanced chemical vapor deposition	25
2.4.3 Sputtering	26
2.4.4 Spin coating	27

2.4.5	Spray pyrolysis	29
2.5	Surface preparation	30
2.6	Effect of film thickness and optical properties requirement	31
2.7	Activation of passivation	32
2.8	Thermal stability	33
2.9	Passivation characteristics of AlO_x /c-Si interface	34
2.10	Emitter passivation	35
2.11	Crystalline silicon solar cells	36
2.11.1	Passivated emitter and rear cell (PERC) cells	36
2.11.2	Passivated emitter rear totally diffused (PERT) cells	36
2.11.3	Passivated emitter and rear locally diffused (PERL) cells	37
2.11.4	Tunnel oxide passivated contact (TOPCon) cells	38
2.11.5	Interdigitated back-contact (IBC) cells	39
2.12	Integration of backside passivation layers in PERC solar cells	40
2.13	Major gaps which are observed from the literature review	41
3	Experimental Methods	44
3.1	AlO_x deposition	44
3.1.1	RCA cleaning	44
3.1.2	AlO_x solution preparation	45
3.2	Characterization methods	45
3.2.1	Four-point probe	46
3.2.2	Ellipsometry	47
3.2.3	Optical microscope	48
3.2.4	Zeta 3D microscope	48
3.2.5	Atomic force microscopy (AFM)	48
3.2.6	Fourier transform infrared spectroscopy (FTIR)	49
3.2.7	X-ray photoelectron spectroscopy (XPS)	49
3.2.8	Transmission electron microscopy (TEM)	50
3.2.9	Electrical characterization of metal insulator semiconductor (MIS) capacitor	50
3.2.10	Series resistance correction	53
3.2.11	Effective lifetime measurement	54

3.2.12 Photoluminescence (PL) measurement	58
4 Preliminary Investigations of AlO_x Deposition by Wet Chemical Processes	61
4.1 Spin coating	61
4.1.1 Deposition method	61
4.1.2 Experimental detail	63
4.1.3 Results and discussion	66
4.2 Spray coating	73
4.2.1 Experimental details	73
4.2.2 Results and discussions	74
4.3 Comparison of the two coating techniques	81
4.4 Summary and conclusions	83
5 Development of Spray Coating Process for Large Area Device Applications	86
5.1 Design of spray deposition system	86
5.1.1 Spraying instrument	86
5.1.2 Design of vacuum chuck	89
5.1.3 Design of hot plate heater	92
5.2 Substrate and solution preparation	93
5.2.1 Silicon surface oxidation by UV/O ₃	93
5.3 AlO _x thin film deposition	96
5.4 Physical and structural characterization	96
5.4.1 Thickness uniformity	96
5.4.2 Surface roughness by AFM	97
5.4.3 FTIR analysis of AlO _x thin film to detect hydrogen	99
5.4.4 Blister Analysis by 2D and 3D optical imaging	103
5.4.5 XPS and HRTEM analysis of AlO _x thin film	104
5.5 Summary and conclusions	106
6 Spray Coated AlO_x Film Deposited by Spraying Instrument for p-type Silicon Surface Passivation	107
6.1 Substrate and sample preparation	107
6.2 Electrical characterization	107

6.2.1	Capacitance-voltage and conductance-voltage measurements	108
6.2.2	Current-voltage measurements	109
6.3	Surface passivation	111
6.3.1	Lifetime measurement	111
6.3.2	Thermal stability	112
6.4	Summary and conclusions	114
7	Preliminary Investigations on Integration of Spray Coated AlO_x in Solar Cells	115
7.1	p ⁺ emitter passivation	115
7.1.1	Experimental details	116
7.1.2	Boron dopant paste diffusion	116
7.1.3	p ⁺ emitter passivation with AlO _x	117
7.2	Two process technologies—photolithography and laser fired contact— for spray coated AlO _x film integration into solar cells	120
7.2.1	Experimental details	120
7.2.2	Photolithography	121
7.2.3	Laser firing of metal through the dielectric	122
7.3	Summary and conclusions	124
8	Summary and Outlook	127
8.1	Summary	127
8.2	Future directions and process improvements	131
	Appendix	133
I	The etch properties of spin coated AlO _x film	133
II	Deposition of aluminum silicate (AlSi _x O _y) film by spin coating method	134
	References	136
	List of publications and patents	179
	Acknowledgements	180

List of Figures

Figure 1.1: Share of India's electricity generation for selected energy sources by single region scenario, data adapted from [17].	3
Figure 2.1: Schematic drawing of a typical industrial PERC solar cell structure [33].	8
Figure 2.2: Process flow of CSUN's industrial PERC solar cell [33].	8
Figure 2.3: Device schematic for J_{0e} measurement.	17
Figure 2.4: Schematic of spray pyrolysis system [156].	29
Figure 3.1: Schematic of MIS capacitor structure for electrical characterization of the dielectric film [50].	50
Figure 3.2: Schematic of the sample used for τ_{eff} measurement.	55
Figure 3.3: Schematic of the photoconductance measurement system (WCT-120 lifetime tester from Sinton Instruments) [264].	55
Figure 3.4: Photoluminescence imaging setup [275].	60
Figure 4.1: Four stages of spin coating [276,277].	61
Figure 4.2: Process flow of Sample A.	64
Figure 4.3: Process flow of Sample B, Sample C and Sample D.	65
Figure 4.4: Process flow of Sample E.	66
Figure 4.5: Process flow of Sample F and Sample G.	66
Figure 4.6: (a) Measured and series resistance corrected C-V and G-V curves of Sample D measured at 100 kHz and 1 MHz. (b) Series resistance corrected C-V characteristics (rescaled version of Figure 4.6 (a)) showing the hysteresis. Hysteresis is seen to be 13 mV and 9 mV for 100 kHz and 1 MHz, respectively. The black arrows indicate the direction of the voltage sweep. The measurement was started from inversion.	69
Figure 4.7: I-V characteristics of Sample D.	70
Figure 4.8: Cross sectional HRTEM image of Sample E after annealing at 800 °C for 10 s in N ₂ ambient.	71
Figure 4.9: Effective carrier lifetime as a function of minority carrier concentration for the Sample F annealed at 800 °C for 10 s in N ₂ . τ_{eff} is 1.9 μs at $\Delta n = 1 \times 10^{15} \text{ cm}^{-3}$.	71
Figure 4.10: Effective carrier lifetime and $S_{\text{eff,max}}$ as a function of minority carrier concentration for the sample G annealed at 780 °C for 130 min in O ₂ ambient (τ_{eff} is	72

160 μs and $S_{\text{eff,max}}$ is 94 $\text{cm}\cdot\text{s}^{-1}$ at $\Delta n = 1 \times 10^{15} \text{ cm}^{-3}$).

Figure 4.11: Experimental setup for AlO_x film deposition by spray coating process using hand-held sprayer. 73

Figure 4.12: (a) Series resistance corrected high frequency capacitance and conductance characteristics of 13 nm AlO_x film after PDA of 520 $^\circ\text{C}$ for 20 min in O_2 ambient measured at 100 kHz. (b) Series resistance corrected C-V characteristics (rescaled version of Figure 4.12 (a)) showing the hysteresis. Hysteresis is seen to be 20 mV. The black arrows indicate the direction of the voltage sweep. The measurement was started from inversion. 75

Figure 4.13: I-V characteristics of 13 nm AlO_x film after PDA of 520 $^\circ\text{C}$ for 20 min in O_2 ambient. 75

Figure 4.14: Injection level dependent lifetimes for the as-deposited AlO_x (0.2 M) film. τ_{eff} is 2 μs at $\Delta n = 1 \times 10^{15} \text{ cm}^{-3}$. 76

Figure 4.15: Injection level dependent lifetimes and $S_{\text{eff,max}}$ for spray coated AlO_x (0.2 M) film after annealing at 520 $^\circ\text{C}$ for 20 min in O_2 ambient. τ_{eff} is 10 μs at $\Delta n = 1 \times 10^{15} \text{ cm}^{-3}$. 76

Figure 4.16: Injection level dependent lifetimes and $S_{\text{eff,max}}$ for spray coated AlO_x (1 M) film after PDA at 520 $^\circ\text{C}$ for 20 min in O_2 . τ_{eff} is 19.3 μs and $S_{\text{eff,max}}$ is 726 $\text{cm}\cdot\text{s}^{-1}$ at $\Delta n = 1 \times 10^{15} \text{ cm}^{-3}$. 77

Figure 4.17: Injection level dependent lifetimes and $S_{\text{eff,max}}$ for spray coated AlO_x (1 M) film after PDA at 520 $^\circ\text{C}$ for 2 hours in O_2 ambient. τ_{eff} is 31.5 μs and $S_{\text{eff,max}}$ is 445 $\text{cm}\cdot\text{s}^{-1}$ at $\Delta n = 1 \times 10^{15} \text{ cm}^{-3}$. 78

Figure 4.18: The $S_{\text{eff,max}}$ at $\Delta n = 1 \times 10^{15} \text{ cm}^{-3}$ for spray coated AlO_x film after PDA at 520 $^\circ\text{C}$ in O_2 for different annealing time. The samples were prepared using 0.2 M and 1 M AlO_x solution. 78

Figure 4.19: Effect of annealing temperature on surface passivation of spray coated AlO_x film (1 M) after annealing for 2 hours in O_2 ambient at $\Delta n = 1 \times 10^{15} \text{ cm}^{-3}$. 79

Figure 4.20: Injection level dependent lifetimes and $S_{\text{eff,max}}$ for the best sample after annealing at 850 $^\circ\text{C}$ for 2 hours in O_2 ambient. τ_{eff} is 502 μs and S_{eff} is 28 $\text{cm}\cdot\text{s}^{-1}$ at $\Delta n = 1 \times 10^{15} \text{ cm}^{-3}$. 79

Figure 4.21: Chemical composition of spray coated AlO_x film after PDA at 850 $^\circ\text{C}$ for 2 hours in O_2 ambient. 80

Figure 4.22: Cross sectional HRTEM image of spray coated AlO _x film after PDA at 850 °C for 2 hours in O ₂ ambient.	80
Figure 5.1: Photograph of the custom designed spraying instrument.	87
Figure 5.2: Photograph of the syringe pump [301].	88
Figure 5.3: Schematic of the chuck-A with design details (all dimensions are in mm). (a) 2D top view (b) 2D section (Z-Z) view. The cutting line marked as Z-Z in Figure 5.3(a) shows where the part is cross-sectioned. (c) 3D view of chuck-A. (d) PL image of AlO _x film deposited using chuck-A.	90
Figure 5.4: Technical drawing of the chuck-B with details of design (all dimensions are in mm) by PTC CREO software. (a) 2D top view. (b) 2D section (Z-Z) view. (c) 2D section (X-X) view. (d) 2D detail view to provide greater clarity about the region of circular groove. In Figure 5.4(b), the detail view border is displayed using dotted circle and annotated with letter 'B' to link the detail view with its parent view. (e) 3D view of chuck-B.	91
Figure 5.5: PL image of 2-inch p-type Si wafer passivated by spray coated AlO _x film showing defect of circle due to O-ring of the chuck-B.	91
Figure 5.6: Technical drawing of the hot plate heater with details of design by PTC CREO software (all dimensions are in mm). (a) 2D top view (b) 2D section (X-X) view (c) 3D view of the object.	92
Figure 5.7: Contact angle on various sample surfaces. (a) A hydrophilic surface ($\theta < 90^\circ$). (b) A hydrophobic surface ($\theta > 90^\circ$) [303].	94
Figure 5.8: Process flow for contact angle measurement.	95
Figure 5.9: (a) AlO _x film thickness (after hot plate drying at 250 °C) variations over a 2-inch silicon wafer. (b) RI uniformity of AlO _x film. Thickness measurements were performed along the four lines shown in the insets. 20 points were measured along each line shown.	97
Figure 5.10: (a) AFM 2D surface image (b) AFM 3D surface image of bare silicon wafer. RMS roughness is 0.68 nm.	98
Figure 5.11: (a) AFM 2D surface image (b) AFM 3D surface image of as-deposited AlO _x film after hot plate drying at 250 °C. RMS roughness is 0.33 nm.	98
Figure 5.12: (a) AFM 2D surface image (b) AFM 3D surface image of AlO _x film after PDA (520 °C, 20 min, O ₂). RMS roughness is 0.33 nm.	98

Figure 5.13: RMS roughness of the plane silicon wafer before AlO _x film deposition, as-deposited AlO _x film after hot plate drying at 250 °C and AlO _x film after PDA over 2-inch silicon wafer.	99
Figure 5.14: FTIR of as-deposited , PDA and RTP-fired (860 °C) AlO _x film from 4000 cm ⁻¹ to 400 cm ⁻¹ (3000 Hyperion Microscope with Vertex 80 FTIR System, Bruker, Germany).	101
Figure 5.15: FTIR of as-deposited, PDA and RTP-fired (860 °C) AlO _x film. (a) From the range of 2400 cm ⁻¹ to 2300 cm ⁻¹ . (b) From the range of 3800 cm ⁻¹ to 3500 cm ⁻¹ .	101
Figure 5.16: Optical surface image of RTP-fired (860 °C) AlO _x film by Olympus MX61 microscope.	104
Figure 5.17: (a) Zeta 2D optical surface image of RTP-fired (860 °C) AlO _x film (b) Zeta 3D optical surface image of RTP-fired (860 °C) AlO _x film for 70 μm × 93 μm area.	104
Figure 5.18: Physical characteristics of the spray coated AlO _x film after PDA at 520 °C for 20 min. (a) XPS depth profile (b) Cross sectional HRTEM image. The thickness of the IL is about 2 nm.	105
Figure 6.1: (a) Series resistance corrected C-V and G-V curves of MIS capacitors measured at 1 MHz. After AlO _x film deposition, PDA was performed in O ₂ at 520 °C for 20 min. (b) C-V characteristics (rescaled version of Figure 6.1 (a)) showing the hysteresis. Hysteresis is seen to be 10 mV. The red arrows indicate the direction of the voltage sweep. The measurement was started from inversion.	108
Figure 6.2: D _{it} and Q _f extracted from series resistance corrected C-V and G-V characteristics. Data extracted from 4 devices are shown.	109
Figure 6.3: (a) I-V characteristics of an MIS capacitor. After deposition, the AlO _x was subjected to PDA in O ₂ at 520 °C for 20 min. (b) Weibull plot of the breakdown voltage (V _{BD}) for 47 MIS capacitors.	110
Figure 6.4: The measured minority carrier lifetime and S _{eff} as a function of injection level for the AlO _x sample annealed at 520 °C for 20 min in O ₂ . τ _{eff} is 471 μs and S _{eff} is 8 cm·s ⁻¹ at Δn of 1 × 10 ¹⁵ cm ⁻³ .	111
Figure 6.5: (a) The temperature profile with a peak of 790 °C used for RTP firing. (b) The measured minority carrier lifetime and S _{eff} as a function of the peak temperature of the RTP process at Δn of 1 × 10 ¹⁵ cm ⁻³ for the AlO _x sample annealed at 520 °C for 20	114

min in O₂.

Figure 7.1: Measured Auger corrected inverse effective carrier lifetime as a function of $(\Delta n + N_{\text{dop}})$ for different BRL removal methods. The silicon samples were double side boron diffused and passivated by spray coated 10 nm AlO_x film. 118

Figure 7.2: Process flow of sample preparation for photolithography and LFC experiments. 121

Figure 7.3: Optical images of optical lithography process steps to pattern the spray coated AlO_x film on textured silicon surface for metallization. a) After MF319 development of PPR (75 μm lines) b) After HF (1%) etching of AlO_x film c) Patterned AlO_x film after PPR removal by acetone. 122

Figure 7.4: Zeta 3D microscope image analysis of a laser-fired contact hole (Z: 30.5 mm) with 2 μm depth (all measurements are in μm). (a) 2D line profile for step height measurement on the sample surface. (b) Analysis report for 2D line profile showing step height ~2 μm between the red markers. (c) 2D view of the sample. (d) 3D view of the sample. 123

Figure 7.5: Zeta 3D microscope image analysis of a laser-fired contact hole (Z: 30.7 mm) with ~3 μm depth (all measurements are in μm). (a) 2D line profile for step height measurement on the sample surface. (b) Analysis report for 2D line profile showing step height ~3 μm between the red markers. (c) 2D composite view of the sample. (d) 3D view of the sample. 124

Figure A.1: Thickness variation of spin coated AlO_x films as a function of etch time for various chemicals. 133

Figure A.2: Process details for aluminum silicate deposition. 134

Figure A.3: Optical images of spin coated AlSi_xO_y film. (a) Scale bar: 200 μm. (b) Scale bar: 50 μm. 135

List of Tables

Table 2.1: Summary of the reported AlO _x film properties deposited by ALD method.	24
Table 2.2: Summary of the reported AlO _x film properties deposited by PECVD method.	25
Table 2.3: Summary of the reported AlO _x film properties deposited by sputtering method.	27
Table 2.4: Summary of the reported AlO _x film properties deposited by spin coating method.	28
Table 2.5: Summary of the reported AlO _x film properties deposited by spray pyrolysis method.	30
Table 4.1: The thickness and RI of spin coated AlO _x film measured by spectroscopic ellipsometer for Sample A. The leftmost column of the table shows the sample indicating the positions where the measurements are performed.	67
Table 4.2: The effect of post deposition RTP annealing on thickness and RI of spin coated AlO _x films—Sample B, Sample C and Sample D—prepared using different molar concentration.	68
Table 4.3: Two coating techniques of film deposition.	81
Table 5.1: Contact angle measurement of the samples A, B and C.	95
Table 5.2: Range of wavenumber and peak position for AlO _x .	102
Table 6.1: Comparison of thermal stability of AlO _x films deposited by various techniques for p-type c-Si surface passivation.	113
Table 7.1: Comparison of passivation properties of AlO _x films deposited by various techniques for p ⁺ emitter.	119
Table A.1: Ellipsometry analysis of spin coated AlSi _x O _y film. The rightmost column of the table shows the sample indicating the positions where the measurements are performed.	135

List of Symbols

Symbol	Description
A	Area, cm^2
$B_{\text{Auger,n}}$	Electron Auger recombination coefficient, $\text{cm}^6 \cdot \text{s}^{-1}$
$B_{\text{Auger,p}}$	Hole Auger recombination coefficient, $\text{cm}^6 \cdot \text{s}^{-1}$
B_r	Coefficient of radiative recombination, $\text{cm}^3 \cdot \text{s}^{-1}$
C_{acc}	Accumulation capacitance, $\text{F} \cdot \text{cm}^{-2}$
$C_{\text{acc,F}}$	Accumulation capacitance in farads, F
C_c	Corrected capacitance, F
C_{FB}	Flat-band capacitance, $\text{F} \cdot \text{cm}^{-2}$
$C_{\text{S,min}}^{\text{HF}}$	Minimum value of semiconductor capacitance at high frequency, $\text{F} \cdot \text{cm}^{-2}$
C_m	Measured capacitance, F
C_{ma}	Measured capacitance in the strong accumulation region, F
C_{max}	Maximum value of capacitance, $\text{F} \cdot \text{cm}^{-2}$
$C_{\text{max,G}}$	Capacitance at voltage corresponding to G_{max} , F
C_{MG}	Capacitance at mid-gap voltage, $\text{F} \cdot \text{cm}^{-2}$
C_{min}	Minimum value of capacitance, $\text{F} \cdot \text{cm}^{-2}$
$C_{\text{S,FB}}$	Semiconductor capacitance at flat-band voltage, $\text{F} \cdot \text{cm}^{-2}$
$C_{\text{S,MG}}$	Semiconductor capacitance at mid-gap voltage, $\text{F} \cdot \text{cm}^{-2}$
D	Minority carrier diffusion constant, $\text{cm}^2 \cdot \text{s}^{-1}$

D_n	Electron diffusion constant, $\text{cm}^2 \cdot \text{s}^{-1}$
D_{it}	Density of interface states, $\text{eV}^{-1} \cdot \text{cm}^{-2}$
d	Solvent density, $\text{g} \cdot \text{cm}^{-3}$
d_0	Initial value of solvent density, $\text{g} \cdot \text{cm}^{-3}$
E_b	Binding energy, eV
E_{BG}	Band gap energy, V
E_c	Conduction band energy, eV
EOT	Equivalent oxide thickness, cm
E_{sp}	Energy of the electron ejected from the material by X-ray, eV
E_t	Defect energy level, eV
E_v	Valance band energy, eV
e	Evaporation rate of the solvent, $\text{cm} \cdot \text{s}^{-1}$
f	Frequency, Hz
G	Electron-hole pair generation rate, $\text{cm}^{-3} \cdot \text{s}^{-1}$
G_c	Corrected conductance, S
G_m	Measured conductance, S
G_{ma}	Measured conductance in the strong accumulation region, S
G_{max}	Peak conductance, S
h	Planck's constant, $4.1357 \times 10^{-15} \text{ eV} \cdot \text{s}$
I	Current, A

J_0	Saturation current density, $A \cdot cm^{-2}$
J_{0e}	Emitter saturation current density, $A \cdot cm^{-2}$
$J_{0e(back)}$	Saturation current density for back emitter region, $A \cdot cm^{-2}$
$J_{0e(front)}$	Saturation current density for front emitter region, $A \cdot cm^{-2}$
J_{rec}	Emitter recombination current density, $A \cdot cm^{-2}$
J_{sc}	Short-circuit current density, $A \cdot cm^{-2}$
k	Boltzmann's constant, $1.33 \times 10^{-23} J \cdot K^{-1}$ or $8.6173 \times 10^{-5} eV \cdot K^{-1}$
K	Relative permittivity or dielectric constant
K_{high-k}	Relative permittivity of the high-k material
K_{ox}	Relative permittivity of the oxide
K_{Si}	Relative permittivity of the silicon
K_{SiO_2}	Relative permittivity of silicon dioxide
L_d	Extrinsic Debye length, cm
M	Molarity, mol·ml
n	Concentration of electrons, cm^{-3}
n_0	Concentration of electrons at thermal equilibrium, cm^{-3}
n_1	Electron SRH density, cm^{-3}
N_A	Acceptor impurity concentration, cm^{-3}
N_C	Effective density of states in the conduction band, cm^{-3}
N_D	Donor impurity concentration, cm^{-3}

N_{dop}	Dopant density of the base, cm^{-3}
n_i	Intrinsic carrier concentration, cm^{-3}
n_s	Concentration of electrons at the surface, cm^{-3}
n_{s0}	Concentration of electrons at the surface in thermal equilibrium, cm^{-3}
N_t	Concentration of the trap centers, cm^{-3}
N_{ts}	Defect density at the surface, cm^{-2}
N_V	Effective density of states in the valence band, cm^{-3}
p	Concentration of holes, cm^{-3}
p_0	Concentration of holes at thermal equilibrium, cm^{-3}
p_1	Hole SRH density, cm^{-3}
p_s	Concentration of holes at the surface, cm^{-3}
p_{s0}	Concentration of holes at the surface in thermal equilibrium, cm^{-3}
Q	elementary charge, $1.6 \times 10^{-19} \text{ C}$
Q_f	Fixed oxide charge density, cm^{-2}
R	Recombination rate, $\text{cm}^{-3} \cdot \text{s}^{-1}$
R_{nrad}	Non radiative recombination rate, $\text{cm}^{-3} \cdot \text{s}^{-1}$
R_{rad}	Radiative recombination rate, $\text{cm}^{-3} \cdot \text{s}^{-1}$
R_R	Total radiative recombination rate, $\text{cm}^{-3} \cdot \text{s}^{-1}$
R_s	Series resistance, S^{-1}
R_{sh}	Sheet resistance, Ω/\square

S	Surface recombination velocity, $\text{cm}\cdot\text{s}^{-1}$
s_1, s_2, s_3 and s	Probe spacings in 4-probe measurements, cm
S_{eff}	Effective surface recombination velocity, $\text{cm}\cdot\text{s}^{-1}$
$S_{\text{eff,max}}$	Maximum effective surface recombination velocity, $\text{cm}\cdot\text{s}^{-1}$
S_{n0}	Surface recombination velocity for electrons, $\text{cm}\cdot\text{s}^{-1}$
S_{p0}	Surface recombination velocity for holes, $\text{cm}\cdot\text{s}^{-1}$
T	Absolute temperature, K
t_f	Final film thickness, cm
t_{ox}	Oxide film thickness, cm
$t_{\text{high-k}}$	Thickness of the high-k dielectric material, cm
U	Net recombination rate, $\text{cm}^{-3}\cdot\text{s}^{-1}$
U_{Auger}	Net Auger recombination rate, $\text{cm}^{-3}\cdot\text{s}^{-1}$
U_{rad}	Net radiative recombination rate, $\text{cm}^{-3}\cdot\text{s}^{-1}$
U_s	Net surface recombination rate, $\text{cm}^{-2}\cdot\text{s}^{-1}$
U_{SRH}	Net Shockley-Read-Hall recombination rate, $\text{cm}^{-3}\cdot\text{s}^{-1}$
V	Voltage, V
V_{BD}	Breakdown voltage, V
V_{FB}	Flat-band voltage, V
V_{MG}	Mid-gap voltage, V
$V_{\text{MG,ideal}}$	Ideal value of mid-gap voltage, V

$V_{oc,max}$	Maximum open-circuit voltage, V
V_{sample}	Output voltage from RF-bridge circuit of lifetime tester, V
V_{th}	Thermal velocity, $cm \cdot s^{-1}$
W	Silicon wafer thickness, cm
X_{dmax}	Maximum depletion width, cm
X_{MG}	Depletion width at mid-gap, cm
α	Scale parameter of Weibull distribution, V
β	Shape parameter of Weibull distribution
Δn	Excess electron density, cm^{-3}
Δp	Excess hole density, cm^{-3}
Δp_s	Excess surface hole concentration, cm^{-3}
Δn_{avg}	Average excess carrier density, cm^{-3}
Δn_s	Excess surface electron concentration, cm^{-3}
$\Delta \sigma$	Excess photoconductance, S
ϵ	Permittivity of the dielectric material, $F \cdot cm^{-1}$
ϵ_0	Permittivity of free space or vacuum, $8.854 \times 10^{-14} F \cdot cm^{-1}$
η	Viscosity, $g \cdot cm^{-1} \cdot s^{-1}$
η_{int}	Internal radiative quantum efficiency
θ	Contact angle, $^\circ$
θ_w	Water contact angle, $^\circ$

μ_n	Electron mobility in the semiconductor, $\text{cm}^2 \cdot \text{V}^{-1} \cdot \text{s}^{-1}$
μ_p	Hole mobility in the semiconductor, $\text{cm}^2 \cdot \text{V}^{-1} \cdot \text{s}^{-1}$
ν	Frequency of X-rays, s^{-1}
ξ_{BD}	Dielectric breakdown field, $\text{V} \cdot \text{cm}^{-1}$
ρ	Resistivity, $\Omega \cdot \text{cm}$
σ	Conductance, S
σ_{Si}	Conductance of the silicon sample at equilibrium, S
σ_{light}	Conductance of the silicon sample due to light illumination, S
σ_n	Electron capture cross section, cm^2
σ_p	Hole capture cross section, cm^2
τ	Recombination lifetime, s
$\tau_{n,\text{Auger}}$	Auger lifetime for electrons in p-type doped material, s
τ_{Auger}	Auger lifetime, s
τ_{bulk}	Bulk lifetime, s
$\tau_{\text{E,hi}}$	Emitter lifetime for an n- and p-type base under high injection, s
$\tau_{\text{E,li}}$	Emitter lifetime for an n- and p-type base under low injection, s
τ_{eff}	Effective lifetime, s
$\tau_{n,\text{rad}}$	Electron minority carrier radiative lifetime, s
τ_{nrad}	Non radiative lifetime, s
$\tau_{p,\text{Auger}}$	Auger lifetime for holes in n-type doped material, s

$\tau_{p,\text{rad}}$	Hole minority carrier radiative lifetime, s
τ_{rad}	Radiative lifetime, s
τ_{SRH}	Shockley-Read-Hall lifetime, s
τ_{surface}	Surface recombination lifetime, s
ϕ_{B}	Bulk potential, V
ϕ_{M}	Metal work function, V
ϕ_{MS}	Work-function difference between the metal gate and semiconductor, V
ϕ_{S}	Semiconductor work function, V
ϕ_{sp}	Work function of the spectrometer, eV
χ	Electron affinity, V
ω	Angular frequency, $\text{rad}\cdot\text{s}^{-1}$
ω_{S}	Angular velocity of spinner, $\text{rad}\cdot\text{s}^{-1}$

List of Acronyms

Acronym	Description
a-Si:H	Hydrogenated amorphous silicon
a-SiC _x :H	Hydrogenated amorphous silicon carbide
a-SiN _x :H	Hydrogenated amorphous silicon nitride
AFM	Atomic force microscope
Ag	Silver
Al	Aluminium
Al(CH ₃) ₃	Trimethylaluminium
AlCl ₃	Aluminum trichloride
ALD	Atomic layer deposition
Al ₂ O ₃	Aluminium oxide (stoichiometric)
AlO _x	Aluminium oxide (non-stoichiometric)
Al(OBu) ₃	Alumina–sec–butoxide
Al(OEt) ₃	Aluminium(III) ethoxide
Al(O ⁱ Pr) ₃	aluminium(III) isopropoxide
Al(NO ₃) ₃ ·9H ₂ O	Aluminium nitrate nonahydrate
AlSi _x O _y	Aluminum silicate
APCVD	Atmospheric pressure chemical vapor deposition
ARC	Anti-reflection coating

Ar	Argon
BBr ₃	Boron tribromide
BCl ₃	Boron trichloride
BHF	Buffered hydrofluoric acid
BO	Boron-oxygen
BRL	Boron-rich layer
BSF	Back surface field
CDF	Cumulative distribution function
CH ₃ OCH ₂ CH ₂ OH	2-methoxyethanol
CIS	Copper indium selenium
CdTe	Cadmium telluride
CIGS	Copper indium gallium selenium
CO ₂	Carbon dioxide
c-Si	Crystalline silicon
C-V	Capacitance versus voltage
Cz	Czochralski
DC	Direct current
DI	Deionized
DSP	Double side polished
EDP	Ethylene diamine pyrocatechal

ESCA	Electron spectroscopy for chemical analysis
eV	Electron volt
FTIR	Fourier transform infrared spectroscopy
FZ	Float-zone
Gt	Gigatonnes
G-V	Conductance versus voltage
H ₂	Hydrogen
H ₂ O ₂	Hydrogen peroxide
HCl	Hydrochloric acid
HF	Hydrofluoric acid
HFCV	High frequency capacitance voltage
HJ-IBC	Heterojunction interdigitated back contact
HNO ₃	Nitric acid
H ₂ O	Water
H ₃ PO ₄	Phosphoric acid
H ₂ SO ₄	Sulphuric acid
HRTEM	High-resolution transmission electron microscope
IC	Integrated circuit
IBC	Interdigitated back contact
ICPCVD	Inductively coupled plasma chemical vapour deposition

IEA	International Energy Agency
IEA-PVPS	International Energy Agency-Photovoltaic Power Systems Programme
IL	Interfacial layer
IPA	Isopropyl alcohol
IR	Infra-red
IRENA	International Renewable Energy Agency
ITRPV	International Technology Roadmap for Photovoltaic
I-V	Current versus voltage
LCO	Laser contact opening
LCOE	Levelised cost of electricity
LeTID	Light and elevated temperature induced degradation
LFC	Laser fired contact
LFICP	Low frequency inductively coupled plasma
LID	Light induced degradation
mc-Si	Multi-crystalline silicon
MIBK	Methyl isobutyl ketone
MIS	Metal insulator semiconductor
MWh	Megawatt-hour
n ⁺	Highly n-type doped silicon
N ₂	Nitrogen

NaOCl	Sodium hypochlorite
NAOS	Nitric acid oxidation of Si
NH ₃	Ammonia
NH ₄ OH	Ammonium hydroxide
O ₂	Oxygen
O ₃	Ozone
p ⁺	Highly p-type doped silicon
PA-ALD	Plasma assisted atomic layer deposition
PC	Personal computer
PDA	Post deposition annealing
PECVD	Plasma-enhanced chemical vapour deposition
PERC	Passivated emitter and rear contacts
PERL	Passivated emitter and rear locally diffused
PERT	Passivated emitter rear totally diffused
PID	Proportional-integral-derivative
PL	Photoluminescence
POCl ₃	Phosphorus oxychloride
PPR	Positive photoresist
PSG	Phosphosilicate glass
PV	Photovoltaic or Photovoltaics

PVD	Physical vapour deposition
QSS	Quasi steady state
RCA	Radio Corporation of America
RF	Radio frequency
RI	Refractive index
RMS	Root mean square
rpm	Rotations per minute
RTP	Rapid thermal processing
SDR	Saw damage removal
SDS	Sustainable Development Scenario
Si	Silicon
SiH ₄	Silane
sccm	Standard cubic centimeter per minute
SiN _x	Silicon nitride
SiN _x :B	Boron doped silicon nitride
SiO ₂	Silicon dioxide (stoichiometric)
SiO _x	Silicon oxide (non-stoichiometric)
slpm	Standard liter per minute
SSP	Single side polished
STEPS	Stated Policies Scenario

SRH	Shockley-Read-Hall
TEM	Transmission electron microscope
TEOS	Tetra-ethyl-orthosilicate
TES	Transforming Energy Scenario
TFEC	Total final energy consumption
TiO _x	Titanium oxide (non-stoichiometric)
TiO ₂	Titanium oxide (stoichiometric)
TMA	Trimethylaluminum
TOPCon	Tunnel oxide passivated contact
TMAH	Tetramethylammonium hydroxide
USD	United States dollar
USP	Ultrasonic spray pyrolysis
UV	Ultraviolet
XPS	X-ray photoelectron spectroscopy

Chapter 1

Introduction

Global demand for electricity is increasing rapidly due to the increase in population and a rise in the modern standard of living. According to the World Population Prospects (2019 revision), published by the Population Division of the UN Department of Economic and Social Affairs, the population of the world is expected to increase in the next 30 years from 7.7 billion in 2019 to 8.5 billion in 2030, 9.7 billion in 2050 and 10.9 billion in 2100 [1]. However, the energy needs of this rising population have to be met. The International Energy Agency (IEA) in 2019 estimated that nearly 770 million people lived their daily lives without access to electricity, mostly from Sub-Saharan Africa (578 billion) and developing Asia (155 billion) [2].

The share of electricity in total final energy consumption (TFEC) has increased since 1971 [3]. In IEA's Sustainable Development Scenario (SDS), electricity's share in TFEC is further increasing until 2040 [3]. In IEA's Stated Policies Scenario (STEPS), demand for global electricity increases by 2.1% per year to 2040. This is twice the rate of global primary energy demand and it leads to an increase in share of electricity in TFEC from 19% in 2018 to 24% in 2040 [4]. In International Renewable Energy Agency (IRENA)'s Transforming Energy Scenario (TES), electricity's share in final energy consumption grows from 20% in 2020 to almost 50% by 2050, half of global energy demand [5].

Fossil fuels (coal-38%, natural gas-23% and oil-2.9%), nuclear (10.1%), and renewable sources such as hydropower (16.2%), wind (4.8%), solar (2.1%), biofuels and waste (2.4%), geothermal, tidal and other sources (0.5%) provide electricity generation worldwide [6]. In 2018, around 64% of global electricity generation was from fossil fuels which are carbon intensive. Energy-related carbon dioxide (CO₂) emissions reached a record high of 33.1 gigatonnes (Gt) CO₂ in 2018 mainly due to rising electricity demand and 30% of global CO₂ emissions were from coal-fired electricity generation [7]. Moreover, fossil fuels are finite resources on earth and will eventually run out due to higher energy demand unless conserved [8].

Nuclear energy provided about 10% of the electricity worldwide in 2018 [6]. Based on a variety of indicators, a research article by Markard et al. suggests that nuclear energy is in a phase of decline at a global scale [9]. Another report by Taeyoung et al. reveals that “nuclear energy does not contribute to carbon reduction unlike renewable energy” [10]. According to a report published by Sovacool et al., “Larger-scale national nuclear attachments do not tend to associate with significantly lower carbon emissions while renewables do” [11].

The share of renewables in electricity generation has already surpassed nuclear. “Renewables grow rapidly in all our scenarios, with solar at the centre of this new constellation of electricity generation technologies.” said the IEA’s report, which also said “In the STEPS, renewables meet 80% of the growth in global electricity demand to 2030” [12]. Globally, around 25% of electricity was provided by renewable energy sources in 2018 [6]. Investments in renewable energy sources such as solar photovoltaics (PV) could ensure a sustainable future for electricity need. Sun is the most important and unlimited source of energy available for us on the earth. Silicon (Si) is the second most abundant element (27.7% by weight) found in the earth's crust after oxygen [13]. Solar radiation from the sun can be used to produce electricity using silicon solar cells [14].

Solar PV is becoming the primary focus of many researchers, engineers and scientists all over the world and they are working on it continuously. As a result, not only the performance is improving, but also the cost has reduced significantly. Renewable energy employment stimulated by investments is increasing worldwide. IRENA's roadmap for 2050 indicates that solar PV would account for almost half of the renewable jobs, followed by bioenergy and wind in the TES [5]. African countries are increasing the investments in solar PV to meet the growing demand for electricity [15,16].

According to the IERNA's new report, solar PV and wind are increasingly the cheapest renewable electricity sources in many markets around the world [5]. A report by IEA indicates that solar PV is steadily cheaper than new coal- or gas-fired power plants in most of the world, and solar power projects now provide the cheapest electricity in history [12]. According to IRENA, the global weighted average levelised cost of electricity (LCOE) generated from solar PV and onshore wind has fallen by 82% (United States dollar (USD) 68.4 per megawatt-hour (MWh)) and 45% (USD 52.8 per MWh) respectively over the period 2000–2019 [5]. IRENA expects that solar and wind power costs will continue to fall till 2030 [5].

In India, solar is emerging as a major source of electricity surpassing other renewable technologies such as wind and hydro in future as shown in Figure 1.1. The electricity production from solar is expected to increase continuously and reaches 52% by 2050, from 3% in 2019 [17].

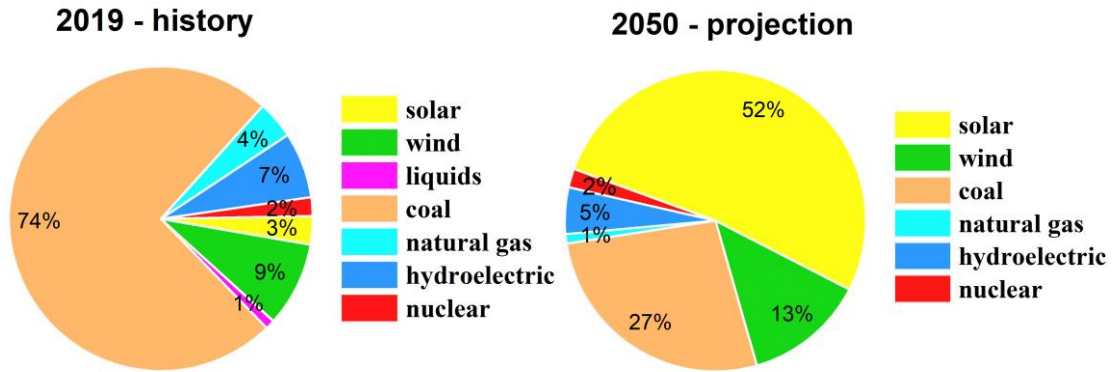


Figure 1.1: Share of India’s electricity generation for selected energy sources by single region scenario, data adapted from [17].

In general, the commercially available solar cell technologies can be classified into three major categories: wafer-based (mono-crystalline silicon and multi-crystalline silicon (mc-Si)), thin film technologies (copper indium selenium (CIS), copper indium gallium selenium (CIGS), cadmium telluride (CdTe) and organic PV) and multi-junction [18]. A photovoltaics report [19] said, “Si-wafer based PV technology accounted for about 95% of the total production in 2020. The share of mono-crystalline technology is now about 84% (compared to 66% in 2019) of total crystalline silicon (c-Si) production”. As reported in [20], the efficiencies of c-Si PV cells have reached above 25%. Although c-Si solar cells have higher efficiency, the cost of c-Si solar cells is high compared to mc-Si solar cells [21]. The next challenge is reduction of c-Si solar cell cost and improving the performance by implementing enhanced solar cell concepts, materials and technologies compatible with mass production at low costs.

Excellent passivation of the c-Si surface mitigates the electronic recombination losses and thereby increasing efficiency of the c-Si solar cells [22]. Aluminium oxide (Al_2O_3) film has proven to be excellent passivation material for p- and p⁺ type c-Si surfaces mainly due to very high negative fixed oxide charge density (Q_f) [22,23]. High negative fixed charges ($\sim 10^{13} \text{ cm}^{-2}$) present in the Al_2O_3 passivation layer repels the minority carriers (electrons) from the surface, thus reduces the recombination loss at the surface [24]. In addition, Al_2O_3

reduces the interface defect density (D_{it}) ($\sim 10^{11} \text{ eV}^{-1} \text{ cm}^{-2}$) by means of chemical passivation [25]. One of the important solar cell concepts—passivation of p-type silicon surface by high quality aluminium oxide (AlO_x) film using a cost-effective deposition process—is investigated in this thesis.

1.1 Motivation

In order to meet the rising global demand for electricity using solar PV, both efficiency enhancement and cost reduction of solar cells are necessary. The best technology solutions probably are development and implementation of novel technologies, materials and production processes that not only increase the efficiency, but also are suitable for mass production at low costs. One important solar cell concept currently leading in industrial production is p-type mono passivated emitter and rear cell (PERC) technology [21]. The solar cell efficiency is significantly affected by recombination losses at the silicon surfaces. In high efficiency PERC solar cells, AlO_x serves as a surface passivation layer on the rear surface and helps to reduce the recombination rate at the rear surface.

Silicon surface passivation by Al_2O_3 films for PV applications was first investigated by Jaeger and Hezel in the 1980s [26,27]. However, Al_2O_3 film as a silicon surface passivation layer gained considerable interest after its reintroduction in the 2000s by Agostinelli et al. [28,29] and Hoex et al. [30] demonstrating the excellent passivation properties of Al_2O_3 film by atomic layer deposition (ALD) technique. Al_2O_3 film is very well suited for the rear surface passivation of industrial PERC solar cells. However, the technique used for Al_2O_3 deposition is an important concern for PV industrial applications. In general, the deposition method which is simple, low cost with high throughput and compatible with the other fabrication steps of silicon solar cells is preferred by PV manufactures.

Al_2O_3 film can be deposited by a variety of techniques. ALD and plasma-enhanced chemical vapour deposition (PECVD) are two techniques currently used for the deposition of high quality Al_2O_3 films in industrial PV applications [21]. The ALD process is based on layer-by-layer growth that limits the deposition rate. In order to improve the throughput, batch ALD and spatial ALD method are also being used [22]. Moreover, hydrogen incorporation during Al_2O_3 deposition by ALD and PECVD methods leads to blister formation during high

temperature annealing processes [22]. Trimethylaluminum (TMA) is the most widely used precursor for Al_2O_3 deposition by ALD for research as well as industry applications [31]. TMA is highly volatile, pyrophoric and extremely reactive. Expensive safety standards with adequate system design are necessary for industrial use of this chemical. Although ALD and PECVD Al_2O_3 films provide good surface passivation, these two techniques are expensive compared to the wet chemistry processes for mass production. Therefore, implementation of a lower cost deposition method for Al_2O_3 film with good surface passivation properties is required and this thesis tries to address these issues of Al_2O_3 deposition.

1.2 Thesis outline

The subject matter of the thesis is organised into eight chapters:

Chapter 1 - contains background, context of problem, motivation, broad societal concern which emphasizes the motivation of this research and objectives, and thesis outline.

Chapter 2 - presents the basic concept of surface passivation using Shockley-Read-Hall (SRH) theory and carrier recombination in semiconductors. It discusses the potential of AlO_x film for surface passivation of silicon surfaces. It also provides literature review of AlO_x film as a surface passivation layer with various properties by existing deposition techniques.

Chapter 3 - gives the details on AlO_x solution preparation processes and sample preparation processes used in this thesis. It also gives the details on characterization techniques used in this work.

Chapter 4 - investigates spin coated and spray coated AlO_x films for p-type crystalline silicon surface passivation using spin coater and hand-held sprayer, respectively.

Chapter 5 - contains development of spray coating process for large area device applications. Details of the spray deposition system are also included in this chapter. It also discusses physical and structural characterization of spray coated AlO_x film deposited using spraying instrument.

Chapter 6 - discusses spray coated AlO_x film for surface passivation of p-type c-Si using spraying instrument.

Chapter 7 - includes preliminary investigations on integration of spray coated AlO_x in solar cells. The study of passivation of spray coated AlO_x film for p^+ -type silicon using spraying instrument also forms part of chapter 7. In addition, patterning of spray coated AlO_x film by photolithography process and laser fired contact process for making local rear contacts through spray coated AlO_x film are also investigated.

Chapter 8 - summarises the thesis, and provides a roadmap for future research based on the processes described in the previous chapters.

Chapter 2

Surface Passivation of Silicon - a Literature Review

In order to develop solution processed AlO_x film as a surface passivation layer, it is necessary to understand the physics of surface recombination and how it can be reduced using a passivation film such as AlO_x . This chapter starts with a discussion of an industrial PERC solar cell structure. It discusses recombination mechanisms in semiconductors. A literature survey reviewing the surface passivation quality of various dielectrics such as silicon dioxide (SiO_2), silicon nitride (SiN_x), hydrogenated amorphous silicon (a-Si:H) and Al_2O_3 is presented. This section also presents a review of the experimental techniques reported in literature to deposit AlO_x films such as ALD, PECVD, sputtering, spin coating and spray coating processes. A literature survey on surface preparation, effect of film thickness, optical properties requirements, activation of surface passivation, thermal stability, and passivation characteristics of $\text{AlO}_x/\text{c-Si}$ interface is presented. A literature survey on emitter passivation is also presented. It also includes review of crystalline silicon solar cells such as PERC, passivated emitter rear totally diffused (PERT), passivated emitter and rear locally diffused (PERL), tunnel oxide passivated contact (TOPCon) and interdigitated back-contact (IBC) cells. It also discusses integration of backside passivation layers in PERC solar cells.

2.1 Structure of PERC solar cell

The structure and the corresponding process flow of an industrial type Al_2O_3 PERC cell are shown in Figure 2.1 and Figure 2.2, respectively. The process flow of a typical industrial PERC cell starts with p-type Czochralski (Cz) c-Si wafer. The wafers usually have surface damages due to saw cutting and saw damage removal (SDR) process is performed to remove the damaged regions. After SDR process, the wafer surface is textured chemically to reduce optical reflection from the silicon surface. Then, an n-type emitter layer is grown by thermal diffusion process using phosphorus oxychloride (POCl_3) as dopant precursor. Edge isolation and rear side polishing is performed to remove electrical shorting between front and rear surfaces and to enhance light reflection from rear side, respectively. Al_2O_3 layer is

deposited for rear surface passivation followed by deposition of SiN_x as capping layer. A SiN_x anti-reflection coating (ARC) layer is deposited on the front emitter layer for emitter passivation and light management. Laser is used to selectively remove $\text{Al}_2\text{O}_3/\text{SiN}_x$ layer from the rear side to form local back surface field (BSF) (p^+) during metallization. Finally, printing and co-firing is carried out for electrical contacts using silver (Ag) paste at the front side and aluminium (Al) paste at the rear side [32].

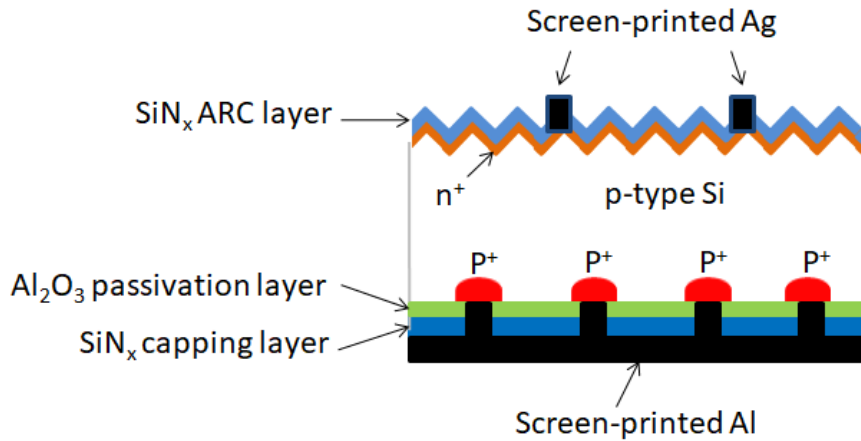


Figure 2.1: Schematic drawing of a typical industrial PERC solar cell structure [33].

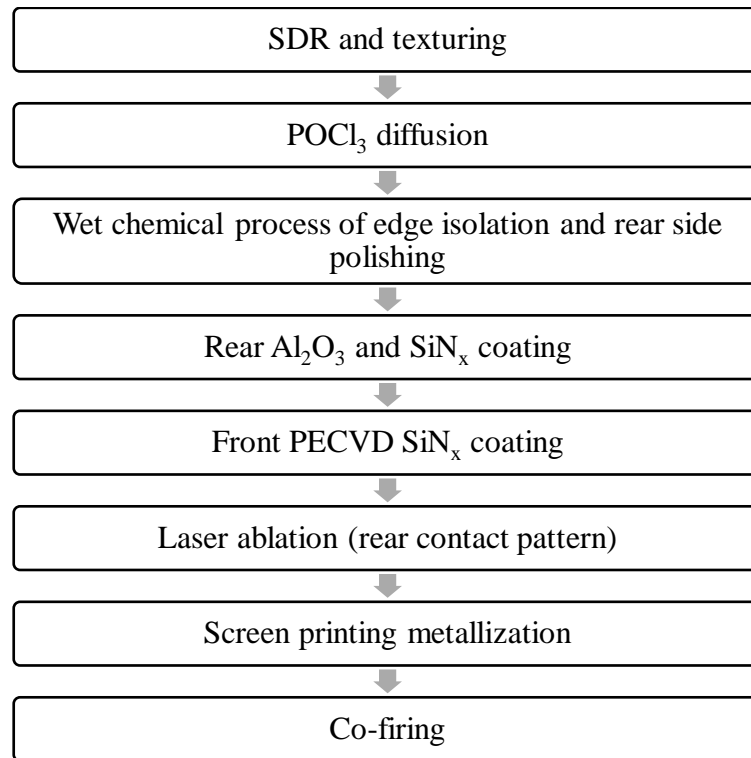


Figure 2.2: Process flow of CSUN's industrial PERC solar cell [33].

2.2 Theory of recombination processes

Recombination process reduces the density of electron-hole pairs and limits the solar cell efficiency. In a silicon solar cell, recombination process restores the non-equilibrium light generated electron-hole pair density to its thermal equilibrium value [34].

2.2.1 Recombination in the c-Si bulk

The recombination in the c-Si bulk can be classified into intrinsic and extrinsic recombination processes. Intrinsic recombination is unavoidable [35]. Intrinsic recombination can be further classified into two types depending on the way the excess energy is released by electron-hole pair recombination: radiative band-to-band recombination and Auger band-band recombination. Extrinsic recombination also known as SRH recombination is facilitated by defects such as impurities [35].

At equilibrium, the concentration of electrons (n_0) (in cm^{-3}) and concentration of holes (p_0) (in cm^{-3}) in silicon are related to the intrinsic carrier concentration (n_i) (in cm^{-3}) by the equation [36]

$$n_0 p_0 = n_i^2 \quad (2.1)$$

After the generation of excess electrons (Δn) (in cm^{-3}) and excess holes (Δp) (in cm^{-3}), the concentration of electrons (n) (in cm^{-3}) and the concentration of holes (p) (in cm^{-3}) becomes [36]

$$n = n_0 + \Delta n \quad p = p_0 + \Delta p \quad (2.2)$$

In silicon solar cells, these excess carriers continue to remain as free carriers for a limited time, as a result of which current and voltage is produced that leads to the generation of electricity.

Assuming $\Delta n = \Delta p$ which is true to optical generation in semiconductors, recombination lifetime (τ) (in s) can be defined as the average time for an electron-hole pair to recombine after generation [36].

$$\tau(\Delta n, n_0, p_0) = \frac{\Delta n}{U(\Delta n, n_0, p_0)} \quad (2.3)$$

where U defines the net recombination rate (in $\text{cm}^{-3}\cdot\text{s}^{-1}$). As can be seen, τ is dependent on both injection condition and doping.

Radiative recombination

This is also called as band-to-band recombination and it is the inverse process of the photon absorption. In the radiative recombination process, direct band-to-band transitions of an electron from the conduction band to the valence band causes emission of photons with energy equal to the band gap of the semiconductor. It is a dominant recombination mechanism in direct band gap semiconductors. Crystalline silicon is an indirect band gap semiconductor material. Due to conservation of momentum, a phonon is necessary for band-to-band transition [37]. Therefore, this process takes place more rapidly in direct band gap semiconductors than in indirect band gap semiconductors. In c-Si, radiative recombination is negligible compared to band-to-band Auger recombination and SRH recombination. Nonetheless, this recombination mechanism can be employed to measure effective lifetime by the photoluminescence (PL) method.

For a non-degenerate semiconductor under non-equilibrium conditions, the net recombination rate U_{rad} (in $\text{cm}^{-3}\cdot\text{s}^{-1}$) is given by [34,38]

$$U_{\text{rad}} = B_r(np - n_i^2) \quad (2.4)$$

where B_r is the coefficient of radiative recombination (in $\text{cm}^3\cdot\text{s}^{-1}$) and it is a property of the material.

The coefficient of radiative recombination, B_r , depends on a material's band gap and the absorption coefficient. For direct band gap materials, it ranges from 10^{-9} – 10^{-11} $\text{cm}^3\cdot\text{s}^{-1}$ and for indirect band gap materials, it varies from 10^{-13} – 10^{-15} $\text{cm}^3\cdot\text{s}^{-1}$ [34]. The constant B_r refers to the probability of a direct band-to-band transition in the semiconductor. For Si, the value of B_r is reported to be 2×10^{-15} $\text{cm}^3\cdot\text{s}^{-1}$ [37].

For p-type materials under low-level injection [34]

$$U_{\text{rad}} \approx B_r N_A \Delta n = \frac{n - n_0}{\tau_{n,\text{rad}}} \quad (2.5)$$

and the electron minority carrier radiative lifetime, $\tau_{n,\text{rad}}$ (in s) is [34]

$$\tau_{n,\text{rad}} = \frac{1}{B_r N_A} \quad (2.6)$$

where N_A is acceptor impurity concentration (in cm^{-3}).

Similarly, for n-type materials under low-level injection [34]

$$U_{\text{rad}} \approx B_r N_D \Delta p = \frac{p - p_0}{\tau_{p,\text{rad}}} \quad (2.7)$$

and the hole minority carrier radiative lifetime, $\tau_{p,\text{rad}}$ (in s) is

$$\tau_{p,\text{rad}} = \frac{1}{B_r N_D} \quad (2.8)$$

where N_D is donor impurity concentration (in cm^{-3}).

For direct band gap materials, since B_r is higher, the radiative lifetime τ_{rad} is generally much shorter ($10^{-9} - 10^{-7}$ s) [34]. For indirect band gap materials τ_{rad} is much higher (10^{-2} s) [34] and radiative processes are less probable.

Auger recombination

In the Auger recombination process, the energy is used to excite another electron in the conduction band or hole in the valence band, instead of photon emission. This excited charge carrier thermalizes towards the band edge, as a result of which the recombination energy is converted into phonons. As three charge carriers are involved, it is also known as three-particle recombination.

For Auger recombination, the net change in recombination rate (in $\text{cm}^{-3} \cdot \text{s}^{-1}$) under non-equilibrium conditions, for two electrons with a hole [34],

$$U_{\text{Auger}} = B_{\text{Auger},p} (n^2 p - n_0^2 p_0) \quad (2.9)$$

where $B_{\text{Auger,p}}$ is the hole Auger recombination coefficient (in $\text{cm}^6 \cdot \text{s}^{-1}$).

Similarly, for two holes [34],

$$U_{\text{Auger}} = B_{\text{Auger,n}}(p^2n - p_0^2n_0) \quad (2.10)$$

where $B_{\text{Auger,n}}$ is the electron Auger recombination coefficient (in $\text{cm}^6 \cdot \text{s}^{-1}$).

For electrons in p-type doped materials under low injection conditions, the Auger lifetime (in s) is given as [34]

$$\tau_{\text{n,Auger}} = \frac{1}{B_{\text{Auger,n}}N_A^2} \quad (2.11)$$

Similarly, for holes in n-type doped materials under low level injection, the Auger lifetime (in s) is given as

$$\tau_{\text{p,Auger}} = \frac{1}{B_{\text{Auger,p}}N_D^2} \quad (2.12)$$

This recombination is the dominant process in good quality silicon with doping concentration greater than 10^{17}cm^{-3} [37].

Bulk recombination through defects

Extrinsic recombination is often referred to as the SRH recombination after the researchers who first derived in 1952 the behaviour of this recombination process [39,40]. The manufacturing of extremely high purity semiconductors without defects and impurities can be difficult. Impurities and defects present in the semiconductors can cause allowed energy levels within the forbidden gap. These defect levels within the band gap of the bulk semiconductor are referred to as trap states. These trap states create a two-step recombination process by capturing free charge carriers.

For a single defect, the net recombination rate U_{SRH} ($\text{cm}^{-3} \cdot \text{s}^{-1}$) is described as [39,40]

$$U_{\text{SRH}} = \frac{(np - n_i^2)v_{\text{th}} N_t}{\sigma_p^{-1}(n + n_1) + \sigma_n^{-1}(p + p_1)} \quad (2.13)$$

where σ_n and σ_p are the capture cross sections for electrons and holes (in cm^2), respectively. N_t is the concentration of the trap centres (in cm^{-3}). v_{th} is the thermal velocity (in $\text{cm}\cdot\text{s}^{-1}$). n_1 and p_1 are the SRH densities (in cm^{-3}) and it is defined as [35]

$$n_1 = N_C e^{\left(\frac{E_t - E_C}{kT}\right)} \quad p_1 = N_V e^{\left(\frac{E_V - E_t}{kT}\right)} \quad (2.14)$$

where E_t is the energy level of the defect (in eV). N_C and N_V are the effective density of states in the conduction and valence band edges (in cm^{-3}), respectively. E_V and E_C represent the valence band and the conduction band energy (in eV) respectively. k represents the Boltzmann's constant which is $8.6173 \times 10^{-5} \text{ eV}\cdot\text{K}^{-1}$ and T represents absolute temperature (in K).

Bulk lifetime

The bulk lifetime (τ_{bulk}) (in s) of the silicon substrate comprises of τ_{rad} , τ_{Auger} and τ_{SRH} . It is given by the relation [35]

$$\frac{1}{\tau_{bulk}} = \frac{1}{\tau_{rad}} + \frac{1}{\tau_{Auger}} + \frac{1}{\tau_{SRH}} \quad (2.15)$$

where, τ_{rad} , τ_{Auger} and τ_{SRH} are lifetime due to radiative recombination, Auger recombination and SRH recombination, respectively (in s).

2.2.2 Recombination at the c-Si surface

Any defect or impurity present in the bulk or surface of silicon causes recombination. The surfaces or interfaces of a silicon substrate show a severe discontinuity of crystal lattice. This discontinuity of crystal structure gives rise to many dangling bonds, and therefore a large density of defect levels is found near the semiconductor surface within the band gap. These defects act as effective recombination centers, causing surface recombination.

The SRH analysis of section 2.1.1 again applies, and it is reformulated in terms of recombination events per unit surface area instead of unit volume. For a single defect at the surface, the net surface recombination rate, U_S in ($\text{cm}^{-2}\cdot\text{s}^{-1}$), is expressed as [35]:

$$U_s = \frac{(n_s p_s - n_i^2)}{\frac{n_s + n_1}{S_{p0}} + \frac{p_s + p_1}{S_{n0}}} \quad (2.16)$$

where $S_{n0} \equiv \sigma_n v_{th} N_{ts}$ and $S_{p0} \equiv \sigma_p v_{th} N_{ts}$ are the surface recombination velocity of electrons and holes (in $\text{cm}\cdot\text{s}^{-1}$), respectively with N_{ts} representing the density of defects at the surface (in cm^{-2}). n_s and p_s are the concentration of electrons and holes at the surface (in cm^{-3}), respectively.

In reality, defect levels of the interface are large and can be considered as continuously distributed throughout the band-gap. Their density and capture cross-sections at the surface will be dependent on their energy level. By integration Eq. (2.16), the surface recombination rate is expressed as [35]

$$U_s = (n_s p_s - n_i^2) \int_{E_v}^{E_c} \frac{v_{th}}{\frac{n_s + n_1}{\sigma_p(E)} + \frac{p_s + p_1}{\sigma_n(E)}} D_{it}(E) dE \quad (2.17)$$

where D_{it} refers to the density of states (in $\text{cm}^{-2}\cdot\text{eV}^{-1}$).

The surface recombination velocity, S (in $\text{cm}\cdot\text{s}^{-1}$), is defined as [35]

$$U_s(\Delta n_s, n_0, p_0) \equiv S(\Delta n_s, n_0, p_0) \Delta n_s \quad (2.18)$$

where $\Delta n_s = n_s - n_{s0} = p_s - p_{s0}$ (in cm^{-3}) refers to excess carrier density at the surface. n_{s0} and p_{s0} are the surface concentration of electrons and holes at thermal equilibrium (in cm^{-3}) (such that $n_{s0} \cdot p_{s0} = n_i^2$ at the surface). Surface recombination velocity [35]

$$S(\Delta n_s, n_0, p_0) = (n_0 + p_0 + \Delta n_s) \int_{E_v}^{E_c} \frac{v_{th}}{\frac{n_0 + n_1 + \Delta n_s}{\sigma_p(E)} + \frac{p_0 + p_1 + \Delta p_s}{\sigma_n(E)}} D_{it}(E) dE \quad (2.19)$$

where Δp_s (in cm^{-3}) is the excess hole concentration at the surface.

2.2.3 Methods to reduce surface recombination

It can be concluded from Eq. (2.17) that there are two fundamental mechanisms available for reducing the surface recombination rate at the silicon surface:

a) Reduction of surface state density

By reducing the interface state density, the surface recombination velocity can be reduced [36]. By growing or depositing a dielectric layer such as silicon oxide layer and aluminium oxide layer, many of the dangling bonds of the silicon can be passivated with oxygen or hydrogen atoms and the $D_{it}(E)$ can be reduced [36].

b) Reduction of the surface concentration of electrons or holes

The surface recombination rate U_S reaches its maximum when the surface carrier concentrations n_s and p_s are approximately equal. Therefore, minimising the minority carrier concentration (electrons or holes) near the surface reduces the surface recombination rate [36]. This can be achieved by formation of the electric field below the silicon surface.

- Doping the surface of silicon to form a high-low junction (p^+ - p or n^+ - n) such as an emitter region reduces the density of minority carriers at the surface [36].
- Deposition of a dielectric layer with fixed oxide charge forms an electric field near the surface causing field effect passivation [36]. The electric field created due to the fixed oxide charge density in the dielectric pushes away the minority carriers which reduces the recombination rate [36].

2.2.4 Emitter recombination

The emitter recombination includes both bulk and surface recombination mechanisms. Emitter doping profile is generally not uniform and the spatial variation in the dopant concentration leads to variations in the minority carrier concentration, Auger recombination, SRH recombination, carrier mobility, free-carrier absorption, effective masses of electron and hole, and the band gap [41] which makes emitter recombination modeling complicated. Other modeling challenges include possibility of a dead layer formation from the diffusion process. Heavily doped regions (e.g., emitters and back-surface fields) are generally characterized by a saturation current density (J_0) (in $A \cdot cm^{-2}$) [42]. The saturation current density of emitter regions (J_{0e}) in the silicon solar cells is a combination of recombination within the heavily doped emitter region and the recombination at the emitter doped surface.

The excess carrier concentration normally remains lower in the emitter region than in the bulk silicon wafer and the dominant bulk recombination mechanism is likely to be Auger

recombination. The recombination current into the emitter, J_{rec} (in $\text{A}\cdot\text{cm}^{-2}$) can be expressed after Kane and Swanson [43] as

$$J_{\text{rec}} = \frac{np}{n_i^2} J_{0e} \quad (2.20)$$

where J_{0e} is defined as emitter saturation current density (in $\text{A}\cdot\text{cm}^{-2}$).

Emitter recombination can be considered as a special case of surface recombination. The effective surface recombination velocity, S_{eff} (in $\text{cm}\cdot\text{s}^{-1}$) is defined as [35]

$$S_{\text{eff}} \equiv \frac{U_S}{\Delta n} \quad (2.21)$$

Combining Eq. (2.20) and Eq. (2.21) gives [44]

$$U_S = S_{\text{eff}} \Delta n = \frac{J_{\text{rec}}}{q} = \frac{np}{qn_i^2} J_{0e} \quad (2.22)$$

where q is the elementary charge of an electron (1.6×10^{-19} C).

By the quasi-static emitter approximation [45,46,47], relation of S_{eff} with J_{0e}

for p-type silicon,

$$S_{\text{eff}} = \frac{N_A + \Delta n}{qn_i^2} J_{0e} \quad (2.23)$$

for n-type silicon,

$$S_{\text{eff}} = \frac{N_D + \Delta n}{qn_i^2} J_{0e} \quad (2.24)$$

Determination of the emitter saturation current

If both sides of a silicon wafer are heavily diffused, the effective lifetime (τ_{eff}) (in s) can be expressed as [43]

$$\frac{1}{\tau_{\text{eff}}} - \frac{1}{\tau_{\text{Auger}}} = \frac{1}{\tau_{\text{SRH}}} + \frac{J_{0e(\text{front})} + J_{0e(\text{back})}}{qn_i^2 W} (N_{\text{dop}} + \Delta n) \quad (2.25)$$

In this expression, $J_{0e(\text{front})}$ and $J_{0e(\text{back})}$ are the saturation current densities for front and back emitter regions, respectively (in $\text{A}\cdot\text{cm}^{-2}$). W is the thickness of the wafer (in cm). N_{dop} is the dopant density of the base (in cm^{-3}).

The effective carrier lifetime (τ_{eff}) and emitter saturation current density (J_{0e}) were obtained from the measurement done using lifetime tester (Sinton instrument WCT-120) in the generalized 1/1 mode. The values of J_{0e} were estimated from the measurements of effective lifetime using a method proposed by Kane and Swanson [43],

$$\frac{1}{\tau_{\text{eff}}} - \frac{1}{\tau_{\text{Auger}}} = \frac{1}{\tau_{\text{SRH}}} + \frac{2J_{0e}}{qn_i^2W}(N_{\text{dop}} + \Delta n) \quad (2.26)$$

Determination of the maximum 1-sun open-circuit voltage ($V_{\text{oc,max}}$)

From the extracted J_{0e} values, the maximum 1-sun open-circuit voltage ($V_{\text{oc,max}}$) (in V) can be calculated using one diode equation for a symmetrical structure as shown in Figure 2.3 [48],

$$V_{\text{oc,max}} = \frac{kT}{q} \ln \left(\frac{J_{\text{sc}}}{2J_{0e}} + 1 \right) \quad (2.27)$$

where J_{sc} is the short-circuit current density (in $\text{A}\cdot\text{cm}^{-2}$). $V_{\text{oc,max}}$ was calculated assuming J_{sc} of $38 \text{ mA}\cdot\text{cm}^{-2}$ [48] and T of 298 K in this thesis.

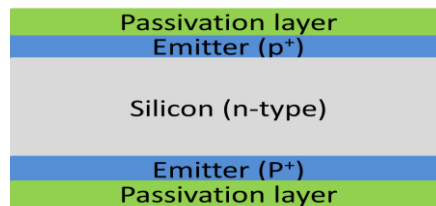


Figure 2.3: Device schematic for J_{0e} measurement.

To form symmetrical test structure for J_{0e} determination, silicon wafers are diffused and passivated using a passivation layer on both sides as shown in Figure 2.3 [43,48].

2.3 Surface passivation materials

High efficiency silicon solar cells strongly rely on surface passivation. The most important silicon surface passivation materials used for PV applications include SiO₂, SiN_x, a-Si:H and Al₂O₃.

2.3.1 Silicon dioxide (SiO₂)

Thermally grown SiO₂ is one of the important and widely used materials for applications in silicon based microelectronics [49,50,51]. In silicon photovoltaics, SiO₂ is a very important material [52]. The low interface state densities associated with the Si/SiO₂ interface reduce the surface recombination significantly and have enabled high solar cell efficiencies. In literature, very low D_{it} of ~10⁹ eV⁻¹·cm⁻² and positive Q_f over a range of 10¹⁰–10¹² cm⁻² was reported [53,54].

From the viewpoint of surface passivation, SiO₂ films provide passivation mainly by reducing the D_{it} at the silicon interface. For field effect passivation, the Q_f must be sufficiently high (> 10¹² cm⁻²). Hence, the main benefit of thermal SiO₂ is the high level of chemical passivation which can be achieved for both n- and p-type Si surfaces [55]. Mark et al. have studied surface passivation of thermal SiO₂ using a variety of commercially available silicon wafers with different substrate resistivities including both p-type (boron) and n-type (phosphorus) dopants [56]. Mark et al. reported S_{eff} of 0.46 cm·s⁻¹ and 2.4 cm·s⁻¹ for 90 Ω·cm and 1.5 Ω·cm n-type c-Si wafers, respectively [56]. In addition, Mark et al. reported S_{eff} of 0.63 cm·s⁻¹ and 1.4 cm·s⁻¹ for 150 Ω·cm and 10 Ω·cm p-type c-Si wafers, respectively [56]. Dingemans et al. reported S_{eff} < 6 cm·s⁻¹ and S_{eff} < 11 cm·s⁻¹ for 2 Ω·cm p-type c-Si and 3.5 Ω·cm n-type c-Si wafers, respectively using SiO_x (50 nm, PECVD)/hydrogenated amorphous silicon nitride (a-SiN_x:H) (70 nm, PECVD) passivation stack [57]. Bhajipale et al. [58] reported S_{eff} of 0.97 cm·s⁻¹ on n-type Cz-Si and 8.07 cm·s⁻¹ on p-type Cz-Si for SiO_x dielectric films (~17 nm) prepared using spray coating method. Here, the wafers were exposed to UV (ultraviolet) radiation for 5 min prior to SiO_x spray coating [58].

Ultrathin SiO_x oxides can also be grown by chemical based methods at low temperatures (< 200 °C). Mihailetchia et al. achieved record high efficiency of 18.3% using ultrathin SiO₂ layer grown by nitric acid oxidation of Si (NAOS) process with SiN_x

antireflection film [59]. Burgers et al. reported solar cell efficiencies of 19.5% on large area (239 cm²) with SiO_x grown by NAOS process [60]. Feldmann et al. reported efficiency of 24.4% for tunnel oxide passivated contact (TOPCon) solar cells using an ultrathin SiO_x oxide (< 2 nm) grown on n-type Si using nitric oxide (HNO₃) for passivation [61]. Grant et al. reported S_{eff} in the range 20–35 cm·s⁻¹ using anodic oxidation procedure after annealing at 400 °C in oxygen and forming gas [62]. Bordihn et al. [63] investigated three different wet chemical solutions: (a) HNO₃ (b) hydrochloric acid (HCl) mixed with hydrogen peroxide (H₂O₂) and (c) sulphuric acid (H₂SO₄) mixed with hydrogen peroxide (H₂O₂) and S_{eff} in the range 4–10 cm·s⁻¹ was reported for the chemical SiO₂ (2–4 nm)/Al₂O₃ (30 nm, ALD) stacks after an anneal treatment at 400 °C in nitrogen (N₂) ambient for 10 min. It is shown in literature that ultrathin SiO_x can be grown using ozone for surface passivation applications. For further discussions see the section 2.6.

Today's industrial silicon solar cells often utilize stack of different surface passivation materials such as SiO_x, SiN_x and Al₂O₃ for front and rear side passivation. SiN_x is often used in stack passivation schemes for front and rear surface passivation. Liu et al. have successfully developed an industrially feasible passivation stack—SiO₂ (~4 nm by thermal oxidation)/SiN_x (PECVD) on front and Al₂O₃ (PECVD)/SiN_x (PECVD) on rear side—for fabrication of PERC solar cells based on the existing PERC c-Si solar cells production line and reported efficiency of 22.15% [64].

2.3.2 Silicon nitride (SiN_x)

Silicon nitride is usually synthesized using a gas mixture of silane (SiH₄) and ammonia (NH₃). SiN_x films exhibit good passivation and anti-reflection performance [65]. The SiN_x passivation layers prepared by PECVD are well used by PV industries [21]. The high quality of surface passivation by SiN_x is due to a combination of the positive fixed charge and the lower interface state density. Elmiger et al. reported D_{it} of 5 × 10¹¹ eV⁻¹·cm⁻² and positive Q_f of 3 × 10¹² cm⁻² for both p- and n-type substrates [66]. Here, the SiN_x films were deposited in a commercial parallel-plate plasma deposition reactor. Positive Q_f of about 2 × 10¹² cm⁻² was reported for 2–3 Ω·cm p-type Si substrate by Zhou et al. [67]. Here, low temperature SiN_x:H films were deposited by low frequency inductively coupled plasma (LFICP) method. Dauwe reported D_{it} of 2.9 × 10¹¹ eV⁻¹·cm⁻² and positive Q_f of 3.1 × 10¹² cm⁻²

² for 1.5 $\Omega\cdot\text{cm}$ p-type Si substrate for SiN_x film deposited by PECVD technique [68]. Lelievre et al. reported S_{eff} of 4 $\text{cm}\cdot\text{s}^{-1}$ and 14 $\text{cm}\cdot\text{s}^{-1}$ for 5 $\Omega\cdot\text{cm}$ n-type and p-type c-Si wafers, respectively using SiN_x films deposited by PECVD technique [69]. Lauinger et al. reported S_{eff} of 4 $\text{cm}\cdot\text{s}^{-1}$ and 20 $\text{cm}\cdot\text{s}^{-1}$ on 1.5 $\Omega\cdot\text{cm}$ and 0.7 $\Omega\cdot\text{cm}$ p-type c-Si wafers, respectively using SiN_x films deposited by PECVD technique [70]. Chen et al. demonstrated $S_{\text{eff}} \leq 2 \text{ cm}\cdot\text{s}^{-1}$ on 1 $\Omega\cdot\text{cm}$ n-type Si wafer using PECVD SiN_x film [71]. Richter et al. reported S_{eff} of $\sim 1.6 \text{ cm}\cdot\text{s}^{-1}$ on 1 $\Omega\cdot\text{cm}$ n-type float-zone (FZ) c-Si wafer using PECVD SiN_x film [72].

Silicon nitride films are also used as a capping layer for AlO_x passivation layer on massive production line of PERC cells [21]. Conversion efficiency of 21.97% for PERC solar cell was demonstrated using rear passivation stack of Al_2O_3 (18 nm, ALD)/ SiN_x (120 nm, inductively coupled plasma chemical vapor deposition (ICPCVD)) and ARC of SiN_x (85 nm, ICPCVD) [73]. Industrial PERC solar cells demonstrated cell efficiencies in the range of 20.5–20.8 % using rear passivation stack of Al_2O_3 (10 nm, ALD)/ SiN_x (100 nm, PECVD) and ARC of SiN_x by PECVD [33]. Conversion efficiency of 22.61% for PERC solar cell was reported using rear AlO_x (PECVD)/ SiN_x (PECVD) stack and passivation/ARC SiN_x (PECVD) layer on front side [74]. Conversion efficiency of 21% for PERC solar cell was achieved using rear Al_2O_3 (30 nm, PECVD)/ SiN_x (130–165 nm, PECVD) stack and ARC of SiN_x (60–80 nm, PECVD) film [75]. 21.63% efficiency was achieved for PERC solar cell using rear Al_2O_3 (ALD)/ SiN_x (PECVD) stack and front SiO_2 (thermal oxidation)/ SiN_x (PECVD) stack [76]. LONGi Solar Energy Technology Co. Ltd. achieved conversion efficiency of 23.83% for a commercial p-type Cz PERC cell using 70–85 nm SiN_x on the front as surface passivation and ARC layer deposited by a PECVD reactor (MAiA, Meyer Burger) [77].

2.3.3 Hydrogenated amorphous silicon (a-Si:H)

Hydrogenated amorphous silicon is a semiconductor material, unlike other passivation materials such as Al_2O_3 , SiO_2 and SiN_x which are all dielectric materials. The a-Si:H layer can be deposited at low temperature ($\leq 350 \text{ }^\circ\text{C}$) by PECVD [78]. Schaper et al. studied the influence of the deposition temperature on the surface passivation performance. Here, $S_{\text{eff}} \leq 10 \text{ cm}\cdot\text{s}^{-1}$ was obtained for the deposition temperature in the range 200–250 $^\circ\text{C}$ with lowest S_{eff} of 3 $\text{cm}\cdot\text{s}^{-1}$ for the deposition temperature 225 $^\circ\text{C}$ on p-type FZ Si wafers and efficiency of 20.1% was obtained for c-Si solar cell [78]. Intrinsic amorphous silicon (a-Si:H(i)) deposited

by PECVD at low temperature in the range of 200–250 °C was shown to have excellent passivation quality on both, p-type ($3 \text{ cm}\cdot\text{s}^{-1}$) and n-type ($7 \text{ cm}\cdot\text{s}^{-1}$) Si wafers [79]. Large amount of hydrogen content passivates the dangling bonds of c-Si surface by H atoms, thereby reducing interface defect states [80]. Garros et al. reported D_{it} of $\sim 10^{11} \text{ eV}^{-1}\cdot\text{cm}^{-2}$ for a-Si:H (physical vapor deposition (PVD))/c-Si interface [81].

However, for industrial application, a-Si:H films have limitations of parasitic absorption effects and the lack of thermal stability during high temperature processes such as contact firing hinders its use for standard screen-printed solar cells [22]. By adding doping gasses during the deposition process, a-Si:H can be doped either n- or p-type which can be used as selective contacts that are selective for either electron collection (n-type a-Si:H) or hole collection (p-type a-Si:H) [82]. Yoshikawa et al. reported conversion efficiency of 26.6% for heterojunction interdigitated back contact (HJ-IBC) solar cell using PECVD a-Si:H film [83]. Yamamoto et al. reported conversion efficiency of 26.7% for the HJ-IBC solar cell using PECVD amorphous Si layer [84].

2.3.4 Aluminum oxide (Al_2O_3)

The Al_2O_3 passivation material has the fundamental advantage of negative fixed oxide charges over other passivation materials [22,23]. In addition to chemical passivation due to a low interface defect density, the presence of a high negative fixed oxide charge density provides field-effect passivation [22]. AlO_x film provides excellent surface passivation on lightly doped p-type and n-type silicon surfaces as well as on highly doped p^+ -type silicon surfaces [22,23,30,85,86,87]. AlO_x film for the passivation of highly doped n^+ -type silicon surface was also reported for a certain range of sheet resistance values [88,89,90]. However, a high negative fixed oxide charge density of AlO_x limits the passivation of n^+ -type silicon surfaces and Duttagupta et al. showed that AlO_x (30 nm, PECVD)/ SiN_x (70 nm, PECVD) passivation stack can passivate n^+ -type c-Si surfaces as long as the negative fixed oxide charge is sufficiently low ($(1-2) \times 10^{12} \text{ cm}^{-2}$) [88]. Van de Loo et al. showed that the negative fixed oxide charge of Al_2O_3 layer deposited by ALD can be controlled or changed by using interfacial layer (IL) of SiO_2 deposited by ALD [91].

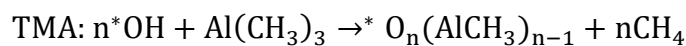
2.4 Methods for deposition of Al₂O₃

This section presents a review of the experimental techniques reported in literature to deposit AlO_x films. Several methods are available for the deposition of AlO_x films. PECVD is the most dominant deposition technique for front and rear side passivation layers in silicon based solar cell manufacturing [21]. Besides PECVD, ALD technique is also gaining significant market share for depositing the AlO_x film for rear side passivation [21]. Other AlO_x deposition methods have been developed as well. However, as per the ITRPV report, other methods are not expected to gain significant market share during the next decade [21]. In addition, various properties of AlO_x film by different deposition methods are also reviewed in this section.

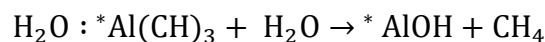
2.4.1 Atomic layer deposition (ALD)

ALD Al₂O₃ films were shown in literature to provide excellent surface passivation on p-type, n-type, and p⁺ type silicon surfaces. The most commonly used and widely studied ALD metal-organic precursor for Al₂O₃ film deposition is trimethylaluminum (TMA; Al(CH₃)₃) in research as well as in industrial applications [31]. Besides TMA, other Al precursors reported for the deposition of Al₂O₃ thin films by ALD include aluminum trichloride (AlCl₃) [92], Al(mmp)₃ (mmp = 1-methoxy-2-methyl-2-propoxide, OCMe₂CH₂OMe) [93], aluminium(III) ethoxide Al(OEt)₃ [94], and aluminium(III) isopropoxide (Al(OⁱPr)₃) [95].

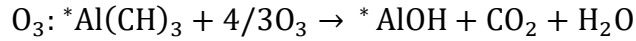
The TMA as a metal-organic precursor is used along with water (H₂O) vapor, ozone (O₃) or oxygen (O₂) plasma as co-reactant [96]. For the dielectric layer deposition, ALD processes are based on a sequence with two surface reactions to deposit a thin film [97]. These sequential gas-surface reactions are referred to as ‘half-reactions’. The first half cycle can be given by the following chemical reaction at the surface (*) for n=1 or 2 [97,98]:



After a purge process, the second ALD half cycle takes place. For thermal ALD, it can be written by the following reaction [97,98]:



As sufficient thermal energy is needed for the latter to take place, highly reactive species such as O₃ or O₂ plasma can be used and the reactions can be described as follows [97,98]:



One ALD cycle consists of TMA exposure followed by a purge step, then oxidant exposure followed by a purge step [97]. ALD processes using water and ozone are called thermal ALD and the process utilizing plasma is known as plasma assisted ALD (PA-ALD). The ALD-cycle can be repeated to achieve the desired film thickness [97]. The measured dielectric constants for ALD Al₂O₃ films are found to vary for different thicknesses and the hydrogen concentration is found to decrease gradually as the growth temperature is raised from 125 °C to 350 °C [99].

Laboratory-scale PA-ALD achieved low S_{eff} of 6 cm·s⁻¹ on p-type c-Si [87] and efficiency of 20.4% on PERC-type solar cell without any capping layer [100]. Hoex et al. [30] demonstrated excellent surface passivation on both lightly doped n-type and p-type c-Si using Al₂O₃ film prepared by PA-ALD (TMA and O₂ plasma). Here, S_{eff} of 2 cm·s⁻¹ and 13 cm·s⁻¹ were reported for n-type and p-type c-Si, respectively using PA-ALD Al₂O₃ film [30]. Dingemans et al. reported S_{eff} of ~3 cm·s⁻¹ on 2 Ω·cm p-type c-Si wafers for thermal ALD and PA-ALD Al₂O₃ film [101]. Richter et al. reported S_{eff} of ~1.3 cm·s⁻¹ on 1 Ω·cm n-type FZ c-Si wafer and S_{eff} of ~4 cm·s⁻¹ on 1 Ω·cm p-type FZ c-Si wafer for PA-ALD Al₂O₃ film [72].

In ALD deposition technique, materials can be synthesized with atomic-scale precision and very thin conformal films with good control of the thickness and composition at the atomic level can be achieved [102]. However, it is unsuitable for the PV industry due to low deposition rate, which is typically in the range of 2 nm·min⁻¹ [103]. Both thermal and plasma ALD suffers from low deposition rate and low throughput. The throughput requirements are significantly higher in the PV industry than in the microelectronics industry. However, the throughput has been significantly enhanced using novel approaches such as ALD batch reactors or spatial ALD. Manufacturers such as Beneq and ASM have redesigned their ALD batch tools to meet the throughput requirements of PV industries. Summary of various AlO_x film properties deposited by ALD method is given in Table 2.1.

Table 2.1: Summary of the reported AlO_x film properties deposited by ALD method.

ALD AlO_x film properties	Plasma assisted-ALD	Thermal ALD
Deposition temperature (°C)	25–400 [104]	25–425 [99,104]
Deposition rate (nm·min ⁻¹)	< 2 [104]	< 1 [104]
S _{eff} (cm·s ⁻¹)	2–13[30,101,105]	3–4 [101,104]
J _{0e} (fA·cm ⁻²)	7–60 (163–31 Ω/□) [23,85]	26–32 (62–51 Ω/□) [106]
Q _f (cm ⁻²)	-(1–10) × 10 ¹² [107]	-(1–10) × 10 ¹² [107]
D _{it} (eV ⁻¹ ·cm ⁻²)	2 × 10 ¹¹ [108]	(1–10) × 10 ¹¹ [107]
Dielectric constant	8.9 [109]	4–7.7 [99]
Effective breakdown field (MV·cm ⁻¹)	8.4 (100 mA) [109]	1–3 [99]
Refractive index (RI)	1.6–1.69 [104,110]	1.6–1.65 [104]
O/Al atomic ratio	1.5–2.15 [109]	1.48–1.7 [99,109]
Hydrogen content	yes [109]	yes [99,109]

Deposition rate up to 72 nm·min⁻¹ [111] and excellent passivation with S_{eff} of 6.5 cm·s⁻¹ was achieved on p-type FZ wafer by spatial ALD [103]. Spatial ALD is less expensive than conventional ALD and the deposition at atmospheric pressure results in high throughput. High throughput greater than 3000 wafers.hour⁻¹ with efficiency of PERC-type solar cells greater than 20% was reported for spatial ALD [112]. However, spatial ALD equipments are complex and costly compared to spray coating instrument. High vapour pressure precursors are also one of the limitations. Lohmuller et al. fabricated PERC solar cell using Al₂O₃ film of 6 nm deposited by a commercial, inline spatial ALD reactor and reported conversion efficiency of 22.1% on conventional p-type 0.8 Ω.cm Cz-Si wafer with pseudo-square M2 wafer format (156.75 mm edge length, 210 mm diameter) [113]. As per the ITRPV report, ALD throughput is 10,000 wafers.hour⁻¹ in 2022 for AlO_x deposition and expected to reach 12,000 wafers.hour⁻¹ from 2024 onwards [21].

2.4.2 Plasma-enhanced chemical vapor deposition

It was shown in [104] that the Al_2O_3 film deposited by PECVD provides a similar level of surface passivation as ALD with higher deposition rates than ALD. The PECVD process is based on a continuous exposure of remote O_2 /argon (Ar) plasma and $\text{Al}(\text{CH}_3)_3$ as the Al precursor. The deposition rate for PECVD was found to scale with the $\text{Al}(\text{CH}_3)_3$ precursor flow introduced into the reactor [114]. Unlike ALD, PECVD technique usually does not deposit perfectly stoichiometric aluminum oxide film and depending on the process parameters, deposition rates of up to $5 \text{ nm}\cdot\text{s}^{-1}$ can be obtained using PECVD [115]. Summary of various AlO_x film properties deposited by PECVD method is given in Table 2.2.

Table 2.2: Summary of the reported AlO_x film properties deposited by PECVD method.

PECVD AlO_x film properties	Value	Reference
Deposition temperature ($^\circ\text{C}$)	25–400	[104,116]
Deposition rate ($\text{nm}\cdot\text{min}^{-1}$)	5	[115]
S_{eff} ($\text{cm}\cdot\text{s}^{-1}$)	2.9–10	[86,104]
J_{0e} ($\text{fA}\cdot\text{cm}^{-2}$)	8–42 (170–30 Ω/\square)	[88]
Q_f (cm^{-2})	$-(1-6) \times 10^{12}$	[86,104]
D_{it} ($\text{eV}^{-1}\cdot\text{cm}^{-2}$)	$(2-5) \times 10^{10}$	[86]
Dielectric constant	9–11	[116]
RI	1.5–1.65	[86,104,116]
O/Al atomic ratio	1.57–1.59	[116]
S_{eff} after firing ($\text{cm}\cdot\text{s}^{-1}$)	12–25	[117]
Hydrogen content	yes	[118]

Al_2O_3 deposited by PECVD achieved a low S_{eff} of $10 \text{ cm}\cdot\text{s}^{-1}$ [119], efficiency of 21.5% on PERC-type solar cell [120] with throughput of $1200 \text{ wafers}\cdot\text{hour}^{-1}$ [121]. Like ALD, PECVD method uses the TMA precursor which is toxic and expensive. Liu et al. [64] fabricated high quality PERC solar cell on $0.7\text{--}1.5 \Omega\cdot\text{cm}$ p-type Cz c-Si wafer (244.31 cm^2)

with rear Al₂O₃ (PECVD)/SiN_x (PECVD) passivation stack and front SiO₂ (thermal)/SiN_x (PECVD) passivation stack mainly by a PECVD tool (Centrotherm) on a massive production line and achieved conversion efficiency of 22.15%. Conversion efficiency of 25.7% was reported for c-Si n-type TOPCon solar cell using 10 nm Al₂O₃ layer deposited by PECVD as passivation layer [122].

2.4.3 Sputtering

Sputtering is one of the widely used physical vapour deposition (PVD) processes to deposit compound films. Unlike chemical vapor deposition, the sputtering process is mainly based on physical processes to deposit the films. Many types of materials can be sputtered using this method and the deposition can be carried out at room temperature [123]. In sputtering, the target material can be a single element or a compound material. The atoms and molecules are ejected from the surface of the target material due to physical collisions and it travels through a relative vacuum in vapour form to be deposited on the surface of the substrate [123]. AlO_x can be deposited by different sputtering methods such direct current (DC) sputtering [124], radio frequency (RF) sputtering [125], pulsed DC sputtering [126].

Sputtering is found to be one of the promising deposition techniques due to its low cost and higher deposition rate. The main disadvantages of sputtering process are plasma damage, film contamination by other materials present in the sputtering chamber [127]. Unlike ALD and PECVD, in the sputtering process, good quality Al₂O₃ can be deposited at room temperature using aluminum target and nontoxic precursors, but requires high vacuum conditions [126]. Passivation quality of sputtered AlO_x film and higher deposition rate makes sputtering method prospective for solar cell industry. Non-toxic, non-explosive and easily available reactants also make this method applicable for solar cell research [128].

Zhang et al. used hydrogen (H₂)/Ar mix instead of pure Ar as the plasma source for sputtering and observed a dramatic improvement in the ability of surface passivation for both n-type and p-type c-Si substrates [129]. Here, S_{eff} of 1 cm·s⁻¹ for 1.5 Ω·cm n-type Cz c-Si and S_{eff} of 13 cm·s⁻¹ for 1 Ω·cm p-type FZ c-Si were achieved using in-situ hydrogenated AlO_x films by reactive sputtering [129]. Kotipalli et al. reported S_{eff} < 10 cm·s⁻¹ on 1–5 Ω·cm p-type FZ c-Si for AlO_x film (35 nm) deposited by DC-magnetron sputtering after PDA (430 °C, 30 min) in forming gas followed by firing at 700 °C and 800 °C for 4.5 min in both O₂

and N₂ atmospheric conditions [124]. Zhang et al. reported S_{eff} as low as ~5 cm·s⁻¹ for sputtered Al₂O₃ on 1.5 Ω·cm n-type Cz c-Si wafer [130]. Schmidt et al. demonstrated conversion efficiency of 20.1% for PERC cell using sputtered Al₂O₃ as rear passivation layer [131]. Summary of various AlO_x film properties deposited by sputtering method is given in Table 2.3.

Table 2.3: Summary of the reported AlO_x film properties deposited by sputtering method.

Sputtered AlO_x film properties	Value	Reference
Deposition temperature (°C)	20–600	[132,133]
Deposition rate (nm·min ⁻¹)	< 146	[134,135,136,137]
S _{eff} (cm·s ⁻¹)	16.5–307	[128]
Q _f (cm ⁻²)	-(1–10) × 10 ¹²	[124,127,138]
	+ 8 × 10 ¹¹	[124]
D _{it} (eV ⁻¹ ·cm ⁻²)	(0.8–2) × 10 ¹¹	[124,138]
Dielectric constant	6.9–9.1	[135,139]
Effective breakdown field (MV·cm ⁻¹)	18.07	[139]
RI	1.42–1.74	[110,139]
O/Al atomic ratio	1.3–1.85	[118,132]
Surface roughness (nm)	0.32–2.64	[118,139]
S _{eff} after firing (cm·s ⁻¹)	< 10	[124]

2.4.4 Spin coating

Spin coating method is the most common wet-chemical process that has been used to deposit a wide variety of metal-oxide thin films such as AlO_x [140], SiO_x [140] and titanium oxide (TiO_x) [141]. It involves deposition of the thin liquid film of metal-organic precursor on the solid substrate by spinning process followed by solvent evaporation and densification of the film at elevated temperatures. Uzum et al. reported negative Q_f of - 4.4 × 10¹² cm⁻² for spin coated AlO_x film using aluminum (III) acetylacetonate as precursor and ethanol as

solvent [142]. Balaji et al. reported negative Q_f of $-9 \times 10^{11} \text{ cm}^{-2}$, D_{it} of $1 \times 10^{12} \text{ eV}^{-1} \cdot \text{cm}^{-2}$ and S_{eff} of $55 \text{ cm} \cdot \text{s}^{-1}$ for spin coated AlO_x film on $1\text{--}3 \ \Omega \cdot \text{cm}$ p-type Cz-Si wafer using aluminum isopropoxide as precursor and diethylene glycol monoethyl ether as solvent [143]. Summary of various AlO_x film properties deposited by spin coating method is given in Table 2.4.

Table 2.4: Summary of the reported AlO_x film properties deposited by spin coating method.

Spin coated AlO_x film properties	Value	Reference
$S_{\text{eff}} \text{ (cm} \cdot \text{s}^{-1}\text{)}$	55–85	[143,144,145]
$Q_f \text{ (cm}^{-2}\text{)}$	$-(4.5\text{--}44) \times 10^{11}$	[142,146,147]
	$+ 3.6 \times 10^{12}$	[147]
$D_{it} \text{ (eV}^{-1} \cdot \text{cm}^{-2}\text{)}$	$(3.2\text{--}3.7) \times 10^{11}$	[144,146]
Dielectric constant	5–6.5	[148,149]
Breakdown field $\text{(MV} \cdot \text{cm}^{-1}\text{)}$	3.5–6.6	[149]
RI	1.45–1.58	[144,146,148]

Spin coating method is currently used by the microelectronics industry for deposition of photoresists. Comets, striations, chuck marks and gradual radial thickness variation are some important defects of spin coating methods [150]. In general, spin coating process is performed in a clean room to avoid the contamination of the film due to dust particles. Uniform thin films in the range of micrometer to nanometre thickness can be deposited using this method. Spin coating processes are more cost-effective since vacuum is not required to synthesize the film. Moreover, reproducibility is good and it is easy to integrate with lithography based fabrication techniques [151]. The spin coating processes are commonly used to fabricate small area cells but it is inappropriate for large-area manufacturing [152]. In order to deposit thin films, the substrate may require high spinning speed. However, large substrates spun at a sufficiently high spinning rate may create defects in the deposited film [153]. Poor material usage is another limitation. In a typical spin coating method, only (2–5)% of the dispensed material is utilized and the remaining (95–98)% of the material is thrown off the substrate [154]. For more discussions, see chapter 4, section 4.3.

2.4.5 Spray pyrolysis

Spray coating process and spray pyrolysis process both can follow similar experimental procedure, but in spray pyrolysis process chemical transformation occurs during the thin film deposition [155]. Spray pyrolysis is a chemical solution deposition technique in which the precursor solution is sprayed onto a preheated substrate [156]. In the spray pyrolysis process, the deposition and thermal processing takes place simultaneously. Aguilar et al. [157] studied the optical, electrical, and structural properties of Al_2O_3 films deposited by spray pyrolysis using aluminum nitrate precursor and ultrasonic generator. Amorphous and stoichiometric AlO_x films with RI close to 1.66, surface roughness in the range of 3.8–18.27 nm and electric field strength up to $2 \text{ MV}\cdot\text{cm}^{-1}$ were reported for AlO_x film prepared by spray pyrolysis technique [157]. Untila et al. developed spray coated AlO_x film by ultrasonic chemical spray pyrolysis method using aluminium acetylacetonate as precursor in methanol and achieved deposition rate up to $130 \text{ nm}\cdot\text{min}^{-1}$ and S_{eff} of $70 \text{ cm}\cdot\text{s}^{-1}$ [158]. The schematic of typical spray pyrolysis process is shown in Figure 2.4. Summary of various AlO_x film properties deposited by spray pyrolysis method is given in Table 2.5.

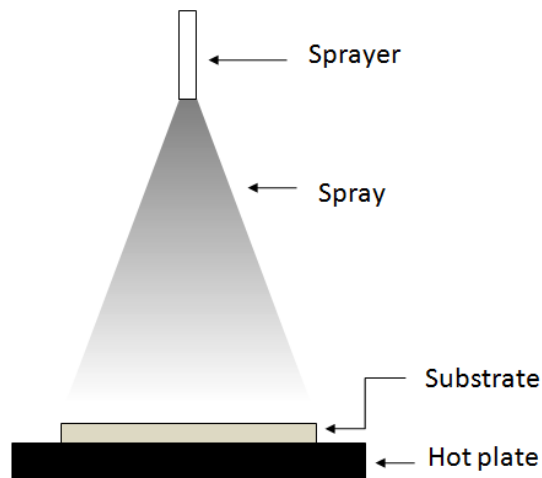


Figure 2.4: Schematic of spray pyrolysis system [156].

Spray pyrolysis has been used for several decades for deposition of semiconductive and photoconductive films [159]. This spray pyrolysis process is well suited to synthesize varieties of coatings on different types of substrates. Spray coating process is a simple and well established method in graphic arts, industrial coatings, and painting [160]. Recently, it is becoming attractive for organic PV [160,161,162]. It is a high-throughput and large-area

deposition technique which is used to prepare coatings on a variety of surfaces with different morphologies and it is used for in-line production as well [163]. In spray coating, the material waste is reduced to minimal quantities, and using shadow mask the deposition can be patterned [163]. The aerosol can cause environmental pollution and hence exhaust system is necessary. During spray coating, dust particles can get deposited in the film. Hence, to deposit a good quality film, the spraying process needs to be carried out in a clean room ambient. For more discussions, see chapter 4, section 4.3.

Table 2.5: Summary of the reported AlO_x film properties deposited by spray pyrolysis method.

AlO _x film properties (spray pyrolysis)	Value	Reference
Deposition temperature (°C)	300–650	[157,164,165,166,167]
Deposition rate (nm·min ⁻¹)	7–540	[157,166,167]
S _{eff} (cm·s ⁻¹)	70	[158]
Q _f (cm ⁻²)	- 3.19 × 10 ¹²	[168]
D _{it} (eV ⁻¹ ·cm ⁻²)	(1–1.6) × 10 ¹¹	[166,167]
Dielectric constant	7.9–7.95	[157,166]
Breakdown field (MV·cm ⁻¹)	2–6.2	[157,166,167]
RI	1.645–1.66	[157,167]
O/Al atomic ratio	1.51	[157]
Surface roughness (nm)	3.8	[157]

2.5 Surface preparation

Bakhshi et al. [169] studied effect of silicon oxide layer grown by ozonated deionized (DI) water on silicon surface passivation quality prior to deposition of AlO_x (14 nm, ALD) film and AlO_x (15 nm, ALD)/SiN_x (80 nm, PECVD) stack on n-type Si wafer and it was found that all the samples treated with ozonated DI water showed improved surface passivation. Increase in τ_{eff} and decrease in D_{it} were observed for the samples treated with ozonated DI

water [169]. In case of single layer AlO_x , the Q_f was found to decrease after ozonated DI water treatment, while the $\text{AlO}_x/\text{SiN}_x$ stack exhibited increase in Q_f value after ozonated DI water treatment [169]. Bakhshi et al. [170] also studied effect of ultraviolet-ozone (UV/ O_3) oxide thickness on passivation qualities prior to deposition of AlO_x (10 nm to 15 nm, ALD) on n-type Cz-Si wafer. Here, SiO_x of 1.5 nm, 1.7 nm, and 1.8 nm were grown for 10 min, 15 min, and 20 min of UV/ O_3 process time, respectively [170]. It was observed that passivation quality varied with UV/ O_3 oxide thickness and 15 min of UV/ O_3 processing time was found to be optimum [170].

Penaud et al. studied the impact of the surface preparation on the passivation properties of Al_2O_3 (ALD)/ Si_xN_y (PECVD) stack using piranha, RCA (Radio Corporation of America)-1, HNO_3 and solar clean ($\text{HNO}_3/\text{H}_2\text{O}/\text{surfactant}$) treatments and demonstrated that HNO_3 -based cleans are the most suitable surface preparations for good passivation quality of Al_2O_3 film [171]. Rothschild et al. investigated various surface preparation procedures prior to Al_2O_3 film (ALD) deposition and identified two hydrophilic cleans— HNO_3 and O_3 based—as suitable candidates for industrial Al_2O_3 based PERC type process flow [172]. Lien et al. employed a very thin stoichiometric silicon dioxide (SiO_2) film deposited by ICPCVD at the interface between Al_2O_3 and silicon wafer to reduce blisters and achieved efficiency of 19.18% for PERC solar cell using stacked SiO_2 (3 nm, ICPCVD)/ Al_2O_3 (8 nm, non-vacuum spatial ALD)/ $\text{SiN}_x:\text{H}$ (70 nm, ICPCVD) rear passivation layers [173]. SiO_2 interlayer of Al_2O_3 stacks allows to control the interface properties and van de Loo et al. employed SiO_2 interlayer (~3 nm to 14 nm, ALD) to control the fixed oxide charges of Al_2O_3 (ALD) [91].

2.6 Effect of film thickness and optical properties requirement

Literature showed that the thickness of AlO_x film above a certain value has no influence on the passivation quality for AlO_x film deposited by atmospheric pressure chemical vapor deposition (APCVD) and the quality of surface passivation increased with AlO_x thickness up to about 15 nm and remained stable for thicker AlO_x layers for n-type c-Si substrates [174]. Al_2O_3 thickness of less than 2 nm was found to be sufficient for Si surface passivation, when combined with a- $\text{SiN}_x:\text{H}$ as ARC and/or capping layer [175,176]. Currently, most of the

today's silicon solar cell concepts that includes passivation scheme based on Al_2O_3 films adopt stacks of dielectric layers to take advantage of each dielectric layer.

In general, there are two kinds of film stacks which are taken into consideration from the perspective of Al_2O_3 passivation layer: (1) SiO_2 as an intentionally introduced interlayer between Al_2O_3 and the Si surface [91] (2) SiN_x or SiO_2 as a capping layer/ARC on top of the Al_2O_3 film. SiN_x capping layer on Al_2O_3 film is commonly used as a protective layer for rear metallization and to enhanced reflection from the rear side. For instance, the SiN_x capping layer increases the chemical stability of Al_2O_3 passivation layer against metal pastes—such as screen printed aluminium paste—used for industrial c-Si solar cells. SiO_2 also acts as a protective layer and prevents etching of Al_2O_3 passivation layer by the etchants present in the metal pastes. During firing steps, the SiN_x capping layer also improves the stability of the surface passivation compared to single layer Al_2O_3 films [105].

The effect of each layer thickness in the $\text{Al}_2\text{O}_3/\text{SiN}_x$ rear passivation stack on the efficiency of p-type c-Si solar cells was investigated by Bordihn from the perspective of the optical performance using PC1D simulations and the optimum thicknesses were found to be 15–30 nm for Al_2O_3 and 100–120 nm for the SiN_x films [177]. Shin et al. achieved optical properties of spray deposited 80 nm Al_2O_3 film identical to the ALD $\text{Al}_2\text{O}_3/\text{PECVD SiN}_x$ stack which suggests that spray deposited Al_2O_3 can also act as the optical trapping layer on the rear [168].

2.7 Activation of passivation

In general, a post deposition thermal treatment is necessary to activate the passivation of Al_2O_3 film. A post deposition anneal (PDA) (10–30 min at ~ 400 °C in N_2 ambient) is typically applied to activate the ALD Al_2O_3 passivation, and the PDA was shown to increase the negative Q_f and reduce the D_{it} [178,179]. To activate the surface passivation for both plasma ALD Al_2O_3 and thermal ALD Al_2O_3 to the full extend, post deposition annealing is required and Dingemans et al. reported that the optimal temperatures to activate the surface passivation are ~ 375 °C \pm 50 °C and ~ 425 °C \pm 50 °C for thermal ALD Al_2O_3 and plasma ALD Al_2O_3 , respectively [180]. Moreover, Dingemans et al. also reported that after deposition, annealing for 10 min in N_2 ambient is sufficient to activate the passivation to the

full extent [180]. Sperlich et al. prepared Al_2O_3 film using a SiNA/MAiA inline PECVD system and reported that 5 min of annealing at 400 °C in air is sufficient to activate the Al_2O_3 layer [181]. Zhang et al. reported S_{eff} of $5 \text{ cm}\cdot\text{s}^{-1}$ after annealing at 450 °C for 30 min in a gas mixture of N_2 and H_2 annealing ambient for sputtered Al_2O_3 films [130]. Uzum et al. reported τ_{eff} of 119.3 μs after annealing in $\text{H}_2\text{O}/\text{O}_2$ ambient at 450 °C for 15 min for spin coated AlO_x film [142].

2.8 Thermal stability

For solar cell applications, a good thermal stability of surface passivation is necessary. It is reported that thermal stability of Al_2O_3 deposited ALD is poor and a SiN_x capping layer may be necessary to stabilize the passivation [182,183]. In case of PECVD, reduction of τ_{eff} from 1 ms to less than $\sim 70 \mu\text{s}$, which is equivalent to as-deposited PECVD Al_2O_3 film, was reported when the samples were annealed at 820 °C for 30 min [184]. Sputtered Al_2O_3 film also showed considerable degradation of S_{eff} at higher temperatures [126]. Thermal ALD films should be subjected to post deposition thermal annealing for activation of passivation [22]. In a typical PERC solar cell process, the passivation layers should be able to withstand the contact metal firing temperatures, which are in the range of 750 °C to 800 °C for a few seconds [185].

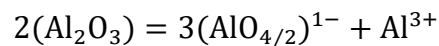
ALD and PECVD Al_2O_3 film were reported to contain high concentration of hydrogen [104]. This may lead to blister formation during high temperature treatment due to out-diffusion of H-containing species [186,187]. Vermang et al. [187] reported blistering of ALD Al_2O_3 films thicker than 10 nm when annealed at temperature higher than 350 °C and no blister formation was reported when the Al_2O_3 film thickness was less than 10 nm. A balance between excessive amounts of hydrogen leading to blistering and sufficient amounts of hydrogen for interface and bulk passivation should be found for passivation layers. Both ALD and PECVD deposited films may have to be capped with silicon nitride for thermal stability [22,183]. Kotipalli et al. proposed an optimum firing temperature and conditions—750 °C for 4.5 min in O_2 ambient—to reach high quality surface passivation and to avoid formation of blisters for sputtered Al_2O_3 film [124].

2.9 Passivation characteristics of AlO_x/c-Si interface

AlO_x is an excellent passivation material due to its combined field effect and chemical passivation properties. The chemical passivation provided by the AlO_x dielectric layer results from low D_{it} at the Si/AlO_x interface. The oxygen or both the hydrogen and oxygen effectively saturates the silicon dangling bonds reducing the interface traps during the PDA. The low density of recombination centers at the surface results in a reduced surface recombination rate.

Al₂O₃ dielectric layers contain intrinsic negative fixed charges, which provide field effect passivation [22]. The fixed oxide charge density in Al₂O₃ film depends on the process parameters of the deposition as well as post annealing conditions [188]. An IL is usually formed between the silicon surface and AlO_x film during deposition [189,190], during post deposition annealing by the diffusion of oxygen towards the interface [191,192], or can be the residual native oxide [193]. The IL was found to consist of SiO_x [107,189,191,192,193] or aluminum silicate (AlSi_xO_y) [194]. The fixed oxide charges in AlO_x films are deduced to be located at the IL [190,195]. The fixed oxide charge density is found to hardly change when the Al₂O₃ film thickness is reduced to 1 nm [25,196]. It is also found that the oxide charge density is not affected by the Al₂O₃ film thickness [180,196]. The combined effect of low D_{it} and high Q_f leads to significant decrease of surface recombination rate.

Non-crystalline Al₂O₃ has two kinds of bonding environments for the Al atoms: (i) a tetrahedrally (T) coordinated Al site having a net negative charge, and (ii) an octahedrally (O) coordinated Al site in which the Al has a positive charge of 3+ [195]. The structural formula of Al₂O₃ can be expressed as [29]



The reason behind the presence of negative fixed oxide charge at the Al₂O₃/Si interface is that the Al ions rearrange in tetrahedrally coordinated Al sites with a net negative charge by bonding directly to the O atoms of the SiO₂ interfacial layer [29,195]. Kimoto et al. [192] reported intense peak T at about 78.2 eV mainly originated from the tetrahedrally coordinated Al near the Si substrate for ALD Al₂O₃ using electron energy loss spectroscopy (EELS) in a TEM. Kim et al. [197] reported high T/O ratio for fired AlO_x sample (oxide charge density is - 2.09 × 10¹² cm⁻²) compared to the as-deposited AlO_x sample (oxide charge density is - 1.18

$\times 10^{12} \text{ cm}^{-2}$) near the interface using scanning transmission electron microscopy (STEM)/EELS. Noircler et al. [198] suggest that the aluminum silicate and/or the silicon oxide at the interface must be stoichiometric for more negative fixed oxide charges.

2.10 Emitter passivation

Considerable attention is paid to n-type c-Si because of several advantages which includes absence of light-induced degradation (LID), insensitivity to common metal impurities, high bulk lifetime, and so on [199,200]. Thus, high efficiency silicon solar cell concepts often rely on n-type c-Si [21]. It was predicted that the market share of n-type mono-Si material will grow from 20% in 2022 to ~71% in 2032, while for p-type mono-Si material it reduces from 70% in 2022 to ~29% in 2032 which indicates industry demand for high efficiency n-type c-Si modules [21]. It is expected that more n-type c-Si based cell designs will enter the mainstream in future [21]. According to the ITRPV report, solar cells using n-type material show highest efficiency potential of today's solar cell concepts [21]. It was predicted that the efficiency of p- and n-type mono-Si solar cells having diffused pn junction on the front side will reach up to 24.5% and 25% respectively, in the next 10 years [21].

Emitter passivation is an essential factor for the realization of high efficiency silicon solar cells. Many materials and stacks were investigated for the passivation of boron doped emitters such as SiO_2 [201], SiN_x [44,202], amorphous silicon carbide (a-SiC_x:H) [203], a-Si:H [204] and Al_2O_3 . There are many reports available for the passivation of p⁺ emitter by Al_2O_3 film deposited by ALD and PECVD [205,206]. High efficiency n-type silicon based solar cells such as n-type PERL with conversion efficiency of 23.4% were fabricated with Al_2O_3 film synthesized by ALD [23,207]. The world-record efficiency of 25.7% and J_{sc} of $42.5 \text{ mA}\cdot\text{cm}^{-2}$ were reported for TOPCon solar cell ($1 \text{ }\Omega\cdot\text{cm}$, n-type c-Si) employing 10 nm Al_2O_3 film by PECVD for p⁺ boron front emitter passivation [122]. However, these deposition processes are vacuum based and costly. Utila et al. [208] have investigated the AlO_x film deposited by ultrasonic spray pyrolysis (USP) process for the surface passivation of boron doped emitter and shown that USP can be used for AlO_x film deposition to fabricate high efficiency n-type silicon solar cells. Here, pseudo-efficiency of 20.2% under front illumination was obtained for ITO/ AlO_x /(p⁺nn⁺)Cz-Si/IFO solar cell structure [208].

2.11 Crystalline silicon solar cells

In order to further improve solar cell efficiency and reduce cost, several PV manufacturing companies, universities and research institutes investigate variety of high efficiency and low cost c-Si solar cells. In this section, different types of high efficiency c-Si solar cells that have been in small scale and/or mass production are presented.

2.11.1 Passivated emitter and rear cell (PERC) cells

PERC [209,210] is currently the dominating technology in the silicon solar market worldwide and its market share is expected to remain high in the next years [21]. PERC concept differs from standard Al-BSF solar cell technology by incorporating a dielectric passivation layer or passivation stack on the rear of the cell to enhance the efficiency [209]. PERC solar cells based on p-type c-Si wafers have gained influence in the commercial solar cell market. The p-type silicon wafers are susceptible to LID caused by boron-oxygen (BO) defects [211]. This degradation can be mitigated by passivation of BO defects using hydrogen and a hydrogenation step is widely used for commercial production of p-type Cz-Si PERC solar cells [77]. A small area (4 cm²) 25.0 ± 0.5% efficiency was reported for a c-Si p-type PERC solar cell and efficiency of 24.0 ± 0.3% for a large area (244.59 cm²) c-Si p-type PERC solar cell [20]. Solar cell industries started to investigate alternative solar cell architectures that may replace current mainstream PERC cells due to fast-approaching efficiency limit and LID related to BO defects.

2.11.2 Passivated emitter rear totally diffused (PERT) cells

The difference between a PERC solar cell and a PERT solar cell is that the back side of the PERT solar cell is further improved to enhance the cell efficiency. Further improvement can be achieved by doping the back side more to further reduce recombination at that location which leads to the PERT cell [212]. In the PERT cell, a dopant diffusion is carried out at the back side similar to front side diffusion, but with the opposite polarity of the dopant [212]. For instance, boron diffusion on the back (p⁺⁺ layer) is carried out if the front is phosphorous diffused and due to the additional p⁺⁺ layer the PERT cell has a better

passivation than the PERC cell [212] providing increase in efficiency of about 0.5% [212]. Unlike PERC cell, in the PERT cell aluminium is used only as metal contact and not for generating the local BSF (p^+).

The economic disadvantage of PERT cells compared to PERC is a second diffusion step is required for generating the BSF. Moreover, for the production of a PERT cell the following additional steps have to be incorporated [212]: (i) boron diffusion (ii) protective layer deposition to protect the boron diffusion so that subsequent phosphorus diffusion and chemical texturing processes do not affect the effects of the boron diffusion and (iii) the boron glass layer etching. PERT solar cells can be fabricated with only a few additional steps. Although PERT modules provide slightly higher efficiencies than PERC modules, the efficiency improvement is achieved at the cost of additional process steps [212]. Currently, the most widely used method to form boron emitter is liquid dopant boron tribromide (BBr_3) diffusion [21]. Due to hazardous nature of liquid BBr_3 , safety requirements need to be increased [200]. In 2022, since boron diffusion processes requires long process times, the throughput is limited to 3,000 wafers.hour⁻¹ [21].

n-type c-Si has many advantages over p-type c-Si as base material [200]. In case of n-type PERT cell with back side emitter, an additional protection layer such as SiO_x is required during co-firing of the boron diffusion and metallisation for boron diffused p^{++} layer production from interference with the Al_2O_3 layer [212]. IMEC in cooperation with Jolywood reported efficiency of 23.2% for bifacial n-type PERT solar cells using the same industry-compatible equipment which is used to produce bifacial p-PERC cells, with the addition of a boron diffusion process [213].

2.11.3 Passivated emitter and rear locally diffused (PERL) cells

PERT cell performance can be further improved by reducing the recombination in the heavily doped full BSF layer. This can be achieved by locally diffused BSF structure on the back side which leads to the passivated emitter and rear locally diffused (PERT) cell structure. The industrial fabrication of PERL solar cells is challenging due to high production costs and complexity to form locally diffused region at the rear side of cell [214]. Norouzi et al. used laser processing to form higher local doping region on the rear side of p-type Cz-Si PERL cells and Al_2O_3 (ALD)/boron doped silicon nitride ($SiN_x:B$)(PECVD) stack was used for both

rear surface passivation and local doping source to form a local p^+ back surface field by laser doping [214]. Lohmuller et al. have reported conversion efficiencies up to 20.4% for 6-inch p-type Cz-Si bifacial PERL (biPERL) solar cells using Al_2O_3 (6 nm, ALD)/ $SiN_x:B$ (75 nm, PECVD) stack on the rear side [215]. Benick et al. reported conversion efficiency of 23.4% for high efficiency n-type PERL silicon solar cell using Al_2O_3 (30 nm, ALD)/ SiN_x (40 nm, PECVD) passivation stack [207].

2.11.4 Tunnel oxide passivated contact (TOPCon) cells

In TOPCon design, the metal does not make direct contact with the silicon wafer but through a thin tunnel oxide and a doped poly-Si layer acts as passivating carrier-selective contact [216]. TOPCon design has become one of the leading next-generation options after monocrystalline PERC concept [216,217]. TOPCon has the advantage of being able to use the current PERC or PERT line with addition of only a few process steps—formation of ultrathin tunnel oxide and deposition of intrinsic/doped poly-Si [216]. TOPCon concept is attractive due to its high efficiency potential [216]. In industrial TOPCon cells, the Al_2O_3/SiN_x and TOPCon/ SiN_x passivation stacks are commonly used on the front and the rear side, respectively [218].

Chen et al. reported 24.58% efficiency for commercial n-type TOPCon silicon solar cells using the front and rear passivation stack of Al_2O_3 (ALD)/ $SiN_x:H$ (PECVD) with hydrogenation step [219]. A small area (4 cm^2) $25.8 \pm 0.5\%$ and $26.0 \pm 0.5\%$ efficiencies were reported for a c-Si n-type and p-type TOPCon solar cells, respectively and $25.2 \pm 0.4\%$ efficiency for a large area (242.97 cm^2) c-Si n-type TOPCon solar cell [20]. Ultrathin SiO_x film ($\sim 1.4\text{ nm}$) grown by UV/ O_3 can be used as tunnel oxides for tunnel oxide passivated contact (TOPCon) solar structures [220].

The major challenges of TOPCon are high thermal budget associated with boron diffusion process, low production efficiency to prepare tunnel and doped poly-Si layer and high metallization cost due to silver paste [221]. Although the equipment for diffusion is similar, boron has lower solid solubility in silicon than phosphorous and requires $900\text{ }^\circ\text{C}$ to $1100\text{ }^\circ\text{C}$ to form boron emitter [221]. Moreover, the BBr_3 diffusion processes severely damages the quartz components [221]. Boron trichloride (BCl_3) diffusion process does harm to quartz components but its diffusion evenness is slightly inferior compared to BBr_3

diffusion process [221]. However, both BBr_3 and BCl_3 are hazardous. Industrial TOPCon solar cells are mainly based on n-type Si substrates which are expensive [216]. LID and light and elevated temperature-induced degradation (LeTID) are not found in n-type Cz-Si wafer based modules [222]. This is the major advantage of n-type TOPCon modules over p-type modules when exposed to strong UV irradiation and heat [222]. Solar cells on n-type silicon material with tunnel oxide passivated contacts at the rear side show higher efficiencies compared to all p-type solar cell concepts in mass production [21].

2.11.5 Interdigitated back-contact (IBC) cells

c-Si solar cells using IBC configurations are more attractive for the solar industry mass production because of its high-efficiency potential. Interdigitated back contacts at the rear help to avoid shading losses. Yoshikawa et al. from Kaneka Corporation have demonstrated efficiency of 26.3% for c-Si HJ (hetero junction)-IBC solar cell over a large area (180 cm^2) [223]. In the Kaneka design, both the anode and the cathode contacts are localized at the rear of the solar cell. As a result, the shadowing losses caused by front grid metallization are completely suppressed. IBC c-Si solar cells require good quality of the bulk and surfaces of the Si wafer [224]. The complexity associated with fabrication of IBC solar cells hinders the mass production with conventional doped regions. One of the simple fabrication methods is to introduce passivation layer at the rear suitable for simultaneous passivation of n^+ and p^+ doped silicon surfaces.

van de Loo et al. demonstrated that fixed oxide charge of Al_2O_3 passivation layer by ALD can be controlled or changed using interfacial layer of SiO_2 by ALD and the ALD $\text{SiO}_2/\text{Al}_2\text{O}_3$ stacks are suitable for the simultaneous passivation of n^+ and p^+ doped silicon surfaces of IBC or bifacial solar cells [91]. Hollemann et al. demonstrated 26.1% high efficiency p-type c-Si IBC solar cell with front surface passivation using 20 nm AlO_x film (ALD) capped by $\text{SiN}_x/\text{SiO}_x$ layer stack (PECVD) [225]. However, complex fabrication process flow of IBC solar cells is a major challenge to fabricate IBC cells for the mass production [226]. Conversion efficiencies of $26.7 \pm 0.5\%$ and $26.6 \pm 0.5\%$ were reported for areas of 79 cm^2 and 179.74 cm^2 respectively, for n-type rear IBC [20]. Haase et al. reported 26.1% efficient IBC solar cell using AlO_x (20 nm ALD) as a front passivation layer capped with $\text{SiN}_y/\text{SiO}_z$ stack by PECVD [227].

2.12 Integration of backside passivation layers in PERC solar cells

The dielectric passivation layer or the passivation layer stack on the rear side has to be locally opened for contact formation. This can be achieved by many ways. Bahr et al. [228] investigated screen printed etch paste (isishape LBSF paste) to etch off the rear side dielectric passivation stack of AlO_x (25 nm, PECVD)/ SiN_x (80 nm, PECVD) followed by full area screen printing with Al paste to fabricate solar grade p-type Cz silicon PERC solar cell of the size $156 \times 156 \text{ mm}^2$ and deeper local BSF of $5 \mu\text{m}$ were obtained for etching paste openings. Lee [229] has demonstrated 19.98 % efficient p-type FZ PERC solar cell with photolithography process to pattern the rear side thermally grown SiO_2 passivation layer. Despite its high resolution, it is not well accepted by photovoltaic industry due to high cost, low throughput and incompatibility with other fabrication processes [230].

Dullweber et al. [231] demonstrated 19 % efficient large area ($125 \times 125 \text{ mm}^2$) p-type PERC solar cell with rear dielectric passivation stack of Al_2O_3 (10 nm, ALD)/ SiN_x (200 nm, PECVD) and screen printed rear contacts. Here, the passivation layer stack at the rear side is locally ablated by laser contact opening (LCO) to form local line openings followed by full area screen printing with commercially available Al paste. Laser assisted processes provide several advantages to fabricate new solar cell structures that is different from conventional solar cell structures. The main advantage of laser-based processes in a production line is that energy can be applied in a selective manner without damaging the entire wafer. Laser-based processes are very useful for large scale silicon solar cell manufacturing as they include simple cost-effective steps while providing considerable efficiency improvement. “PERC ablation: Laser technology has become the dominant way to create openings on the back side of PERC PV cells, with no rival technologies at the moment relevant on the market” as stated in the report of pv-magazine [232].

Laser fired contact (LFC) technique is an effective alternative to make back side contacts in silicon solar cells. As of 2020, the high efficiency PERC/PERL solar cells which have nearly 70% market share extensively use lasers for creating contacts to the solar cell on the rear side [232,233,234]. Laser doped selective emitter currently have about 50 % market share and it is expected to be the mainstream after 2021 and predicted to have market share of more than 80% by 2031 [233]. Norouzi et al. used laser processing to form higher local

doping region (p^+) on the rear side of p-type Cz-Si PERL cells and Al_2O_3 (ALD)/ SiN_x :B (PECVD) stack was used for both rear surface passivation and local doping source [214].

Haase et al. reported conversion efficiency of 26.1% for IBC solar cell with laser ablation process [227]. Liu et al. reported conversion efficiency of 22.15% for PERC solar cell with area of 244.31 cm^2 using rear $\text{Al}_2\text{O}_3/\text{SiN}_x$ passivation layer stack and laser contact opening [64]. Chen et al. reported 23.83% efficient c-Si PERC solar cell using laser for doping and to create contact openings [77].

2.13 Major gaps which are observed from the literature review

Crystalline silicon PV cells and modules presently dominate the PV market, with world market share of about 95% [21]. It is expected that c-Si would remain the mainstream absorber material in the PV industry at least for the next few decades. For the realization of high efficiency solar cells such as PERC, IBC and passivated contact solar cells, passivation of silicon surfaces is a crucial requirement. Al_2O_3 is a widely used material for passivation of p-type silicon surface [21,22,30]. Al_2O_3 films are successfully used as passivation layer for both p-type and n-type solar cell applications. The excellent passivation performance of Al_2O_3 layers is related to a combination of chemical and field-effect surface passivation [22]. The charges in Al_2O_3 usually exhibit negative polarity and hence the field-effect passivation is particularly efficient for p-type silicon surfaces.

ALD Al_2O_3 provides excellent surface passivation for lowly [29,30] and highly [23,235] boron-doped p-type silicon surfaces. Hoex et al. reported S_{eff} of $6 \text{ cm}\cdot\text{s}^{-1}$ for $2 \Omega\cdot\text{cm}$ p-type FZ silicon using ALD Al_2O_3 [87]. Benick et al. reported solar cell efficiency of 23.2% using ALD Al_2O_3 film as a passivation layer on p^+ emitter [235]. Saint-Cast et al. reported S_{eff} of $10 \text{ cm}\cdot\text{s}^{-1}$ for high resistivity p-type silicon wafers using PECVD Al_2O_3 [86]. Ye et al. demonstrated large area PERC solar cell with efficiency of 22.13% using p-type Cz wafer [161]. The back surface in these cells was passivated using a stack of Al_2O_3 and SiN_x deposited by PECVD. Al_2O_3 was also successfully used as a passivation layer in heterojunction solar cells [236,237,238]. Bullock et al. used a thin layer of Al_2O_3 to form a passivated contact in silicon solar cells to achieve very low levels of surface recombination under the contact region [239].

Al_2O_3 can be deposited by a variety of techniques. Al_2O_3 deposition techniques such as ALD [23,29,30,87,235], PECVD [86,161,162,240], APCVD [27,241], and reactive sputtering [125,126,242] were explored for silicon solar cell passivation applications. ALD and PECVD processes are widely considered for industrial PERC solar cell manufacturing [21]. Many of the industrial p-type silicon PERC cells employ Al_2O_3 capped with SiN_x for backside passivation using high cost, sophisticated ALD and PECVD equipments [21].

Two of the low cost alternative technologies available for Al_2O_3 film deposition are spin and spray coating methods. Passivation property of Al_2O_3 for p-type silicon surface by these processes is less explored. Spray coating of Al_2O_3 is a process of interest for silicon surface passivation applications [158]. Spray coated AlO_x films have many potential advantages. Spray coating is a low cost technology and AlO_x can be spray coated in a clean room ambient, whereas both ALD and PECVD are vacuum deposition techniques [158]. AlO_x can be spray coated using precursors that are much more benign compared to TMA. Most of the industrial processes for deposition of Al_2O_3 using ALD and PECVD require TMA, which is a highly flammable material requiring high level of safety precautions in manufacturing. Spray coating process saves the cost associated with the safety infrastructure. Spray coating is a familiar process in the solar cell manufacturing industry, especially for the emitter doping using in-line spray coating of phosphoric acid [243,244,245].

Untila et al. reported S_{eff} of $70 \text{ cm}\cdot\text{s}^{-1}$ for 100 nm AlO_x films obtained by spray pyrolysis on highly boron doped p-type Cz silicon [158]. Here, the film was deposited at 400°C . It was not reported whether the film would be thermally stable to the temperatures applied in industrial solar cell manufacturing processes. Even though the spray coating process is promising for deposition of AlO_x for passivation, the process has not received the attention it deserves and much work needs to be carried out to fully assess the potential of spray coating for industrial solar cell applications.

In our work, AlO_x films deposited by wet chemical processes are investigated for p-type c-Si surface passivation. The following aspects are investigated:

- Synthesis of transparent and clear AlO_x solution using aluminium nitrate nonahydrate precursor and 2-methoxy ethanol solvent by ultrasonic agitation at room temperature.
- Deposition of AlO_x films using prepared AlO_x solution by spin coating and spray coating techniques—hand-held sprayer and spraying instrument—on silicon substrates.

- Optimization of chuck design for spraying instrument using PL imaging.
- Custom designed spraying instrument and hot plate heater with large area capabilities.
- Implementation of ultrathin SiO_x film grown by UV/ O_3 prior to AlO_x spray coating by spraying instrument.
- Investigation of physical, electrical and surface passivation properties of deposited AlO_x films.
- Investigation of p^+ emitter passivation by spray coated AlO_x film.
- Patterning of spray coated AlO_x film by photolithography.
- Laser fired contact process for making local rear contacts through spray coated AlO_x film.

Chapter 3

Experimental Methods

In this chapter, important sample processing procedures, AlO_x precursor preparation and characterization methods are presented in detail. Cross-references are used whenever they are applied in other chapters of the thesis. Many of the sample preparations and characterizations were carried out in a clean room ambient. Chemical protective shield, chemically resistant or clean room aprons, chemically resistant or clean room shoes, chemical resistant gloves and/or latex gloves, acid face mask and safety goggles were used whenever required.

3.1 AlO_x deposition

In this section, some of the process steps that are performed prior to AlO_x film deposition are discussed. The silicon wafers used in this thesis work were first chemically cleaned. The wafer cleaning procedures used in this work are based on the standard cleaning process developed at Radio Corporation of America (RCA) and published in 1970 [246]. This section also covers synthesis of AlO_x precursor solution.

3.1.1 RCA cleaning

The process of cleaning silicon wafers to avoid contamination is a key step for preparing silicon surface for the deposition of passivation film. Contaminants present on the surface of silicon wafers can degrade the surface passivation. The RCA cleaning process does not attack silicon, and only a very thin layer of silicon dioxide is removed after chemical oxidation in the process.

The RCA clean is the standard industry procedure for removing contaminants from the wafer surfaces. The chemicals used in RCA cleaning are all dangerous and safety measures and training is necessary. Hydrofluoric acid (HF) is an extremely toxic and dangerous acid and Teflon labware must be used to handle the HF acid. The RCA cleaning was carried out

under a laminar flow bench in the clean room. In this work, the RCA cleaning procedure has three major steps including HF dips in the beginning as well as at the end of RCA-1 and RCA-2. The RCA cleaning procedures are listed below in detail.

RCA-1: DI water rinse, ammonium hydroxide (NH_4OH) (29%) + hydrogen peroxide (H_2O_2) (30%) + H_2O (1:2:7 ratio by volume) for 3–6 min at 75–80 °C.

RCA-2: DI water rinse, hydrochloric acid (HCl) (37%) + H_2O_2 (30%) + H_2O (1:2:7 ratio by volume) for 6–8 min at 75–80 °C.

HF dip: DI water rinse, HF (2%) for 30 s at room temperature, DI water rinse.

RCA: HF (2%) dip → RCA-1 → HF (2%) dip → RCA-2 → HF (2%) dip.

RCA-1, organic clean step was used to remove insoluble organic contaminants. RCA-2, ionic clean was used to remove ionic and heavy metal contaminants. HF dip, oxide strip was used to remove the thin silicon dioxide layer where contaminants may have accumulated. At the end of all three wet-chemical steps, the wafers were rinsed in DI water. The RCA procedure followed in this work is described in [247].

3.1.2 AlO_x solution preparation

The AlO_x solution is prepared in the following way. To prepare 0.2 M AlO_x solution, 0.75 g of aluminium nitrate nonahydrate, $\text{Al}(\text{NO}_3)_3 \cdot 9\text{H}_2\text{O}$ (purity: 99.997%, Sigma-Aldrich) was dissolved in 10 ml of 2-methoxyethanol, $\text{CH}_3\text{OCH}_2\text{CH}_2\text{OH}$ (purity: 99.9%, concentration: ~100%, Sigma-Aldrich). For AlO_x solution of 0.1 M, 0.5 M and 1 M, aluminium nitrate nonahydrate of 0.37 g, 1.87 g and 3.75 g, respectively were dissolved in 10 ml of 2-methoxyethanol. The AlO_x solution was sonicated for 60 min at room temperature using an ultrasonicator (Roop Telsonic Ultrasonix Ltd). After ultrasonication, a clear and transparent solution was obtained.

3.2 Characterization methods

In this section, the basic theory behind some of the characterization techniques used in this thesis is presented. Four-point probe method was used to measure the sheet resistance of

the silicon wafers. Film thickness and RI of the AlO_x films were measured using a spectroscopic ellipsometer. 2D/3D optical microscope was used for analysis of AlO_x film surface. The root mean square (RMS) roughness of the AlO_x film was determined by atomic force microscope (AFM). Fourier transform infrared spectroscopy (FTIR) was utilized to determine the presences of various chemical bonds in the films. The elemental composition of AlO_x film, especially the IL composition influences the passivation property. The composition of the AlO_x film and the IL were determined by X-ray photoelectron spectroscopy (XPS) through elemental depth profile. Besides, transmission electron microscope (TEM) was used for structural characterization of the film. Electrical properties of the AlO_x film and its interface with silicon were characterized by metal insulator semiconductor (MIS) capacitor. Passivation properties were investigated through effective lifetime measurement of silicon coated with AlO_x film. PL measurement was used to spatially resolve defects in the AlO_x passivation.

3.2.1 Four-point probe

The four-point probe was originally proposed by Wenner to measure the resistivity of the earth [248]. Later, it was adopted for semiconductor wafer resistivity measurements [249]. It consists of four probes generally arranged in-line with equal space between the probes. It can be used to measure the type and resistivity of the silicon wafer and sheet resistance of doped regions.

The four-point probe resistivity, ρ (in $\Omega \cdot \text{cm}$) expression is given by [250]

$$\rho = \frac{2\pi}{\left(\frac{1}{s_1} - \frac{1}{s_2+s_3} - \frac{1}{s_1+s_2} + \frac{1}{s_3}\right)} \frac{V}{I} \quad (3.1)$$

where V is voltage (in V), I is current (in A), and s_1 , s_2 , and s_3 are probe spacings (in cm). If the probe spacings are equal, i.e, $s = s_1 = s_2 = s_3$, Eq. (3.1) reduces to

$$\rho = 2\pi s \frac{V}{I} \quad (3.2)$$

Semiconductor wafers are not semi-infinite in extent. Therefore, Eq. (3.2) must be corrected for finite geometries. The resistivity for an arbitrarily shaped sample can be written as

$$\rho = 2\pi sF \frac{V}{I} \quad (3.3)$$

where F corrects for probe location near sample edges, sample thickness, sample diameter, probe placement, and sample temperature [250,251].

Thin layers such as diffused or ion-implanted regions are usually characterized by sheet resistance R_{sh} (in Ω/\square). For uniformly doped samples, the sheet resistance is given by [250]

$$R_{sh} = \frac{\rho}{W} = \frac{\pi}{\ln(2)} \frac{V}{I} = 4.532 \frac{V}{I} \quad (3.4)$$

where W is the wafer thickness (in cm) with constraint $W \leq s/2$. The sheet resistance of the p⁺ diffused wafers in this work was measured using four-point probe method (Jandel/MHP-12 Multi-PT8, Jandel Engineering Limited). The equipment consist of a finely machined tungsten carbide multi height probe having tip radius of 4 mils or 100 μm and tip spacing of 40 mils or 1 mm [247]. A Keithley 2000 multimeter is employed as a voltmeter and a Keithley 220 programmable current source as current source.

3.2.2 Ellipsometry

Ellipsometry is a contactless and non-invasive optical characterization technique. It operates by measuring changes in the polarization state of light reflected from a sample surface [252]. The name “ellipsometry” stems from the fact that the incident plane-polarized light usually becomes elliptically polarized upon light reflection or vice-versa [250]. By modelling this measurement, the refractive indices, the extinction coefficients, and the thicknesses of film that has been deposited on a reflective substrate can be calculated. In this work, the measurements of thickness and RI were carried out using a spectroscopic ellipsometer (SE 800 from Sentech Instruments).

3.2.3 Optical microscope

Optical microscope is a simple contactless optical characterization tool that has been used for many years for many applications such as defect determination and integrated circuit (IC) inspection. In this work, the surface image of the as-deposited, annealed and rapid thermal processing (RTP)-fired AlO_x films and the actual area of the evaporated aluminium dots were measured with an optical microscope-Olympus-MX61-F. It offers a wide range of imaging and analysis facilities with a variety of digital cameras as well as software. The optical microscope is equipped with a personal computer (PC) interface for control of the microscope.

3.2.4 Zeta 3D microscope

For conventional microscopes, the depth of focus is limited. The Zeta system scans a sample over a user specified vertical range or in Z-direction. Using the Zeta Optics Module, it records the XY location and the precise Z height of the pixels. Later, this information is used for creating a true color 3D image and a 2D composite image. The image obtained by zeta microscope has an extended depth of focus and hence the sample surface is seen clearly. It is used for many PV applications such as blister analysis of the passivation film, analysis of pyramid after texturing, analysis of screen-printed metal contacts and depth of the laser fired contacts. In this work, 3D images of the surface were acquired using the Zeta-20 3D Optical Profiler from Zeta Instruments for blister analysis and laser fired contacts.

3.2.5 Atomic force microscopy (AFM)

AFM measurement is suitable for characterizing conducting as well as insulating samples. AFM measures the force between a probe and the sample and this interaction force depends on the nature of the sample, the distance between the probe and the sample surface, the probe geometry, sample surface topography and contamination [250]. AFM instrument consists of a cantilever with a sharp tip on its end that scans the surface of the sample to sense surface forces and the cantilever is usually fabricated from silicon, silicon oxide or silicon nitride materials [250]. AFMs can be operated in several modes such as contact mode, non-

contact mode and tapping mode. In this work, the RMS roughnesses were measured by AFM (Pico-SPM, Pico Scan 210 from Agilent Technologies).

3.2.6 Fourier transform infrared spectroscopy (FTIR)

FTIR spectra provide information about chemical bonding between atoms in a sample or molecular structure of the materials. During FTIR spectra measurement, a sample is exposed to an infra-red (IR) radiation and it transmits and reflects the IR radiation at different frequencies [253]. This technique is based on the fact that a molecule exposed to IR rays will absorb IR energy at frequencies characteristic to that molecule [254]. The interaction of IR radiation with organic molecules takes place most often at the wavenumbers between 4000 and 400 cm^{-1} [255]. For further discussion, refer to [256,257]. In this thesis, FTIR measurements were used to understand the presence of various bonds of AlO_x film.

3.2.7 X-ray photoelectron spectroscopy (XPS)

X-ray photoelectron spectroscopy is generally used to identify chemical species at the surface of a sample. It is also known as electron spectroscopy for chemical analysis (ESCA). XPS is an application of the photoelectric effect which was discovered by Heinrich Rudolph Hertz in 1887. When X-rays of 1–2 KeV (high-energy photons) interact with atoms of the material, electrons are ejected from the core levels [250]. The energy of the electron ejected from the material, E_{sp} is measured at the spectrometer. The binding energy (E_b) (in eV) of the electrons is given by [250],

$$E_b = h\nu - E_{\text{sp}} - \phi_{\text{sp}} \quad (3.5)$$

where $h\nu$ is the energy of the X-rays (in eV) (ν is the frequency in units of s^{-1} and Planck's constant, h is 4.1357×10^{-15} eV·s), ϕ_{sp} is the work function of the spectrometer (in eV), and E_{sp} is the measured energy of the ejected electron at the spectrometer (in eV).

Binding energies for different elements and compounds are available in [258,259]. In this work, the film composition was investigated by XPS-PHI5000 Versa Probe II with Al $K\alpha$ X-ray source from ULVAC-PHI.

3.2.8 Transmission electron microscopy (TEM)

In a transmission electron microscope (TEM), an image is formed when a beam of electrons is transmitted through a very thin electron-transparent sample. TEM uses electromagnetic lenses to focus the electrons into a very thin beam. In a high-resolution transmission electron microscope (HRTEM), the resolution is up to ~0.2 nm that enables us to observe atomic arrangements and nanostructures directly. In this thesis, HRTEM (2010F from Jeol) was used to obtain cross sectional images of the AlO_x/Si interface.

3.2.9 Electrical characterization of metal insulator semiconductor (MIS) capacitor

MIS capacitor is a simple two terminal semiconductor device used to study various properties and quality of the dielectric layer, and the nature of interface between the dielectric and semiconductor. Figure 3.1 shows the schematic of MIS capacitors used in this thesis. Thermally evaporated aluminium (Al) was used for making the top and bottom contacts.

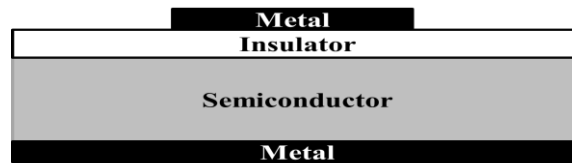


Figure 3.1: Schematic of MIS capacitor structure for electrical characterization of the dielectric film [50].

For electrical characterization, MIS capacitors were fabricated by depositing Al top electrodes through a shadow mask by thermal evaporation method. The back side of the wafer was HF (2%) cleaned to remove native oxide and Al metallization was subsequently carried out by thermal evaporation.

The permittivity of the dielectric material (in F·cm⁻¹) is given by

$$\epsilon = K\epsilon_0 \quad (3.6)$$

where, K represent relative permittivity of the dielectric also defined as dielectric constant of the material, and ϵ_0 represents permittivity of free space which is 8.854×10^{-14} F·cm⁻¹.

The equivalent oxide thickness (EOT) (in cm) is given by

$$\text{EOT} = \frac{K_{\text{SiO}_2} \epsilon_0}{C_{\text{acc}}} \quad (3.7)$$

where C_{acc} is the accumulation capacitance (in $\text{F}\cdot\text{cm}^{-2}$) and K_{SiO_2} is the dielectric constant of SiO_2 (3.9). The EOT can be determined from capacitance versus voltage (C-V) measurement by measuring the insulator capacitance.

EOT can be expressed as:

$$\text{EOT} = \frac{K_{\text{SiO}_2} t_{\text{high-k}}}{K_{\text{high-k}}} \quad (3.8)$$

where, $K_{\text{high-k}}$ is the dielectric constant of the high-k material and $t_{\text{high-k}}$ is the thickness of the high-k dielectric material (in cm). $t_{\text{high-k}}$ can be measured using spectroscopic ellipsometer.

The dielectric constant, $K_{\text{high-k}}$ can be determined as follows:

$$K_{\text{high-k}} = \frac{3.9 \times t_{\text{high-k}}}{\text{EOT}} \quad (3.9)$$

If we assume that the substrate is uniformly doped, the substrate doping, N_A can be calculated from high frequency C-V measurement [50]

$$\frac{1}{C_{\text{Smin}}^{\text{HF}}} = \frac{1}{C_{\text{min}}} - \frac{1}{C_{\text{acc}}} \quad (3.10)$$

$$C_{\text{Smin}}^{\text{HF}} = \frac{K_{\text{Si}} \epsilon_0}{X_{\text{dmax}}} \quad (3.11)$$

and, the maximum depletion width, X_{dmax} (in cm) is [50,260],

$$X_{\text{dmax}} = \sqrt{\frac{4K_{\text{Si}} \epsilon_0 \phi_B}{qN_A}} \quad (3.12)$$

and, the bulk potential, ϕ_B (in V) is [50,260],

$$\phi_B = \frac{kT}{q} \ln\left(\frac{N_A}{n_i}\right) \quad (3.13)$$

where C_{Smin}^{HF} is minimum value of semiconductor capacitance extracted from high frequency C-V (HFCV) plot (in $F \cdot cm^{-2}$) using the Eq. (3.10). C_{min} is the minimum high frequency C-V capacitance (in $F \cdot cm^{-2}$), K_{Si} is the relative permittivity of the Si (11.7).

N_A can be estimated using the above two equations for X_{dmax} and ϕ_B .

Flat-band voltage, V_{FB} (in V) is the voltage at which $C=C_{FB}$ and is given by [50],

$$\frac{1}{C_{FB}} = \frac{1}{C_{acc}} + \frac{1}{C_{S,FB}} \quad (3.14)$$

where [50],

$$C_{S,FB} = \frac{K_{Si}\epsilon_0}{L_d}, \quad L_d = \sqrt{\frac{kTK_{Si}\epsilon_0}{q^2N_A}} \quad (3.15)$$

where L_d is the extrinsic Debye length (in cm), $C_{S,FB}$ is semiconductor flat-band capacitance (in $F \cdot cm^{-2}$) and C_{FB} is flat-band capacitance (in $F \cdot cm^{-2}$).

Mid-gap voltage, V_{MG} is the voltage (in V) at which $C=C_{MG}$ [50]

$$\frac{1}{C_{MG}} = \frac{1}{C_{acc}} + \frac{1}{C_{S,MG}} \quad (3.16)$$

where, $C_{S,MG}$ is semiconductor mid-gap capacitance (in $F \cdot cm^{-2}$). C_{MG} is mid-gap capacitance (in $F \cdot cm^{-2}$).

$$C_{S,MG} = \frac{K_{Si}\epsilon_0}{X_{MG}}, \quad X_{MG} = \sqrt{\frac{2K_{Si}\epsilon_0\phi_B}{qN_A}} \quad (3.17)$$

where X_{MG} represents depletion width at mid-gap (in cm)

Fixed Oxide charges, Q_f (cm^{-2}) can be determined from V_{MG} [50]

$$Q_f = C_{acc} (V_{MG,ideal} - V_{MG})/q \quad (3.18)$$

and the ideal mid-gap voltage, $V_{MG,ideal}$ (in V) is [50]

$$V_{MG,ideal} = \phi_{MS} + \phi_B + \frac{qN_A X_{MG}}{C_{acc}} \quad (3.19)$$

and the work function difference, ϕ_{MS} (in V) [260]

$$\phi_{MS} = \phi_M - \phi_S = \phi_M - \left(\chi + \frac{E_{BG}}{2q} + \phi_B \right) \quad (3.20)$$

where, ϕ_S is the semiconductor work function (in V), ϕ_M is work function of metal gate (in V), χ is the electron affinity (in V), and E_{BG} denotes the band gap energy of silicon ($E_{BG}/q = 1.12$ V).

Interface trap density, D_{it} ($eV^{-1} \cdot cm^{-2}$) can be determined using the single frequency approximation method described by Hill et al. [261].

$$D_{it} = \frac{2}{qA} \frac{\frac{G_{max}}{\omega}}{\left(\frac{G_{max}}{\omega C_{acc,F}} \right)^2 + \left(1 - \frac{C_{max,G}}{C_{acc,F}} \right)^2} \quad (3.21)$$

where, $C_{acc,F}$ is the accumulation capacitance in farads (in F), G_{max} is the peak value of conductance (in S) from the conductance versus voltage (G-V) curve, $C_{max,G}$ is the capacitance (in F) corresponding to the voltage of G_{max} , A represents the area of capacitor (in cm^2), and ω represents measurement angular frequency ($\omega = 2\pi f$, f is the measured frequency in Hz) (in $rad \cdot s^{-1}$).

In this work, the MIS devices were characterized using C-V, G-V and current versus voltage (I-V) measurements using Keithley 4200 parameter analyzer. Double C-V sweeps were performed to detect hysteresis in the characteristics. During C-V and G-V measurements, the bias was applied to the bottom contact and the gate contact was grounded to avoid noise signals.

3.2.10 Series resistance correction

Series resistance (R_s) (in S^{-1}) correction is performed by extracting the R_s followed by correction of the measured capacitance and conductance with the extracted R_s [50].

$$R_s = \frac{G_{ma}}{G_{ma}^2 + \omega^2 C_{ma}^2} \quad (3.22)$$

where, G_{ma} (in S) and C_{ma} (in F) are the measured conductance and capacitance in the strong accumulation region.

Corrected capacitance C_c (in F) and corrected conductance G_c (in S) are given by [50]

$$C_c = \frac{(G_m^2 + \omega^2 C_m^2) C_m}{a^2 + \omega^2 C_m^2} \quad (3.23)$$

$$G_c = \frac{(G_m^2 + \omega^2 C_m^2) a}{a^2 + \omega^2 C_m^2} \quad (3.24)$$

and,

$$a = G_m - (G_m^2 + \omega^2 C_m^2) R_s \quad (3.25)$$

where, G_m is the measured conductance (in S) and C_m is the measured capacitance (in F).

Series resistance corrections for C-V and G-V curves were performed in this thesis work based on the procedure provided in this subsection.

3.2.11 Effective lifetime measurement

Photoconductance based lifetime measurement is one of the widely used standard measurement techniques for the measurement of effective carrier lifetime of the silicon samples. It is a non-destructive, contactless, convenient and fast measurement technique. The experimental apparatus used for injection-dependent lifetime measurements in this thesis work was Sinton WCT-120 lifetime tester from Sinton Instruments. The passivation quality of AlO_x film on silicon wafer was studied by the measurement of effective lifetime and high effective lifetimes are indicative of good passivation property of the material.

Figure 3.2 shows the schematic of the sample used for τ_{eff} measurements. Schematic of the sample used for J_{0e} measurement is shown in Figure 2.3 of chapter 2. Using lifetime measurements, effective surface recombination velocity, S_{eff} ($cm \cdot s^{-1}$) and emitter saturation current, J_{0e} ($A \cdot cm^{-2}$) can be extracted. The Kane and Swanson method was proven to be very useful for extraction of J_{0e} .

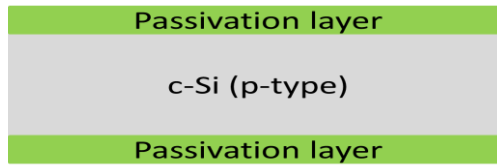


Figure 3.2: Schematic of the sample used for τ_{eff} measurement.

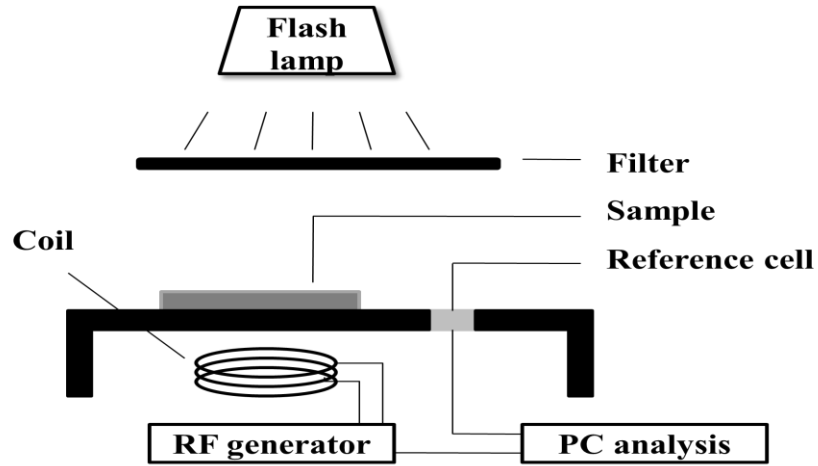


Figure 3.3: Schematic of the photoconductance measurement system (WCT-120 lifetime tester from Sinton Instruments) [262].

Figure 3.3 shows the schematic of the photoconductance measurement system (Sinton WCT-120 lifetime tester). During the photoconductance lifetime measurement, the sample is placed above the coil. A flash lamp is used to generate excess carriers within the silicon wafer and as a result, the conductance of the silicon wafer increases. The change in conductance is measured inductively by the coil. The sample signal (silicon wafer) is inductively coupled using a photoconductance-sensor coil, which in turn is part of an RF bridge circuit that senses changes in the permeability of the sample and therefore its conductance as a function of time after illumination [36]. The conductance (σ) (in S) of the silicon wafer is a quadratic function of the output voltage (V_{sample}) (in V) from RF-bridge circuit.

V_{sample} is related to the conductance by [44]

$$\sigma(t) = a V(t)_{\text{sample}}^2 + b V(t)_{\text{sample}} + c \quad (3.26)$$

where a , b and c are calibration constants. RF-bridge circuit can be calibrated using reference wafers of known dark conductance. Using a set of reference wafers with known

conductance, a calibration curve ($\sigma(t)$ versus $V(t)_{\text{sample}}$) can be obtained which can then be used to find the conductance of the silicon sample.

The conductance of the silicon sample (σ_{Si}) (in S) at equilibrium is dependent on the equilibrium electron and hole concentrations (n_0 and p_0) within the silicon sample [263]

$$\sigma_{\text{Si}} = qW(n_0\mu_n + p_0\mu_p) \quad (3.27)$$

where μ_n , μ_p are the electron and hole mobilities in the semiconductor (in $\text{cm}^2 \cdot \text{V}^{-1} \cdot \text{s}^{-1}$).

When the silicon sample is illuminated, excess carriers are generated within the silicon sample and the excess carriers change the conductance into (for insignificant trapping, $\Delta n = \Delta p$) [263],

$$\sigma_{\text{light}} = qW[(n_0 + \Delta n)\mu_n + (p_0 + \Delta n)\mu_p] = \sigma_{\text{Si}} + \Delta\sigma \quad (3.28)$$

where, σ_{light} is the conductance of the silicon sample due to light illumination (in S), and the excess photoconductance ($\Delta\sigma$) (in S)

$$\Delta\sigma = qW\Delta n(\mu_n + \mu_p) \quad (3.29)$$

The conductance measurement is spatially averaged over an area determined by the size of the coil (coil with diameter of 18 mm can cover an area of approximately 254 mm^2). The average excess carrier density (Δn_{avg}) (in cm^{-3}) can be determined from the difference between the excited conductance and the dark conductance ($\Delta\sigma$) as [263],

$$\Delta n_{\text{avg}} = \frac{\Delta\sigma}{q(\mu_n + \mu_p)W} \quad (3.30)$$

A measure of $\Delta\sigma$ is a measure of Δn_{avg} .

The spectrum of the flash is quite similar to the solar spectrum. To achieve a homogeneous photogeneration throughout the sample, the light of the flash is filtered using a 700 nm IR pass filter.

Recombination lifetime

When light (steady state or transient) is incident on a p-type semiconductor, the continuity equation for electron-hole pair generation and zero surface recombination is [250]

$$\frac{d\Delta n(t)}{dt} = G - R = G - \frac{\Delta n(t)}{\tau_{\text{eff}}} \quad (3.31)$$

where G is the electron-hole pair generation rate (in $\text{cm}^{-3}\cdot\text{s}^{-1}$), and R is the recombination rate (in $\text{cm}^{-3}\cdot\text{s}^{-1}$).

Solving Eq. (3.31) for τ_{eff} [250],

$$\tau_{\text{eff}}(\Delta n) = \frac{\Delta n(t)}{G(t) - d\Delta n(t)/dt} \quad (3.32)$$

In the transient photoconductance decay (PCD) method, with $G(t) \ll d\Delta n(t)/dt$ [250]

$$\tau_{\text{eff}}(\Delta n) = -\frac{\Delta n(t)}{d\Delta n(t)/dt} \quad (3.33)$$

In the steady-state method, with $G(t) \gg d\Delta n(t)/dt$ [250]

$$\tau_{\text{eff}}(\Delta n) = \frac{\Delta n}{G} \quad (3.34)$$

Effective lifetime

Effective lifetime is given by [36],

$$\frac{1}{\tau_{\text{eff}}} = \frac{1}{\tau_{\text{bulk}}} + \frac{1}{\tau_{\text{surface}}} = \frac{1}{\tau_{\text{rad}}} + \frac{1}{\tau_{\text{Auger}}} + \frac{1}{\tau_{\text{SRH}}} + \frac{1}{\tau_{\text{surface}}} \quad (3.35)$$

where τ_{surface} is surface recombination lifetime (in s). In the semiconductor, the effective minority carrier lifetime, τ_{eff} comprises the effects of all the recombination including bulk as well as surface.

For a symmetrically passivated silicon wafer, according to Grivickas et al. [264], the effective minority carrier lifetime (τ_{eff}) is related to the bulk lifetime (τ_{bulk}) and the effective surface recombination velocity (S_{eff}) as follows

$$\frac{1}{\tau_{\text{eff}}} = \frac{1}{\tau_{\text{bulk}}} + \left[\frac{W}{2S_{\text{eff}}} + \frac{1}{D} \left(\frac{W}{\pi} \right)^2 \right]^{-1} \quad (3.36)$$

where, D represents minority carrier diffusion constant (in $\text{cm}^2 \cdot \text{s}^{-1}$). For p-Si wafer, the electron diffusion constant (D_n) is $30 \text{ cm}^2 \cdot \text{s}^{-1}$ [36]. The above approximate τ_{eff} solution is found to deviate less than 5% from the exact τ_{eff} [36,265].

For small values of S_{eff} ($S_{\text{eff}} \ll \pi^2 D/2W$) [266],

$$\frac{1}{\tau_{\text{eff}}} = \frac{1}{\tau_{\text{bulk}}} + \frac{2S_{\text{eff}}}{W} \quad (3.37)$$

If τ_{bulk} is assumed to be infinite as the best case scenario for τ_{bulk} , recombination exclusively takes place at the two surfaces. Hence, an upper limit for S_{eff} , $S_{\text{eff,max}}$ (in s) is given by [266]

$$S_{\text{eff,max}} = S_{\text{eff}} \leq \frac{W}{2\tau_{\text{eff}}} \quad (3.38)$$

Bulk lifetime measurement

Bulk lifetime measurements of minority carriers in silicon wafers are extremely useful to calculate the surface recombination velocity. To evaluate the bulk lifetime (τ_{bulk}) of silicon wafers, double side polished silicon wafers were passivated chemically utilizing quinhydrone-methanol solution (0.07 M) after RCA cleaning and 2% HF dip [267,268].

3.2.12 Photoluminescence (PL) measurement

Unlike photoconductance method, where the lifetime is spatially averaged, PL imaging can finely resolve the regions of good and bad effective lifetimes [269]. When excitation light is applied to silicon wafers, electron-hole pairs are generated by absorption of light photons. When electron-hole pairs recombine, it causes light emission due to radiative recombination.

The radiative recombination rate (R_{rad}) (in $\text{cm}^{-3} \cdot \text{s}^{-1}$) can be expressed in terms of the excess carrier density and recombination lifetime as [270]

$$R_{\text{rad}} = \frac{\Delta n}{\tau_{\text{rad}}} \quad (3.39)$$

Similarly, the non radiative recombination rate (R_{nrad}) (in $\text{cm}^{-3}\cdot\text{s}^{-1}$) is

$$R_{\text{nrad}} = \frac{\Delta n}{\tau_{\text{nrad}}} \quad (3.40)$$

where, τ_{rad} and τ_{nrad} are radiative and non radiative recombination lifetime, respectively (in s).

The internal radiative quantum efficiency (η_{int}) can be expressed as the ratio of the rate of radiative recombination to the total recombination rate [270]

$$\eta_{\text{int}} = \frac{R_{\text{rad}}}{R_{\text{rad}} + R_{\text{nrad}}} \quad (3.41)$$

Therefore, η_{int} can be expressed in terms of the radiative and non-radiative lifetimes [270]

$$\eta_{\text{int}} = \frac{1/\tau_{\text{rad}}}{1/\tau_{\text{rad}} + 1/\tau_{\text{nrad}}} = \frac{1}{1 + \tau_{\text{rad}}/\tau_{\text{nrad}}} \quad (3.42)$$

A maximum η_{int} can be obtained by keeping $\tau_{\text{rad}}/\tau_{\text{nrad}}$ small (i.e., by making τ_{nrad} long compared to τ_{rad}). Growing or depositing materials which provide low defect densities and eliminating impurities which cause non radiative deep levels are few techniques to improve the quantum efficiency [270].

PL imaging of passivated silicon samples was carried out using a laboratory built apparatus as shown in Figure 3.4 with two banks of 48 RED LEDs (λ is ~ 630 nm) as illumination source and 8.3 MP Si CCD camera (Sensovation) coupled with specially designed Si filters [271].

PL measurement is a contactless, nondestructive method. When the bulk lifetime is high, the PL intensity represents the surface recombination and hence the quality of passivation layer. PL imaging can be used to access the uniformity of the passivation of silicon wafers by the deposited passivation layer. PL images can also be used for solar cell characterization to evaluate the texture uniformity of set of wafers with similar diffusion and

passivation layers [272]. PL imaging can be useful to characterize the quality of silicon wafers [273]. In this thesis work, PL imaging was used to optimize the chuck design for spraying instrument by means of analyzing and understanding the inhomogeneity in the PL images obtained by the passivated silicon wafers.

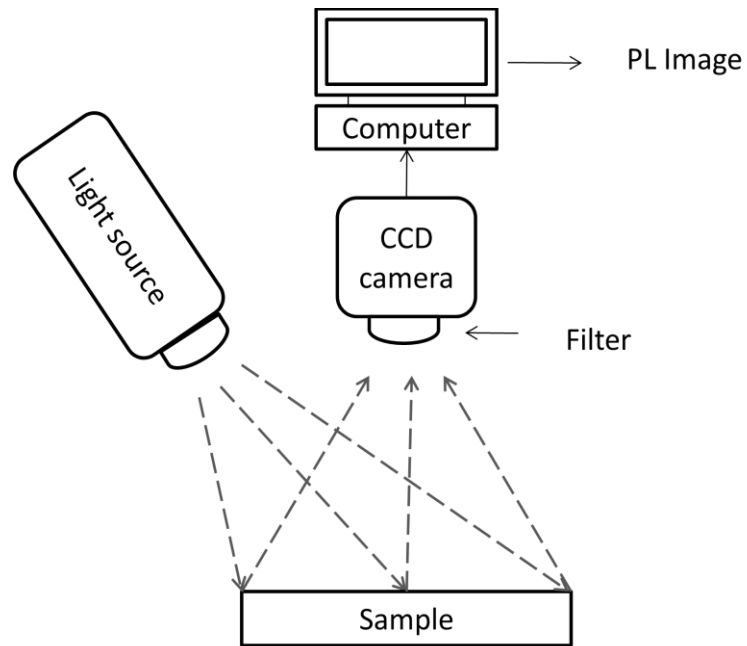


Figure 3.4: Photoluminescence imaging setup [273].

Chapter 4

Preliminary Investigations of AlO_x Deposition by Wet Chemical Processes

There is an acute need from the solar market for solution-processable metal oxide thin films that can be used in fabrication of c-Si solar cells. To date, many Al_2O_3 film deposition methods including ALD and PECVD rely on high-cost equipment. In this chapter, AlO_x thin films deposited by spin coating method and spray coating method by hand-held sprayer are investigated for surface passivation of p-type c-Si.

4.1 Spin coating

Spin coating process is one of the most often used deposition methods in semiconductor industries and it is a simple low cost deposition technique. Spin coating is a procedure used to deposit uniform thin films on flat substrates. It is particularly attractive for AlO_x deposition as it removes the need for costly precursors such as TMA. A machine used for spin coating process is called a spin coater or a spinner.

4.1.1 Deposition method

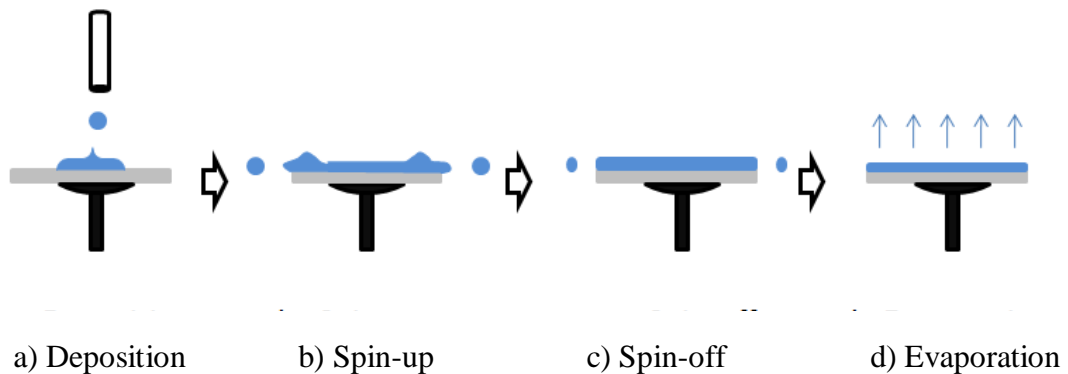


Figure 4.1: Four stages of spin coating [274,275].

In spin coating process, the thin films are deposited by centrifugal draining and evaporation [276]. Bornside et al. [274] divided the whole spin coating process into four stages: deposition, spin-up, spin-off and evaporation. The four stages of the spin coating process are shown in Figure 4.1 [274,275].

a) Deposition

During the stage of deposition, the substrate is placed on the spin coater and the solution is deposited on the surface of substrate as shown in Figure 4.1(a) by a micropipette. Static dispense and dynamic dispense are two common methods to dispense the solution [277]. If the substrate is not rotating during solution dispense, it is called static dispense. If the substrate is rotating at a low speed, it is called dynamic dispense. In static dispense, the substrate does not spin and a small amount of solution is applied on or near the center of the substrate. In general, highly viscous solution and/or larger substrates require a large amount of solution to ensure full coverage of the substrate [277].

On the other hand, in dynamic dispense, the solution is dispensed while the substrate is spinning at low speed typically around 500 rotations per minute (rpm) to spread the solution over the whole substrate [277]. Since it is usually not necessary to deposit large amount of solution to cover the entire surface of the substrate, dynamic dispense results in less waste of material [277]. If dispensing tips are cut unevenly or have burrs or defects, it can create air bubbles in dispensed fluid [278]. Presences of particles on the substrate surface prior to dispense may create comets, streaks, flares and pinholes [278]. Insufficient dispense volume may lead to uncoated areas [278].

b) Spin-up

After the deposition of material, the substrate is accelerated up to the desired final rotational speed and large amount of the material is ejected from the surface of the substrate by the rotational process [279] as seen from the Figure 4.1(b). The thickness of the spin coated layer is influenced by the spinning speed, rotating time and solution viscosity [280]. Higher spinning speeds and longer spinning times in general create thinner films [278].

c) Spin-off

In this stage, gradual fluid thinning takes place [277]. Fluid thinning is usually quite uniform as seen from the Figure 4.1(c). At this stage, the substrate is spinning at a constant speed and solution is stably out flowing from the substrate [277]. The viscous forces dominate

the behaviour of fluid thinning [277]. If spin time is too short and/or spin speed is too high, it can create swirl pattern on the film [278].

d) Evaporation

The film drying stage starts when the spin-off stage ends [279]. In this stage, the substrate still spins at a constant speed but centrifugal outflow stops as seen from the Figure 4.1(d). Thinning of the film is due to solvent evaporation [279]. Depending on the volatility of the solvent, the transition from the third stage to fourth stage takes place [281].

Final film thickness and other film properties depend on the nature of the solution (viscosity, drying rate, etc.), surface tension, air temperature, humidity and the parameters used for the spin coating process such as amount of the delivered solution, final spinning speed, acceleration, spin time [277,279].

According to Meyerhofer [282], the final film thickness of a spin-coated layer

$$t_f = \left(1 - d/d_0\right) \left(\frac{3 \eta e}{2 d \omega_s^2}\right)^{1/3} \quad (4.1)$$

where t_f is the final film thickness (in cm), d is the solvent density (in $\text{g}\cdot\text{cm}^{-3}$), d_0 is the initial value of d (in $\text{g}\cdot\text{cm}^{-3}$), η is viscosity (in $\text{g}\cdot\text{cm}^{-1}\cdot\text{s}^{-1}$), ω_s is the angular velocity of spinner (in $\text{rad}\cdot\text{s}^{-1}$) and e is the evaporation rate (in $\text{cm}\cdot\text{s}^{-1}$) of the solvent [279].

Since the evaporation rate (e), viscosity (η) and solvent density (d) change during the spin coating process, this formula is only to guide the experiments. In practice, the parameters related to the film thickness are determined empirically. A simple formula which is mostly used is [279]

$$t_f = A\omega_s^{-B} \quad (4.2)$$

where A and B are constants that can be determined empirically. In most of the cases, B lies somewhere between 0.4 and 0.7 [283].

4.1.2 Experimental detail

Single side polished (SSP) p-type Cz c-Si wafers (2-inch, <100>, 4–7 $\Omega\cdot\text{cm}$, 300 μm) were used to investigate the physical and electrical characteristics of the spin coated AlO_x

film. Double side polished (DSP) p-type FZ c-Si wafers (4-inch, <100>, 1–5 $\Omega\cdot\text{cm}$, 300 μm) were chosen as a substrate for surface passivation experiments of spin coated AlO_x film. For spin coating processes, synthesis of the AlO_x solution was done by following the procedure described in chapter 3, section 3.1.2. Prior to AlO_x spin coating, all silicon wafers were cleaned using RCA procedure described in chapter 3, section 3.1.1. Film thicknesses and RI values were obtained by spectroscopic ellipsometer. RTP annealing was performed using AS-One 150 RTP from AnnealSys.

To investigate the uniformity of the spin coated AlO_x films, AlO_x solution of 0.2 M was spin coated on a silicon substrate at a speed of 3000 rpm for 10 s using a spinner followed by annealing at 220 $^\circ\text{C}$ for 5 min using a hot plate. The spinning-hot plate annealing cycle was repeated one more time based on references [284,285] followed by spectroscopic ellipsometry measurements. The process flow of prepared sample, named as Sample A is shown in Figure 4.2.

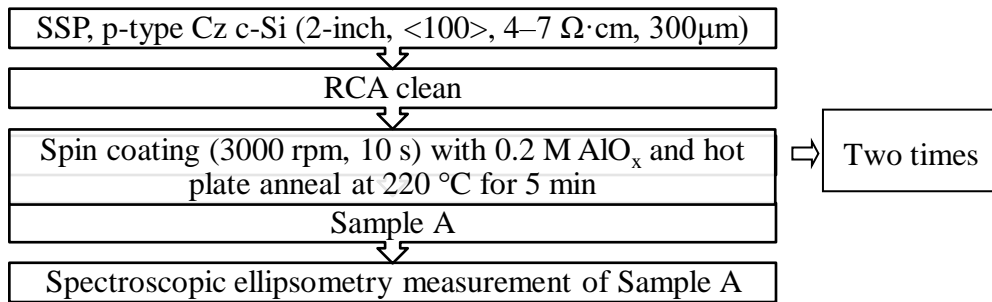


Figure 4.2: Process flow of Sample A.

Xia et al. [286] demonstrated good quality spin coated Al_2O_3 film serving as a gate dielectric using AlO_x solution prepared by dissolving aluminium nitrate nonahydrate ($\geq 98\%$, Aldrich) in 2-methoxyethanol ($\geq 99.9\%$, Aldrich) with a concentration of 0.5 M. The AlO_x solution 0.5 M was then spin coated on the n^{++} silicon substrate at 3000 rpm for 10 s, and subsequently annealed on a hotplate at 220 $^\circ\text{C}$ for 10 min [286]. Spinning-hot plate annealing cycle was repeated one more time to prepare amorphous Al_2O_3 layer as the gate dielectric [286]. Aluminium was thermally evaporated through a shadow mask to fabricate $\text{Al}/\text{Al}_2\text{O}_3/n^{++}$ Si structure for study of the electrical characteristics [286]. In this thesis work, electrical characteristics of $\text{Al}/\text{AlO}_x/p\text{-Si}/\text{Al}$ structure are investigated with spin coated AlO_x film prepared using 0.5 M AlO_x solution. Vitanov et al. used different spinning speed and spinning time for different solutions and these conditions were chosen experimentally depending on the

viscosity of the solution with the aim of depositing homogeneous layers on silicon wafers for surface passivation of p-type c-Si [140].

To investigate the effect of post deposition RTP annealing on oxide thickness and RI of samples prepared using different molarities, AlO_x solution of 0.1 M (sample B), 0.2 M (sample C) and 0.5 M (sample D) [286,287] was spin coated on silicon wafers and subsequently annealed on a hot plate. The spinning-hot plate annealing cycle was repeated one more time based on references [284,285,286] for all samples, followed by spectroscopic ellipsometry measurement. The films were exposed to elevated temperature of 800 °C for 10 s in N_2 ambient using RTP tool followed by spectroscopic ellipsometry measurement. Further, to investigate electrical characteristics, MIS capacitors were fabricated for Sample D using aluminium as top and bottom contacts. Circular shaped aluminum contacts with diameters of 400 μm were used for electrical characterization. The process flow of prepared samples, named as Sample B, Sample C and Sample D are shown in Figure 4.3.

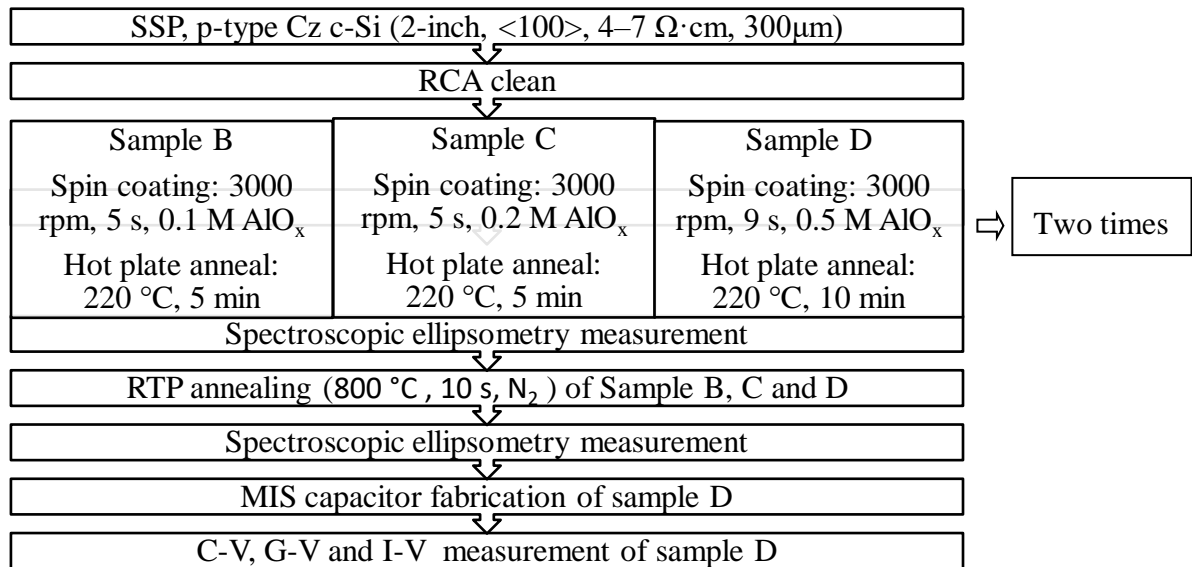


Figure 4.3: Process flow of Sample B, Sample C and Sample D.

The physical properties of AlO_x films were investigated using HRTEM. The silicon wafer was spin coated using 0.5 M AlO_x solution and annealed at 220 °C for 10 min on a hot plate. Spinning-hot plate annealing cycle was repeated one more time based on references [284,285,286]. The sample was annealed at 800 °C for 10 s, in N_2 ambient using RTP tool. 300 nm aluminium metal layer was thermally evaporated on AlO_x film before the cross-sectional TEM sample preparation process. The process flow of prepared sample, named as Sample E is shown in Figure 4.4.

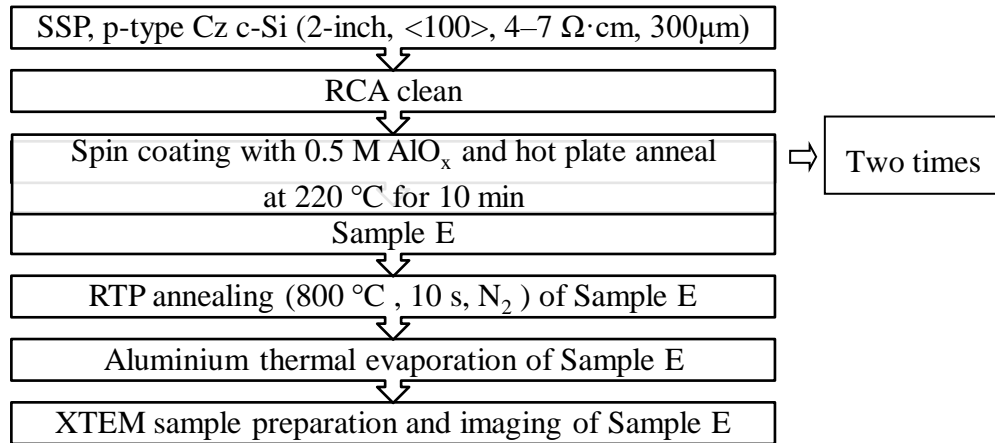


Figure 4.4: Process flow of Sample E.

For surface passivation study, 0.5 M AlO_x solution was spin coated (3000 rpm for 9 s) twice on the front and rear side of double side polished FZ silicon wafer with hot plate annealing at 220 °C for 10 min. Sample F was annealed using RTP at 800 °C for 10 s in N₂ and Sample G was annealed at 780 °C for 130 min in O₂ using furnace. Effective minority carrier lifetime measurements for Sample F and Sample G were performed by WCT-120 Sinton lifetime tester. The process flow of prepared samples, named as Sample F and Sample G is shown in Figure 4.5.

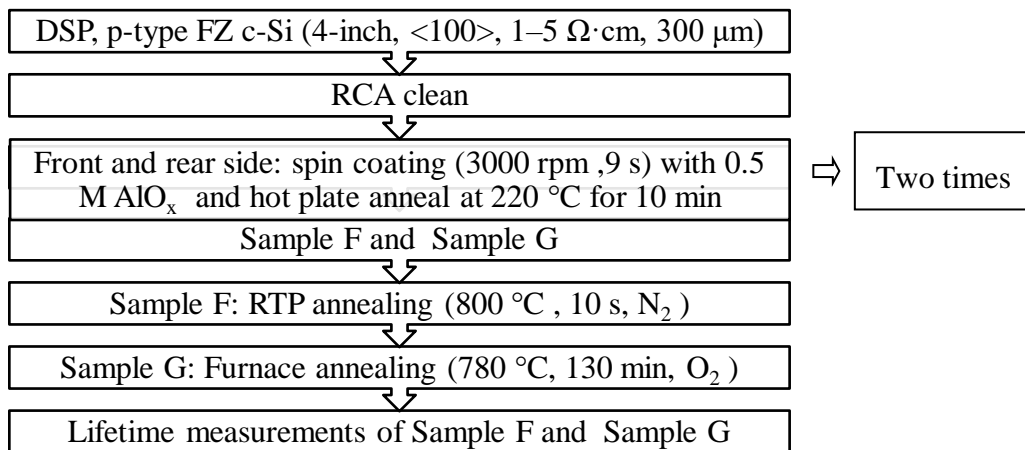


Figure 4.5: Process flow of Sample F and Sample G.

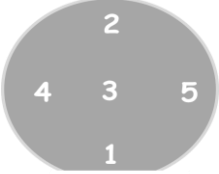
4.1.3 Results and discussion

The results obtained from the investigations of spin coated AlO_x films such as uniformity, electrical characterization of MIS capacitors, physical characterization and surface passivation are presented in this section.

(a) Uniformity of spin coated AlO_x Film

Table 4.1 contains the oxide thickness and RI of Sample A measured by spectroscopic ellipsometer at 5 different places over the 2-inch Si wafer. The mean value of AlO_x film thickness was 57.45 nm and the standard deviation was 0.27 nm. The mean of the RI was 1.55 and the standard deviation was below measurement resolution. All measurements from different parts of AlO_x film exhibited the same RI. It was established that thickness and RI of the spin coated AlO_x film are almost uniform over 2-inch silicon wafer. Vitanov et al. reported thickness uniformity of 2–5% on a 3-inch silicon wafer for spin coated Al₂O₃ film [146]. In literature [146,288], RI values in the range of 1.51–1.6 were reported for spin coated Al₂O₃ films.

Table 4.1: The thickness and RI of spin coated AlO_x film measured by spectroscopic ellipsometer for Sample A. The leftmost column of the table shows the sample indicating the positions where the measurements are performed.

	Position on sample	Thickness (nm)	RI
	1	57.39	1.55
	2	57.93	1.55
	3	57.93	1.55
	4	57.67	1.55
	5	57.35	1.55

(b) Effect of post deposition RTP annealing on thickness and RI of sample prepared using different molarities

Table 4.2 shows the spectroscopic ellipsometry results for Sample B, Sample C and Sample D. The thickness and RI for each sample was measured at five different locations and is reported as the average \pm standard deviation. The standard deviation of RI was below measurement resolution. The thickness and RI measurements of Sample B, Sample C and Sample D showed increase in RI and considerable reduction of film thickness (~50%) after RTP anneal which can be attributed to the densification of AlO_x film. RI of 1.58 was reported

by Vitanov et al. for spin coated Al₂O₃ film (56 nm) after 750 °C annealing temperature (60 min, O₂) using alumina–sec–butoxide (Al(OBu)₃) precursor [146].

Table 4.2: The effect of post deposition RTP annealing on thickness and RI of spin coated AlO_x films—Sample B, Sample C and Sample D—prepared using different molar concentration.

Sample Name	Molar concentration	As-deposited		RTP anneal (800 °C, 10 s, N ₂)	
		Thickness (nm)	RI	Thickness (nm)	RI
Sample B	0.1 M	25 ± 0.3	1.56	12 ± 0.3	1.79
Sample C	0.2 M	40.1 ± 0.4	1.56	18.1 ± 0.4	1.73
Sample D	0.5 M	172.1 ± 0.4	1.56	88 ± 0.4	1.58

(c) C-V and G-V characteristics of Sample D

The C-V and G-V characteristics for Sample D were measured at 100 kHz and 1 MHz. Double C-V sweeps were performed to find hysteresis in the electrical characteristics. Series resistance correction was applied to the measured capacitance and conductance following the procedure given in chapter 3, subsection 3.2.10. The D_{it} was calculated from the peak of the G-V curve using the single frequency conductance method [261] and the Q_f was calculated from the shift in mid-gap voltage from its ideal value [50]. The measured and series resistance corrected C-V and G-V characteristics of a MIS capacitor for 100 kHz and 1 MHz frequencies are shown in Figure 4.6(a) for 88 nm AlO_x film after RTP annealing at 800 °C for 10 s in N₂. The series resistance corrected C-V curves of 100 kHz and 1 MHz frequencies for a shorter range of voltage to reveal hysteresis are shown in Figure 4.6(b). There is a sharp peak in the G-V curve due to the interface state between AlO_x and silicon. The hysteresis in the C-V curve is measured to be 13 mV and 9 mV for 100 kHz and 1 MHz frequencies, respectively and is considered negligible.

The dielectric constant from the series resistance corrected C-V was calculated to be 7.6 using oxide thickness obtained by ellipsometry measurement. Dielectric constant in the range of 5–6.5 was reported in literature for spin coated Al₂O₃ film [148,149]. The Q_f and D_{it}

extracted from the corrected C-V and G-V curves of 100 kHz are found to be $-5.5 \times 10^{12} \text{ cm}^{-2}$ and $3.9 \times 10^{11} \text{ eV}^{-1} \cdot \text{cm}^{-2}$ which are comparable with the results reported in literature for spin coated AlO_x film [146]. Vitanov et al. reported Q_f of $-4.5 \times 10^{11} \text{ cm}^{-2}$ and D_{it} of $3.7 \times 10^{11} \text{ eV}^{-1} \cdot \text{cm}^{-2}$ for spin coated Al_2O_3 film annealed at $750 \text{ }^\circ\text{C}$ [146].

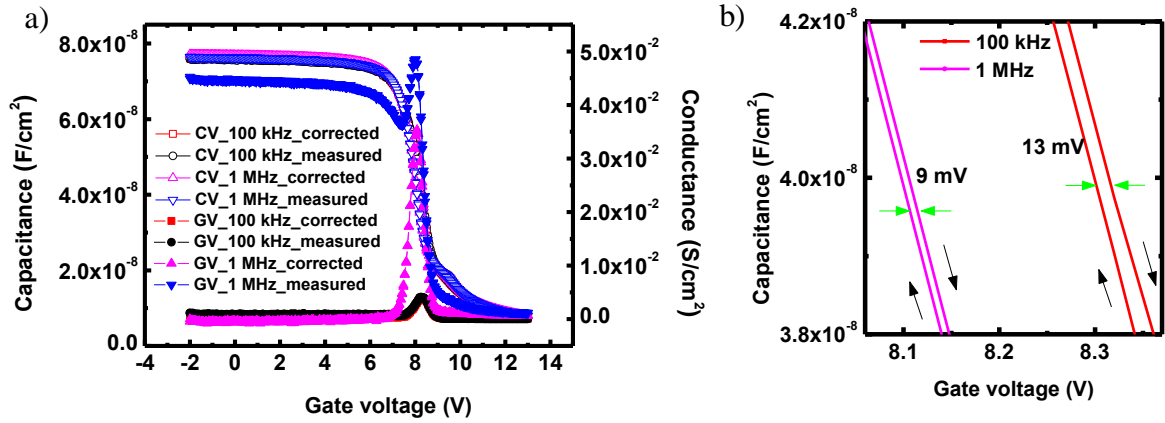


Figure 4.6: (a) Measured and series resistance corrected C-V and G-V curves of Sample D measured at 100 kHz and 1 MHz. (b) Series resistance corrected C-V characteristics (rescaled version of Figure 4.6 (a)) showing the hysteresis. Hysteresis is seen to be 13 mV and 9 mV for 100 kHz and 1 MHz, respectively. The black arrows indicate the direction of the voltage sweep. The measurement was started from inversion.

Shin et al. [168] investigated the suitability of solution processed Al_2O_3 film (spray coating) for rear surface passivation and optical trapping for PERC Si solar cells. Shin et al. [168] reported Q_f of $-3.19 \times 10^{12} \text{ cm}^{-2}$ for an 80 nm Al_2O_3 film, demonstrating passivation properties of the film. Shin et al. [168] also achieved optical properties of spray coated 80 nm Al_2O_3 film identical to the $\text{Al}_2\text{O}_3/\text{SiN}_x$ stack deposited ALD and PECVD, indicating that it can be used as optical trapping layer. Shin et al. [168] suggest that spray coated 80 nm Al_2O_3 film is a promising candidate to replace the $\text{Al}_2\text{O}_3/\text{SiN}_x$ passivation stack in PERC Si solar cells. Dobrzanski et al. [289] investigated 80 nm of Al_2O_3 film deposited by ALD as antireflection coating layer and it was found that Al_2O_3 ARC layer had a significant impact on the silicon solar cell. Here, the best results were obtained for 80 nm of Al_2O_3 film in the wavelength range of 400 nm to 800 nm with reflection less than 1% [289].

(d) I-V characteristics of Sample D

The breakdown field strength of AlO_x film was investigated by I-V analysis. Figure 4.7 shows the I-V characteristics of 88 nm AlO_x film after RTP annealing at 800 °C for 10 s in N_2 .

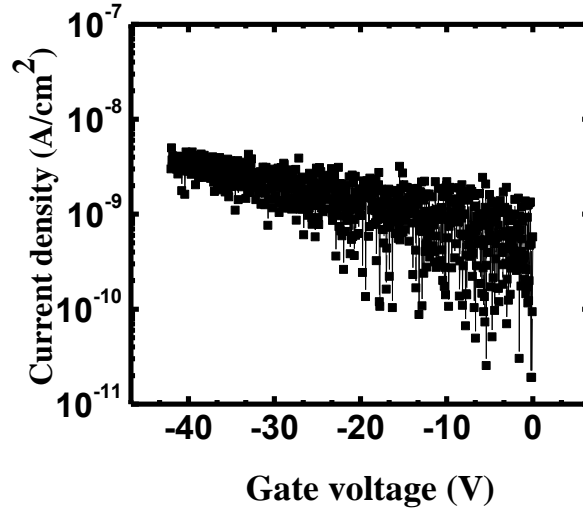


Figure 4.7: I-V characteristics of Sample D.

Due to limitation of the measurement system—voltage applied to the terminals is limited up to ± 42 V—the voltage sweep was performed up to the maximum voltage of - 42 V and it can be observed from the figure that the device is not breaking down till - 42 V. Hence, it can be concluded that the breakdown voltage of deposited AlO_x film (88 nm) is more than - 42 V and corresponding breakdown field would be $> 3.8 \text{ MV}\cdot\text{cm}^{-1}$. From I-V curve, the leakage current density of $3 \times 10^{-9} \text{ A}\cdot\text{cm}^{-2}$ was obtained at - 42 V. The leakage current density in the order of $10^{-7} \text{ A}\cdot\text{cm}^{-2}$ at an electrical field of $0.5 \text{ MV}\cdot\text{cm}^{-1}$ was reported for 56 nm spin coated Al_2O_3 film annealed at 750 °C [146]. In literature, breakdown field in the range of 3.5–6.6 $\text{MV}\cdot\text{cm}^{-1}$ was reported for spin coated Al_2O_3 film [149].

(e) Physical characterization of Sample E

Figure 4.8 shows the cross-sectional TEM image of Sample E that shows the presence of IL of ~ 9 nm in thickness. The spin coated AlO_x film was found to be amorphous. Vitanov et al. observed formation of some grains after the highest annealing temperature of 750 °C through SEM analysis of spin coated Al_2O_3 film [146]. Amorphous nature of Al_2O_3 film helps in minimizing the leakage current and maximizing the breakdown voltage due to the absence of crystal grain boundaries [285].

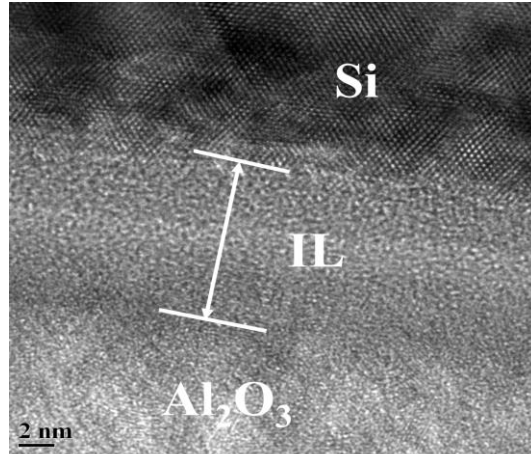


Figure 4.8: Cross sectional HRTEM image of Sample E after annealing at 800 °C for 10 s in N₂ ambient.

(f) Surface passivation of spin coated AlO_x film

RTP annealing

Figure 4.9 shows the lifetime measurement of Sample F after RTP annealing at 800 °C for 10 s, in N₂. The RTP annealed AlO_x film resulted in very poor surface passivation of the silicon wafer, as indicated by very low τ_{eff} value of about 1.9 μs at $\Delta n = 1 \times 10^{15} \text{ cm}^{-3}$.

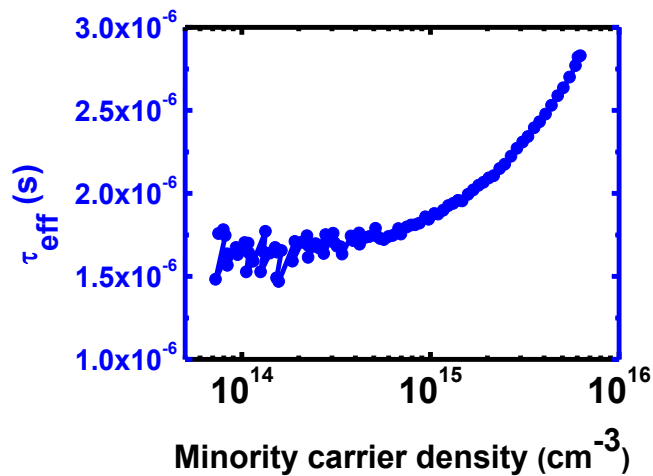


Figure 4.9: Effective carrier lifetime as a function of minority carrier concentration for the Sample F annealed at 800 °C for 10 s in N₂. τ_{eff} is 1.9 μs at $\Delta n = 1 \times 10^{15}$.

Dingemans et al. [290] showed that annealing prior to the firing step was not necessary, as the firing process itself can activate the surface passivation of SiO₂ (PECVD)/Al₂O₃ (ALD) stack. Here, $S_{\text{eff}} < 3 \text{ cm}\cdot\text{s}^{-1}$ was achieved after direct firing at $\sim 800 \text{ }^\circ\text{C}$ in an industrial belt-line firing furnace [290]. Richter et al, investigated performance of Al₂O₃ (2.6 nm, ALD)/SiN_x (70 nm, PECVD) passivation stack, and reported J_{0e} values of 186 fA·cm⁻² and 57 fA·cm⁻² for as-deposited sample and after firing at 800 °C in conveyor belt furnace, respectively. Bordihn et al. demonstrated excellent $S_{\text{eff}} < 10 \text{ cm}\cdot\text{s}^{-1}$ for Al₂O₃ (30 nm, ALD) films on n-type and p-type Cz silicon wafers after a direct industrial firing step at 850 °C [63].

Furnace annealing

Figure 4.10 shows the effective carrier lifetime and calculated $S_{\text{eff,max}}$ as a function of minority carrier density for Sample G after high temperature annealing for prolonged annealing time.

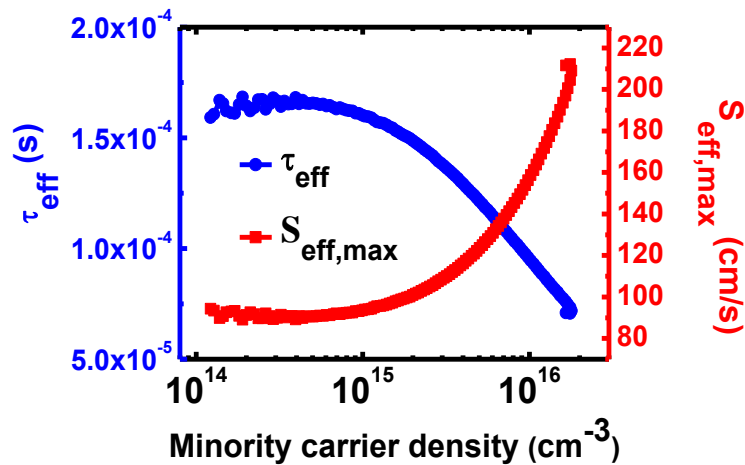


Figure 4.10: Effective carrier lifetime and $S_{\text{eff,max}}$ as a function of minority carrier concentration for the sample G annealed at 780 °C for 130 min in O₂ ambient (τ_{eff} is 160 μs and $S_{\text{eff,max}}$ is 94 $\text{cm}\cdot\text{s}^{-1}$ at $\Delta n = 1 \times 10^{15} \text{ cm}^{-3}$).

According to the report by Vermarien et al. high temperature annealing in oxygen for a prolonged annealing time could improve the passivation quality of spin coated (Al₂O₃)₃(TiO₂)₂ film [291]. Vermarien et al. achieved effective minority carrier lifetimes of 143 μs and 113 μs after annealing at 780 °C in O₂ ambient for 100 min and 50 min, respectively [291]. In this work, Sample F annealed at 780 °C for 130 min in O₂ ambient

resulted in τ_{eff} of 160 μs and $S_{\text{eff,max}}$ of 94 $\text{cm}\cdot\text{s}^{-1}$ for $\Delta n = 1 \times 10^{15} \text{ cm}^{-3}$. Here, $S_{\text{eff,max}}$ was calculated using Eq. (3.38). For spin coated AlO_x film, S_{eff} values in the range of 55–85 $\text{cm}\cdot\text{s}^{-1}$ were reported in literature [143,144,145].

4.2 Spray coating

Spray coating technique is one of the deposition methods to prepare thin films. It is attractive for low cost applications. In this section, AlO_x thin films deposited by a spray coating process using hand-held sprayer is discussed for surface passivation of p-type c-Si. The results obtained from the investigations such as electrical characterization and physical characterization are also presented in this section.

4.2.1 Experimental details

The experimental setup for the spray coating process is shown in Figure 4.11. The specifications of p-type, $\langle 100 \rangle$ oriented c-Si wafers chosen in the experiment are as follows: (i) 2-inch single side polished Cz wafers with thickness of 300 μm and resistivity of 4–7 $\Omega\cdot\text{cm}$ were used for electrical characterization. (ii) 4-inch double side polished FZ wafers with thickness of 280 μm and resistivity of 1–5 $\Omega\cdot\text{cm}$ were used for passivation study and XPS analysis.

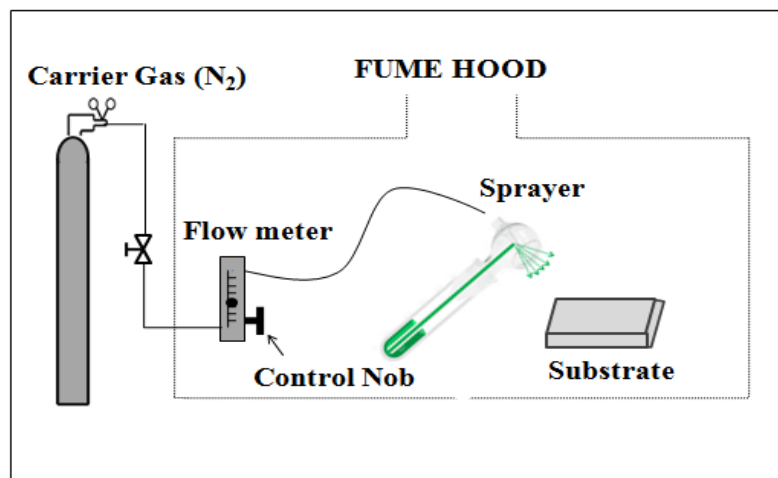


Figure 4.11: Experimental setup for AlO_x film deposition by spray coating process using hand-held sprayer.

The wafers were first cleaned using the RCA cleaning process described in Chapter 3, section 3.1.1. AlO_x solution of 0.2 M was prepared by following the procedure described in Chapter 3, section 3.1.2 and spray coated on a 2-inch silicon wafer at room temperature using N_2 as carrier gas. The sample was annealed using a hot plate at 400 °C for 5 min. According to literature [157,164,165,166,167], the deposition of the AlO_x films can be achieved by spray pyrolysis process at different substrate temperatures in the range of 300 °C to 650 °C. The thickness and RI of AlO_x film measured using a spectroscopic ellipsometer were 19 nm and 1.57 respectively. The sample underwent PDA in a preheated furnace at 520 °C for 20 min in O_2 ambient. The thickness of the AlO_x film reduced to 13 nm and RI increased to 1.63 after PDA due to densification of the AlO_x film. MIS capacitors of 200 μm diameter were fabricated with aluminum as front and back contact. High frequency C-V and G-V measurements were carried out using the Keithley 4200-semiconductor characterization system.

To study surface passivation properties, AlO_x solution (0.2 M and 1 M) was spray coated on both sides of RCA cleaned FZ wafers. To investigate influence of annealing temperature on surface passivation, AlO_x solution of 1 M was spray coated on both sides of the silicon surface and after hot plate annealing at 220 °C for 5 min, the samples were annealed in O_2 ambient at temperatures from 400 °C to 850 °C for 2 hours.

Effective lifetime was measured using Sinton Instruments WCT lifetime tester. Chemical composition of AlO_x film was studied using XPS depth profile analysis. For HRTEM imaging, the sample was prepared by mechanical polishing, followed by ion milling. Aluminum was deposited on AlO_x to protect the surface of AlO_x layer during the sample preparation process.

4.2.2 Results and discussions

Figure 4.12(a) shows the series resistance corrected high frequency C-V and G-V of the MIS capacitors after PDA of 520 °C for 20 min in O_2 ambient measured at 100 kHz. The C-V for a shorter range of voltage to reveal hysteresis is shown in Figure 4.12(b). The film showed minimal hysteresis behavior in the C-V curve and the hysteresis in the C-V curve was measured to be 20 mV and is considered negligible. Single frequency conductance method [261] was used to find D_{it} from the peak of the G-V curve. From C-V and G-V curve shown

in Figure 4.12(a), dielectric constant of 6, Q_f of $-4.2 \times 10^{12} \text{ cm}^{-2}$ and D_{it} of $1.9 \times 10^{11} \text{ eV}^{-1} \cdot \text{cm}^{-2}$ were extracted. Shin et al. reported Q_f of $-3.19 \times 10^{12} \text{ cm}^{-2}$ for an 80 nm spray deposited Al_2O_3 film [168]. D_{it} in the range of $(1-1.6) \times 10^{11} \text{ eV}^{-1} \cdot \text{cm}^{-2}$ was reported for AlO_x film deposited by spray pyrolysis process in literature [166,167].

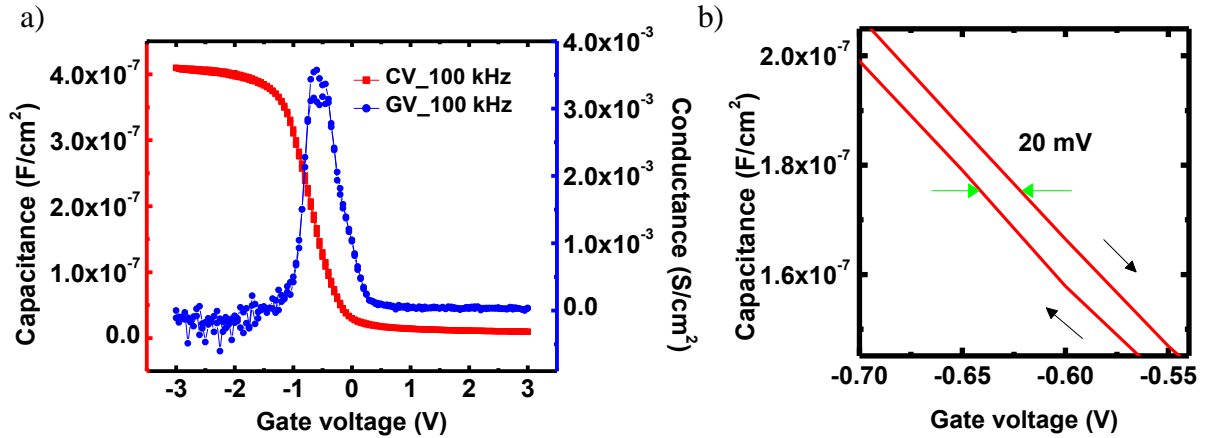


Figure 4.12: (a) Series resistance corrected high frequency capacitance and conductance characteristics of 13 nm AlO_x film after PDA of 520°C for 20 min in O_2 ambient measured at 100 kHz. (b) Series resistance corrected C-V characteristics (rescaled version of Figure 4.12 (a)) showing the hysteresis. Hysteresis is seen to be 20 mV. The black arrows indicate the direction of the voltage sweep. The measurement was started from inversion.

Figure 4.13 shows the I-V characteristics of the MIS capacitors in accumulation. From the I-V characteristics, breakdown voltage (V_{BR}) of 14.4 V was observed and the corresponding breakdown electric field calculated was $10.2 \text{ MV} \cdot \text{cm}^{-1}$.

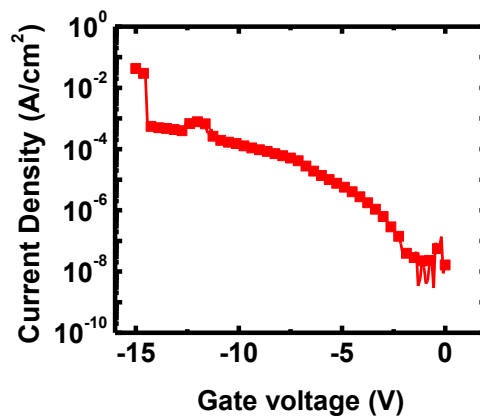


Figure 4.13: I-V characteristics of 13 nm AlO_x film after PDA of 520°C for 20 min in O_2 ambient.

Breakdown field in the range of 2–6.2 MV·cm⁻¹ was reported in literature for AlO_x films deposited by spray pyrolysis [157,166,167].

Surface passivation of as-deposited and annealed spray coated AlO_x films was investigated and the results are presented in Figure 4.14 and Figure 4.15, respectively. Here, S_{eff,max} was calculated using Eq. (3.38). For the as-deposited AlO_x film, τ_{eff} value of 2 μs was obtained at Δn = 1 × 10¹⁵ cm⁻³, whereas τ_{eff} of 10 μs and S_{eff,max} of 1356 cm·s⁻¹ was obtained at Δn = 1 × 10¹⁵ cm⁻³ for the sample prepared using 0.2 M AlO_x solution after PDA at 520 °C for 20 min in O₂ which indicates annealing is necessary to activate the passivation.

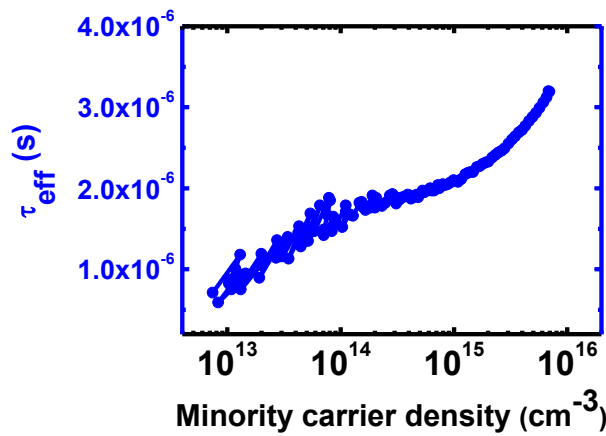


Figure 4.14: Injection level dependent lifetimes for the as-deposited AlO_x (0.2 M) film. τ_{eff} is 2 μs at Δn = 1 × 10¹⁵ cm⁻³.

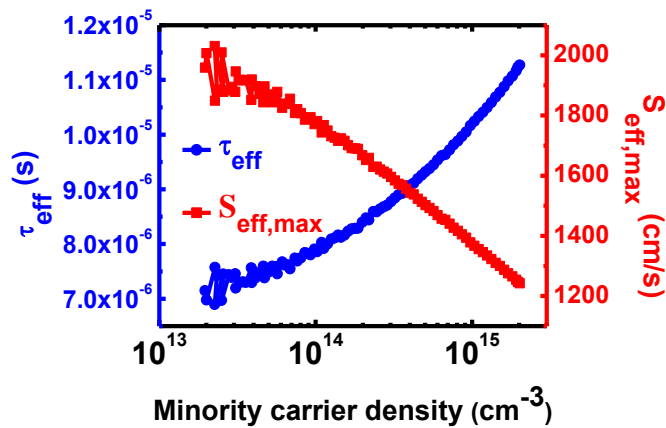


Figure 4.15: Injection level dependent lifetimes and S_{eff,max} for spray coated AlO_x (0.2 M) film after annealing at 520 °C for 20 min in O₂ ambient. τ_{eff} is 10 μs at Δn = 1 × 10¹⁵ cm⁻³.

Schmidt et al. reported $\tau_{\text{eff}} < 3 \mu\text{s}$, for as-deposited Al_2O_3 films prepared by ALD indicating that as-deposited Al_2O_3 film does not provide any surface passivation [183]. Hoex et al, showed that the post deposition annealing is necessary to obtain surface passivation and reported τ_{eff} values in the range of 2–8 μs for as-deposited Al_2O_3 films prepared by ALD [30]. Bhaire reported τ_{eff} of 0.1 μs for as-deposited AlO_x film deposited by pulsed-DC reactive sputter deposition technique [292].

Surface passivation was further improved by using 1 M AlO_x solution. Injection level dependent lifetimes and $S_{\text{eff,max}}$ for the sample prepared using 1 M AlO_x solution after PDA at 520 °C for 20 min in O_2 are shown in Figure 4.16. Improved $S_{\text{eff,max}}$ value of 726 $\text{cm}\cdot\text{s}^{-1}$ at an injection level of $1 \times 10^{15} \text{ cm}^{-3}$ was obtained for the sample prepared using 1 M AlO_x solution.

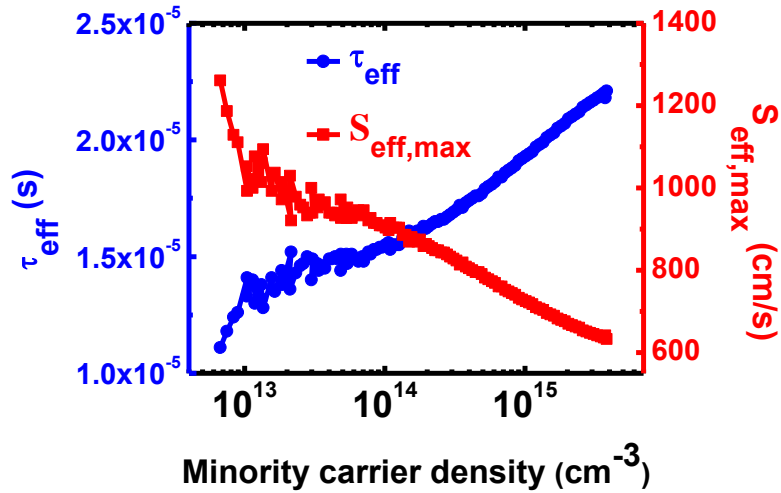


Figure 4.16: Injection level dependent lifetimes and $S_{\text{eff,max}}$ for spray coated AlO_x (1 M) film after PDA at 520 °C for 20 min in O_2 . τ_{eff} is 19.3 μs and $S_{\text{eff,max}}$ is 726 $\text{cm}\cdot\text{s}^{-1}$ at $\Delta n = 1 \times 10^{15} \text{ cm}^{-3}$.

Surface passivation was further improved by prolonged annealing time. Injection level dependent lifetimes and $S_{\text{eff,max}}$ for the sample after PDA at 520 °C for 2 hours in O_2 are shown in Figure 4.17. $S_{\text{eff,max}}$ value of 445 $\text{cm}\cdot\text{s}^{-1}$ at an injection level of $1 \times 10^{15} \text{ cm}^{-3}$ was obtained for the sample prepared using 1 M AlO_x solution after prolonged annealing at 520 °C.

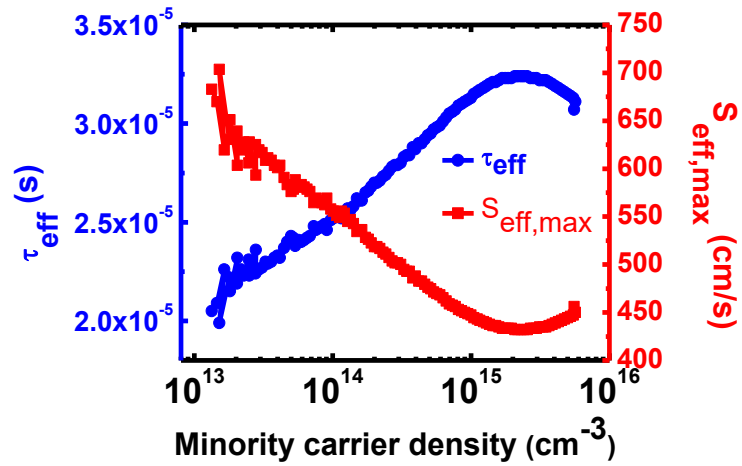


Figure 4.17: Injection level dependent lifetimes and $S_{\text{eff,max}}$ for spray coated AlO_x (1 M) film after PDA (520 °C for 2 hours in O_2) τ_{eff} is 31.5 μs and $S_{\text{eff,max}}$ is 445 $\text{cm}\cdot\text{s}^{-1}$ at $\Delta n = 1 \times 10^{15} \text{ cm}^{-3}$.

The results are summarized in Figure 4.18 which shows the $S_{\text{eff,max}}$ at $\Delta n = 1 \times 10^{15} \text{ cm}^{-3}$ for spray coated AlO_x film prepared using 0.2 M and 1 M AlO_x solution after PDA at 520 °C in O_2 for different annealing time. The $S_{\text{eff,max}}$ for the sample (1 M) which was annealed for 2 hours at 520 °C in O_2 is 445 $\text{cm}\cdot\text{s}^{-1}$.

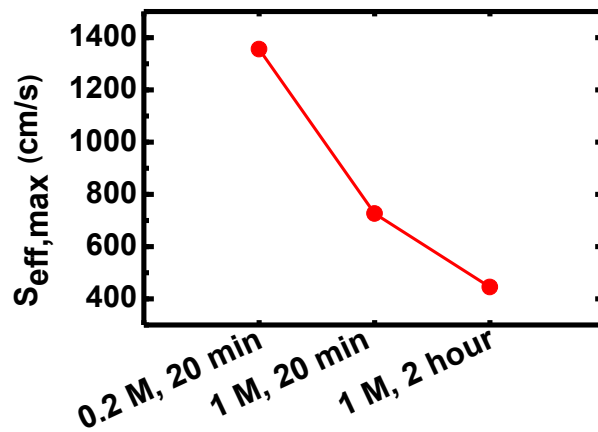


Figure 4.18: The $S_{\text{eff,max}}$ at $\Delta n = 1 \times 10^{15} \text{ cm}^{-3}$ for spray coated AlO_x film after PDA at 520 °C in O_2 for different annealing time. The samples were prepared using 0.2 M and 1 M AlO_x solution.

The investigation of annealing temperature on surface passivation was carried out by annealing the AlO_x films in O₂ ambient at different temperatures from 400 °C to 850 °C for 2 hours and the results are presented in Figure 4.19. The effective lifetime was seen to increase with increasing anneal temperature as shown in Figure 4.19.

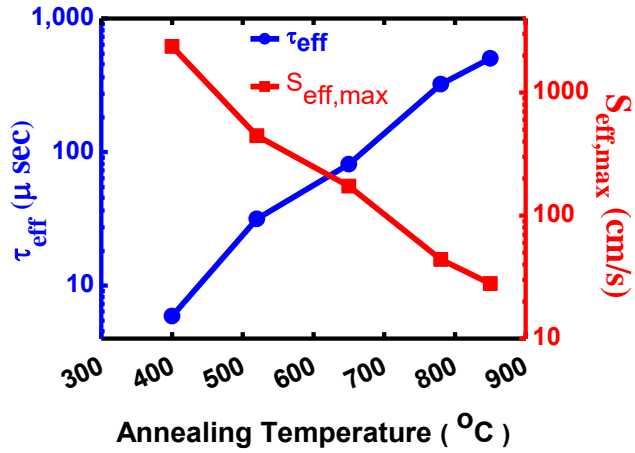


Figure 4.19: Effect of annealing temperature on surface passivation of spray coated AlO_x film (1 M) after annealing for 2 hours in O₂ ambient at $\Delta n = 1 \times 10^{15} \text{ cm}^{-3}$.

Injection level dependent lifetimes and $S_{eff,max}$ for the best sample which was annealed at 850 °C for 2 hours in O₂ are shown in Figure 4.20. The $S_{eff,max}$ value of 28 cm·s⁻¹ at an injection level of $1 \times 10^{15} \text{ cm}^{-3}$ was obtained for 850 °C annealed sample. Shin et al. obtained S_{eff} value of 35.89 cm·s⁻¹ for spray deposited Al₂O₃ film after post annealing at 550 °C for 1 hour [168].

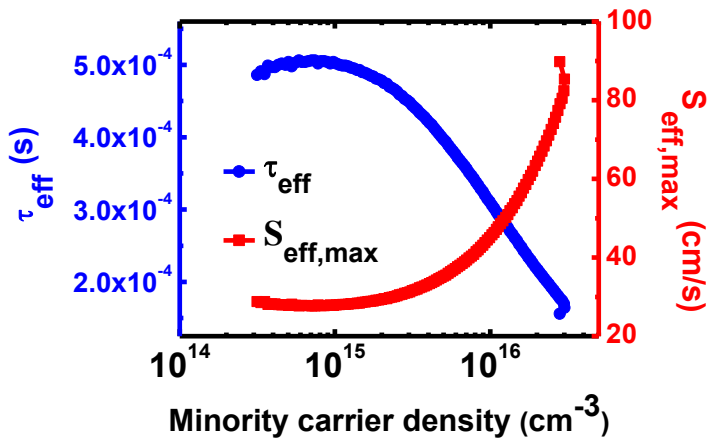


Figure 4.20: Injection level dependent lifetimes and $S_{eff,max}$ for the best sample after annealing at 850 °C for 2 hours in O₂ ambient. τ_{eff} is 502 μ s and S_{eff} is 28 cm·s⁻¹ at $\Delta n = 1 \times 10^{15} \text{ cm}^{-3}$.

Figure 4.21 shows the XPS depth profile of AlO_x film annealed at $850\text{ }^\circ\text{C}$. The carbon and nitrogen content is almost zero throughout the sample although organic precursor was used in this method for AlO_x film deposition. The carbon signal just at the surface is attributed to unavoidable inclusion of carbon from the XPS instrument.

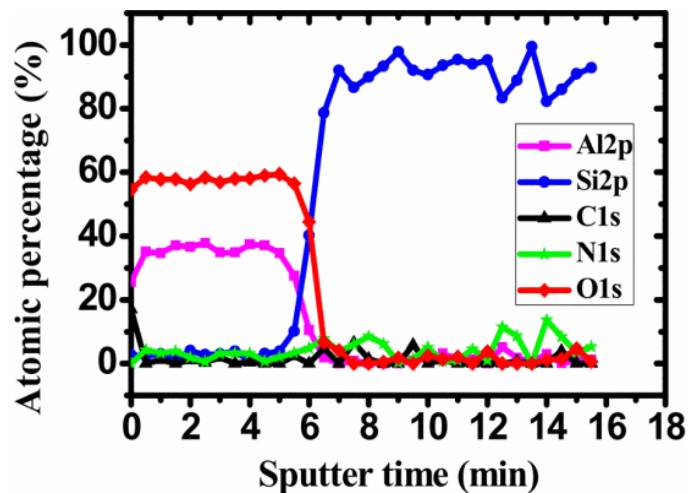


Figure 4.21: Chemical composition of spray coated AlO_x film after PDA at $850\text{ }^\circ\text{C}$ for 2 hours in O_2 ambient.

The atomic percentage of chemical components present in the spray coated AlO_x film indicates that the AlO_x film was almost stoichiometric in nature which is in agreement with the work reported by Aguilar-Frutis et al. for Al_2O_3 film deposited by spray pyrolysis [166]. Spray deposited AlO_x film obtained by Shin et al. is slightly Al rich with Al to O ratio of 1:1.28 [168]. Figure 4.22 shows the cross-sectional HRTEM image of 25 nm AlO_x sample annealed at $850\text{ }^\circ\text{C}$ which shows the presence of IL of 4 nm in thickness.

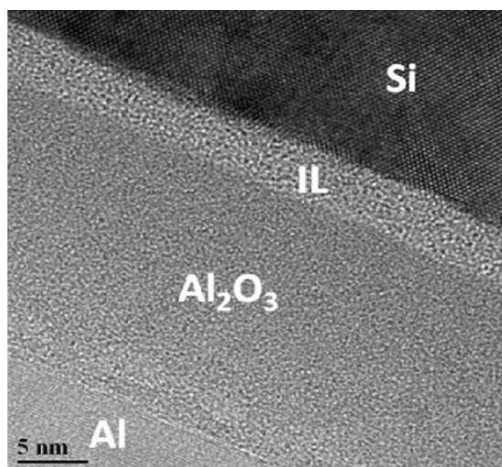


Figure 4.22: Cross sectional HRTEM image of spray coated AlO_x film after PDA at $850\text{ }^\circ\text{C}$ for 2 hours in O_2 ambient.

The spray coated AlO_x film was found to be amorphous. This is in agreement with Al_2O_3 films deposited by spray pyrolysis in literature [166].

4.3 Comparison of the two coating techniques

Table 4.3 shows the $S_{\text{eff,max}}$ achieved using two coating techniques—spin coating and spray coating—and the advantages and disadvantages of these two techniques. After high temperature annealing with prolonged annealing time, $S_{\text{eff,max}} < 100 \text{ cm}\cdot\text{s}^{-1}$ at $\Delta n = 1 \times 10^{15} \text{ cm}^{-3}$ was achieved using these two techniques. Both spin coating and spray coating technique are simple, low cost and non-vacuum deposition technique and the AlO_x films can be deposited at room temperature followed by hot plate annealing. Deposition of AlO_x films can be carried out in air ambience for both spin coating and spray coating processes.

Process flow of industrial PERC cells typically includes two wet chemical etching steps for the rear side after alkaline double side texturing step [293]. First etching step is performed to polish the previously textured rear surface (pyramid smoothing) and thus reduce rear surface roughness [293]. Second etching step is performed after POCl_3 diffusion to remove the PSG and rear emitter [293]. Cornagliotti et al. [293] investigated the impact of the rear side chemical polishing on the performance of industrial large area c-Si PERC solar cells and suggested that a complete planarization of the rear side can be detrimental and a moderate smoothing is required in order to increase efficiencies. Here, maximum efficiency of 20.1% was achieved for rear side roughness of $\sim 330 \text{ nm}$ (removal of $\sim 6 \mu\text{m}$ silicon) after the second etching step and before the passivation stack was applied [293]. Al_2O_3 thin film with SiN_x (ARC) capping layer is used on the textured (average pyramid height of $\sim 14 \mu\text{m}$) front side of the silicon solar cells (e.g., n-type cells with front-side boron emitter) for emitter passivation [176]. Compared to spin coating, spray coating method is especially more suitable to coat high topography surfaces, noncircular wafers and substrates with etched through via holes [294].

Table 4.3: Two coating techniques of film deposition.

Technique	$S_{\text{eff,max}}$	Advantages	Disadvantages
Spin coating (Deposition of uniform thin films on relatively flat substrates by rotation of the substrate)	94 cm·s⁻¹ ($\Delta n = 1 \times 10^{15}$ cm ⁻³) (after annealing at 780 °C for 130 min in O ₂)	<ol style="list-style-type: none"> 1) Simple, low cost and non-vacuum process 2) Thin and uniform coating 3) Suitable for deposition on small areas in laboratory-scale researches 4) Reproducibility 5) Ability to use different substrate materials [295] 6) Easy integration with lithography-based fabrication techniques 	<ol style="list-style-type: none"> 1) Relatively low throughput 2) Requirement of smooth and flat substrate 3) Thin film deposition may require high spinning speed and it is difficult to deposit defect-free thin films on large size samples with high spinning speed [152,153,154,296] 4) Comets, striations, chuck marks and gradual radial thickness variation are some important defects [150] 5) Poor material efficiency [154]
Spray coating (Spray coating of the solution via a nozzle on the substrates to deposit films)	28 cm·s⁻¹ ($\Delta n = 1 \times 10^{15}$ cm ⁻³) (after annealing at 850 °C for 120 min in O ₂)	<ol style="list-style-type: none"> 1) Simple, low cost and non-vacuum process 2) Film deposition even on highly structured surfaces 3) Deposition on large size samples 4) Great potential for large scale production with low wastage of material 5) Ability to use different substrate materials 	<ol style="list-style-type: none"> 1) Relatively low throughput 2) Reproducibility is difficult with hand-held sprayer 3) Hand-held sprayers are not suitable for large area applications. It is difficult to achieve uniformity over large area substrates using hand-held sprayer. 4) Quality of the film deposited by hand-held sprayers depends on the skills of the operator.

Spin coating is commonly used in microelectronics industry to deposit photoresist films. Lederer et al. reported the critical spin speed (sensible rotation speed limit) as 2000 rpm for 300-mm wafers and above which the phenomenon of spin marks takes place [153]. To deposit thin passivation films (e.g., sub-20-nm thickness), very high spinning speed may be required to allow the film to thin down and high-speed spinning of large size non-flat samples may lead to defects in the spin coated film that may affect the surface passivation. Moreover, comets, striations, chuck marks and gradual radial thickness variation are some important defects of spin coating methods.

4.4 Summary and conclusions

This chapter consists of two sections: spin coating and spray coating process. The AlO_x films were developed successfully for p-type c-Si surface passivation by spin coating and spray coating processes using aluminium nitrate nonahydrate as a precursor and 2-methoxyethanol as a solvent. In this work, transparent and clear AlO_x solution without any precipitation was successfully obtained using ultrasonic agitation.

Uniformity of AlO_x film thickness and RI was successfully demonstrated for spin coated AlO_x film. The film was uniform and standard deviations were 0.27 nm and below measurement resolution for thickness and RI, respectively over 2-inch silicon wafer based on 5-point measurements. The thickness of spin coated AlO_x film was reduced significantly after post deposition high temperature RTP annealing at 800 °C for 10 s in N_2 . The RTP annealing reduced the AlO_x film thickness by ~50% which may be attributed to film densification. For spin coated AlO_x film developed using 0.5 M AlO_x solution, Q_f and D_{it} were found to be - $5.5 \times 10^{12} \text{ cm}^{-2}$ and $3.9 \times 10^{11} \text{ eV}^{-1} \cdot \text{cm}^{-2}$ respectively after RTP annealing at 800 °C for 10 s in N_2 which are comparable with the results reported in literature for spin coated AlO_x film, and, in addition, breakdown field was $> 3.8 \text{ MV} \cdot \text{cm}^{-1}$. Cross-sectional TEM images of spin coated AlO_x film after RTP annealing at 800 °C for 10 s in N_2 revealed that, the film was amorphous. It also revealed the presence of IL. For the sample annealed at 800 °C for 10 s in N_2 ambient, τ_{eff} of spin coated AlO_x film was 1.9 μs . Spin coated AlO_x film annealed at 780 °C for 130 min, in O_2 ambient resulted in improved τ_{eff} of 160 μs and $S_{\text{eff,max}}$ of 94 $\text{cm} \cdot \text{s}^{-1}$. Promising

passivation characteristic of spin coated AlO_x film was obtained only after high temperature annealing (780 °C) with prolonged annealing time.

AlO_x thin films deposited by a spray coating process using hand-held sprayer was investigated for surface passivation of p-type c-Si. The dielectric constant, Q_f and D_{it} were found to be 6, $-4.2 \times 10^{12} \text{ cm}^{-2}$ and $1.9 \times 10^{11} \text{ eV}^{-1} \cdot \text{cm}^{-2}$ after annealing at 520 °C for 20 min in O_2 ambient, which demonstrates its potential for silicon surface passivation. High breakdown electric field up to $10.2 \text{ MV} \cdot \text{cm}^{-1}$ was obtained for 13 nm spray coated AlO_x film which indicates the high quality of the AlO_x film. It was found that annealing is necessary to activate the passivation of spray coated AlO_x film. For FZ wafers passivated by spray coated AlO_x films, τ_{eff} of 502 μs and corresponding $S_{\text{eff,max}}$ of $28 \text{ cm} \cdot \text{s}^{-1}$ was obtained after annealing the films at 850 °C for 2 hours in O_2 . The films showed excellent thermal stability. XPS analysis revealed that the film was almost stoichiometric with negligible carbon and nitrogen content. HRTEM revealed presence of IL and the spray coated AlO_x film was amorphous. These promising passivation characteristics were obtained only after annealing at 850 °C with prolonged annealing time.

Good quality and thermally stable AlO_x films were deposited on silicon substrates by spin and spray coating technique. ALD and PECVD techniques are costly, vacuum-based and use hazardous precursors such as TMA which increases safety requirements. Reducing the production cost of c-Si solar cells is one of the major challenges in PV industries. Solution processed deposition techniques are simple, less hazardous and especially useful for low cost applications. Since these are non-vacuum deposition processes, the important advantage of these processes is low investment costs. The advantage of spin coating process is ability to produce very thin and uniform films and suitable for deposition on small areas in laboratory-scale researches. The disadvantage is that it is difficult to achieve defect-free films on large area samples. To deposit thin passivation films (e.g., sub-20 nm thickness), very high spinning speed may be required to allow the film to thin down and high-speed spinning of large size samples may lead to defects in the spin coated film that may affect the surface passivation. Moreover, comets, striations, chuck marks and gradual radial thickness variation are some important defects of spin coating methods. However, the presence of comets can be reduced or eliminated by working in cleaner environments.

Comparatively, spray coating technique is an attractive technique for PV industries to deposit thin films for several reasons: spin coating processes are relatively slow and low

throughput process as it is not amenable to batch processing (single substrate deposition with 4 main stages) in contrast to spray coating processes. The material efficiency of spin coating technique is very low compared to spray coating technique. For spray coating, the film deposition can be patterned using shadow mask. Unlike spin coating process, spray coating process is suitable for large area applications. It has no limitation for substrate size and shows great potential for large scale production with low wastage of material. It is a promising substitute for conventional spin coating methods. In this work, a simple, inexpensive, and easy-to-use hand-held sprayer was used to achieve the deposition. However, it is not suitable for large area applications. The film deposition by spraying is not easily controllable. For instance, precise controls of flow rate and X-Y movements are difficult to achieve. The success of the spray coating to deposit film with desired properties depends on the skill of the operator. However, scaling-up for large scale production is easy unlike spin coating. Manual sprayer is typically used for small area applications, while spraying instruments are useful for high production processes.

In this work, good surface passivation ($S_{\text{eff,max}} < 100 \text{ cm}\cdot\text{s}^{-1}$) for both spin coated and spray coated AlO_x films were achieved only after a prolonged annealing at a high temperature. Nevertheless, there is an ample scope for improvements and further studies in this cost-effective spray coating technology to get better passivation results. The passivation capability of spin and spray coated AlO_x film for p-type c-Si surfaces demonstrated in this work will probably achieve a basic aim of educating the researchers, to further enhance the best use of this method for solar cell applications and provide a pathway towards a scalable automated process for fabricating good quality, large area and reproducible passivation films for solar cell applications.

Chapter 5

Development of Spray Coating Process for Large Area Device Applications

The aim of the work discussed in this chapter is to develop the spray coating process to achieve uniform and good quality AlO_x film by spraying instrument for large area applications. Large-area deposition of AlO_x films is essential for their potential use in mass production. This chapter attempts to address the major issues in the AlO_x manual spray coating process using hand-held sprayer—discussed in the previous chapter. The customized automated spraying instrument provides facility to precisely control the flow rate, duration, spray ON/OFF, speed and X-Y movements with ability for large area deposition and spraying process can be carried out according to the parameters already set. In addition, incorporation of ultrathin SiO_x layer by UV/ O_3 is investigated in an attempt to improve the passivation quality of spray coated AlO_x film without the need for high thermal budget annealing reported in the previous chapter.

5.1 Design of spray deposition system

Spray coating technique is one of the deposition methods to prepare thin films. Spray coating is recognized for their applications in many fields [243,244,245,297,298]. Spray coated films are used for passivation applications [208]. There are various parameters in spray coating to enhance the quality of the thin film. In this section, custom-designed spraying instrument, vacuum chuck and hot plate heater are discussed.

5.1.1 Spraying instrument

Figure 5.1 shows the photograph of the custom made automated spraying instrument. In this work, to deposit AlO_x thin films, the custom-made spraying instrument from Holmarc Opto-Mechatronics Pvt. Ltd, India, was used. This spraying instrument is specifically

designed and built for solar cell applications and the largest substrate size capacity of this equipment is 200 mm × 200 mm.



Figure 5.1: Photograph of the custom designed spraying instrument.

The spray coating set-up consists mainly of the following parts: a spraying unit, precursor feeding unit. The spraying unit includes a gas cylinder, pressure regulator, a three-axis stepper motor controller, and simple easy to use software. The precursor feeding unit consists of a stepper motor-controlled syringe pump and a glass syringe.

- Pressure regulator

Gas cylinder (N_2/O_2) supplies pressurized air required to spray the coating solution on to the substrate. A pressure regulator controls the air pressure coming from the gas cylinder at a specified level set by the user. The carrier gas (N_2 or O_2 or mix of O_2 and N_2) can be made to flow through the spray nozzle.

- X-Y Spray Mechanism

The movement of the spray head in the X-Y plane is achieved through stepper motor driven stages. There are limit switches at both ends of the stages to prevent overdrive. These stages are driven using stepper motors that can be controlled by the spray controller placed inside the machine. The spray head attached to the X-Y stage inside the spray enclosure can

be moved to and fro in X-axis ($10 \text{ mm}\cdot\text{s}^{-1} - 800 \text{ mm}\cdot\text{s}^{-1}$) and Y-axis ($1 \text{ mm}\cdot\text{s}^{-1} - 12 \text{ mm}\cdot\text{s}^{-1}$) or to the desired location using the software. The speed of spray head movement can be precisely controlled by the software.

- Syringe pump

The syringe pump is attached to the X-Y stage inside the spray enclosure. Syringe pump helps deliver a precise amount of fluid at specified flow rate. The syringe pump is connected to the spray controller for controlling its flow rate. The dispensing rate ($50 \mu\text{l}\cdot\text{s}^{-1} - 10,000 \mu\text{l}\cdot\text{s}^{-1}$) of the solution can be precisely controlled by a software. A photograph of the syringe pump is shown in the Figure 5.2.

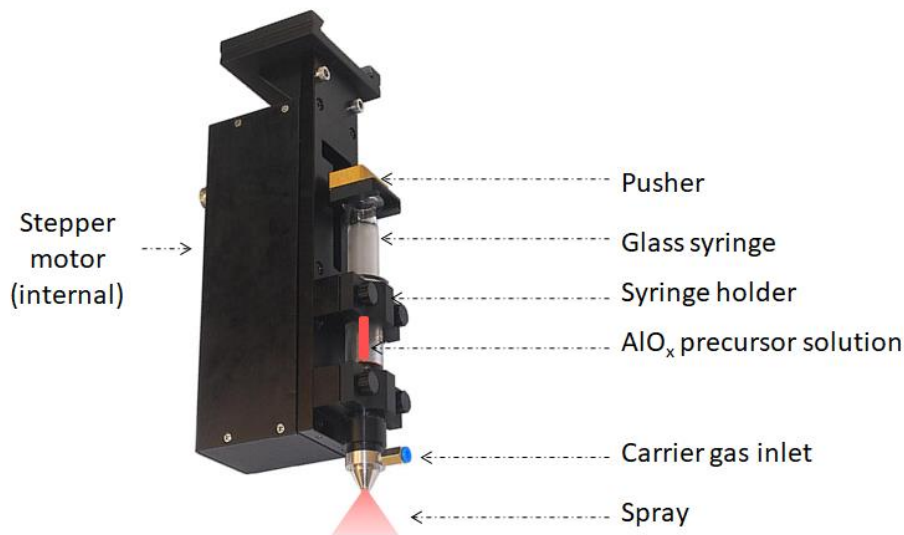


Figure 5.2: Photograph of the syringe pump [299].

- Glass syringe

The dispensing of the coating solution is achieved using stepper motor controlled piston placed inside the glass syringe. A needle is attached to the glass syringe to enable the spraying process. The precursor solution to be sprayed is contained in a glass syringe which can be attached to a spray-head using screws. Glass syringe is primarily chosen for applications where the flow rate must be carefully controlled, particularly for thin film deposition which requires low flow rate. Flow rates mainly depend on the speed at which the syringe plunger is moved downwards. To achieve good spraying, the pumping action must be very smooth. This can be achieved by automating the process using microprocessor-controlled stepper motor drive mechanism via software program.

- Position controller Software

Position controller is an easy-to-use software interface. It allows the user to operate the system in manual and programmable modes. The software interface enables to create a program using simple commands (Instruction Set) such as HOME, MOVE [X(mm), Y(mm)], SPEED [X(mm·s⁻¹), Y(mm·s⁻¹)], SPRAY ON/OFF, AIR ON/OFF, WAIT (ms), LOOP [index, from address], SPRAY DURATION (s). It helps to automate the spraying process and to increase the process reliability.

An exhaust fan (4-inch diameter) installed at the back of the spraying instrument helps to remove spray fumes during spray coating process from the chamber by suction using an exhaust-pipe of 4-inch diameter.

5.1.2 Design of vacuum chuck

Vacuum chucks for spray coating system were designed and supplied by Excel Instruments (Palghar, Maharashtra) to hold the substrate during spray coating process. The vacuum chuck was attached to a stand with a provision to turn ON/OFF vacuum and to adjust the height. Technical 2D and 3D drawings of the chucks were designed using Parametric Technology Company (PTC) CREO software. The vacuum chuck-A was designed with the aim to provide uniform vacuum under the entire silicon wafer by the provision of circular grooves on the chuck during spray coating processes as shown in Figure 5.3. Figure 5.3(a) shows the 2D top view of chuck-A, Figure 5.3 (b) shows the 2D section (Z-Z) view (the cutting line marked as Z-Z in the Figure 5.3 (a) shows where the part is cross-sectioned), Figure 5.3 (c) shows the 3D view of chuck-A and Figure 5.3 (d) shows the PL image of AlO_x passivation film deposited using chuck-A.

For surface passivation measurement, the silicon wafers need to be coated with AlO_x film on both sides of the wafer. The PL image obtained for 2-inch p-type Si wafer passivated by spray coated AlO_x film using chuck-A showed defects of three circles due to three circular features of the vacuum chuck-A. These defects may be attributed to the localized stress on front side AlO_x film at the portion of the grooves on chuck-A during AlO_x film deposition on rear side of the Si wafer by spray coating.

The design of chuck-A was optimized further in such a way that the silicon wafer makes minimum contact with the metal chuck during the spray coating process. This was achieved with the help of circular rubber O-ring. The O-ring was installed in the circular groove and wafer was placed on top of the O-ring without touching the chuck during spray coating. In this way, the wafer was not making any contact with the chuck except the O-ring. The design details of chuck-B—optimized design of chuck-A—is shown in Figure 5.4.

Figure 5.4 (a) shows 2D top view of chuck-B, Figure 5.4 (b) shows 2D section (Z-Z) view, Figure 5.4 (c) shows 2D section (X-X) view, Figure 5.4 (d) shows 2D detail (B) view to provide greater clarity about the region of circular groove shown in Figure 5.4(b) and Figure 5.4 (e) shows 3D view of chuck-B. The PL image of the spray coated AlO_x film deposited using chuck-B is shown in Figure 5.5 with defect of circle due to O-ring. In this thesis work, chuck-B was used for deposition of AlO_x film by spray coating processes.

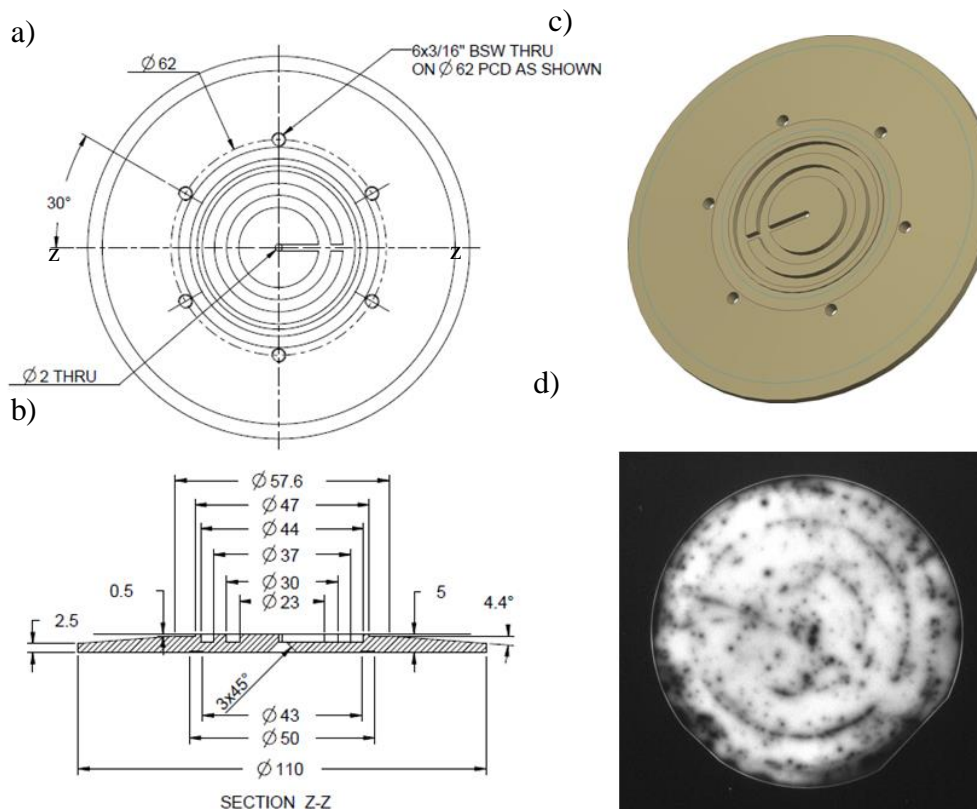


Figure 5.3: Schematic of the chuck-A with design details (all dimensions are in mm). (a) 2D top view (b) 2D section (Z-Z) view. The cutting line marked as Z-Z in Figure 5.3(a) shows where the part is cross-sectioned. (c) 3D view of chuck-A. (d) PL image of AlO_x film deposited using chuck-A.

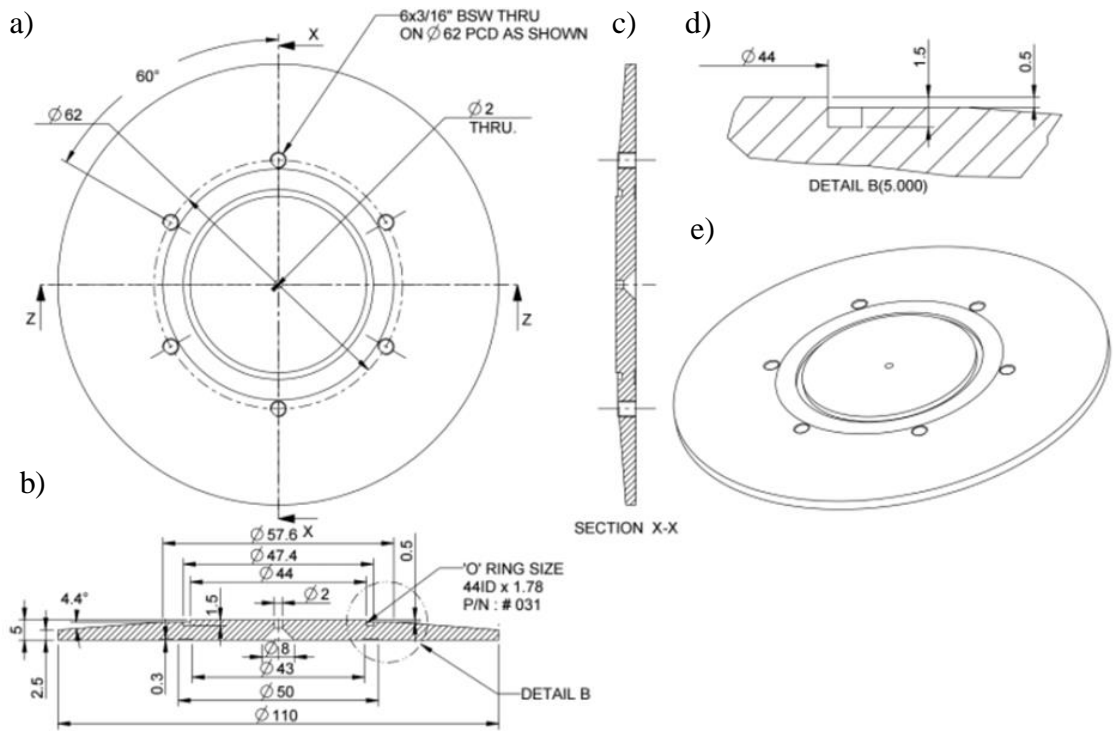


Figure 5.4: Technical drawing of the chuck-B with details of design (all dimensions are in mm) by PTC CREO software. (a) 2D top view. (b) 2D section (Z-Z) view. (c) 2D section (X-X) view. (d) 2D detail view to provide greater clarity about the region of circular groove. In Figure 5.4(b), the detail view border is displayed using dotted circle and annotated with letter 'B' to link the detail view with its parent view. (e) 3D view of chuck-B.

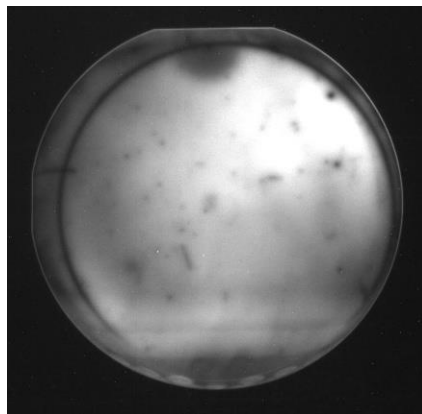


Figure 5.5: PL image of 2-inch p-type Si wafer passivated by spray coated AlO_x film showing defect of circle due to O-ring of the chuck-B.

5.1.3 Design of hot plate heater

The hot plate heater was custom designed and supplied by Excel Instruments (Palghar, Maharashtra) for 6 inch \times 6 inch substrates using stainless steel (SS316) material. It can withstand temperatures up to 500 °C and the temperature is controlled by a proportional-integral-derivative (PID) controller. Brown bakelite sheet with thickness of 5 mm was used to mount the hot plate heater. In addition, the exhaust hood with door serves to remove vapour released into the air during hot plate annealing of the sample. Figure 5.6 shows the technical drawing of the hot plate heater with details of design (all dimensions are in mm). Figure 5.6(a) shows the 2D top view, Figure 5.6(b) shows the section (X-X) view (the cutting line marked as X-X in Figure 5.6(a) shows where the part is cross-sectioned) and Figure 5.6(c) shows the 3D view for a more visual look.

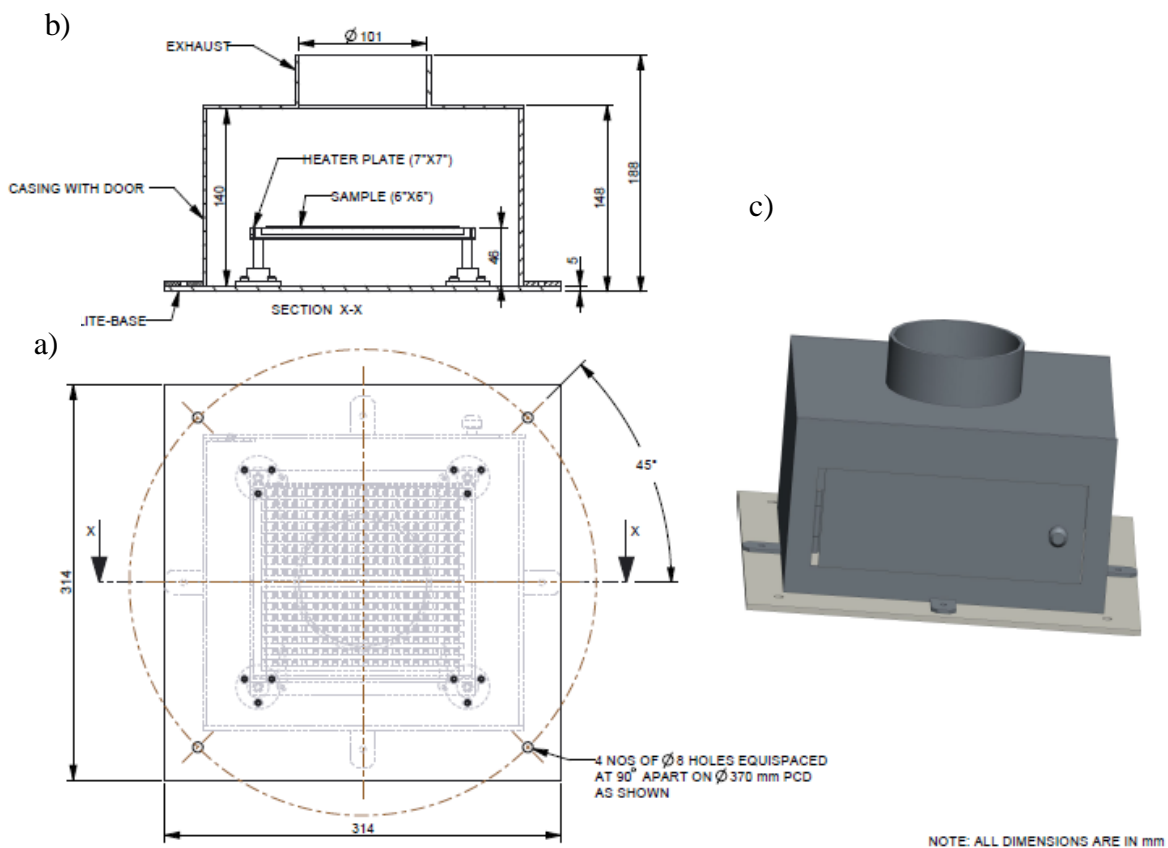


Figure 5.6: Technical drawing of the hot plate heater with details of design by PTC CREO software (all dimensions are in mm). (a) 2D top view (b) 2D section (X-X) view (c) 3D view of the object.

5.2 Substrate and solution preparation

Single side polished p-type Cz c-Si wafers (2-inch, <100>, 4–7 $\Omega\cdot\text{cm}$, 270 $\mu\text{m} \pm 10 \mu\text{m}$) were used for the experiment. In all cases, the wafers were initially cleaned using RCA-1, RCA-2, and a dilute (2%) HF solution, as discussed in chapter 3, section 3.1.1. AlO_x solution of 0.2 M was prepared by following the procedure described in chapter 3, section 3.1.2. Before AlO_x spray coating, the wafers were exposed to UV radiation (185 nm and 254 nm, 4 W, UV Chamber, Holmarc Opto-Mechatronics Pvt. Ltd, India) for 5 min in oxygen ambient at room temperature. The process sequence is described below.

UV/ O_3 : DI water rinse, 2% HF dip for 30 s at room temperature, wafer drying using N_2 spray gun, UV/ O_3 treatment for 5 min.

The chemical SiO_x grown by UV treatment in oxygen ambient prior to spray deposition of the AlO_x film was found to be around 1.4 nm by spectroscopic ellipsometer.

5.2.1 Silicon surface oxidation by UV/ O_3

Contact angle (θ) refers to the angle that a liquid forms with the sample surface when it is deposited on the sample surface and it is one of the common methods to measure the surface wettability. The smaller the contact angle, the more hydrophilic is the sample surface. More hydrophilic silicon surface is desirable for solution processed Al_2O_3 film deposition [285]. Hydrophilic cleans (-OH terminated) prior to Al_2O_3 deposition by ALD are preferred over hydrophobic ones (-H terminated) due to better surface passivation [172]. O_3 based hydrophilic clean prior to Al_2O_3 film (ALD) deposition is suitable candidate for industrial Al_2O_3 based PERC type process flow [172]. Ultrathin oxide layer with thickness of ~1.4 nm was reported by Moldovan et al. after UV/ O_3 treatment [220]. It was also shown that ultrathin SiO_x layer grown by UV/ O_3 exposure improves surface passivation and well suited as tunnel oxides for TOPCon solar structures [220].

Wetting ability in general can be categorized into four different regimes based on the water contact angle (θ_w). When θ_w is in the range of $0^\circ < \theta < 10^\circ$, the surface is superhydrophilic in nature. When θ_w is in the range of $10^\circ < \theta < 90^\circ$, the surface is hydrophilic in nature. When θ_w is in the range of $90^\circ < \theta < 150^\circ$, it is called hydrophobic surface and when θ_w is in the range of $150^\circ < \theta < 180^\circ$, it is termed as superhydrophobic

surface [300]. Figure 5.7(a) and Figure 5.7(b) show a hydrophilic and hydrophobic sample surfaces, respectively.

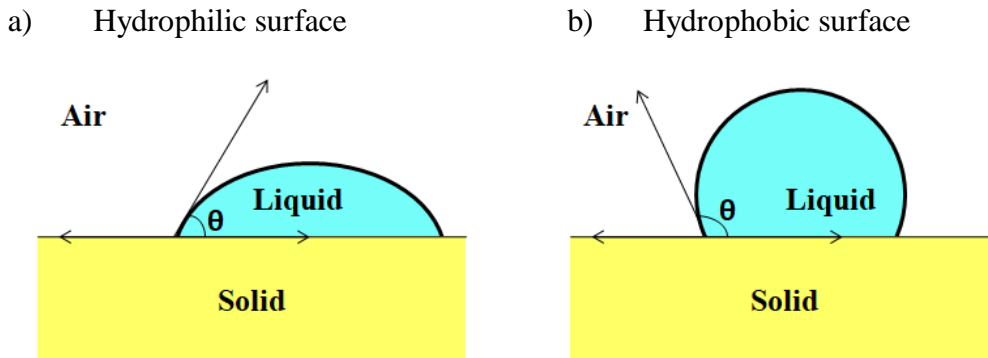


Figure 5.7: Contact angle on various sample surfaces. (a) A hydrophilic surface ($\theta < 90^\circ$). (b) A hydrophobic surface ($\theta > 90^\circ$) [301].

Hydrophobicity and hydrophilicity are identified by the presence of certain chemical species on the sample surface [302,303,304]. The origin of silicon surface hydrophilicity is OH-groups coupled to the surface which act as adsorption sites for water molecules and for hydrophobic silicon surfaces, the origin is characterized by Si-H and probably F, O, and C in minor quantities [304]. Backlund et al. investigated twelve different surface treatments and etchants—RCA-1, $\text{H}_2\text{SO}_4:\text{H}_2\text{O}_2$, $\text{H}_2\text{SO}_4:\text{H}_2\text{O}_2$ and RCA-2, RCA-1 and RCA-2 (100 °C), RCA-1 and RCA-2 (95 °C), KOH etching, $\text{H}_2\text{O}_2:\text{H}_2\text{O}$, oxidized (wet O_2 ambient), original, EDP (ethylene diamine pyrocatechal) etching, $\text{HNO}_3:\text{HF}$ etching and HF-dipping—for silicon wafers and reported water contact angle in the range of $5^\circ - 70^\circ$ [304] and smallest water contact angle of 5° was achieved for RCA-1.

Zazzera et al. [303] showed that anhydrous HF treatment followed by UV/ozone treatment modify the surface chemistry by affecting the most abundant surface atoms: Si, O, C, H, and F. Here, anhydrous HF in conjunction with H_2O vapor removed the silicon native oxide and created the silicon surface terminated by F, C, and H. When the fluorinated surface was rinsed with water, the fluorine concentration was reduced and the trace metal impurities Na, Mg, Al, and Ca were removed. In addition, it promoted initial SiO_2 formation [303]. Afterwards, the UV/ozone exposure reduced the hydrocarbon concentration on the HF-etched surface and removed fluoride species. In addition, it produced 0.8 nm SiO_2 passivation layer [303]. Zazzera et al. achieved cleanest silicon surface with respect to hydrocarbon and metallic impurities with a modified RCA clean + HF etch + H_2O rinse + UV/ozone oxidation processing scheme and the UV/ozone exposure reduced hydrocarbon concentration [303].

To investigate the effect of UV/O₃ treatment on silicon surface, three silicon wafers were chosen and the process flow of sample preparation is shown in Figure 5.8.

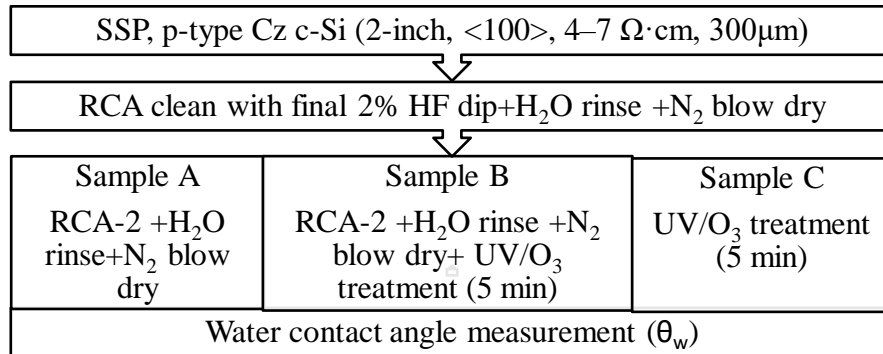


Figure 5.8: Process flow for contact angle measurement.

All the silicon wafers were cleaned using the RCA cleaning process described in Chapter 3, section 3.1.1. Sample A was oxidized by RCA-2 process. Sample B was oxidized by RCA-2 process followed by UV/O₃ treatment for 5 min. Sample C was treated with UV/O₃ for 5 min. Table 5.1 shows the results of water contact angle measurement performed on three samples immediately and after one hour.

Table 5.1: Contact angle measurement of the samples A, B and C.

Sample details	Water contact angle	Water contact angle after 1 hour
Sample A (without UV/O ₃ treatment)	10.5°	-
Sample B (with UV/O ₃ treatment)	< 1°	< 1°
Sample C (with UV/O ₃ treatment)	< 1°	< 1°

The contact angle of sample A was 10.5°. The surfaces of samples B and C which were treated with UV/O₃ turned to superhydrophilic. The major reason behind the decrease in the water contact angle after UV/O₃ treatment is due to change of chemical composition of the silicon surface. Ultrathin SiO_x film thickness of 1.42 nm and RI of 1.47 was obtained for sample C by spectroscopic ellipsometry measurement. It is found that the wetting behavior is improved after UV/O₃ treatment.

5.3 AlO_x thin film deposition

For spray coating, 10 ml of AlO_x solution was loaded into a 20 ml glass syringe and injected through a stainless-steel needle with a 90° blunt end. The length and diameter of the needle were 8 mm and 0.5 mm, respectively. Oxygen gas at a pressure of 1.8 kg·cm⁻¹ was used as a carrier gas and the flow rate of solution was 350 μl·min⁻¹. The speed of sprayer in X and Y directions were 400 mm·s⁻¹ and 3 mm·s⁻¹, respectively. The nozzle to substrate distance was 55 mm and the diameter of the nozzle was 1 mm. The vacuum chuck-B was used to hold the substrate and the substrate was kept at room temperature during the spray coating process. The solution was sprayed (downwards) directly onto the substrate using spraying instrument (Figure 5.1). After spray coating, a thin liquid film was formed on the surface of the substrate. The liquid film was then immediately dried in a clean room ambient (ISO-6 class) for 30 s at 250 °C on a preheated hot plate, followed by a final 20 min PDA at 520 °C in O₂ ambient using a quartz furnace.

5.4 Physical and structural characterization

The measurements of thickness and RI were carried out using spectroscopic ellipsometer. Surface roughness was measured by AFM. FTIR of the films was carried out using Vertex 80 FTIR System from Bruker Corporation. 2D optical image was obtained by Olympus MX61 microscope. 3D images of the surface were acquired using the Zeta microscope. The film composition was investigated by XPS. HRTEM was used to obtain insights about the AlO_x/Si interface. For structural characterization, the samples were prepared using the spraying process described in section 5.3.

5.4.1 Thickness uniformity

The oxide thickness and RI were measured before and after the PDA process by ellipsometer at 80 different spots over the 2-inch wafer. The results of oxide thickness and RI are shown in Figure 5.9 (a) and Figure 5.9 (b), respectively. The mean value of AlO_x film thickness was 12.4 nm and the standard deviation was 0.3 nm before PDA. The mean of RI

was 1.63 and the standard deviation was 0.01. The mean values of film thickness and RI were found to be 10.3 nm and 1.64, respectively after PDA. A small increase in RI and ~17% shrinking of the AlO_x film thickness after the PDA can be attributed to film densification. The RI values are comparable to those reported for ALD and PECVD Al_2O_3 films (1.55–1.65) [104].

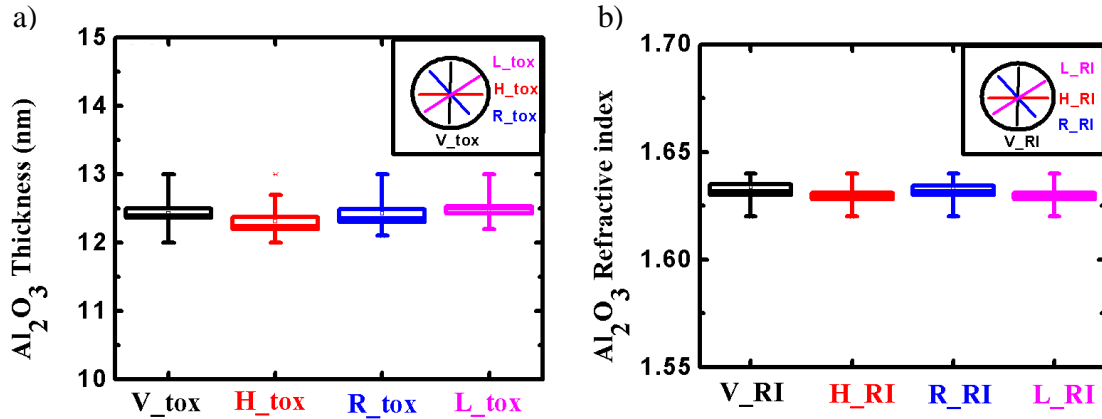


Figure 5.9: (a) AlO_x film thickness (after hot plate drying at 250 °C) variations over a 2-inch silicon wafer. (b) RI uniformity of AlO_x film. Thickness measurements were performed along the four lines shown in the insets. 20 points were measured along each line shown.

5.4.2 Surface roughness by AFM

It was found that the AlO_x film deposition by spray coating increases the smoothness of the wafer surface which can be explained on the basis of surface roughness results of the substrates before and after AlO_x film deposition. The RMS roughness was measured by AFM, and was found to be 0.33 nm before and after PDA. The RMS roughness of the bare silicon substrate was 0.68 nm. Figure 5.10(a), Figure 5.11(a) and Figure 5.12(a) show the AFM 2D images of the surfaces of the bare silicon wafer before AlO_x film deposition, as-deposited AlO_x film and PDA annealed AlO_x film, respectively. Figure 5.10(b), Figure 5.11(b) and Figure 5.12(b) show the AFM 3D images of the surfaces of the bare silicon wafer before AlO_x film deposition, as-deposited AlO_x film and PDA annealed AlO_x film, respectively. Figure 5.13 shows the RMS roughness of the plane silicon wafer before AlO_x film deposition, as-deposited AlO_x film after hot plate drying at 250 °C and AlO_x film after PDA over 2-inch silicon wafer. The roughness of the silicon wafer was decreased significantly after the deposition of AlO_x film due to spreading of uniform thin liquid film of AlO_x solution on the

silicon wafer surface. Shin et al. reported RMS roughness value of 0.52 nm for spray deposited Al_2O_3 film on polished Cz Si(100) substrates after post deposition annealing in N_2 at 550 °C for 1 hour [168].

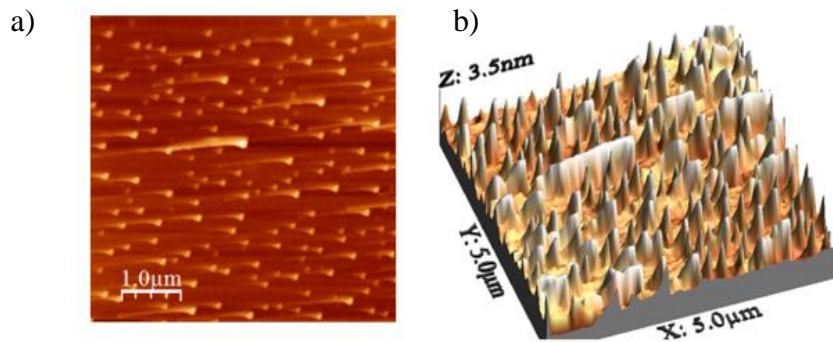


Figure 5.10: (a) AFM 2D surface image (b) AFM 3D surface image of bare silicon wafer. RMS roughness is 0.68 nm.

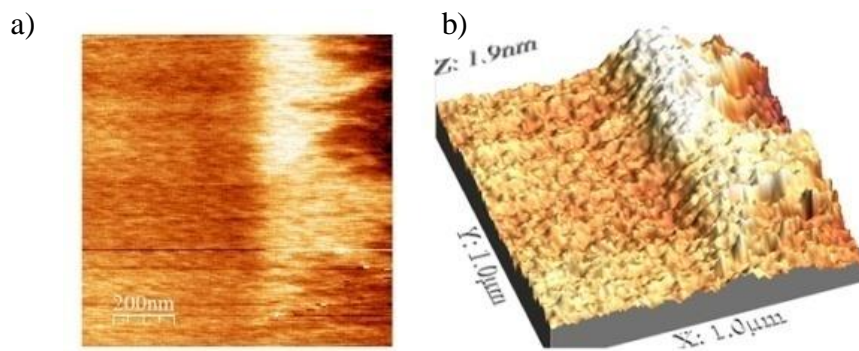


Figure 5.11: (a) AFM 2D surface image (b) AFM 3D surface image of as-deposited AlO_x film after hot plate drying at 250 °C. RMS roughness is 0.33 nm.

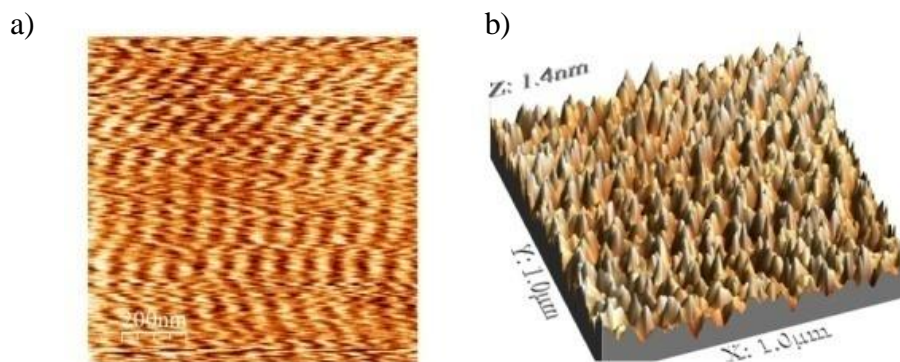


Figure 5.12: (a) AFM 2D surface image (b) AFM 3D surface image of AlO_x film after PDA (520 °C, 20 min, O_2). RMS roughness is 0.33 nm.

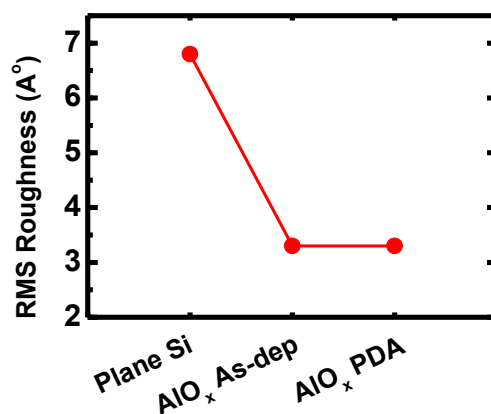


Figure 5.13: RMS roughness of the plane silicon wafer before AlO_x film deposition, as-deposited AlO_x film after hot plate drying at 250 °C and AlO_x film after PDA over 2-inch silicon wafer.

5.4.3 FTIR analysis of AlO_x thin film to detect hydrogen

Al₂O₃ film deposited by ALD and PECVD were reported to contain high concentration of hydrogen [104]. This may cause blister formation during high temperature treatment such as firing due to out-diffusion of H-containing species [186,187]. Al₂O₃/SiN_x passivation stack may partially delaminate during firing process that can affect the passivation quality and the optical properties of the passivation stack [305]. In literature, different approaches are provided to prevent blistering. One approach is an extra thermal out-gassing step between Al₂O₃ and SiN_x capping layer deposition [306]. Another approach is to use very thin AlO_x passivation layer [305].

Vermang et al. [306] reported efficiency of 19% for blister-free screen printed large-area (148.25 cm²) p-type Si PERC solar cells with Al₂O₃/SiO_x/SiN_x passivation stack. Here, out-gassing annealing step was performed at 700 °C for 20 min in N₂ after the Al₂O₃ deposition (10 nm, ALD) and prior to the SiO_x (PECVD)/SiN_x (PECVD) capping layer deposition steps [306]. Vermang et al. suggested that using a thin Al₂O₃ film (≤ 10 nm) and performing an out-gassing annealing step prior to capping layer deposition as a solution to fabricate blister-free Al₂O₃ based passivation stacks [306].

Vermang et al. reported blistering in ALD Al₂O₃ films with thickness more than 10 nm when annealed at temperature higher than 350 °C [187]. Here, no blister formation was

reported when the Al_2O_3 film thickness was less than 10 nm [187]. Richter et al reported considerable blistering after firing at 800 °C for Al_2O_3 (ALD)/ SiN_x (70 nm, PECVD) passivation stack for Al_2O_3 thickness of 5.8 nm and 11.5 nm and no blistering was observed for Al_2O_3 thickness of 3.9 nm without an additional out-gassing step [305]. A balance between excessive amounts of hydrogen leading to blistering and sufficient amounts of hydrogen for interface and bulk passivation is necessary for passivation layers. Both ALD and PECVD deposited films may have to be capped with silicon nitride for thermal stability [22,183].

Hydrogen bonding can be detected in many ways and the IR spectroscopy is one of the easy to use methods. The FTIR spectrum can be interpreted by seeing which absorption bands are absent. This is called as negative spectral interpretation [307]. It can also be interpreted by examining which absorption bands are present. This is termed as positive spectral interpretation [307]. If certain absorption bands are absent in the given region of spectrum where the given functional group always exhibits strong absorption, then the given functional group may be excluded [307].

In literature, the technique of negative spectral interpretation is used to confirm presence of hydrogen. Gong et al. used FTIR to investigate presence of hydrogen related bond in the sample to determine the quality of the passivation [308]. The Si-H peak at 2200 cm^{-1} of AlO_x (ALD) and the AlO_x (ALD)/ SiO_x (spin coating) stack plays a major role on chemical passivation of c-Si surface [308]. Gong et al. observed no Si-H peak in the FTIR spectra of single layer SiO_x and attributed the absence of Si-H peak to limited passivation effect caused by poor chemical passivation. However, Gong et al. observed Si-H peak for AlO_x / SiO_x stack and AlO_x layer and attributed the presence of Si-H peak to improved surface passivation caused by saturation of dangling bonds at the c-Si surface by hydrogen [308].

In this work, the technique of negative spectral interpretation is used to confirm presence of hydrogen and no hydrogen peaks are observed in our case in any of the wave number ranges reported for hydrogen peaks in literature. FTIR of the films was carried out using Vertex 80 FTIR System from Bruker Corporation and the results are shown in Figure 5.14. Peng et al. [309] had used the FTIR peaks corresponding to SiO-H and SiOH-O for identifying hydrogen in the aluminum oxide film deposited by ALD processes. Here, SiO-H bonds were reported in the range of 3800 cm^{-1} to 3500 cm^{-1} and SiOH-O bonds were identified in the range of 2400 cm^{-1} to 2300 cm^{-1} . Hydrogen related bonds [309] were not

observed by FTIR absorption spectroscopy in our case in any of these wave number ranges as shown in Figure 5.15(a) and Figure 5.15(b).

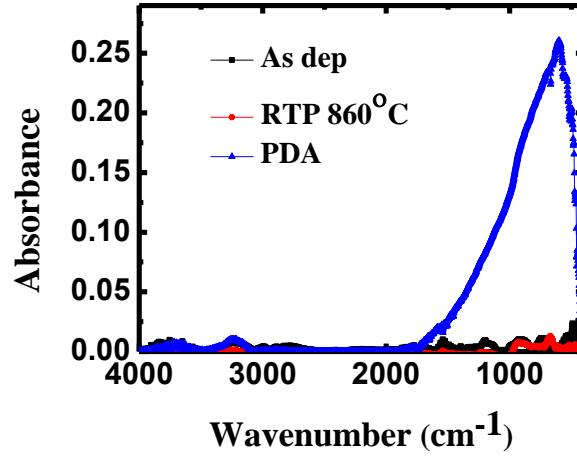


Figure 5.14: FTIR of as-deposited, PDA and RTP-fired (860 °C) AlO_x film from 4000 cm^{-1} to 400 cm^{-1} (3000 Hyperion Microscope with Vertex 80 FTIR System, Bruker, Germany).

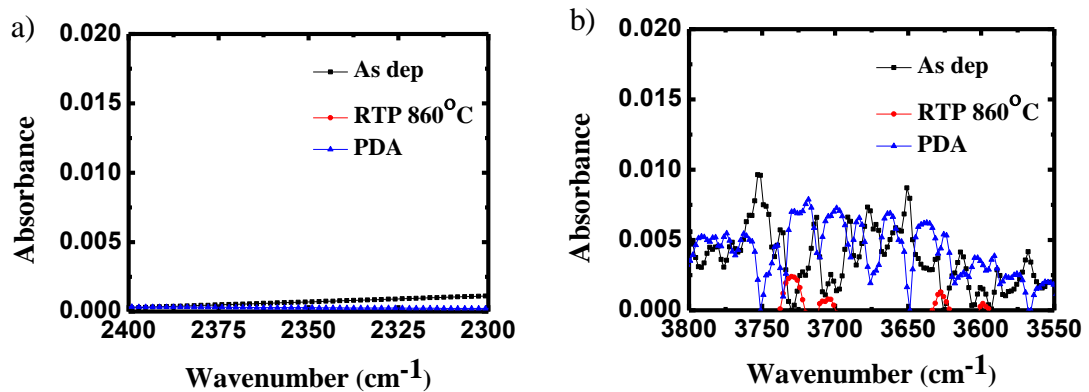


Figure 5.15: FTIR of as-deposited, PDA and RTP-fired (860 °C) AlO_x film. (a) From the range of 2400 cm^{-1} to 2300 cm^{-1} . (b) From the range of 3800 cm^{-1} to 3500 cm^{-1} .

In literature, it is observed that FTIR spectra of AlO_x exhibits broad feature in the range of $400\text{--}1200 \text{ cm}^{-1}$ [184,310,311,312,313,314,315]. Table 5.2 contains various chemical band and range of wave number for AlO_x from literature. In this work, a broad and strong absorbance band which appears in the range of $400\text{--}1700 \text{ cm}^{-1}$ centered at $\sim 600 \text{ cm}^{-1}$ for PDA sample is due to overlapping of several absorbance bands including bands of A-O and Si-O chemical bonds. Since the broad feature is due to overlapping of several bands, it is difficult to go further into the interpretation.

Table 5.2: Range of wavenumber and peak position for AlO_x.

Spectra of AlO _x		
Wavenumber (cm ⁻¹)	Chemical Bond	Reference
400–530	Al-O ₆ octahedral stretching	[184,316]
500–680	AlO ₆ octahedra	[316]
513	Al-O ₆ octahedra stretching	[317]
567	Al-O ₆ octahedra stretching	[317]
611	Al-O ₂ bending	[317]
640	O-Al-O bending	[314]
650 –700	O-Al-O bending (octahedral and tetrahedral matrix)	[184,191]
650 –800	AlO ₄ tetrahedra	[316]
700 –900	AlO ₄ tetrahedra	[316]
710	Al-O stretching	[314]
739	Al-O ₄ tetrahedra stretching	[317]
750–850	Al-O stretching	[191]
889	Al-O ₄ tetrahedra	[317]
900–1200	Si-O/O-Si-O stretching	[184]
968	Al-O stretching	[317]
1050	Si-O-Si rocking	[310]
1070	Si-O-Si	[314]
1107	Si-O stretching	[317]
1100–1300	SiO ₂ optical phonon	[184]
1345-1696	Al=O stretching	[318]
1345	Al=O	[310]
2200	Si-H	[308]
2300–2400	SiOH-O	[309]
2940-3660	AlO-H stretching	[318]
3500–3800	SiO-H	[309]
3716	AlO-H Stretching	[317]

After thermal treatment of AlO_x film in O_2 ambient, Vitanov et al. observed a broad absorption band at 1060 cm^{-1} which indicates presence of Al-O-Si bond or to Al-O-A bond [146]. Verlaan et al. [310] attributed the bands present in the region between 400 and 1000 cm^{-1} to Al-O related stretching vibrations and the intensity of the Al-O absorption peak was found to increase with increase in the substrate temperature, almost linearly with the Al volume density. Here, it was also observed that the shape of the absorption feature changes for the films when deposited at different substrate temperatures [310].

Kim et al. observed broad absorbance band in the range of $590\text{--}1200\text{ cm}^{-1}$ and interpreted that the broad absorbance band is due to overlapping of the absorbance peaks of the O-C=O bending mode ($590\text{--}700\text{ cm}^{-1}$), O-Al-O bending mode ($650\text{--}700\text{ cm}^{-1}$), Al-O stretching mode ($750\text{--}850\text{ cm}^{-1}$) and Al-CH₃ stretching mode ($1000\text{--}1200\text{ cm}^{-1}$) [319]. Dorsey et al. interpreted that the absorption bands in the region of $2940\text{--}3660\text{ cm}^{-1}$ (AlO-H bond indicate the presence of water; either free, adsorbed, or combined as hydroxide [318]). Sah et al. reported one broad feature in the range of $(450\text{--}1100)\text{ cm}^{-1}$ centered at 690 cm^{-1} for FTIR spectra of ALD Al_2O_3 on Si and assigned to Al-O stretching mode [313].

5.4.4 Blister Analysis by 2D and 3D optical imaging

Optical microscope 2D and 3D images were used to analyse the presence of blisters. Optical surface images of RTP-fired ($860\text{ }^\circ\text{C}$) AlO_x film by Olympus MX61 microscope and Zeta 3D microscope are shown in Figure 5.16 and Figure 5.17 respectively. Figure 5.17(a) shows Zeta 2D optical surface image of RTP-fired ($860\text{ }^\circ\text{C}$) AlO_x film and Figure 5.17(b) shows Zeta 3D optical surface image of RTP-fired ($860\text{ }^\circ\text{C}$) AlO_x film for $70\text{ }\mu\text{m} \times 93\text{ }\mu\text{m}$ area. 2D optical imaging using Olympus microscope and 3D optical imaging using the Zeta microscope (Figure 5.16 and Figure 5.17, respectively) confirmed that there were no blisters in the film for annealing temperature up to $860\text{ }^\circ\text{C}$. Absence of blisters for spray coated AlO_x film may be related to the absence of H-species in the film [320]. Richter et al. observed presence of blisters through 2D optical microscope images for p-type Cz Si samples passivated with 5.8 nm and 11.5 nm Al_2O_3 (ALD) films capped by SiN_x (70 nm, PECVD) after firing at $800\text{ }^\circ\text{C}$ [305].

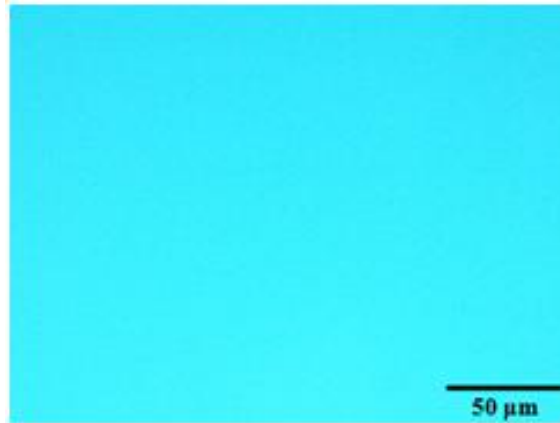


Figure 5.16: Optical surface image of RTP-fired (860 °C) AlO_x film by Olympus MX61 microscope.

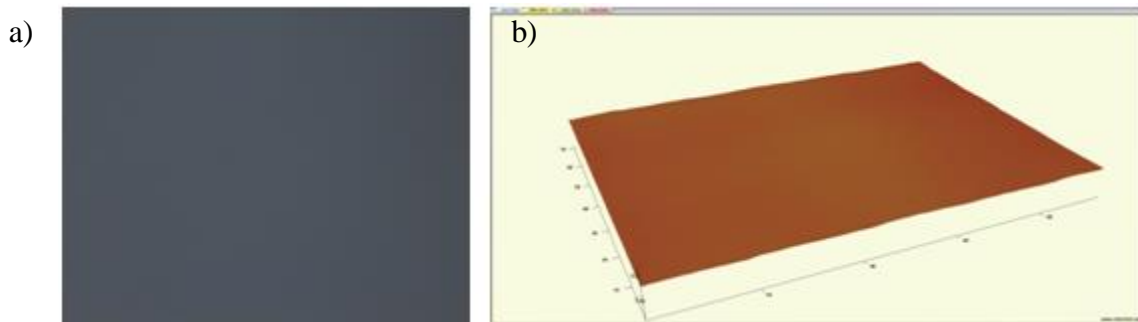


Figure 5.17: (a) Zeta 2D optical surface image of RTP-fired (860 °C) AlO_x film (b) Zeta 3D optical surface image of RTP-fired (860 °C) AlO_x film for 70 μm × 93 μm area.

5.4.5 XPS and HRTEM analysis of AlO_x thin film

XPS and HRTEM measurement results are shown in Figure 5.18. From the XPS and HRTEM analysis, three regions can be identified, namely the AlO_x film, an IL and silicon substrate. The total thickness of the dielectric stack on silicon is 10 nm, which is close to the ellipsometry measurement results (10.3 nm). An IL with thickness of about 2 nm is observed. From the XPS data, it is seen that the oxygen to aluminium (O/Al) ratio increases steadily from ~1.6 near the surface of AlO_x to ~2.5 towards the silicon substrate. The silicon concentration in the IL increases towards the silicon substrate. It can be concluded that the IL is aluminium silicate with increasing concentration of Si towards the IL/Si interface. It is

observed that the nitrogen and carbon content in the AlO_x film is near or below the detection limit of XPS.

Batra et al. reported O/Al ratio of 1.28 for AlO_x film deposited by ALD [321]. Naumann et al. investigated AlO_x film prepared by ALD and reported that initial growth was nonstoichiometric with the O/Al ratio > 20 for samples with one ALD cycle and O/Al ratio of 1.5 for 125 ALD cycles [322]. The O/Al ratio of PECVD film varied from 2.2 to 1.4 for the substrate temperature range of 100 °C to 300 °C [321]. It was observed that the IL plays an important role in the passivation of the silicon surface [25,120,192]. The thickness of the IL was reported to be in the range of 1 nm in the case of ALD [25] and PECVD [120] processes. Kimoto et al. reported that the IL in ALD deposited films is aluminium silicate [192]. Bhaire et al. reported aluminium silicate IL layer of 8 nm for pulsed-DC reactive sputter deposited AlO_x films [126]. The IL thickness was found to be 4 nm after annealing at 850 °C for 2 hours as reported in section 4.2.2 of this thesis for spray coated AlO_x film using hand-held sprayer.

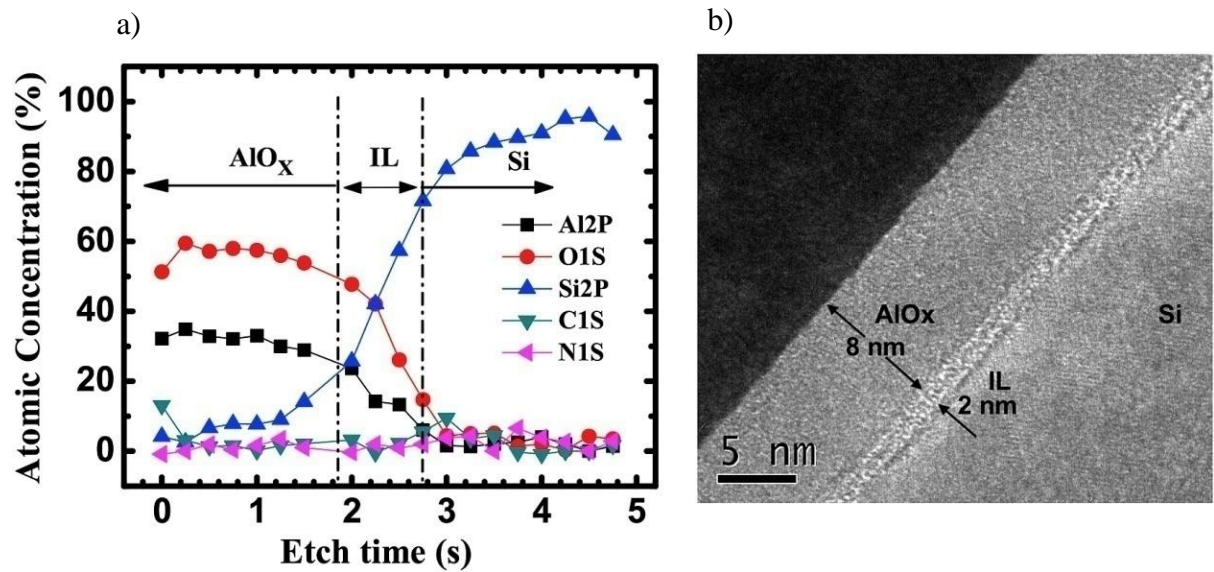


Figure 5.18: Physical characteristics of the spray coated AlO_x film after PDA at 520 °C for 20 min. (a) XPS depth profile (b) Cross sectional HRTEM image. The thickness of the IL is about 2 nm.

5.5 Summary and conclusions

In this chapter, the deposition of AlO_x film with thickness of ~ 10 nm by spray coating process using spraying instrument is demonstrated. The spraying equipment is specifically designed and built for solar cell applications and the largest wafer size capacity of the equipment is $200 \text{ mm} \times 200 \text{ mm}$. Details of the custom designed spray instrument are also provided. The hot plate heater is also custom designed for $6 \text{ inch} \times 6 \text{ inch}$ substrates. Contact angle measurements are carried out on the surface of the silicon wafer after UV/ O_3 exposure and it is found that the UV/ O_3 treatment improves the wetting behavior. The ultrathin SiO_x film grown by UV treatment in oxygen ambient is incorporated prior to AlO_x deposition. In a major departure from the spray pyrolysis process reported in literature, wherein the substrate was heated during spraying, in this work the solution is sprayed on the substrate at room temperature and then dried to obtain the film, a process sequence amenable to conveyer belt processing with high throughput. The vacuum chuck design is optimized using PL imaging to minimize defect generation during the spray process. The film properties are investigated by optical microscope, ellipsometer, AFM, XPS and HRTEM. The film thickness and RI are found to be uniform before and after PDA by spectroscopic ellipsometry measurements. AFM analysis indicates that the roughness of the silicon wafer is decreased significantly after the deposition of AlO_x film due to spreading of uniform thin liquid film of AlO_x solution on the silicon wafer surface. 2D and 3D images obtained using optical microscope are used to analyse the presence of blisters and it is confirmed that there are no blisters in the film for annealing temperature up to $860 \text{ }^\circ\text{C}$. In addition, no hydrogen peaks are observed by FTIR measurements. An IL with thickness of about 2 nm is observed from HRTEM image. It is revealed by XPS analysis that the IL is aluminium silicate. These promising structural characteristics of spray coated AlO_x films are obtained for low thermal budget annealing with the incorporation of UV/ O_3 grown ultrathin SiO_x film.

Chapter 6

Spray Coated AlO_x Film Deposited by Spraying Instrument for p-type Silicon Surface Passivation

The objective of this chapter is to investigate the electrical and passivation properties of the spray coated AlO_x film prepared using the spraying setup discussed in the chapter 5. Thermal stability of AlO_x films deposited by spray coating is also investigated and compared with various other deposition techniques for p-type c-Si surface passivation.

6.1 Substrate and sample preparation

Single side polished and double side polished p-type Cz c-Si wafers (2-inch, <100>, 4–7 Ω·cm, 270 μm ± 10 μm) were used for electrical characterization and lifetime measurements, respectively. In all cases, the wafers were initially cleaned using RCA-1, RCA-2, and a dilute (2%) HF solution, as discussed in chapter 3, section 3.1.1. AlO_x solution of 0.2 M was prepared by following the procedure described in chapter 3, section 3.1.2. Before AlO_x spray coating, the wafers were exposed to UV/O₃ for 5 min as discussed in chapter 5, section 5.2. The chemical SiO_x grown by UV treatment in oxygen ambient prior to spray deposition of the AlO_x film was found to be around 1.4 nm by spectroscopic ellipsometer. AlO_x film was prepared following the procedure discussed in chapter 5.

6.2 Electrical characterization

Electrical characterization of the AlO_x films were carried out on MIS capacitors fabricated on single side polished p-type Cz c-Si wafers. AlO_x film with thickness of approximately 10 nm was deposited on the polished side of the silicon wafer by the spray coating process. Aluminium shadow mask were used to evaporate aluminium dots with a nominal area of 0.025 mm² on the surface of the AlO_x film. The native oxide at the back surface of the wafers was etched using 2% HF, and aluminium back contacts were fabricated by thermal evaporation. The actual areas of the evaporated aluminium dots were measured

using an optical microscope and was found to average $\sim 24420 \mu\text{m}^2$. The MIS devices were characterized using C-V, G-V and I-V measurements by Keithley 4200 parameter analyzer.

6.2.1 Capacitance-voltage and conductance-voltage measurements

The C-V and G-V characteristics were measured at 1 MHz. Double C-V sweeps were performed to find hysteresis in the electrical characteristics. Series resistance correction was applied to the measured capacitance and conductance following the procedure discussed in chapter 3, subsection 3.2.10. The D_{it} was calculated from the peak of the G-V curve using the single frequency conductance method [261] and the Q_f was calculated from the shift in mid-gap voltage from its ideal value [50]. The C-V and G-V characteristics of a MIS capacitor are shown in Figure 6.1(a). The C-V for a shorter range of voltage to reveal hysteresis is shown in Figure 6.1(b). The hysteresis in the C-V curve is measured to be 10 mV and is considered negligible. The flat band voltage of the MIS capacitor (V_{FB}) was - 0.21 V and this indicates a right shift compared to the ideal value. The rightward shift is indicative of the negative charges in the insulator, and it is a requirement for field effect passivation of p-type silicon.

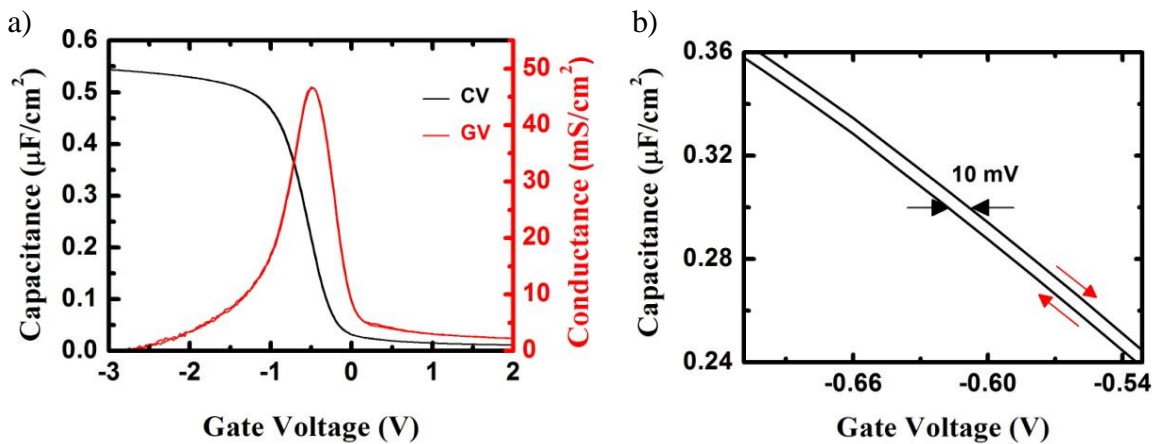


Figure 6.1: (a) Series resistance corrected C-V and G-V curves of MIS capacitors measured at 1 MHz. After AlO_x film deposition, PDA was performed in O_2 at 520°C for 20 min. (b) C-V characteristics (rescaled version of Figure 6.1 (a)) showing the hysteresis. Hysteresis is seen to be 10 mV. The red arrows indicate the direction of the voltage sweep. The measurement was started from inversion.

The Q_f and D_{it} extracted from the corrected C-V and G-V curves are shown in Figure 6.2. The D_{it} is found to be in the range of $(8.5\text{--}10) \times 10^{10} \text{ eV}^{-1}\cdot\text{cm}^{-2}$ whereas the Q_f is in the range of $-(5.2\text{--}5.5) \times 10^{12} \text{ cm}^{-2}$. The D_{it} and Q_f values are comparable to those reported for ALD and PECVD Al_2O_3 (see Table 2.1 and Table 2.2 of chapter 2), and are in the range of interest for high quality passivation of p-type silicon surface. The dielectric constant of the AlO_x was calculated as 6.5 from the accumulation capacitance and the film thickness obtained by ellipsometer. This is lower than 9, the value expected for Al_2O_3 [323]. The low value of dielectric constant in our experiment may be attributed to the presence of the IL, which is a significant fraction of the overall thickness of the gate insulator.

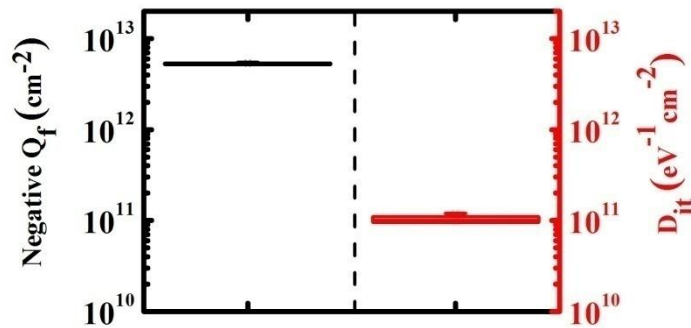


Figure 6.2: D_{it} and Q_f extracted from series resistance corrected C-V and G-V characteristics. Data extracted from 4 devices are shown.

6.2.2 Current-voltage measurements

The I-V of an MIS structure, measured in accumulation is shown in Figure 6.3(a). The dielectric breakdown characteristic is an indication of the quality of the dielectric and its suitability for withstanding high voltages. In IBC cells, if the cell goes to reverse bias due to partial shadowing of the module [324], the dielectrics used on the backside could be subjected to high voltages. AlO_x film must be robust enough to withstand the reverse bias voltage condition. The breakdown voltage of a dielectric layer is the minimum voltage that causes a portion of a dielectric layer to become electrically conductive. In the AlO_x film, breakdown can occur at defects or weak spots [325].

The dielectric breakdown voltage distribution is known to follow the Weibull distribution [326,327] and the cumulative distribution function (CDF) for two-parameter Weibull distribution [328] is given by

$$F_{BD} = 1 - \exp \left[- \left(\frac{V_{BD}}{\alpha} \right)^\beta \right] \quad (6.1)$$

where V_{BD} is the breakdown voltage (6.3 V in Figure 6.3(a)). α is the scale parameter (in V) (width of the distribution) and it indicates the voltage at which 63.2% of the devices are expected to fail. β is defined as the shape parameter. A large value of α indicates high electrical breakdown strength and a large value of β indicates high uniformity [329]. For the Weibull plot, median ranks were obtained using Benard's approximation [330]. The Weibull plot of V_{BD} is shown in Figure 6.3(b). α of 5 V and β of 15 are obtained from the intercept and slope of the Weibull plot, respectively.

The dielectric breakdown field is defined as

$$\xi_{BD} = \frac{|V_{BD} - V_{FB}|}{t_{ox}} \quad (6.2)$$

where, t_{ox} is the thickness of the AlO_x film (10.3 nm) measured using ellipsometer. Mean breakdown field of $4.7 \text{ MV}\cdot\text{cm}^{-1}$ is calculated from the mean value of V_{BD} obtained from the Weibull plot. The passivation dielectrics in solar cells are usually not subjected to such high electric fields.

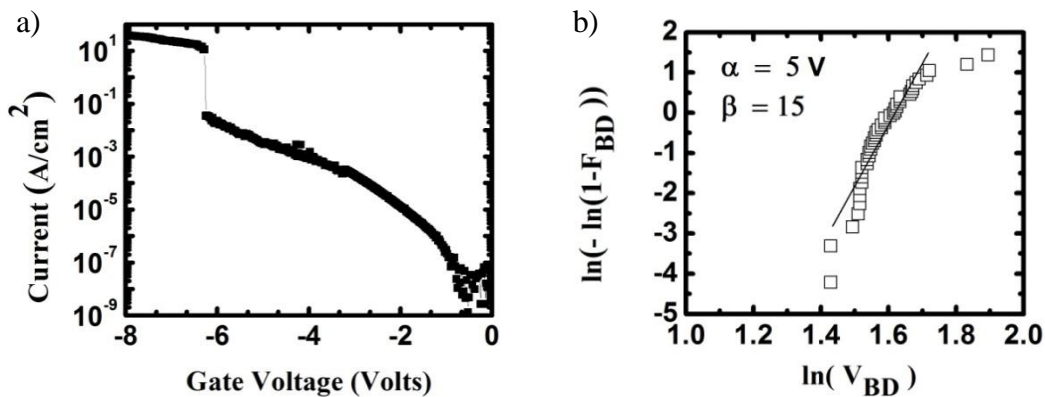


Figure 6.3: (a) I-V characteristics of an MIS capacitor. After deposition, the AlO_x was subjected to PDA in O_2 at $520 \text{ }^\circ\text{C}$ for 20 min. (b) Weibull plot of the breakdown voltage (V_{BD}) for 47 MIS capacitors.

6.3 Surface passivation

For surface passivation studies, the AlO_x films were deposited on both sides of the double side polished wafers by the spray deposition process described in chapter 5. The bulk lifetime of minority carriers (τ_{bulk}) in the silicon wafer was evaluated by wet chemical passivation utilizing quinhydrone/methanol (0.07 M) [267] using double side polished wafers subjected to RCA cleaning and 2% HF etch. The effective minority carrier lifetime was measured using transient or QSS photo conductance mode on a Sinton WCT-120 lifetime tester from Sinton Instruments [262]. The bulk lifetime of the bare silicon wafer was measured to be 636 μs . All stated carrier lifetimes were extracted for excess minority carrier density of $1 \times 10^{15} \text{ cm}^{-3}$. The S_{eff} was calculated using Eq. (3.36), in chapter 3.

6.3.1 Lifetime measurement

Figure 6.4 shows the effective minority carrier lifetime (τ_{eff}) for the annealed (PDA) sample. For the sample, τ_{eff} of 471 μs and S_{eff} of $8 \text{ cm}\cdot\text{s}^{-1}$ are obtained at Δn of $1 \times 10^{15} \text{ cm}^{-3}$ after PDA and it indicates that the silicon surface is well passivated.

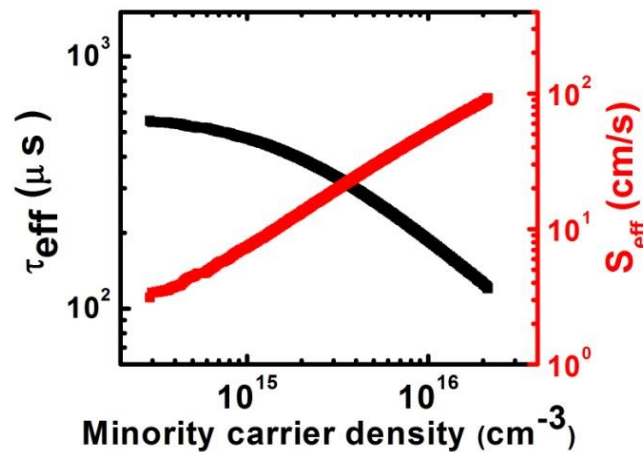


Figure 6.4: The measured minority carrier lifetime and S_{eff} as a function of injection level for the AlO_x sample annealed at 520 $^{\circ}\text{C}$ for 20 min in O_2 . τ_{eff} is 471 μs and S_{eff} is $8 \text{ cm}\cdot\text{s}^{-1}$ at Δn of $1 \times 10^{15} \text{ cm}^{-3}$.

A S_{eff} of $28 \text{ cm}\cdot\text{s}^{-1}$ was reported in chapter 4, section 4.2 for films deposited using a hand-held sprayer. Further, good passivation was obtained only after PDA at 850 $^{\circ}\text{C}$ for 2

hours, a prohibitively high thermal budget for industrial solar cell processing. The low S_{eff} obtained in this spray method with substantially lower thermal budget for PDA may be due to the chemical oxide grown by UV treatment in oxygen ambient prior to spray deposition of the AlO_x film. For ALD and PECVD Al_2O_3 films, the S_{eff} reported in literature are in the range of 2–10 $\text{cm}\cdot\text{s}^{-1}$, for example [86,87]. In literature, S_{eff} of 70 $\text{cm}\cdot\text{s}^{-1}$ was reported for AlO_x film deposited by spray pyrolysis technique [158] and S_{eff} of 55 $\text{cm}\cdot\text{s}^{-1}$ was reported for spin coating process [143]. Though the S_{eff} reported in Figure 6.4 is higher than that reported for ALD and PECVD techniques, it is sufficiently low for back surface passivation applications for p-type PERC solar cells. To the best of our knowledge, it is also the best reported S_{eff} value so far in literature for AlO_x deposited by any solution processing technique.

6.3.2 Thermal stability

To study the thermal stability of the AlO_x passivation, the samples after PDA were further subjected to firing processes at different temperatures from 700 °C to 860 °C in $\text{O}_2 + \text{N}_2$ ambient ($\text{O}_2/\text{N}_2 = 1.5$) using a RTP tool (AW610 from Allwin 21 Corporation). The temperature profiles used were similar to the silver paste firing profile used in fabrication of PERC solar cells [185]. An example of the temperature profile used is shown in Figure 6.5(a). The τ_{eff} and the corresponding S_{eff} from these experiments are plotted in Figure 6.5(b) as a function of the peak temperature of the RTP process. It is observed that the S_{eff} is maintained at 8 $\text{cm}\cdot\text{s}^{-1}$ up to an annealing temperature of 700 °C and is 12 $\text{cm}\cdot\text{s}^{-1}$ for 750 °C. After annealing at 790 °C, the S_{eff} increases to 48 $\text{cm}\cdot\text{s}^{-1}$. This is achieved without the use of a capping layer. For ALD and PECVD films, SiN_x capping layer may be necessary to stabilize the passivation [22,183].

For p-type PERC solar cells, the rear side dielectrics should be chosen to enhance light trapping in the solar cell. According to Dullweber et al., a dielectric of at least 100 nm thickness is needed at the rear side of PERC solar cells [331]. One approach is to use a stack of AlO_x and SiN_x , wherein the thin AlO_x (10 nm) provides the passivation and the stack enhances the reflection of the long wavelength light [306,331]. Saint-Cast et al. reported p-type PERC solar cells with 21.5% efficiency using 100 nm AlO_x deposited by PECVD for rear side passivation and light confinement [120]. Table 6.1 lists the thermal stability data for AlO_x films synthesized by a variety of methods reported in literature. The S_{eff} values obtained

in our experiments with firing up to 750 °C are comparable to that of the ALD and PECVD films reported in literature. The S_{eff} obtained for the annealing temperature of 790 °C is also promising for the p-type PERC solar cell applications.

Table 6.1: Comparison of thermal stability of AlO_x films deposited by various techniques for p-type c-Si surface passivation.

Passivation layer(s)	S_{eff} ($\text{cm}\cdot\text{s}^{-1}$)	Additional details	Reference
Al_2O_3 (ALD)	15 ^(a)	10–12 $\Omega\cdot\text{cm}$, p-type Cz, direct firing at 850 °C in N_2	[63]
Al_2O_3 (ALD)	300 ^(a,b)	1.5 $\Omega\cdot\text{cm}$, p-type FZ, after PDA followed by firing in an IR conveyor-belt furnace at 830 °C for ~3 s	[183]
Al_2O_3 (ALD)	25 ^(b)	2 $\Omega\cdot\text{cm}$, p-type, after annealing and subsequent firing in industrial belt line furnace at 850 °C	[332]
Al_2O_3 (ALD)/ SiN_x (75 nm)	44 ^(a)	1.5 $\Omega\cdot\text{cm}$, p-type FZ, after PDA followed by firing in an IR conveyor-belt furnace at 830 °C for ~3 s	[183]
AlO_x (PECVD)	12–25 ^(b)	1 $\Omega\cdot\text{cm}$, p-type FZ, after PDA at 450 °C for 10 min in N_2 followed by firing at 870 °C	[117]
AlO_x (Spin coating)	94 ^(a,b)	1–5 $\Omega\cdot\text{cm}$, p-type c-Si, FZ, furnace anneal at 780 °C for 130 min in O_2	This work
AlO_x (Spray coating)	28 ^(a,b)	1–5 $\Omega\cdot\text{cm}$, p-type c-Si, FZ, furnace anneal at 850 °C in O_2 for 2 hours (hand-held sprayer)	This work
AlO_x (Spray coating)	12 ^(a)	4–7 $\Omega\cdot\text{cm}$, p-type c-Si, Cz, PDA at 520 °C in O_2 for 20 min followed by RTP at 750 °C in O_2+N_2	This work
AlO_x (Spray coating)	48 ^(a)	Firing at 790 °C. Rest of the details is the same as in the row just above this.	This work

^(a) at $\Delta n = 10^{15}\text{cm}^{-3}$, ^(b) $S_{\text{eff,max}}$

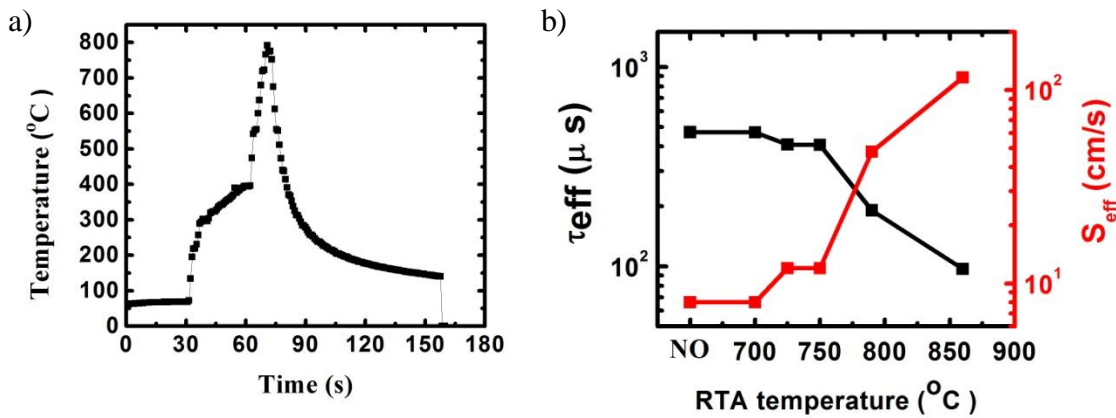


Figure 6.5: (a) The temperature profile with a peak of 790 °C used for RTP firing. (b) The measured minority carrier lifetime and S_{eff} as a function of the peak temperature of the RTP process at Δn of $1 \times 10^{15} \text{ cm}^{-3}$ for the AlO_x sample annealed at 520 °C for 20 min in O_2 .

6.4 Summary and conclusions

Electrical characterization of the AlO_x films was carried out using MIS capacitors. Lifetime studies were conducted on test structures where the film was deposited on both sides of double side polished silicon wafers. The D_{it} was found to be in the range of $(8.5\text{--}10) \times 10^{10} \text{ eV}^{-1}\cdot\text{cm}^{-2}$ whereas the Q_f was in the range of $-(5.2\text{--}5.5) \times 10^{12} \text{ cm}^{-2}$. Both these values are in the range of interest for high quality passivation of p-type silicon surface. The breakdown field of the film is seen to be sufficiently high for passivation applications. Surface recombination velocity of $8 \text{ cm}\cdot\text{s}^{-1}$ was obtained after post deposition anneal at 520 °C and the passivation is seen to be stable up to 750 °C, a peak temperature close to the typical peak temperature used for firing of silver contacts in PERC solar cells. Spray deposition seems to be very promising for mainstream PERC solar cell production, especially considering its low cost of ownership. High temperature stability of AlO_x layers is necessary for majority of solar cell applications. Lifetime samples were annealed at various temperatures to study the thermal stability of surface passivation. Surface recombination velocity of $12 \text{ cm}\cdot\text{s}^{-1}$ is obtained for anneal temperature of 750 °C. An important challenge would be optimization of spray coating process to obtain uniform good quality thin AlO_x passivation film on textured silicon surfaces for passivation of p^+ emitters on n-type wafer based solar cells.

Chapter 7

Preliminary Investigations on Integration of Spray Coated AlO_x in Solar Cells

AlO_x film provides excellent surface passivation on highly doped p^+ -type silicon surfaces [23,88]. In this chapter, surface passivation of highly boron doped p-type silicon by 10 nm AlO_x thin film deposited using spray coating process is investigated. Industrially relevant screen printing process using boron dopant paste as a dopant source was used to form p^+ emitters on n-type wafers. Development of spray coated AlO_x film with good passivation properties for highly boron doped p-type silicon can open the way to application of the AlO_x passivation film on a wider range of solar cell designs.

In the previous chapters, spin coated and spray coated AlO_x film for the surface passivation of p-type silicon is presented. In chapter 4, $S_{\text{eff,max}}$ of $28 \text{ cm}\cdot\text{s}^{-1}$ was obtained for spray coated AlO_x film on p-type FZ silicon wafers after annealing at $850 \text{ }^\circ\text{C}$ for 2 hours using hand-held sprayer. In chapter 5, the method of depositing AlO_x thin film was presented through spray coating using spraying instrument, and S_{eff} of $8 \text{ cm}\cdot\text{s}^{-1}$ was achieved for p-type silicon substrates as reported in chapter 6. In this chapter, spray coated AlO_x for p^+ emitter passivation is presented. The boron-rich layer (BRL) removal process influences the passivation of p^+ silicon surface. In this chapter, passivation properties of p^+ emitter using AlO_x film deposited by the spraying instrument are investigated with wet chemical HNO_3 oxidation and ozone oxidation for BRL removal.

In this chapter, two metallisation schemes—photolithography and laser fired contact (LFC)—are investigated for spray coated AlO_x film integration into silicon solar cells. Photolithography based technique is costly and not very attractive for PV manufacturing. Laser processes are cost-effective and used in large scale silicon solar cell manufacturing [21].

7.1 p^+ emitter passivation

To investigate the surface passivation characteristics of AlO_x film for p⁺ emitter, the optimised AlO_x film of 10 nm developed by spray coating process presented in the chapter 5 of this thesis was used for p⁺ emitter passivation. This section also includes a review on passivation properties of AlO_x films deposited by various techniques for p⁺ emitter passivation.

7.1.1 Experimental details

Double side polished, n-type Cz, 2-inch c-Si wafers with 4–7 Ω·cm bulk resistivity, <100> orientation and 270 μm ± 10 μm thickness were used for investigation. The wafers were initially cleaned using RCA procedure described in chapter 3, section 3.1.1. Before boron dopant paste screen-printing, the wafer surfaces were exposed to UV/O₃ for 5 min as discussed in chapter 5, section 5.2. The ozone oxidation step prior to the screen printing process was carried out in order to clean the silicon wafer surface and the thin oxide layer formed can protect the surface of silicon wafer by avoiding direct contact with the dopant paste material.

7.1.2 Boron dopant paste diffusion

Boron doping paste was printed on the silicon wafers by a screen printer (p-200S from Haiku Technology) using 2-inch circular blanket screen (Mesh: 250/30, Mesh Angle: 45°, Tension: (25–27) N, EOM: 11+/-1). The squeegee speed of the printer was set at 200 mm·s⁻¹. After screen-printing, the samples were dried at 150 °C for 1.5 min in the nitrogen-oxygen ambience (N₂:O₂ = 4:1) using a hot air oven (4 kW, 230 V, Gayatri Scientific, Mumbai) to remove the solvent. Boron dopant paste was screen-printed on both sides of silicon wafer to fabricate lifetime structures for passivation study.

The diffusion was then performed in a horizontal quartz tube furnace at 900 °C and 950 °C for 20 min in the N₂ ambient air flow of 1 standard liter per minute (slpm). The samples were loaded at 700 °C. After 10 min of stabilization, the temperature was increased to the diffusion process temperature. After 20 min, the temperature was decreased to 700 °C and the samples were unloaded. Boron paste residue from the diffused surfaces was removed in 5% HF solution. The sheet resistance of the p⁺ diffused wafers was measured using four-

point probe method. The measurements were done at three different points of the diffused wafer and the average value was calculated. The average sheet resistance values were $70 \Omega/\square$ and $34 \Omega/\square$ with relative standard deviations of $1.1 \Omega/\square$ and $0.7 \Omega/\square$ for 900°C and 950°C , respectively based on three points of measurements on the diffused wafers.

7.1.3 p^+ emitter passivation with AlO_x

p^+ emitter passivation study was carried out for the samples with sheet resistance of $70 \Omega/\square$ and $34 \Omega/\square$ employing a typical wet chemical HNO_3 oxidation process for BRL removal. In addition, p^+ emitter passivation for the sample with sheet resistance of $70 \Omega/\square$ was also investigated with UV/ O_3 based BRL removal process. In the HNO_3 chemical oxidation process, BRL of the diffused sample was oxidized by HNO_3 (37%) acid at 80°C for 30 min. In case of ozone oxidation, the samples were exposed to UV/ O_3 for 5 min with O_2 flow rate of 2 slpm. In both cases, the samples were then dipped in 2% HF to remove the oxidized layer.

After BRL removal, the wafers were cleaned using RCA procedure [246] described in chapter 3, section 3.1.1. Before AlO_x spray coating, the wafer surfaces were exposed to UV/ O_3 for 5 min as discussed in chapter 5, section 5.2. AlO_x film of 10 nm was deposited by spraying instrument on both the sides of sample followed by PDA for 20 min in a quartz furnace at 520°C in O_2 ambience. The method and process details of AlO_x film deposition were provided in chapter 5.

The values of J_{0e} were estimated from the measurements of effective lifetime using Eq. 2.26. From the extracted J_{0e} values, the maximum 1-sun open-circuit voltage ($V_{oc,max}$) was calculated using Eq. 2.27. In Figure 7.1, the Auger corrected inverse effective carrier lifetime is plotted as a function of $(\Delta n + N_{dop})$ using Eq. (2.26) and the J_{0e} values were extracted from the linear fit. The inverse lifetime values were observed to be very linear for both BRL removal methods. The J_{0e} values of $92 \text{ fA}\cdot\text{cm}^{-2}$ and $120 \text{ fA}\cdot\text{cm}^{-2}$, $V_{oc,max}$ values of 673 mV and 667 mV for 1-sun were obtained for HNO_3 and UV/ O_3 oxidation based BRL removal methods, respectively for p^+ emitter with sheet resistance of $70 \Omega/\square$.

The results demonstrate that the HNO_3 wet chemical process is better than ozone oxidation for the removal of BRL. Ozone oxidation, comparatively a fast and less complex process could still be explored as an option for removing BRL. The J_{0e} values of $145 \text{ fA}\cdot\text{cm}^{-2}$ and $V_{oc,max}$ values of 662 mV for 1-sun were obtained for HNO_3 oxidation method for p^+

emitter with sheet resistance of $34 \Omega/\square$. Further experiments are needed to collect statistically significant amount of data to confirm this observation. There does not appear to be any published J_{0e} data for boron-diffused silicon emitters passivated with AlO_x film using spray coating method. The J_{0e} values for AlO_x films synthesized by a variety of methods reported in literature and a comparison with our results are shown in Table 7.1. Based on these reference data, the J_{0e} values obtained in our experiments need to be reduced further to enable the spray coating process more acceptable.

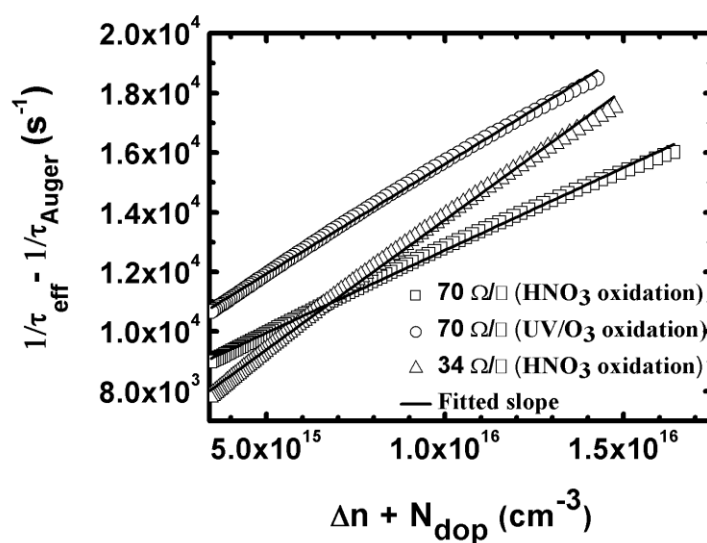


Figure 7.1: Measured Auger corrected inverse effective carrier lifetime as a function of $(\Delta n + N_{\text{dop}})$ for different BRL removal methods. The silicon samples were double side boron diffused and passivated by spray coated 10 nm AlO_x film.

Table 7.1: Comparison of passivation properties of AlO_x films deposited by various techniques for p⁺ emitter.

Passivation layer(s)	Deposition method	p ⁺ emitter	J _{0e} (fA·cm ⁻²)	Reference
AlO _x (10 nm)	Spray coating	p ⁺ /n-Cz/p ⁺ , 70 Ω/□ emitter (screen printing process), BRL removed by HNO ₃ oxidation	92	This work
AlO _x (10 nm)	Spray coating	p ⁺ /n-Cz/p ⁺ , 70 Ω/□ emitter (screen printing process), BRL removed by UV/O ₃ oxidation	120	This work
AlO _x (10 nm)	Spray coating	p ⁺ /n-Cz/p ⁺ , 34 Ω/□ emitter (screen printing process), BRL removed by HNO ₃ oxidation	145	This work
Al ₂ O ₃ /SiN _x	ALD/PECVD	p ⁺ /n-Si/p ⁺ , 70–73 Ω/□ emitter (screen printing process)	96 ± 3	[205]
Al ₂ O ₃ /SiN _x	PECVD	p ⁺ /n-Cz/p ⁺ , 170–30 Ω/□ emitter (BBr ₃ diffusion process)	8–42	[88]
Al ₂ O ₃ (27 nm)	Plasma ALD	p ⁺ /n-FZ/p ⁺ , 90 Ω/□ emitter (BBr ₃ diffusion process)	60	[85]
Al ₂ O ₃ (20 nm)	Thermal ALD	p ⁺ /n-Cz/p ⁺ , 62–51 Ω/□ emitter (BBr ₃ diffusion process)	26–32	[106]
Al ₂ O ₃ /SiN _x	PECVD/PECVD	p ⁺ /n-FZ/p ⁺ , 87 Ω/□ emitter	48 ± 5	[206]
Al ₂ O ₃ /SiN _x	ALD/ PECVD	p ⁺ /n-FZ/p ⁺ , 87 Ω/□ emitter	38 ± 2.5	[206]
Al ₂ O ₃ /SiN _x	PA-ALD/PECVD	p ⁺ /n-FZ/p ⁺ , 86 Ω/□ emitter	21	[176]
Al ₂ O ₃ /SiN _x	PA-ALD/PECVD	p ⁺ /n-FZ/p ⁺ , 49 Ω/□ emitter	110.7	[176]
Al ₂ O ₃ /SiN _x	ALD/ PECVD	p ⁺ /n-Cz/p ⁺ , 75 Ω/□ emitter	50	[305]

7.2 Two process technologies—photolithography and laser fired contact—for spray coated AlO_x film integration into solar cells

The contact on the rear side of the c-Si solar cells can be formed by selectively removing the passivation layer using photolithography, followed by Al metal deposition. Local rear contact can also be formed using laser fired contact (LFC) of aluminium (Al) through the rear surface passivation layer.

7.2.1 Experimental details

P-type (boron doped), Cz, 5-inch, pseudo-square, $\langle 100 \rangle$ oriented c-Si wafers were used for the experiments. The process detail for sample preparation is described in Figure 7.2. All the wafers underwent SDR process using hot sodium hypochlorite (NaOCl) and potassium hydroxide (KOH) followed by texturing process using KOH . The wafers underwent HCl cleaning process at $70\text{ }^\circ\text{C}$ for 15–20 min followed by a dip in 2% HF solution. The diffusion process was carried out in a tube diffusion furnace (Protemp USA, Sirius PRO 200) using phosphorus oxychloride as the dopant source. Using PECVD, 100 nm SiN_x was deposited on the front side and rear phosphosilicate glass (PSG) was removed by a dip in 2% HF . The wafers underwent SDR process for rear diffusion removal followed by SiN_x and PSG removal on the front side in 2% HF . All wafers underwent HCl cleaning followed by a dip in 2% HF . Ultrathin SiO_x was grown by UV/O_3 on the front and back sides of the Si wafer. Using PECVD, 75 nm SiN_x was deposited on the front side. SiO_x was removed at the back by dilute HF solution. Ultrathin SiO_x was grown by UV/O_3 on back side followed by AlO_x deposition on the back side by spraying instrument using the process described in chapter 5 followed by PDA at $520\text{ }^\circ\text{C}$ for 20 min. Two different approaches—photolithography and laser fired contact—for spray coated AlO_x film were explored.

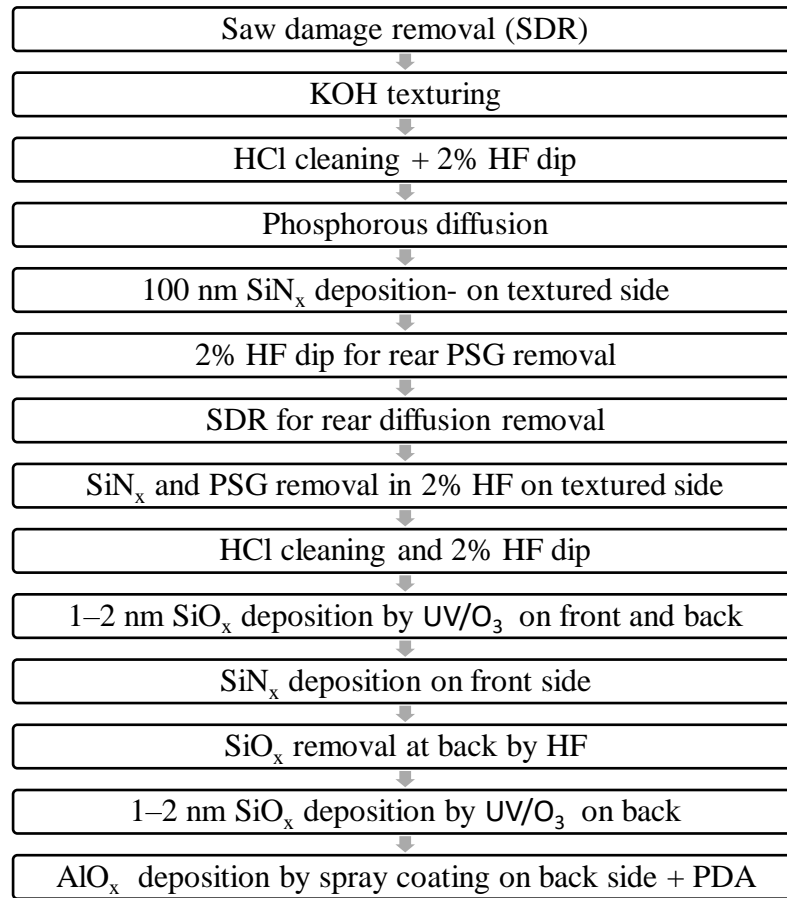


Figure 7.2: Process flow of sample preparation for photolithography and LFC experiments.

7.2.2 Photolithography

The sample surface was dehydrated at 90 °C for 10 min followed by positive photoresist (PPR) film deposition by spin coating (3000 rpm, 30 s). The wafer underwent soft bake at 90 °C for 5 min. The sample was selectively exposed to UV light through a mask for 2 min and the exposed sample was developed in MF319. The optical image of the sample after the MF319 development is shown in Figure 7.3(a). The sample was dipped in 1% HF for ~30 s to etch AlO_x film.

The optical image of the sample after HF (1%) etching of AlO_x film is shown in Figure 7.3(b). The positive photoresist film was removed using acetone and the sample was cleaned in isopropyl alcohol (IPA) and DI water. The patterned AlO_x film after PPR removal is shown in Figure 7.3(c). Photolithography process is used for metallization processes in high efficiency silicon solar cells [122] in laboratories. However, for industrial production of high

efficiency silicon solar cell, photolithography is not a feasible process due to high cost involved.

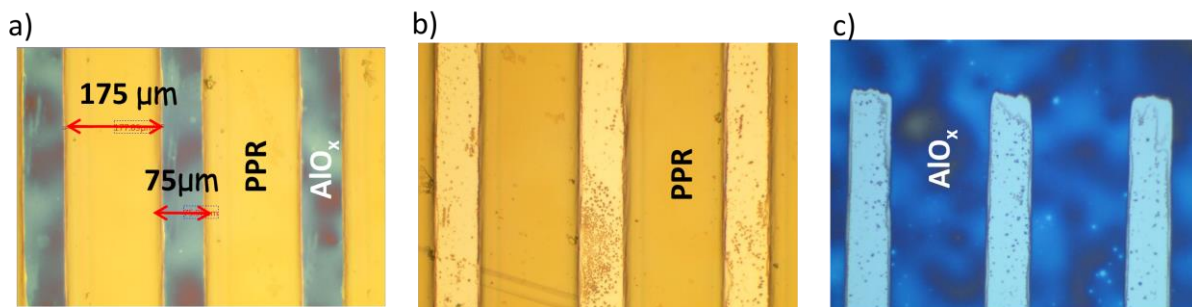


Figure 7.3: Optical images of optical lithography process steps to pattern the spray coated AlO_x film on textured silicon surface for metallization. a) After MF319 development of PPR (75 μm lines) b) After HF (1%) etching of AlO_x film c) Patterned AlO_x film after PPR removal by acetone.

7.2.3 Laser firing of metal through the dielectric

In the laser firing process, the back surface of the silicon wafer is passivated with a dielectric layer in order to reduce the rear recombination and aluminium metal is evaporated on top of the dielectric layer. To define the back contact between the silicon and aluminium metal layer, aluminium is sintered by local-laser firing through the dielectric layer. As a result, the aluminium gets diffused into the silicon bulk, even to the point that p/p⁺ local regions can be achieved due to laser treatment.

In this work, Al metal layer of 1 μm thickness was deposited by electron beam evaporation over the AlO_x film and laser firing was performed to make local contacts. Zeta 3D optical microscope was used for imaging. The laser system used in this experiment consists of a laser source, a laser beam expander, a focusing lens and X-Y translation stage. A 1070 nm μs-pulsed laser was used for the experiment. A pulse length of 10 μs was fixed to make laser fired contacts while the distance (the Z-coordinate) between laser head and sample was varied to obtain desired depth. The optical images of samples fired at Z distance of 30.5 mm and 30.7 mm obtained using zeta 3D microscope are shown in Figure 7.4 and Figure 7.5, respectively. Laser fired contact hole of ~2 μm depth (Z-coordinate: 30.5 mm) and ~3 μm depth (Z-coordinate: 30.7 mm) are obtained from Figure 7.4 and Figure 7.5, respectively. However, this is still subject to further analysis and optimization.

Figure 7.4(a) shows the 2D line profile for step height measurement on the sample surface. The sample was fired at Z distance of 30.5 mm. Figure 7.4(b) shows the analysis report obtained for the 2D line profile showing step height $\sim 2 \mu\text{m}$ between the red markers. Figure 7.4(c) shows the 2D view of the sample fired at Z distance of 30.5 mm. A white line drawn on the sample indicates the region of 2D line profile performed and Figure 7.4(d) shows the 3D view of the sample.

Figure 7.5(a) shows the 2D line profile for step height measurement on the sample surface. The sample was fired at Z distance of 30.7 mm. Figure 7.5(b) shows the analysis report obtained for the 2D line profile showing step height $\sim 3 \mu\text{m}$ between the red markers. Figure 7.5(c) shows the 2D view of the sample fired at Z distance of 30.7 mm. A white line drawn on the sample indicates the region of 2D line profile performed and Figure 7.5(d) shows the 3D view of the sample.

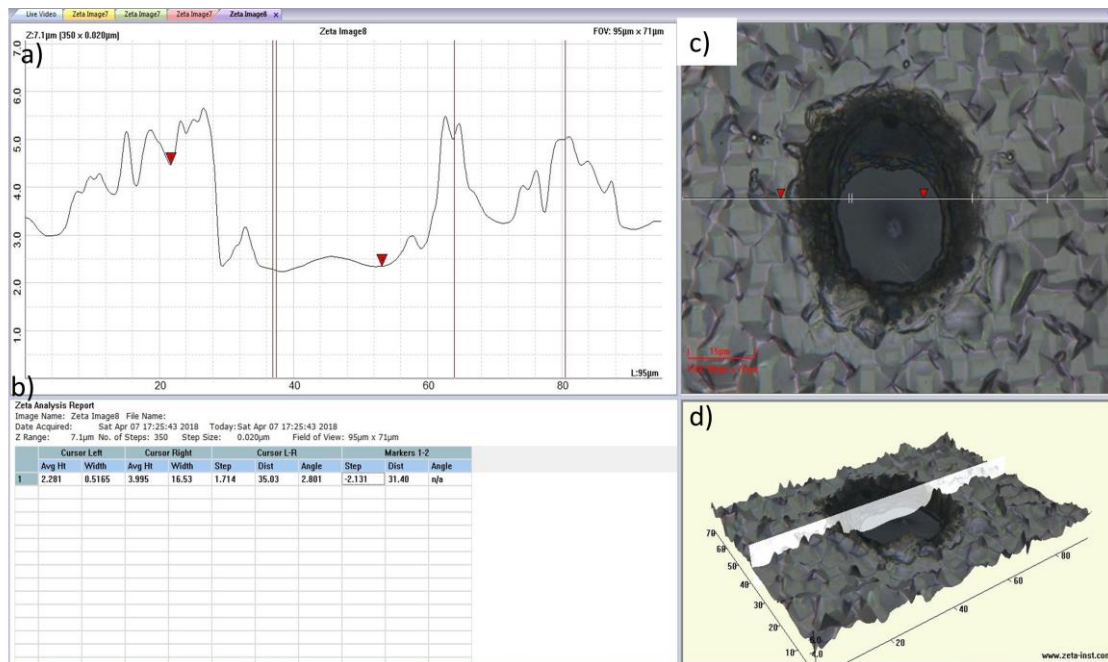


Figure 7.4: Zeta 3D microscope image analysis of a laser-fired contact hole (Z: 30.5 mm) with $2 \mu\text{m}$ depth (all measurements are in μm). (a) 2D line profile for step height measurement on the sample surface. (b) Analysis report for 2D line profile showing step height $\sim 2 \mu\text{m}$ between the red markers. (c) 2D view of the sample. (d) 3D view of the sample.

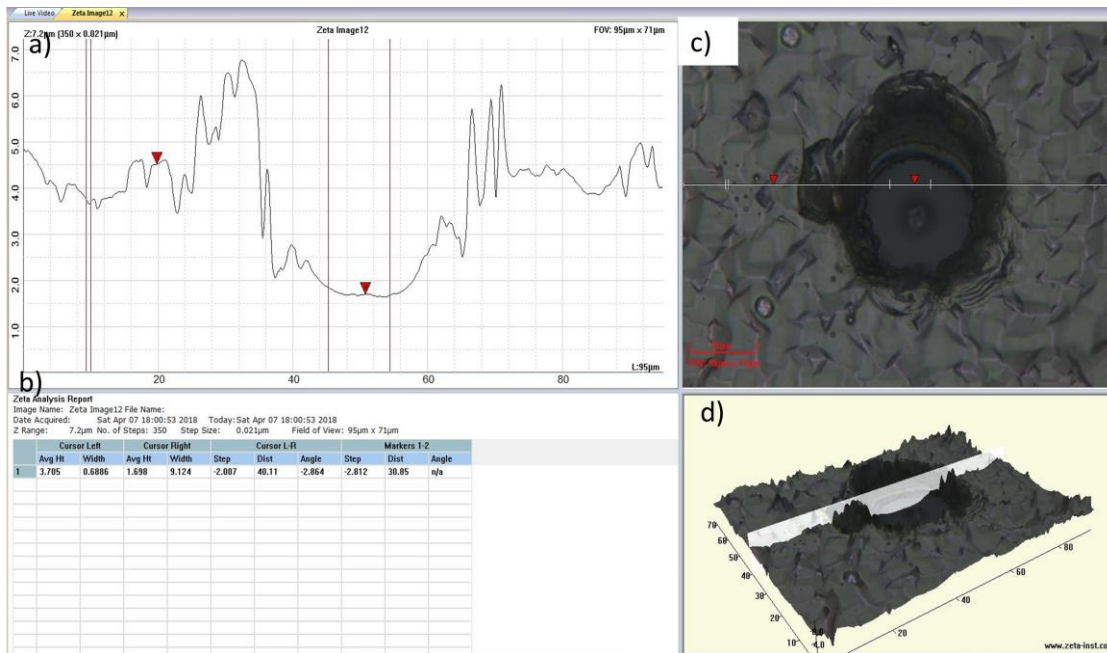


Figure 7.5: Zeta 3D microscope image analysis of a laser-fired contact hole (Z: 30.7 mm) with $\sim 3 \mu\text{m}$ depth (all measurements are in μm). (a) 2D line profile for step height measurement on the sample surface. (b) Analysis report for 2D line profile showing step height $\sim 3 \mu\text{m}$ between the red markers. (c) 2D view of the sample. (d) 3D view of the sample.

7.3 Summary and conclusions

In this chapter, we have investigated the passivation property of spray coated AlO_x thin film by spraying instrument for highly boron doped p^+ silicon surfaces. Wet chemical nitric acid oxidation and UV/O_3 oxidation were used to remove the BRL in this thesis work. When nitric acid was employed for BRL removal, J_{0e} values of $92 \text{ fA}\cdot\text{cm}^{-2}$ and $145 \text{ fA}\cdot\text{cm}^{-2}$ were obtained for $70 \Omega/\square$ and $34 \Omega/\square$ p^+ emitters, respectively. When UV/O_3 was employed to remove BRL, J_{0e} of $120 \text{ fA}\cdot\text{cm}^{-2}$ was achieved for $70 \Omega/\square$ p^+ emitter. The obtained J_{0e} values are towards the values reported in literature for solar cell applications. Further optimization is required to reduce the emitter saturation current density below $20 \text{ fA}\cdot\text{cm}^{-2}$. Preliminary results on two process technologies—photolithography and laser fired contact—were reported for rear contact to explore the possibility of integrating spray coated AlO_x film into PERC solar cell. Patterning of spray coated AlO_x film was made by selectively removing the passivation layer using photolithography. This process is suitable for fabrication at

laboratory scale, but it is an expensive process for large volume industrial production. Laser firing of aluminium metal through the rear surface spray coated AlO_x passivation layer was attempted as an alternative method for rear contact. Laser fired contact hole with $\sim 2 \mu\text{m}$ depth was obtained after laser firing, however it is subject to further analysis and optimizations.

Chapter 8

Summary and Outlook

8.1 Summary

Well passivated silicon surfaces are necessary to achieve a high efficiency c-Si solar cell. Low cost deposition method is required to reduce the cost of solar cell. In this thesis, solution processed AlO_x deposition processes for p-type crystalline silicon surface passivation was investigated experimentally. This includes study of a simple, inexpensive non-vacuum spin coating and spray coating processes for AlO_x film deposition with regard to the passivation properties. In spray pyrolysis process, a thin film is deposited by spraying a precursor solution on a heated surface. On the other hand, in this work, the spray coating was performed on the silicon substrates at room temperature. The deposited film was treated with two step annealing processes. The two step annealing comprises low temperature hot plate annealing to obtain thin solid AlO_x film and high temperature furnace annealing to improve the surface passivation of the film. In the final part of the thesis, passivation of highly boron doped p⁺ silicon using spray coated AlO_x thin film was investigated. In order to explore the possibility of integrating spray coated AlO_x film into PERC solar cell, preliminary experiments were carried out using two process technologies—photolithography and laser fired contact.

The main conclusions of this work can be summarized as follows:

- Good uniformity of spin coated AlO_x film was obtained over 2-inch silicon wafer. The thickness and RI of AlO_x film were measured by spectroscopic ellipsometer at 5 different places and the mean value of AlO_x film thickness was 57.45 nm and the standard deviation was 0.27 nm. The mean of the RI was 1.55 and the standard deviation was below measurement resolution.
- Effective minority carrier lifetime of 160 μs and S_{eff,max} of 94 cm·s⁻¹ were obtained at an injection level of Δn = 1 × 10¹⁵ cm⁻³ for spin coated AlO_x film after annealing at 780 °C

for 130 min in O₂ ambient. This promising surface passivation was achieved only after high temperature annealing for prolonged annealing time.

- Moreover, spin coating is suitable for film deposition on small areas in laboratory-scale researches. It is not well accepted by solar industries for large scale production. Spin coating is limited to batch processing and has a relatively low throughput compared to spray coating. Spin coating process demands relatively smooth and flat substrates, whereas, silicon substrates used for typical commercial solar cells have textured surface.
- To deposit thin passivation films (e.g., sub-20 nm thickness), very high spinning speed may be required to allow the film to thin down and high speed spinning of large size samples may lead to defects in the spin coated film that may affect the surface passivation. Moreover, comets, striations, chuck marks and gradual radial thickness variation are some important defects of spin coating methods. In case of spin coating, material usage is also poor compared to spray coating.
- In a major departure from the spray pyrolysis process wherein the substrate was heated during spraying, in this work, the solution was sprayed on the substrate at room temperature and then dried to obtain the film, a process sequence amenable to conveyer belt processing with high throughput.
- Effective minority carrier lifetime of 502 μs and $S_{\text{eff,max}}$ of 28 $\text{cm}\cdot\text{s}^{-1}$ were obtained for spray coated AlO_x films deposited using hand-held sprayer after annealing at 850 °C for 2 hours in O₂. This promising surface passivation was obtained only after high temperature annealing with prolonged annealing time.
- Hand-held sprayers are not suitable for large area applications. It is difficult to achieve uniformity over large area substrates using hand-held sprayer and it has relatively low throughput. Moreover, reproducibility is difficult with hand-held sprayer and quality of the film deposited by hand-held sprayers depends on the skills of the operator. However, spray coating process has great potential for large scale production with low wastage of material unlike spin coating.
- The spraying instrument used in this work was specifically designed and built for solar cell applications and the largest wafer size capacity of this equipment is 200 mm × 200 mm. The customized automated spraying instrument provides facility to precisely control the flow rate, duration of spray, spray ON/OFF and X-Y movements with speed. The control of entire spraying process can be achieved through a software program and spray coating can be performed according to the parameters already set using the software

program. The vacuum chuck design was optimized using PL imaging to minimize defect generation.

- Superhydrophilic silicon surfaces with water contact angle less than 1° was obtained after UV-ozone exposure and it was found that the UV-ozone treatment improves silicon surface wetting behavior. The ultrathin SiO_x film grown by UV-ozone treatment was incorporated prior to AlO_x deposition by spray coating as part of surface passivation scheme. Promising structural, electrical and passivation characteristics of spray coated AlO_x films by spray instrument were obtained for low thermal budget annealing with the incorporation of UV-ozone grown ultrathin SiO_x film.
- Excellent film thickness uniformity was achieved for spray coated AlO_x film using spraying instrument. The film thickness and RI was found uniform before and after PDA at 520°C for 20 min in O_2 . The mean value of AlO_x film thickness was 12.4 nm and the standard deviation was 0.3 nm before PDA. The mean of RI was 1.63 and the standard deviation was 0.01 before PDA. The mean values of film thickness and RI were found to be 10.3 nm and 1.64, respectively after PDA.
- The spray coated AlO_x film was found to be smooth with RMS roughness of 0.33 nm before and after PDA by AFM measurements.
- Hydrogen related bonds were not observed by FTIR measurements for as-deposited, PDA and RTP-fired (860°C) AlO_x films. 2D optical imaging using Olympus microscope and 3D optical imaging using the Zeta microscope confirmed that there were no blisters in the film for annealing temperature up to 860°C and absence of blisters for spray coated AlO_x film may be related to the absence of H-species in the film.
- An Interfacial layer with thickness of about 2 nm was observed from HRTEM image. It was revealed by XPS analysis that the interfacial layer is aluminium silicate.
- Mean breakdown field of $4.7 \text{ MV}\cdot\text{cm}^{-1}$ was calculated from the Weibull plot. The passivation dielectrics in solar cells are usually not subjected to such high electric fields.
- After post deposition annealing at 520°C for 20 min in O_2 , D_{it} was found to be in the range of $(8.5\text{--}10) \times 10^{10} \text{ eV}^{-1}\cdot\text{cm}^{-2}$ whereas the Q_f was in the range of $-(5.2\text{--}5.5) \times 10^{12} \text{ cm}^{-2}$. The D_{it} and Q_f values are comparable to those reported for ALD and PECVD Al_2O_3 and are in the range of interest for high quality passivation of p-type silicon surface.

- Effective minority carrier lifetime of 471 μs and S_{eff} of $8 \text{ cm}\cdot\text{s}^{-1}$ were obtained for the sample at Δn of $1 \times 10^{15} \text{ cm}^{-3}$ after PDA at 520 $^{\circ}\text{C}$ for 20 min in O_2 and it indicates that the silicon surface is well passivated.
- Good thermal stability was demonstrated for spray coated AlO_x films. High temperature stability of AlO_x layers is necessary for majority of solar cell applications. It is observed that the S_{eff} is maintained at $8 \text{ cm}\cdot\text{s}^{-1}$ up to an annealing temperature of 700 $^{\circ}\text{C}$ and is $12 \text{ cm}\cdot\text{s}^{-1}$ for 750 $^{\circ}\text{C}$ and this is found to be comparable to literature reports. This is achieved without the use of a capping layer. For ALD and PECVD films, SiN_x capping layer may be necessary to stabilize the passivation.
- Good surface passivation for highly boron doped p^+ -type silicon was achieved by spray coated AlO_x thin film. Industrially relevant screen-printing process using boron dopant paste as a dopant source was used to form p^+ emitters on n-type crystalline silicon wafers. The BRL on the surface of the emitter was removed by wet chemical nitric acid oxidation. An emitter saturation current density as low as $92 \text{ fA}\cdot\text{cm}^{-2}$ and $145 \text{ fA}\cdot\text{cm}^{-2}$ were obtained on p^+ emitter of $70 \Omega/\square$ and $34 \Omega/\square$ sheet resistance, respectively. An alternative method based on UV-ozone for removing BRL was attempted and an emitter saturation current density of $120 \text{ fA}\cdot\text{cm}^{-2}$ was obtained. The results demonstrate that highly doped p-type silicon surfaces can be passivated by spray coated AlO_x film.
- Two process technologies for rear contact were also studied to explore the possibility of integrating spray coated AlO_x film into PERC solar cell. Patterning of spray coated AlO_x film was made by selectively removing the passivation layer using photolithography. This process is suitable for fabrication at laboratory scale, but it is an expensive process for large volume industrial production. Laser firing of aluminium metal through the rear surface spray coated AlO_x passivation layer was attempted as an alternative method for rear contact. Laser fired contact hole with $\sim 2 \mu\text{m}$ depth was obtained after laser firing, however it is subject to further analysis and optimizations.

The work of this thesis has demonstrated that solution processed AlO_x is suitable for the p-type crystalline silicon surface passivation and has the potential of being applied to commercial solar cells. The spray coated AlO_x could be an effective alternative to AlO_x films deposited by other methods for fabrication of commercial solar cells and this would be the direction of future research work on spray coated AlO_x . Spray deposition seems to be very promising for mainstream PERC solar cell production, especially considering its low cost of ownership.

8.2 Future directions and process improvements

From this work, there are a number of areas that can be further investigated. They include:

- Optimization and fabrication of PERC solar cell using spin coated AlO_x films and $\text{AlO}_x/\text{SiN}_x$ (PECVD) stack for rear surface passivation.
- Fabrication of PERC solar cell using spray coated AlO_x films and $\text{AlO}_x/\text{SiN}_x$ (PECVD) stack for rear surface passivation.
- Optimization of deposition and annealing conditions of spray coated AlO_x films for the passivation of highly boron diffused emitters.
- Fabrication of n-type solar cell using spray coated AlO_x films for emitter passivation.
- Optimization of deposition and annealing conditions of spray coated AlO_x films for passivation of textured silicon surfaces.
- Optimization of deposition and annealing conditions of spray coated AlO_x films for passivation as well as ARC application.

Appendix I : The etch properties of spin coated AlO_x film

Single side polished p-type Cz c-Si wafer was used to investigate the etch characteristics of spin coated AlO_x film by wet chemicals. The wafer was initially cleaned using RCA procedure described in chapter 3, section 3.1.1. AlO_x solution of 1 M was prepared following the procedure described in chapter 3, section 3.1.2. The AlO_x solution was spin coated on the silicon substrate using spinner and the sample was annealed using a hot plate at 300 °C for 20 min. The thickness of the AlO_x film was measured using spectroscopic ellipsometer and the thickness was found to be 150 nm. Figure A.1 shows thickness variation of spin coated AlO_x films as a function of etch time for various chemicals.

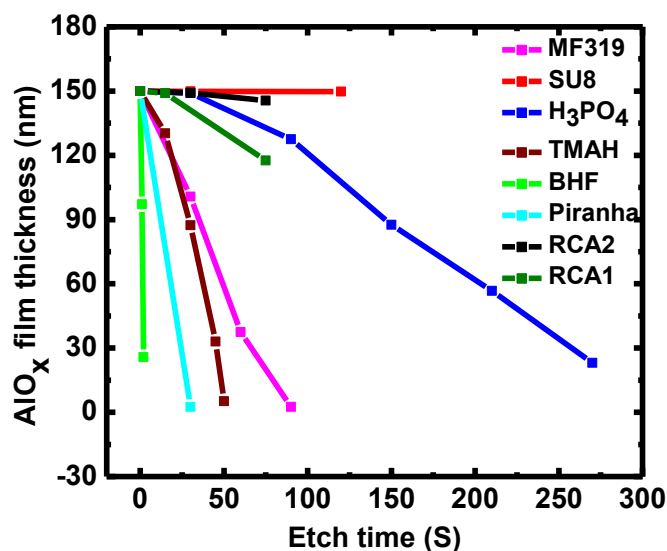


Figure A.1: Thickness variation of spin coated AlO_x films as a function of etch time for various chemicals.

The etch properties of spin coated AlO_x films was investigated using 11 different wet chemicals, namely 5% buffered hydrofluoric acid (BHF), RCA-1 solution, RCA-2 solution, piranha solution (96% H₂SO₄ + 30% H₂O₂ with ratio of 3:1 by volume), 85% phosphoric acid (H₃PO₄), 25% tetramethylammonium hydroxide (TMAH), MF319 developer, SU8-negative photoresist, acetone, IPA and 1:3 Methyl isobutyl ketone (MIBK)/IPA developer. The samples were immersed in the wet chemicals at room temperature for few seconds for etching process to take place and the corresponding thicknesses (in nm) were measured using a spectroscopic ellipsometer. Etch rate is the amount of material that is etched per second (in nm·s⁻¹). It was found that 1:3 MIBK/IPA developer, SU8-negative photoresist, acetone and

IPA are the chemicals that have negligible etch rate or does not etch the spin coated AlO_x . The etch rates are found to be $62.12 \text{ nm}\cdot\text{s}^{-1}$, $0.46 \text{ nm}\cdot\text{s}^{-1}$, $0.06 \text{ nm}\cdot\text{s}^{-1}$, $150 \text{ nm}\cdot\text{s}^{-1}$, $0.49 \text{ nm}\cdot\text{s}^{-1}$, $2.91 \text{ nm}\cdot\text{s}^{-1}$, $1.68 \text{ nm}\cdot\text{s}^{-1}$ for 5% BHF, RCA-1 solution, RCA-2 solution, piranha solution, H_3PO_4 , TMAH, MF319 developer, respectively.

Appendix II : Deposition of aluminum silicate (AlSi_xO_y) film by spin coating method

The investigation presented in this section is related to the development of spin coating process for deposition of AlSi_xO_y film. Single side polished, p-type, Cz, 2-inch, $\langle 100 \rangle$ oriented c-Si wafer with thickness of $300 \mu\text{m}$ and resistivity of $4\text{--}7 \Omega\cdot\text{cm}$ was used for film deposition. The wafer was first cleaned using the RCA cleaning process described in Chapter 3, section 3.1.1. AlO_x solution of 0.2 M was prepared by the procedure described in Chapter 3, section 3.1.2. Tetra-ethyl-orthosilicate (TEOS) (purity: 99.999%, Sigma-Aldrich) of 0.4 ml was added to the prepared AlO_x solution and the final solution was treated ultrasonically for 100 min at room temperature. The $\text{AlO}_x\text{-SiO}_x$ solution was spin coated on a silicon wafer at 6000 rpm for 30 s and subsequently annealed on a hot plate at $250 \text{ }^\circ\text{C}$ for 4 min. The procedure followed to deposit AlSi_xO_y film is described in Figure A.2.

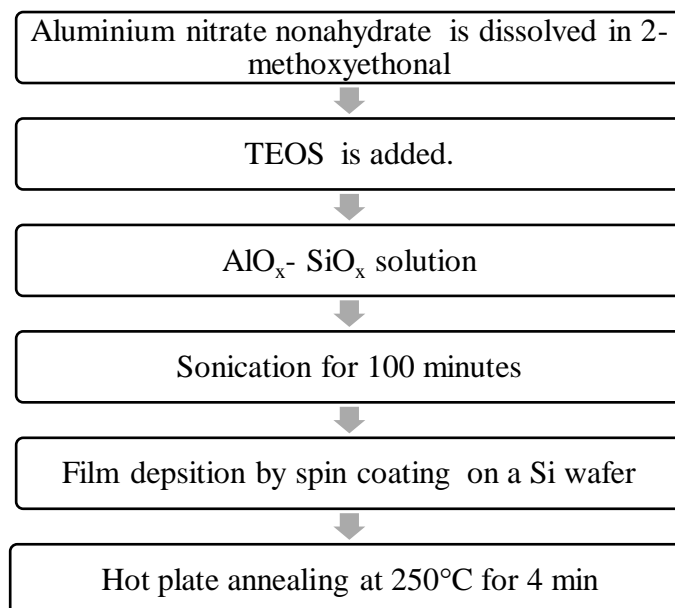
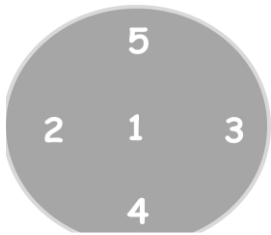


Figure A.2: Process details for aluminum silicate deposition.

The thickness and RI of the spin coated AlSi_xO_y thin film were measured using spectroscopic ellipsometer and the results are presented in Table A.1. The average thickness of 80 nm and RI of 1.49 were obtained. The images of AlSi_xO_y film obtained using optical microscope—Olympus-MX61—revealed that the deposited AlSi_xO_y film was smooth as shown in Figure A.3. Figure A.3(a) and Figure A.3(b) show the optical image of AlSi_xO_y film with scale bars 200 μm and 50 μm , respectively. As mentioned earlier in chapter 6, the IL of spray coated AlO_x was aluminium silicate. Future work can be optimization of the AlSi_xO_y film and investigation of $\text{AlSi}_x\text{O}_y/\text{AlO}_x$ stack for surface passivation.

Table A.1: Ellipsometry analysis of spin coated AlSi_xO_y film. The rightmost column of the table shows the sample indicating the positions where the measurements are performed.

Position	Thickness	RI	
1	80 nm	1.49	
2	80 nm	1.49	
3	80 nm	1.49	
4	79 nm	1.49	
5	80 nm	1.49	

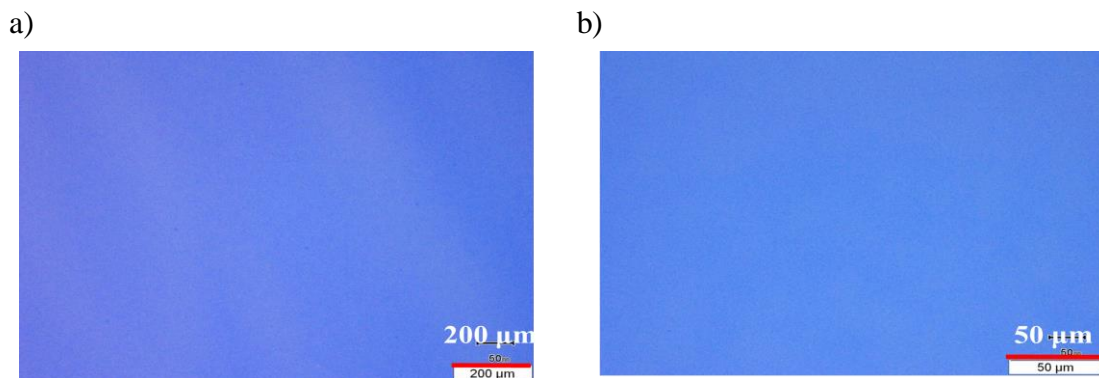


Figure A.3: Optical images of spin coated AlSi_xO_y film. (a) Scale bar: 200 μm . (b) Scale bar: 50 μm .

References

- [1] United Nations, Department of Economic and Social Affairs, Population Division (2019), “World Population Prospects 2019: Highlights (ST/ESA/SER.A/423),” 2019. [Online]. Available: https://population.un.org/wpp/Publications/Files/WPP2019_Highlights.pdf
- [2] IEA (2020), “SDG7: Data and Projections, IEA, Paris,” 2020. [Online]. Available: <https://www.iea.org/reports/sdg7-data-and-projections>
- [3] IEA, “Share of electricity in total final energy consumption, historical and SDS, IEA, Paris,” 2019. [Online]. Available: <https://www.iea.org/data-and-statistics/charts/share-of-electricity-in-total-final-energy-consumption-historical-and-sds>
- [4] IEA (2019), “World Energy Outlook 2019, IEA, Paris,” 2019. [Online]. Available: <https://www.iea.org/reports/world-energy-outlook-2019>
- [5] IRENA, “Global Renewables Outlook: Energy transformation 2050 (Edition: 2020),” Abu Dhabi, UAE, 2020. [Online]. Available: <https://www.irena.org/publications/2020/Apr/Global-Renewables-Outlook-2020>
- [6] IEA, “World gross electricity production, by source, 2018, IEA, Paris,” 2018. [Online]. Available: <https://www.iea.org/data-and-statistics/charts/world-gross-electricity-production-by-source-2018>
- [7] IEA, “Global Energy & CO₂ Status Report 2019, IEA, Paris,” 2019. [Online]. Available: <https://www.iea.org/reports/global-energy-co2-status-report-2019>
- [8] R. McMullan, *Environmental Science in Building*, Bloomsbury Publishing, 2017. [Online]. Available: <https://books.google.co.in/books?id=2RxHEAAAQBAJ>
- [9] Markard, N. Bento, N. Kittner, and A. Nunez-Jimenez, “Destined for decline? Examining nuclear energy from a technological innovation systems perspective,” *Energy Research & Social Science*, vol. 67, 2020. [Online]. Available: <https://doi.org/10.1016/j.erss.2020.101512>
- [10] T. Jin and J. Kim, “What is better for mitigating carbon emissions—Renewable energy or nuclear energy? A panel data analysis,” *Renewable and Sustainable Energy Reviews*, vol. 91, pp. 464–471, 2018. [Online]. Available: <https://doi.org/10.1016/j.rser.2018.04.022>

- [11] B. K. Sovacool, P. Schmid, A. Stirling, G. Walter, and G. MacKerron, “Differences in carbon emissions reduction between countries pursuing renewable electricity versus nuclear power,” *Nature Energy*, vol. 5, pp. 928–935, 2020. [Online]. Available: <https://doi.org/10.1038/s41560-020-00696-3>
- [12] IEA (2020), “World Energy Outlook 2020, IEA, Paris,” 2020. [Online]. Available: <https://www.iea.org/reports/world-energy-outlook-2020>
- [13] A. Ndimofor, *The Fundamentals of Crystallography and Mineralogy*, Spears Media Press, 2018. [Online]. Available: https://www.google.co.in/books/edition/The_Fundamentals_of_Crystallography_and/I41IDwAAQBAJ?hl=en&gbpv=0
- [14] D. M. Chapin, C. S. Fuller, and G. L. Pearson, “A New Silicon p-n Junction Photocell for Converting Solar Radiation into Electrical Power,” *Journal of Applied Physics*, vol. 25, no. 5, pp. 676–677, 1954. [Online]. Available: <https://doi.org/10.1063/1.1721711>
- [15] Global Solar Council, “Global Solar Council supports new PV markets in Africa: collaboration for solar growth and universal access to electricity,” *PV Magazine*, November 2020. [Online]. Available: <https://www.pv-magazine.com/press-releases/global-solar-council-supports-new-pv-markets-in-africa-collaboration-for-solar-growth-and-universal-access-to-electricity/>
- [16] IEA (2019), “Africa Energy Outlook 2019, IEA, Paris,” 2019. [Online]. Available: <https://www.iea.org/reports/africa-energy-outlook-2019>
- [17] EIA, “Interregional Electricity Trade in India,” October 2020. [Online]. Available: https://www.eia.gov/outlooks/ieo/section_issue_India.php
- [18] N. Belyakov, *Sustainable Power Generation: Current Status, Future Challenges, and Perspectives*, Elsevier, 2020. [Online]. Available: <https://www.sciencedirect.com/book/9780128170120/sustainable-power-generation>
- [19] S. Philips and W. Warmuth, “Photovoltaics Report-Fraunhofer Institute for Solar Energy Systems, ISE with support of PSE Projects GmbH,” 2022. [Online]. Available: <https://www.ise.fraunhofer.de/content/dam/ise/de/documents/publications/studies/Photovoltaics-Report.pdf>

- [20] M. A. Green, E. D. Dunlop, J. Hohl-Ebinger, M. Yoshita, N. Kopidakis, and X. Hao, “Solar cell efficiency tables (version 59),” *Progress in Photovoltaics: Research and Applications*, vol. 30, no. 1, pp. 3–12, 2022. [Online]. Available: <https://doi.org/10.1002/pip.3506>
- [21] International Technology Roadmap for Photovoltaic (ITRPV), 2021 Results, 13th edition, March 2022. [Online]. Available: <https://www.vdma.org/international-technology-roadmap-photovoltaic>
- [22] G. Dingemans and W. M. M. Kessels, “Status and prospects of Al₂O₃-based surface passivation schemes for silicon solar cells,” *Journal of Vacuum Science & Technology A*, vol. 30, no. 4, 2012. [Online]. Available: <https://doi.org/10.1116/1.4728205>
- [23] B. Hoex, J. Schmidt, R. Bock, P. P. Altermatt, M. C. M. van de Sanden and W. M. M. Kessels, “Excellent passivation of highly doped p-type si surfaces by the negative-charge-dielectric Al₂O₃,” *Applied Physics Letters*, vol. 91, no. 11, 2007. [Online]. Available: <https://doi.org/10.1063/1.2784168>
- [24] S. Duttagupta, F. Lin, K. D. Shetty, A. G. Aberle, and B. Hoex, “Excellent boron emitter passivation for high-efficiency Si wafer solar cells using AlO_x/SiN_x dielectric stacks deposited in an industrial inline plasma reactor,” *Progress in Photovoltaics: Research and Applications*, vol. 21, no. 4, pp. 760–764, 2013. [Online]. Available: <https://doi.org/10.1002/pip.1259>
- [25] F. Werner, B. Veith, D. Zielke, L. Kuhnemund, C. Tegenkamp, M. Seibt, R. Brendel, and J. Schmidt, “Electronic and chemical properties of the c-Si/Al₂O₃ interface,” *Journal of Applied Physics*, vol. 109, no. 11, 2011. [Online]. Available: <https://doi.org/10.1063/1.3587227>
- [26] K. Jaeger and R. Hezel, “A novel thin silicon solar cell with Al₂O₃ as surface passivation,” in: *18th IEEE Photovoltaic Specialists Conference*, 1985, pp. 1752–1753.
- [27] R. Hezel and K. Jaeger, “Low-temperature surface passivation of silicon for solar cells,” *Journal of the Electrochemical Society*, vol. 136, no. 2, pp. 518–523, 1989. [Online]. Available: <https://doi.org/10.1149/1.2096673>
- [28] G. Agostinelli, P. Vitanov, Z. Alexieva, A. Harizanova, H. Dekkers, S. De Wolf, and G. Beaucarne, “Surface passivation of silicon by means of negative charge

- dielectrics,” in: *19th European Photovoltaic Solar Energy Conference*, 2004, pp. 132–134. [Online]. Available: https://www.researchgate.net/publication/266851024_Surface_passivation_of_silicon_by_means_of_negative_charge_dielectric
- [29] G. Agostinelli, A. Delabie, P. Vitanov, Z. Alexieva, H. F. W. Dekkers, S. De Wolf and G. Beaucarne, “Very low surface recombination velocities on p-type silicon wafers passivated with a dielectric with fixed negative charge,” *Solar Energy Materials and Solar Cells*, vol. 90, no. 18–19, pp. 3438–3443, 2006. [Online]. Available: <https://doi.org/10.1016/j.solmat.2006.04.014>
- [30] B. Hoex, S. B. S. Heil, E. Langereis, M. C. M. van de Sanden, and W. M. M. Kessels, “Ultralow surface recombination of c-si substrates passivated by plasma-assisted atomic layer deposited Al₂O₃,” *Applied Physics Letters*, vol. 89, no. 4, 2006. [Online]. Available: <https://doi.org/10.1063/1.2240736>
- [31] R. L. Puurunen, “Surface chemistry of atomic layer deposition: A case study for the trimethylaluminum/water process,” *Journal of Applied Physics*, vol. 97, no. 12, 2005. [Online]. Available: <https://doi.org/10.1063/1.1940727>
- [32] K. Kumar, R. S. Rao, O. Kaiwartya, M. S. Kaiser, and S. Padmanaban (Eds.), *Sustainable Developments by Artificial Intelligence and Machine Learning for Renewable Energies*, Elsevier, 2022. [Online]. Available: <https://doi.org/10.1016/C2020-0-04074-0>
- [33] H. Huang, J. Lv, Y. Bao, R. Xuan, S. Sun, S. Sneek, S. Li, C. Modanese, H. Savin, A. Wang, and J. Zhao, “20.8% industrial PERC solar cell: ALD Al₂O₃ rear surface passivation, efficiency loss mechanisms analysis and roadmap to 24%,” *Solar Energy Materials and Solar Cells*, vol. 161, pp.14–30, 2017. [Online]. Available: <https://doi.org/10.1016/j.solmat.2016.11.018>
- [34] A. Reinders, P. Verlinden, W. V. Sark, and A. Freundlich (Eds.), *Photovoltaic Solar Energy: From Fundamentals to Applications*, John Wiley & Sons, 2017. [Online]. Available: <https://doi.org/10.1002/9781118927496>
- [35] T. Mueller, *Heterojunction Solar Cells (a-Si/c-Si): Investigations on PECV Deposited Hydrogenated Silicon Alloys for use as High-Quality Surface Passivation and Emitter/BSF*, Logos Verlag Berlin GmbH, 2009. [Online]. Available: <https://books.google.co.in/books?id=Bmkifg2HKeUC>

- [36] S. Rein, Lifetime spectroscopy: A Method of Defect Characterization in Silicon for Photovoltaic Applications, Springer, 2005. [Online]. Available: <https://doi.org/10.1007/3-540-27922-9>
- [37] M. A. Green, Solar Cells: Operating Principles, Technology and System Applications, Prentice-Hall, 1982.
- [38] S. S. Li, Semiconductor Physical Electronics, Springer New York, 2006. [Online]. Available: <https://doi.org/10.1007/0-387-37766-2>
- [39] W. Shockley and W. T. Read, “Statistics of the Recombinations of Holes and Electrons,” *Physical Review*, vol. 87, no. 5, pp. 835–842, 1952. [Online]. Available: <https://link.aps.org/doi/10.1103/PhysRev.87.835>
- [40] R. N. Hall, “Electron-Hole Recombination in Germanium,” *Physical Review*, vol. 87, no. 2, pp. 387–387, 1952. [Online]. Available: <https://link.aps.org/doi/10.1103/PhysRev.87.387>
- [41] K. R. McIntosh, P. P. Altermatt, T. J. Ratcliff, K. C. Fong, L. E. Black, S. C. Baker-Finch, and M. D. Abbott, “An Examination of Three Common Assumptions Used to Simulate Recombination in Heavily Doped Silicon,” in: *28th European Photovoltaic Solar Energy Conference and Exhibition*, 2013, pp. 1672–1679. [Online]. Available: <https://www.eupvsec-proceedings.com/proceedings?paper=26301>
- [42] R. Muller, Ion Implantation for High-Efficiency Silicon Solar Cells, Fraunhofer Verlag, 2017. [Online]. Available: https://www.google.co.in/books/edition/Ion_Implantation_for_High_Efficiency_Si/ljIDQAAQBAJ?hl=en&gbpv=0
- [43] D. E. Kane and R. M. Swanson, “Measurement of the emitter saturation current by a contactless photoconductivity decay method (silicon solar cells),” in: *18th IEEE Photovoltaic Specialists Conference*, 1985, pp. 578–583.
- [44] M. J. Kerr, Surface emitter and bulk recombination in silicon and development of silicon nitride passivated solar cells, Ph.D thesis, Australian National University, 2002. [Online]. Available: <https://openresearch-repository.anu.edu.au/bitstream/1885/47459/6/02whole.pdf>
- [45] F. A. Lindholm and C. T. Sah, “Normal modes of semiconductor p-n-junction devices for material-parameter determination,” *Journal of Applied Physics*, vol.

- 47, no. 9, pp. 4203–4205, 1976. [Online]. Available: <https://doi.org/10.1063/1.323290>
- [46] A. Neugroschel, F. A. Lindholm, and C. Sah, “A method for determining the emitter and base lifetimes in pn junction diodes,” *IEEE Transactions on Electron Devices*, vol. 24, no. 6, pp. 662–671, 1977. [Online]. Available: <https://ieeexplore.ieee.org/stamp/stamp.jsp?tp=&arnumber=1478992&tag=1>
- [47] S. Jain and R. Muralidharan, “Effect of emitter recombinations on the open circuit voltage decay of a junction diode,” *Solid-State Electronics*, vol. 24, no. 12, pp. 1147–1154, 1981. [Online]. Available: [https://doi.org/10.1016/0038-1101\(81\)90183-0](https://doi.org/10.1016/0038-1101(81)90183-0)
- [48] C. Reichel, F. Granek, J. Benick, O. Schultz-Wittmann, and S. Glunz, “Comparison of emitter saturation current densities determined by injection-dependent lifetime spectroscopy in high and low injection regimes,” *Progress in Photovoltaics: Research and Applications*, vol. 20, no. 1, pp. 21–30, 2012. [Online]. Available: <https://doi.org/10.1002/pip.942>
- [49] B. E. Deal, D. W. Hess, J. D. Plummer, and C. P. Ho, “Kinetics of the Thermal Oxidation of Silicon in O₂/H₂O and O₂/Cl₂ Mixtures,” *Journal of The Electrochemical Society*, vol. 125, no.2, 1978. [Online]. Available: <https://doi.org/10.1149/1.2131442>
- [50] E. H. Nicollian and J. R. Brews, *MOS (Metal Oxide Semiconductor) Physics and Technology*, Wiley, 2002.
- [51] B. E. Deal and A. S. Grove, “General Relationship for the Thermal Oxidation of Silicon,” *Journal of Applied Physics*, vol. 36, no. 12, pp. 3770–3778, 2004. [Online]. Available: <https://doi.org/10.1063/1.1713945>
- [52] S. W. Glunz and F. Feldmann, “SiO₂ surface passivation layers—a key technology for silicon solar cells,” *Solar Energy Materials and Solar Cells*, vol. 185, pp. 260–269, 2018. [Online]. Available: <https://doi.org/10.1016/j.solmat.2018.04.029>
- [53] G. Declerck, R. Van Overstraeten, and G. Broux, “Measurement of low densities of surface states at Si-SiO₂-interface,” *Solid-State Electronics*, vol. 6, no. 12, pp. 1451–1460, 1973. [Online]. Available: [https://doi.org/10.1016/0038-1101\(73\)90062-2](https://doi.org/10.1016/0038-1101(73)90062-2)
- [54] B. E. Deal, M. Sklar, A. S. Grove, and E. H. Snow, “Characteristics of the Surface-State Charge (Q_{ss}) of Thermally Oxidized Silicon,” *Journal of the*

- Electrochemical Society*, vol. 114, no. 3, pp. 266–274, 1967. [Online]. Available: <https://doi.org/10.1149/1.2426565>
- [55] X. Wang and Z. M. Wang (Eds.), *High-Efficiency Solar Cells: Physics, Materials, and Devices*, Springer, 2014. [Online]. Available: <https://doi.org/10.1007/978-3-319-01988-8>
- [56] M. J. Kerr and A. Cuevas, “Very low bulk and surface recombination in oxidized silicon wafers,” *Semiconductor Science and Technology*, vol. 17, no. 1, 2002. [Online]. Available: <https://doi.org/10.1088/0268-1242/17/1/306>
- [57] G. Dingemans, M. M. Mandoc, S. Bordihn, M. C. M. van de Sanden, and W. M. M. Kessels, “Effective passivation of Si surfaces by plasma deposited SiO_x/a-SiN_x:H stacks,” *Applied Physics Letters*, vol. 98, no. 22, 2011. [Online]. Available: <https://doi.org/10.1063/1.3595940>
- [58] J. Bhajipale and A. Kottantharayil, “Passivation of n- and p-Type Silicon Surfaces With Spray-Coated Sol-Gel Silicon Oxide Thin Film,” *IEEE Transactions on Electron Devices*, vol. 67, no. 11, pp. 5045–5052, 2020. [Online]. Available: <https://doi.org/10.1109/TED.2020.3025981>
- [59] V. D. Mihailetchia, Y. Komatsu, and L. J. Geerligs, “Nitric acid pretreatment for the passivation of boron emitters for n-type base silicon solar cells,” *Applied Physics Letters*, vol. 92, no. 6, 2008. [Online]. Available: <https://doi.org/10.1063/1.2870202>
- [60] A. R. Burgers, L. J. Geerligs, A. J. Carr, A. Gutjahr, D. S. Saynova, L. Li, X. Zhuo, W. Hongfang, A. Haijiao, H. Hu, P. R. Venema, and A. H. G. Vlooswijk, “19.5% Efficient n-Type Si Solar Cells Made in Production,” in: *26th European Photovoltaic Solar Energy Conference and Exhibition*, 2011, pp. 1144–1147. [Online]. Available: <https://www.eupvsec-proceedings.com/proceedings?paper=12903>
- [61] F. Feldmann, M. Bivour, C. Reichel, H. Steinkemper, M. Hermle, and S. W. Glunz, “Tunnel oxide passivated contacts as an alternative to partial rear contacts,” *Solar Energy Materials and Solar Cells*, vol. 131, pp. 46–50, 2014. [Online]. Available: <https://doi.org/10.1016/j.solmat.2014.06.015>
- [62] N. E. Grant and K. R. McIntosh, “Silicon surface passivation by anodic oxidation annealed at 400 °C,” *ECS Journal of Solid State Science and Technology*, vol. 3, 2013. [Online]. Available: <https://doi.org/10.1149/2.009402jss>

- [63] S. Bordihn, P. Engelhart, V. Mertens, G. Kesser, D. Kohn, G. Dingemans, M. M. Mandoc, J. W. Muller, and W. Kessels, "High surface passivation quality and thermal stability of ALD Al₂O₃ on wet chemical grown ultra-thin SiO₂ on silicon," *Energy Procedia*, vol. 8, pp. 654–659, 2011. [Online]. Available: <https://doi.org/10.1016/j.egypro.2011.06.197>
- [64] H. Liu, Y. Wang, L. Dong, H. Wang, and Z. Zhang, "Improved Al₂O₃/SiN_x and SiO₂/SiN_x stack passivation layer structure PERC sc-silicon solar cells on mass production line," *International Journal of Energy Research*, vol. 45, no. 4, 2020. [Online]. Available: <https://doi.org/10.1002/er.6201>
- [65] A. G. Aberle, "Overview on SiN surface passivation of crystalline silicon solar cells," *Solar Energy Materials and Solar Cells*, vol. 65, no. 1–4, pp. 239–248, 2001. [Online]. Available: [https://doi.org/10.1016/S0927-0248\(00\)00099-4](https://doi.org/10.1016/S0927-0248(00)00099-4)
- [66] J. R. Elmiger and M. Kunst, "Investigation of charge carrier injection in silicon nitride/silicon junctions," *Applied Physics Letters*, vol. 69, no. 4, 1996. [Online]. Available: <https://doi.org/10.1063/1.117772>
- [67] H. P. Zhou, D. Y. Wei, L. X. Xu, Y. N. Guo, S. Q. Xiao, S. Y. Huang, and S. Xu, "Low temperature SiN_x:H films deposited by inductively coupled plasma for solar cell applications," *Applied Surface Science*, vol. 264, pp. 21–26, 2013. [Online]. Available: <https://doi.org/10.1016/j.apsusc.2012.09.050>
- [68] S. Dauwe, Low-Temperature Surface Passivation of Crystalline Silicon and its Application to the Rear Side of Solar Cells, Ph.D thesis, University of Hannover, 2004. [Online]. Available: <https://www.repo.uni-hannover.de/bitstream/handle/123456789/6379/380801663.pdf?sequence=1>
- [69] J. F. Lelievrea, E. Fourmonda, A. Kaminskia, O. Palaisb, D. Ballutaudc, and M. Lemitia, "Study of the composition of hydrogenated silicon nitride SiN_x:H for efficient surface and bulk passivation of silicon," *Solar Energy Materials and Solar Cells*, vol. 93, no. 8, pp. 1281–1289, 2009. [Online]. Available: <https://doi.org/10.1016/j.solmat.2009.01.023>
- [70] T. Lauinger, J. Schmidt, A. G. Aberle, and R. Hezel, "Record low surface recombination velocities on 1 Ω.cm p-silicon using remote plasma silicon nitride passivation," *Applied Physics Letters*, vol. 68, no. 9, pp. 1232–1234, 1996. [Online]. Available: <https://doi.org/10.1063/1.115936>

- [71] W. L. F. Chen, PECVD Silicon Nitride for n-type Silicon Solar Cells, Ph.D thesis, University of New South Wales, 2008. [Online]. Available: <https://unsworks.unsw.edu.au/fapi/datastream/unsworks:4044/SOURCE01?view=true>
- [72] A. Richter, S. W. Glunz, F. Werner, J. Schmidt, and A. Cuevas, “Improved quantitative description of Auger recombination in crystalline silicon,” *Physical Review B*, vol. 86, no. 16, 2012. [Online]. Available: <https://doi.org/10.1103/PhysRevB.86.165202>
- [73] C. H. Hsu, Y. S. Cho, W. Y. Wu, S. Y. Lien, X. Y. Zhang, W. Z. Zhu, S. Zhang, and S. Y. Chen, “Enhanced Si passivation and PERC solar cell efficiency by atomic layer deposited aluminum oxide with two-step post annealing,” *Nanoscale Research Letters*, vol. 14, no. 1, pp. 1–10, 2019. [Online]. Available: <https://doi.org/10.1186/s11671-019-2969-z>
- [74] F. Ye, Y. Li, X. Jia, H. Guo, X. Wang, J. Ding, N. Yuan, and Z. Feng, “Optimization of phosphorus dopant profile of industrial p-type mono PERC solar cells,” *Solar Energy Materials and Solar Cells*, vol. 190, pp. 30–36, 2019. [Online]. Available: <https://doi.org/10.1016/j.solmat.2018.10.002>
- [75] J. S. Chiu, Y. M. Zhao, S. Zhang, and D. S. Wu, “The role of laser ablated backside contact pattern in efficiency improvement of mono crystalline silicon PERC solar cells,” *Solar Energy*, vol. 196, pp. 462–467, 2020. [Online]. Available: <https://doi.org/10.1016/j.solener.2019.12.044>
- [76] P. Zheng, J. Xu, H. Sun, F. Zhang, Y. Guo, H. Pan, K. S. Chan, J. Jin, H. Wang, W. Chen, X. Zhang, and H. Jin, “21.63% industrial screen-printed multicrystalline Si solar cell,” *Physica Status Solidi (RRL)–Rapid Research Letters*, vol. 13, no. 3, 2017. [Online]. Available: <https://doi.org/10.1002/pssr.201600453>
- [77] R. Chen, H. Tong, H. Zhu, C. Ding, H. Li, D. Chen, B. Hallam, C. M. Chong, S. Wenham, and A. Ciesla, “23.83% efficient mono-PERC incorporating advanced hydrogenation,” *Progress in Photovoltaics: Research and Applications*, vol. 28, no. 12, pp. 1239–1247, 2020. [Online]. Available: <https://doi.org/10.1002/pip.3243>
- [78] M. Schaper, J. Schmidt, H. Plagwitz, and R. Brendel, “20.1%-efficient crystalline silicon solar cell with amorphous silicon rear-surface passivation,” *Progress in Photovoltaics: Research and Applications*, vol. 13, no. 5, pp. 381–386, 2005. [Online]. Available: <https://doi.org/10.1002/pip.641>

- [79] S. Dauwe, J. Schmidt, and R. Hezel, “Very low surface recombination velocities on p- and n-type silicon wafers passivated with hydrogenated amorphous silicon films,” in: *29th IEEE Photovoltaic Specialists Conference*, 2002, pp. 1246–1249. [Online]. Available: <https://doi.org/10.1109/PVSC.2002.1190834>
- [80] W. G. J. H. M. Sark, L. Korte, and F. Roca (Eds.), *Physics and Technology of Amorphous-Crystalline Heterostructure Silicon Solar Cells*, Springer, 2012. [Online]. Available: <https://link.springer.com/book/10.1007/978-3-642-22275-7>
- [81] X. Garros, G. Reimbold, J. Cluzel, D. Munoz, and P. J. Ribeyron, “Interface states characterization in heterojunction solar cells from CV–GV measurements and modeling,” *Microelectronic Engineering*, vol. 88, no. 7, pp. 1247–1250, 2011. [Online]. Available: <https://doi.org/10.1016/j.mee.2011.03.113>
- [82] G. P. Willeke and E. R. Weber (Eds.), *Advances in Photovoltaics: Part 3*, vol. 90, pp. 2–146, 2014. [Online]. Available: <https://doi.org/10.1016/B978-0-12-388417-6.00003-9>
- [83] K. Yoshikawa, W. Yoshida, T. Irie, H. Kawasaki, K. Konishi, H. Ishibashi, T. Asatani, D. Adachi, M. Kanematsu, H. Uzu, and K. Yamamoto, “Exceeding conversion efficiency of 26% by heterojunction interdigitated back contact solar cell with thin film Si technology,” *Solar Energy Materials and Solar Cells*, vol. 173, pp. 37–42, 2017. [Online]. Available: <https://doi.org/10.1016/j.solmat.2017.06.024>
- [84] K. Yamamoto, K. Yoshikawa, H. Uzu, and D. Adachi, “High-efficiency heterojunction crystalline Si solar cells,” *Japanese Journal of Applied Physics*, vol. 57, 2018. [Online]. Available: <https://doi.org/10.7567/JJAP.57.08RB20>
- [85] J. Benick, A. Richter, M. Hermle, and S. W. Glunz, “Thermal stability of the Al₂O₃ passivation on p-type silicon surfaces for solar cell applications,” *Physica Status Solidi (RRL)–Rapid Research Letters*, vol. 3, no. 7–8, pp. 233–235, 2009. [Online]. Available: <https://doi.org/10.1002/pssr.200903209>
- [86] P. Saint-Cast, D. Kania, M. Hofmann, J. Benick, J. Rentsch, and R. Preu, “Very low surface recombination velocity on p-type c-Si by high-rate plasma-deposited aluminum oxide,” *Applied Physics Letters*, vol. 95, no. 15, 2009. [Online]. Available: <https://doi.org/10.1063/1.3250157>
- [87] B. Hoex, J. Schmidt, P. Pohl, M. C. M. van de Sanden, and W. M. M. Kessels, “Silicon surface passivation by atomic layer deposited Al₂O₃,” *Journal of Applied*

- Physics*, vol. 104, no. 4, 2008. [Online]. Available: <https://doi.org/10.1063/1.2963707>
- [88] S. Duttagupta, F. Ma, S. F. Lin, T. Mueller, A. G. Aberle, and B. Hoex, "Progress in Surface Passivation of Heavily Doped n-Type and p-Type Silicon by Plasma-Deposited $\text{AlO}_x/\text{SiN}_x$ Dielectric Stacks," *IEEE Journal of Photovoltaics*, vol. 3, no. 4, pp. 1163–1169, 2013. [Online]. Available: <https://doi.org/10.1109/JPHOTOV.2013.2270350>
- [89] B. Hoex, M. C. M. van de Sanden, J. Schmidt, R. Brendel, and W. M. M. Kessels, "Surface passivation of phosphorus-diffused n^+ -type emitters by plasma-assisted atomic-layer deposited Al_2O_3 ," *Physica Status Solidi (RRL)–Rapid Research Letters*, vol. 6, no. 1, pp. 4–6, 2012. [Online]. Available: <https://doi.org/10.1002/pssr.201105445>
- [90] S. Bordihn, G. Dingemans, V. Mertens, J. W. Muller, and W. M. M. Kessels, "Passivation of n^+ -Type Si Surfaces by Low Temperature Processed $\text{SiO}_2/\text{Al}_2\text{O}_3$ Stacks," *IEEE Journal of Photovoltaics*, vol. 3, no. 3, pp. 925–929, 2013. [Online]. Available: <https://doi.org/10.1109/JPHOTOV.2013.2248415>
- [91] B. W. H. van de Loo, H. C. M. Knoop, G. Dingemans, G. J. M. Janssen, M. W. P. E. Lamers, I. G. Romijn, A. W. Weeber, and W. M. M. Kessels, "'Zero-charge' $\text{SiO}_2/\text{Al}_2\text{O}_3$ stacks for the simultaneous passivation of n^+ and p^+ doped silicon surfaces by atomic layer deposition," *Solar Energy Materials and Solar Cells*, vol. 143, pp. 450–456, 2015. [Online]. Available: <https://doi.org/10.1016/j.solmat.2015.07.040>
- [92] P. I. Raisanen, M. Ritala, and M. Leskela, "Atomic layer deposition of Al_2O_3 films using AlCl_3 and $\text{Al}(\text{O}^i\text{Pr})_3$ as precursors," *Journal of Materials Chemistry*, vol. 12, no. 5, pp. 1415–1418, 2002. [Online]. Available: <https://doi.org/10.1039/B201385C>
- [93] Y. Min, Y. J. Cho, and C. S. Hwang, "Atomic Layer Deposition of Al_2O_3 Thin Films from a 1-Methoxy-2-methyl-2-propoxide Complex of Aluminum and Water," *Chemistry of Materials*, vol. 17, no. 3, pp. 626–631, 2005. [Online]. Available: <https://pubs.acs.org/doi/10.1021/cm048649g>
- [94] L. Hiltunen, H. Kattelus, M. Leskela, M. Makela, L. Niinisto, E. Nykanen, P. Soininen, and M. Tiittad, "Growth and characterization of aluminium oxide thin films deposited from various source materials by atomic layer epitaxy and

- chemical vapor deposition processes,” *Materials Chemistry and Physics*, vol. 28, no. 4, pp. 379–388, 1991. [Online]. Available: [https://doi.org/10.1016/0254-0584\(91\)90073-4](https://doi.org/10.1016/0254-0584(91)90073-4)
- [95] M. Tiitta, E. Nykanen, P. Soininen, L. Niinisto, M. Leskela, and R. Lappalainen, “Preparation and characterization of phosphorus-doped aluminum oxide thin films,” *Materials Research Bulletin*, vol. 33, no. 9, pp. 1315–1323, 1998. [Online]. Available: [https://doi.org/10.1016/S0025-5408\(98\)00119-6](https://doi.org/10.1016/S0025-5408(98)00119-6)
- [96] H. Wang, Y. Liu, H. Liu, Z. Chen, P. Xiong, X. Xu, F. Chen, K. Li, and Duan Y, “Effect of Various Oxidants on Reaction Mechanisms, Self-Limiting Natures and Structural Characteristics of Al₂O₃ Films Grown by Atomic Layer Deposition,” *Advanced Materials Interfaces*, vol. 5, no. 14, 2018. [Online]. Available: <https://doi.org/10.1002/admi.201701248>
- [97] T. F. Kuech (Ed.), *Handbook of Crystal Growth: Thin Films and Epitaxy*, Elsevier, 2015. [Online]. Available: <https://doi.org/10.1016/C2013-0-09792-7>
- [98] J. Bachmann (Ed.), *Atomic Layer Deposition in Energy Conversion Applications*, John Wiley & Sons, 2017. [Online]. Available: <https://onlinelibrary.wiley.com/doi/book/10.1002/9783527694822>
- [99] M. Groner, J. Elam, F. Fabreguette, and S. M. George, “Electrical characterization of thin Al₂O₃ films grown by atomic layer deposition on silicon and various metal substrates,” *Thin Solid Films*, vol. 413, no. 1–2, pp. 186–197, 2002. [Online]. Available: [https://doi.org/10.1016/S0040-6090\(02\)00438-8](https://doi.org/10.1016/S0040-6090(02)00438-8)
- [100] J. Schmidt, A. Merkle, R. Brendel, B. Hoex, M. C. M. van de Sanden, and W. M. M. Kessels, “Surface passivation of high-efficiency silicon solar cells by atomic-layer-deposited Al₂O₃,” *Progress in Photovoltaics: Research and Applications*, vol. 16, no. 6, pp. 461–466, 2008. [Online]. Available: <https://doi.org/10.1002/pip.823>
- [101] G. Dingemans, P. Engelhart, R. Seguin, M. M. Mandoc, M. C. M. van de Sanden, and W. M. M. Kessels, “Comparison between aluminum oxide surface passivation films deposited with thermal ALD, plasma ALD and PECVD,” in: *35th IEEE Photovoltaic Specialists Conference*, 2010, pp. 003118–003121. [Online]. Available: <https://doi.org/10.1109/PVSC.2010.5614508>

- [102] S. M. George, "Atomic layer deposition: an overview," *Chemical Reviews*, vol. 110, pp. 111–131, 2010. [Online]. Available: <https://pubs.acs.org/doi/pdf/10.1021/cr900056b>
- [103] F. Werner, B. Veith, V. Tiba, P. Poodt, F. Roozeboom, R. Brendel, and J. Schmidt, "Very low surface recombination velocities on p- and n-type c-Si by ultrafast spatial atomic layer deposition of aluminum oxide," *Applied Physics Letters*, vol. 97, no. 16, 2010. [Online]. Available: <https://doi.org/10.1063/1.3505311>
- [104] G. Dingemans, M. C. M. van de Sanden, and W. M. M. Kessels, "Influence of the Deposition Temperature on the c-Si Surface Passivation by Al₂O₃ Films Synthesized by ALD and PECVD," *Electrochemical and Solid-State Letters*, vol. 13, no. 3, pp. H76–H79, 2010. [Online]. Available: <https://doi.org/10.1149/1.3276040>
- [105] G. Dingemans, P. Engelhart, R. Seguin, F. Einsele, B. Hoex, M. C. M. van de Sanden, and W. M. M. Kessels, "Stability of Al₂O₃ and Al₂O₃/a-SiN_x:H stacks for surface passivation of crystalline silicon," *Journal of Applied Physics*, vol. 106, no. 11, 2009. [Online]. Available: <https://doi.org/10.1063/1.3264572>
- [106] B. Liao, R. Stangl, F. Ma, Z. Hameiri, T. Mueller, D. Chi, A. G. Aberle, C. S. Bhatia, and B. Hoex, "Deposition temperature independent excellent passivation of highly boron doped silicon emitters by thermal atomic layer deposited Al₂O₃," *Journal of Applied Physics*, vol. 114, no. 9, 2013. [Online]. Available: <https://doi.org/10.1063/1.4819970>
- [107] B. Hoex, J. J. H. Gielis, M. C. M. van de Sanden, and W. M. M. Kessels, "On the c-Si surface passivation mechanism by the negative-charge-dielectric Al₂O₃," *Journal of Applied Physics*, vol. 104, no. 11, 2008. [Online]. Available: <https://doi.org/10.1063/1.3021091>
- [108] J. Benick, A. Richter, T. T. A. Li, N. E. Grant, K. R. McIntosh, Y. Ren, K. J. Weber, M. Hermle, and S. W. Glunz, "Effect of a post-deposition anneal on Al₂O₃/Si interface properties," in: *35th IEEE Photovoltaic Specialists Conference*, 2010, pp. 000891–000896. [Online]. Available: <https://doi.org/10.1109/PVSC.2010.5614148>
- [109] J. L. Van Hemmen, S. B. S. Heil, J. H. Klootwijk, F. Roozeboom, C. J. Hodson, M. C. M. van de Sanden, and W. M. M. Kessels, "Plasma and thermal ALD of Al₂O₃ in a commercial 200 mm ALD reactor," *Journal of the Electrochemical*

- Society*, vol. 154, no. 7, pp. G165–G169, 2007. [Online]. Available: <https://doi.org/10.1149/1.2737629>
- [110] P. Singh, R. K. Jha, R. K. Singh, and B. R. Singh, “Preparation and characterization of Al₂O₃ film deposited by RF sputtering and plasma enhanced atomic layer deposition,” *Journal of Vacuum Science & Technology B*, vol. 36, no. 4, 2018. [Online]. Available: <https://doi.org/10.1116/1.5023591>
- [111] P. Poodt, A. Lankhorst, F. Roozeboom, K. Spee, D. Maas, and A. Vermeer, “High-Speed Spatial Atomic-Layer Deposition of Aluminum Oxide Layers for Solar Cell Passivation,” *Advanced Materials*, vol. 22, no. 32, pp. 3564–3567, 2010. [Online]. Available: <https://doi.org/10.1002/adma.201000766>
- [112] E. H. A. Granneman, V. I. Kuznetsov, and P. Vermont, “Spatial ALD, Deposition of Al₂O₃ Films at Throughputs Exceeding 3000 Wafers per Hour,” *ECS Transactions*, vol. 61, no. 3, pp. 3–16, 2014. [Online]. Available: <https://doi.org/10.1149/06103.0003ecst>
- [113] E. Lohmuller, J. Greulich, P. Saint-Cast, S. Lohmuller, S. Schmidt, U. Belledin, T. Fellmeth, S. Mack, G. Emanuel, K. Krieg, M. Zimmer, R. Kunert, F. Zobel, M. Linse, J. Horzel, M. Meßmer, A. Wolf, and R. Preu, “Front side optimization on boron-and gallium-doped Cz-Si PERC solar cells exceeding 22% conversion efficiency,” in: *37th European Photovoltaic Solar Energy Conference and Exhibition*, 2020, pp. 516–520. [Online]. Available: <https://doi.org/10.4229/EUPVSEC20202020-2DV.3.19>
- [114] G. Dingemans, Nanolayer surface passivation schemes for silicon solar cells, Ph.D thesis, Eindhoven University of Technology, 2011. [Online]. Available: <https://doi.org/10.6100/IR719798>
- [115] B. A. Veith-Wolf, Crystalline silicon surface passivation using aluminum oxide: fundamental understanding and application to solar cells, Ph.D thesis, Leibniz University Hannover, 2018. [Online]. Available: <https://doi.org/10.15488/3685>
- [116] C. Cibert, H. Hidalgo, C. Champeaux, P. Tristant, C. Tixier, J. Desmaison, and A. Catherinot, “Properties of aluminum oxide thin films deposited by pulsed laser deposition and plasma enhanced chemical vapor deposition,” *Thin Solid Films*, vol. 516, no. 6, pp. 1290–1296, 2008. [Online]. Available: <https://doi.org/10.1016/j.tsf.2007.05.064>

- [117] P. Saint-Cast, D. Kania, R. Heller, S. Kuehnhold, M. Hofmann, J. Rentsch, and R. Preu, “High-temperature stability of c-Si surface passivation by thick PECVD Al₂O₃ with and without hydrogenated capping layers,” *Applied Surface Science*, vol. 258, no. 21, pp. 8371–8376, 2012. [Online]. Available: <https://doi.org/10.1016/j.apsusc.2012.03.171>
- [118] K. Koski, J. Holsa, and P. Juliet, “Properties of aluminium oxide thin films deposited by reactive magnetron sputtering,” *Thin Solid Films*, vol. 339, no. 1–2, pp. 240–248, 1999. [Online]. Available: [https://doi.org/10.1016/S0040-6090\(98\)01232-2](https://doi.org/10.1016/S0040-6090(98)01232-2)
- [119] S. Miyajima, J. Irikawa, A. Yamada, and M. Konagai, “Hydrogenated Aluminium Oxide Films Deposited by Plasma Enhanced Chemical Vapor Deposition for Passivation of p-Type Crystalline Silicon,” in: *23rd European Photovoltaic Solar Energy Conference and Exhibition*, 2008, pp. 1029–1032. [Online]. <https://www.eupvsec-proceedings.com/proceedings?paper=2672>
- [120] P. Saint-Cast, J. Benick, D. Kania, L. Weiss, M. Hofmann, J. Rentsch, R. Preu, and S.W. Glunz, “High-Efficiency c-Si Solar Cells Passivated With ALD and PECVD Aluminum Oxide,” *IEEE Electron Device Letters*, vol. 31, no. 7, pp. 695–697, 2010. [Online]. Available: <https://doi.org/10.1109/LED.2010.2049190>
- [121] M. Hofmann, N. Kohn, F. Schwarz, S. Nolker, S. Kastl, R. Beckmann, R. Ferre, T. Pernau, D. Trogus, S. Kuhnhold, P. Saint-Cast, and J. Rentsch, “High-Power-Plasma PECVD of SiN_x and Al₂O₃ for Industrial Solar Cell Manufacturing,” in: *28th European Photovoltaic Solar Energy Conference and Exhibition*, 2013, pp. 1184–1187. [Online]. Available: <https://www.eupvsec-proceedings.com/proceedings?paper=25974>
- [122] A. Richter, J. Benick, F. Feldmann, A. Fell, M. Hermle, and S. W. Glunz, “n-Type Si solar cells with passivating electron contact: Identifying sources for efficiency limitations by wafer thickness and resistivity variation,” *Solar Energy Mater Solar Cells*, vol. 173, pp. 96–105, 2017. [Online]. Available: <https://doi.org/10.1016/j.solmat.2017.05.042>
- [123] J. D. Plummer, *Silicon VLSI Technology Fundamentals, Practice and Modeling*, Pearson Education, 2009. [Online]. Available: https://www.google.co.in/books/edition/Silicon_VLSI_Technology/U97p5pHY-h4C?hl=en&gbpv=0

- [124] R. V. R. Kotipalli, R. Delamare, F. Henry, J. Proost, and D. Flandre, “Thermal stability analysis of DC-sputtered Al₂O₃ films for surface passivation of c-Si solar cells,” in: *28th European Photovoltaic Solar Energy Conference and exhibition*, 2013, pp. 1278–1281. [Online]. Available: <https://doi.org/10.4229/28thEUPVSEC2013-2BV.2.22>
- [125] T. Li and A. Cuevas, “Effective surface passivation of crystalline silicon by rf sputtered aluminum oxide,” *Physica Status Solidi (RRL) – Rapid Research Letters*, vol. 3, no. 5, pp. 160–162, 2009. [Online]. Available: <https://doi.org/10.1002/pssr.200903140>
- [126] M. Bhaisare, A. Misra, and A. Kottantharayil, “Aluminum oxide deposited by pulsed-dc reactive sputtering for crystalline silicon surface passivation,” *IEEE Journal of Photovoltaics*, vol. 3, no. 3, pp. 930–935, 2013. [Online]. Available: <https://doi.org/10.1109/JPHOTOV.2013.2251057>
- [127] L. Tsu-Tsung, Surface Passivation of Crystalline Silicon by Sputtered Aluminium Oxide, Ph.D thesis, The Australian National University, 2010. [Online]. Available: <https://openresearch-repository.anu.edu.au/bitstream/1885/7369/2/02whole.pdf>
- [128] S. Banerjee and M. K. Das, “A review of Al₂O₃ as surface passivation material with relevant process technologies on c-Si solar cell,” *Optical and Quantum Electronics*, vol. 53, no. 60, 2021. [Online]. Available: <https://doi.org/10.1007/s11082-020-02689-8>
- [129] X. Zhang and A. Cuevas, “Plasma hydrogenated, reactively sputtered aluminium oxide for silicon surface passivation,” *Physica Status Solidi (RRL)–Rapid Research Letters*, vol. 7, no. 9, pp. 619–622, 2013. [Online]. Available: <https://doi.org/10.1002/pssr.201308027>
- [130] X. Zhang, A. Thomson, and A. Cuevas, “Silicon Surface Passivation by Sputtered Aluminium Oxide: Influence of Annealing Temperature and Ambient Gas,” *ECS Solid State Letters*, vol. 3, no. 11, pp. N37–N39, 2014. [Online]. Available: <https://doi.org/10.1149/2.0021412ssl>
- [131] J. Schmidt, F. Werner, B. Veith-Wolf, D. Zielke, R. Bock, V. Tiba, P. Poodt, F. Roozeboom, T.A. Li, A. Cuevas, and R. Brendel, “Industrially Relevant Al₂O₃ Deposition Techniques for the Surface Passivation of Si Solar Cells,” in: *25th European Photovoltaic Solar Energy Conference and Exhibition*, 2010, pp. 1130–1133. [Online]. Available: <https://doi.org/10.4229/25thEUPVSEC2010-2AO.1.6>

- [132] B. G. Segda, M. Jacquet, and J. P. Besse, “Elaboration characterization and dielectric properties study of amorphous alumina thin films deposited by r.f. magnetron sputtering,” *Vacuum*, vol. 62, no. 1, pp. 27–38, 2001. [Online]. Available: [https://doi.org/10.1016/S0042-207X\(01\)00114-2](https://doi.org/10.1016/S0042-207X(01)00114-2)
- [133] R. G. Frieser, “Phase changes in thin reactively sputtered alumina films,” *Journal of The Electrochemical Society*, vol. 113, no. 4, pp. 357–360, 1966. [Online]. Available: <https://doi.org/10.1149/1.2423960>
- [134] M. K. Olsson, K. Macak, U. Helmersson, and B. Hjorvarsson, “High rate reactive dc magnetron sputter deposition of Al₂O₃ films,” *Journal of Vacuum Science & Technology A*, vol. 16, no. 2, pp. 639–643, 1998. [Online]. Available: <https://doi.org/10.1116/1.581081>
- [135] H. Bartzsch, D. Gloß, B. Bocher, P. Franch, and K. Goddicke, “Properties of SiO₂ and Al₂O₃ films for electrical insulation applications deposited by reactive pulse magnetron sputtering,” *Surface and Coatings Technology*, vol. 174, pp. 774–778, 2003. [Online]. Available: [https://doi.org/10.1016/S0257-8972\(03\)00384-0](https://doi.org/10.1016/S0257-8972(03)00384-0)
- [136] Y. Zhao, Y. Qian, W. Yu, and Z. Chen, “Surface roughness of alumina films deposited by reactive r.f. sputtering,” *Thin Solid Films*, vol. 286, no. 1–2, pp. 45–48, 1996. [Online]. Available: [https://doi.org/10.1016/S0040-6090\(95\)08514-9](https://doi.org/10.1016/S0040-6090(95)08514-9)
- [137] R. S. Nowicki, “Properties of rf-sputtered Al₂O₃ films deposited by planar magnetron,” *Journal of Vacuum Science and Technology*, vol. 14, no. 1, pp. 127–133, 1977. [Online]. Available: <https://doi.org/10.1116/1.569103>
- [138] M. Bhisare, D. Sutar, A. Misra, and A. Kottantharayil, “Effect of power density on the passivation quality of pulsed — DC reactive sputtered Aluminum oxide on P-Type crystalline silicon,” in: *IEEE 39th Photovoltaic Specialists Conference (PVSC)*, 2013, pp. 1207–1211. [Online]. Available: <https://ieeexplore.ieee.org/abstract/document/6744357>
- [139] M. Bhisare, A. Misra, M. Waikar, and A. Kottantharayil, “High Quality Al₂O₃ Dielectric Films Deposited by Pulsed-DC Reactive Sputtering Technique for High-k Applications,” *Nanoscience and Nanotechnology Letters*, vol. 4, no. 6, pp. 645–650, 2012. [Online]. Available: <https://doi.org/10.1166/nnl.2012.1362>

- [140] P. Vitanov, A. Harizanova, T. Ivanova, M. Perego, G. Stokkan, and A. Ulyashin, “Effective surface passivation of Si surfaces by chemical deposition of $(\text{Al}_2\text{O}_3)_x(\text{B}_2\text{O}_3)_{1-x}$ thin layers,” *Physica Status Solidi (A)*, vol. 210, no. 4, pp. 701–706, 2013. [Online]. Available: <https://doi.org/10.1002/pssa.201200749>
- [141] S. Y. Lien, D. S. Wu, W. C. Yeh, and J. C. Liu, , “Tri-layer antireflection coatings ($\text{SiO}_2/\text{SiO}_2\text{--TiO}_2/\text{TiO}_2$) for silicon solar cells using a sol–gel technique,” *Solar Energy Materials and Solar Cells*, vol. 90, no. 16, pp. 2710–2719, 2006. [Online]. Available: <https://doi.org/10.1016/j.solmat.2006.04.001>
- [142] Uzum, H. Kanda, T. Noguchi, Y. Nakazawa, S. Taniwaki, Y. Hotta, Y. Haruyama, N. Shibayama, and S. Ito, “ $\text{H}_2\text{O}/\text{O}_2$ Vapor Annealing Effect on Spin Coating Alumina Thin Films for Passivation of Silicon Solar Cells,” *International Journal of Photoenergy*, 2019. [Online]. Available: <https://doi.org/10.1155/2019/4604932>
- [143] N. Balaji, C. Park, J. Raja, M. Ju, M. R. Venkatesan, H. Lee, and J. Yi, “Low Surface Recombination Velocity on P-Type Cz–Si Surface by Sol–Gel Deposition of Al_2O_3 Films for Solar Cell Applications,” *Journal of Nanoscience and Nanotechnology*, vol. 15, no. 7, pp. 5123–5128, 2015. [Online]. Available: <https://doi.org/10.1166/jnn.2015.9851>
- [144] P. Vitanov, X. Loozen, A. Harizanova, T. Ivanova, and G. Beaucarne, “A study of sol-gel deposited Al_2O_3 films as passivating coatings for solar cells application,” in: *23rd European Photovoltaic Solar Energy Conference and Exhibition*, 2008, pp. 1596–1599. [Online]. Available: <https://doi.org/10.4229/23rdEUPVSEC2008-2CV.5.5>
- [145] R. Watanabe, T. Koyama, and Y. Saito, “Evaluation of spin-coated alumina passivation layer for point-contacted rear electrode passivation of silicon solar cells,” *IEICE Transactions on Electronics*, vol. E100.C, no. 1, pp. 101–107, 2017. [Online]. Available: <https://doi.org/10.1587/transele.E100.C.101>
- [146] P. Vitanov, A. Harizanova, T. Ivanova, and T. Dimitrova, “Chemical deposition of Al_2O_3 thin films on Si substrates,” *Thin Solid Films*, vol. 517, no. 23, pp. 6327–6330, 2009. [Online]. Available: <https://doi.org/10.1016/j.tsf.2009.02.085>
- [147] R. Watanabe, M. Kawashima, and Y. Saito, “Film properties of alumina passivation layer for silicon solar cells prepared by spin-coating method,” *Thin*

- Solid Films*, vol. 590, pp. 98–102, 2015. [Online]. Available: <https://doi.org/10.1016/j.tsf.2015.07.044>
- [148] G. Agostinelli, J. Szlufcik, P. Vitanov, and A. Harizanova, Method for backside surface passivation of solar cells and solar cells with such passivation, U.S. Patent No: 7,659,475 B2, February 9, 2010. [Online]. Available: <https://patents.google.com/patent/US20050022863A1/en>
- [149] T. B. Daunis, G. Gutierrez-Heredia, O. Rodriguez-Lopez, J. Wang, W. E. Voit, and J. W. P. Hsu, “Solution-deposited Al₂O₃ dielectric towards fully-patterned thin film transistors on shape memory polymer,” in: *Proceeding of SPIE*, 2017, vol. 10105, pp. 101051Z-1–101051Z-8. [Online]. Available: <https://doi.org/10.1117/12.2250393>
- [150] T. Schneller, R. Waser, M. Kosec, and D. Payne (Eds.), *Chemical Solution Deposition of Functional Oxide Thin Films*, Springer, 2013. [Online]. Available: <https://doi.org/10.1007/978-3-211-99311-8>
- [151] Z. Cui and G. Korotcenkov (Eds.), *Solution Processed Metal Oxide Thin Films for Electronic Applications*, Elsevier, 2020. [Online]. Available: <https://doi.org/10.1016/C2017-0-02104-3>
- [152] S. Park, T. Kim, S. Yoon, C. W. Koh, H. Y. Woo, and H. J. Son, “Progress in Materials, Solution Processes, and Long-Term Stability for Large-Area Organic Photovoltaics,” *Advanced Materials*, vol. 32, no. 51, 2020. [Online]. Available: <https://doi.org/10.1002/adma.202002217>
- [153] K. Q. Lederer, S. R. Hornig, and R. Schuster, “Selected implications of photoresist processing in 300-mm manufacturing,” *Journal of Micro/Nanolithography, MEMS, and MOEMS*, Vol. 4, no. 1, 2005. [Online]. Available: <https://doi.org/10.1117/1.1856929>
- [154] N. Sahu, B. Parija, and S. Panigrahi, “Fundamental understanding and modeling of spin coating process: A review,” *Indian Journal of Physics*, vol. 83, no. 4, pp. 493–502, 2009. [Online]. Available: <https://doi.org/10.1007/s12648-009-0009-z>

- [155] R. Rajasekar, C. Moganapriya, and A. Mohankumar (Eds.), *Materials for Solar Energy Conversion: Materials, Methods and Applications*, Wiley, 2021. [Online]. Available: <https://doi.org/10.1002/9781119752202>
- [156] D. Perednis and L. J. Gauckler, “Thin film deposition using spray pyrolysis,” *Journal of Electroceramics*, vol. 14, no. 2, pp. 103–111, 2005. [Online]. Available: <https://doi.org/10.1007/s10832-005-0870-x>
- [157] M. Aguilar-Frutis, J. Guzman-Mendoza, T. Alejos, M. Garcia-Hipolito, and C. Falcony, “Aluminum oxide thin films deposited on silicon substrates from $\text{Al}(\text{NO}_3)_3$ and an organic solvent by spray pyrolysis,” *Physica Status Solidi (a)*, vol. 199, no. 2, pp. 227–232, 2003. [Online]. Available: <https://doi.org/10.1002/pssa.200306642>
- [158] G. Untila, T. Kost, A. Chebotareva, M. Zaks, A. Sitnikov, and O. Solodukha, “Pyrosol deposited AlO_x as surface passivation for Si solar cells,” in: *25th European Photovoltaic Solar Energy Conference and Exhibition*, 2010, pp. 2592–2595. [Online]. Available: <https://doi.org/10.4229/25theupvsec2010-2dv.1.53>
- [159] J. E. Hill and R. R. Chamberlin, Process for making conductive film, U.S. Patent No: 3,148,084, September 8, 1964. [Online]. Available: <https://patents.google.com/patent/US3148084A/en>
- [160] M. Sankir and N. D. Sankir (Eds.), *Printable solar cells*, John Wiley & Sons, 2017. [Online]. Available: https://www.google.co.in/books/edition/Printable_Solar_Cells/6tO1DgAAQBAJ?hl=en&gbpv=0
- [161] F. Ye, W. Deng, W. Guo, R. Liu, D. Chen, Y. Chen, Y. Yang, N. Yuan, J. Ding, Z. Feng, P. P. Altermatt, and P. J. Verlinden, “22.13% Efficient industrial p-type mono PERC solar cell,” in: *IEEE 43rd Photovoltaic Specialists Conference (PVSC)*, 2016, pp. 3360–3365. [Online]. Available: <https://doi.org/10.1109/PVSC.2016.7750289>
- [162] B. Veith, T. Dullweber, M. Siebert, C. Kranz, F. Werner, N. Harder, J. Schmidt, B. Roos, T. Dippell, and R. Brendel, “Comparison of ICP- AlO_x and ALD- Al_2O_3 Layers for the Rear Surface Passivation of C-Si Solar Cells,” *Energy Procedia*,

- vol. 27, pp. 379–384, 2012. [Online]. Available: <https://doi.org/10.1016/j.egypro.2012.07.080>
- [163] C. Girotto, B. P. Rand, J. Genoe, and P. Heremans, “Exploring spray coating as a deposition technique for the fabrication of solution-processed solar cells,” *Solar Energy Materials and Solar Cells*, vol. 93, no. 4, pp. 454–458, 2009. [Online]. Available: <https://doi.org/10.1016/j.solmat.2008.11.052>
- [164] J. Guzman-Mendoza, M. Garcia-Hipolito, M. Aguilar-Frutis, and C. Falcony-Guajardo, “Structural characteristics of Al₂O₃ thin films prepared by spray pyrolysis,” *Journal of Physics: Condensed Matter*, vol. 13, no. 50, 2001. [Online]. Available: <https://doi.org/10.1088/0953-8984/13/50/101>
- [165] K. S. Shamala, L. C. S. Murthy, M. C. Radhakrishna, and K. N. Rao, “Characterization of Al₂O₃ thin films prepared by spray pyrolysis method for humidity sensor,” *Sensors and Actuators A: Physical*, vol. 135, no. 2, pp. 552–557, 2007. [Online]. Available: <https://doi.org/10.1016/j.sna.2006.10.004>
- [166] M. Aguilar-Frutis, M. Garcia, and C. Falcony, “Optical and electrical properties of aluminum oxide films deposited by spray pyrolysis,” *Applied Physics Letters*, vol. 72, no. 14, pp. 1700–1702, 1998. [Online]. Available: <https://doi.org/10.1063/1.121156>
- [167] A. Ortiz and J. C. Alonso, “High quality-low temperature aluminum oxide films deposited by ultrasonic spray pyrolysis,” *Journal of Materials Science: Materials in Electronics*, vol. 13, no. 1, pp. 7–11, 2002. [Online]. Available: <https://doi.org/10.1023/A:1013134727665>
- [168] W. J. Shin, W. Huang, and M. Tao, “Spray-Deposited Al₂O₃ for Rear Passivation and Optical Trapping in Silicon Solar Cells,” *ECS Journal of Solid State Science and Technology*, vol. 8, no. 10, pp. N151–N157, 2019. [Online]. Available: <http://dx.doi.org/10.1149/2.0211910jss>
- [169] S. Bakhshi, N. Zin, K. O. Davis, M. Wilson, I. Kashkoush, and W. V. Schoenfeld, “Improving Silicon Surface Passivation with a Silicon Oxide Layer Grown via Ozonated Deionized Water,” in: *IEEE 44th Photovoltaic Specialist Conference (PVSC)*, 2017, pp. 322–325. [Online]. Available: <https://doi.org/10.1109/PVSC.2017.8366153>

- [170] S. Bakhshi, N. Zin, H. Ali, M. Wilson, D. Chanda, K. O. Davis, and W. V. Schoenfeld, "Simple and versatile UV-ozone oxide for silicon solar cell applications," *Solar Energy Materials and Solar Cells*, vol. 185, pp. 505–510, 2018. [Online]. Available: <https://doi.org/10.1016/j.solmat.2018.06.006>
- [171] J. Penaud, P. Jaffrennou, A. Rothschild, and B. Lombardet, "Impact of surface preparation prior to Al₂O₃ deposition for i-PERC cells," in: *38th IEEE Photovoltaic Specialists Conference*, pp. 001083–001088, 2012. [Online]. Available: <https://doi.org/10.1109/PVSC.2012.6317791>
- [172] A. Rothschild, J. Toman, J. Penaud, P. Jaffrennou, P. Choulat, E. Cornagliotti, M. Recamán Payo, B. J. Pawlak, J. Das, A. Uruena, S. Singh, and J. Horzel, "Impact of Surface Preparation Prior to ALD-Al₂O₃ for PERC Type Solar Cell," in: *27th European Photovoltaic Solar Energy Conference*, 2012, pp. 1974–1977. [Online]. Available: <http://dx.doi.org/10.4229/27thEUPVSEC2012-2CV.6.60>
- [173] S. Lien, C. Yang, K. Wu, and C. Kung, "Investigation on the passivated Si/Al₂O₃ interface fabricated by non-vacuum spatial atomic layer deposition system," *Nanoscale Research Letters*, vol. 10, no. 1, pp. 1–9, 2015. [Online]. Available: <https://dx.doi.org/10.1186%2Fs11671-015-0803-9>
- [174] J. Engelhardt, B. Gapp, F. Mutter, G. Hahn, and B. Terheiden, "Well Passivating and Highly Temperature Stable Aluminum Oxide Deposited by Atmospheric Pressure Chemical Vapor Deposition for PERC and PERT Solar Cell Concepts," in: *35th European Photovoltaic Solar Energy Conference and Exhibition*, 2018, pp. 390–394. [Online]. Available: <https://dx.doi.org/10.4229/35thEUPVSEC20182018-2BO.4.4>
- [175] W. Liang, K. J. Weber, and A. F. Thomson, "Effective SiN_x:H capping layers on 1 nm Al₂O₃ for p⁺ surface passivation," *IEEE Journal of Photovoltaics*, vol. 4, no. 6, pp. 1405–1412, 2014. [Online]. Available: <https://doi.org/10.1109/JPHOTOV.2014.2344757>
- [176] A. Richter, J. Benick, and M. Hermle, "Boron emitter passivation with Al₂O₃ and Al₂O₃/SiN_x stacks using ALD Al₂O₃," *IEEE Journal of Photovoltaics*, vol. 3, no. 1, pp. 236–245, 2013. [Online]. Available: <http://dx.doi.org/10.1109/JPHOTOV.2012.2226145>

- [177] S. Bordihn, Surface passivation by Al₂O₃-based film stacks for Si solar, Ph.D thesis, Eindhoven University of Technology, 2014. [Online]. Available: <https://pure.tue.nl/ws/files/3996041/781512.pdf>
- [178] G. Dingemans, N. M. Terlinden, D. Pierreux, H. B. Profijt, M. C. M. van de Sanden, and W. M. M. Kessels, “Influence of the Oxidant on the Chemical and Field-Effect Passivation of Si by ALD Al₂O₃,” *Electrochemical and Solid-State Letters*, vol. 14, no. 1, pp. H1–H4, 2011. [Online]. Available: <https://doi.org/10.1149/1.3501970>
- [179] B. Liao, R. Stangl, F. Ma, T. Mueller, F. Lin, A. G. Aberle, C. S. Bhatia, and B. Hoex, “Excellent c-Si surface passivation by thermal atomic layer deposited aluminum oxide after industrial firing activation,” *Journal of Physics D: Applied Physics*, vol. 46, no. 38, 2013. [Online]. Available: <https://doi.org/10.1088/0022-3727/46/38/385102>
- [180] G. Dingemans, R. Seguin, P. Engelhart, M. C. M. V. Sanden, and W.M. M. Kessels, “Silicon surface passivation by ultrathin Al₂O₃ films synthesized by thermal and plasma atomic layer deposition,” *Physica Status Solidi (RRL)–Rapid Research Letters*, vol. 4, no. 1–2, pp. 10–12, 2010. [Online]. Available: <https://doi.org/10.1002/pssr.200903334>
- [181] H. P. Sperlich, D. Decker, P. Saint-Cast, E. Erben, and L. Peters, “High Productive Solar Cell Passivation on Roth&Rau MAiA® MW-PECVD Inline Machine – A Comparison of Al₂O₃, SiO₂ and SiN_x-H Process Conditions and Performance,” in: *25th European Photovoltaic Solar Energy Conference and Exhibition / 5th World Conference on Photovoltaic Energy Conversion*, 2010, pp. 1352–1357. [Online]. Available: <https://doi.org/10.4229/25thEUPVSEC2010-2CO.3.6>
- [182] G. Dingemans, P. Engelhart, R. Seguin, B. Hoex, M. C. M. van de Sanden, and W. M. M. Kessels, “Firing stability of atomic layer deposited Al₂O₃ for c-Si surface passivation,” in: *34th IEEE Photovoltaic Specialists Conference*, 2009, pp. 000705–000708. [Online]. Available: <https://doi.org/10.1109/PVSC.2009.5411187>
- [183] J. Schmidt, B. Veith, and R. Brendel, “Effective surface passivation of crystalline silicon using ultrathin Al₂O₃ films and Al₂O₃/SiN_x stacks,” *Physica Status Solidi*

- (*RRL*)—*Rapid Research Letters*, vol. 3, no. 9, pp. 287–289, 2009. [Online]. Available: <https://doi.org/10.1002/pssr.200903272>
- [184] S. Kuhnhold, P. Saint-Cast, B. Kafle, M. Hofmann, F. Colonna, and M. Zacharias, “High-temperature degradation in plasma-enhanced chemical vapor deposition Al_2O_3 surface passivation layers on crystalline silicon,” *Journal of Applied Physics*, vol. 116, no. 5, 2014. [Online]. Available: <https://doi.org/10.1063/1.4891634>
- [185] Heraeus, Side silver paste for knotless screen-sol9641ax/bx series, 2017.
- [186] M. Li, H. S. Shin, K. S. Jeong, S. K. Oh, H. Lee, K. Han, G. W. Lee, and H. D. Lee, “Blistering Induced Degradation of Thermal Stability Al_2O_3 Passivation Layer in Crystal Si Solar Cells,” *Journal of Semiconductor Technology and Science*, vol. 14, no. 1, pp. 53–60, 2014. [Online]. Available: <http://dx.doi.org/10.5573/JSTS.2014.14.1.053>
- [187] B. Vermang, H. Goverde, V. Simons, I. De Wolf, J. Meersschaut, S. Tanaka, J. John, J. Poortmans, and R. Mertens, “A study of blister formation in ALD Al_2O_3 grown on silicon,” in: *38th IEEE Photovoltaic Specialists Conference*, 2012, pp. 001135–001138. [Online]. Available: <https://doi.org/10.1109/PVSC.2012.6317802>
- [188] Q. Li (Ed.), *Nanomaterials for Sustainable Energy*, Springer, 2016. [Online]. Available: <https://www.springer.com/gp/book/9783319320212>
- [189] J. Gielis, B. Hoex, M. C. M. van de Sanden, and W. M. M. Kessels, “Negative charge and charging dynamics in Al_2O_3 films on Si characterized by second-harmonic generation,” *Journal of Applied Physics*, vol. 104, no. 7, 2008. [Online]. Available: <https://doi.org/10.1063/1.2985906>
- [190] S. Miyajima, J. Irikawa, A. Yamada, and M. Konagai, “High Quality Aluminum Oxide Passivation Layer for Crystalline Silicon Solar Cells Deposited by Parallel-Plate Plasma-Enhanced Chemical Vapor Deposition,” *Applied Physics Express*, vol. 3, no. 1, 2009. [Online]. Available: <https://doi.org/10.1143/APEX.3.012301>
- [191] A. Roy Chowdhuri, C. Takoudis, R. Klie, and N. Browning, “Metalorganic chemical vapor deposition of aluminum oxide on Si: Evidence of interface SiO_2

- formation,” *Applied Physics Letters*, vol. 80, no. 22, pp. 4241–4243, 2002. [Online]. Available: <https://doi.org/10.1063/1.1483903>
- [192] K. Kimoto, Y. Matsui, T. Nabatame, T. Yasuda, T. Mizoguchi, I. Tanaka, and A. Toriumi, “Coordination and interface analysis of atomic-layer-deposition Al₂O₃ on Si(001) using energy-loss near-edge structures,” *Applied Physics Letters*, vol. 83, no. 21, pp. 4306–4308, 2003. [Online]. Available: <https://doi.org/10.1063/1.1629397>
- [193] R. Katamreddy, R. Inman, G. Jursich, A. Soulet, and C. Takoudis, “ALD and Characterization of Aluminum Oxide Deposited on Si(100) using Tris(diethylamino) Aluminum and Water Vapor,” *Journal of the Electrochemical Society*, vol. 153, no. 10, pp. C701–C706, 2006. [Online]. Available: <https://doi.org/10.1149/1.2239258>
- [194] T. Klein, D. Niu, W. Epling, W. Li, D. Maher, C. Hobbs, R. Hegde, I. J. R. Baumvol, and G. Parsons, “Evidence of aluminum silicate formation during chemical vapor deposition of amorphous Al₂O₃ thin films on Si(100),” *Applied Physics Letters*, vol. 75, no. 25, pp. 4001–4003, 1999. [Online]. Available: <https://doi.org/10.1063/1.125519>
- [195] R. S. Johnson, G. Lucovsky, and I. Baumvol, “Physical and electrical properties of noncrystalline Al₂O₃ prepared by remote plasma enhanced chemical vapor deposition,” *Journal of Vacuum Science & Technology A*, vol. 19, no. 4, pp. 1353–1360, 2001. [Online]. Available: <https://doi.org/10.1116/1.1379316>
- [196] N. Terlinden, G. Dingemans, M. C. M. van de Sanden, and W. M. M. Kessels, “Role of field-effect on c-Si surface passivation by ultrathin (2–20 nm) atomic layer deposited Al₂O₃,” *Applied Physics Letters*, vol. 96, no. 11, pp. 112101, 2010. [Online]. Available: <https://doi.org/10.1063/1.3334729>
- [197] K. Kim, N. Nandakumar, X. Zheng, S. Lim, and Z. Hameiri, “Subnanoscale Investigation of the Interface Between c-Si and PECVD AlO_x and Its Effect on Surface Passivation,” *IEEE Journal of Photovoltaics*, vol. 11, no. 3, pp. 620–626, 2021. [Online]. Available: <https://doi.org/10.1109/JPHOTOV.2021.3056676>

- [198] G. Noircler, F. Lebreton, E. Drahi, P. de Coux, and B. Warot-Fonrose, “STEM-EELS investigation of c-Si/a-AlO_x interface for solar cell applications,” *Micron*, vol. 145, 2021. [Online]. Available: <https://doi.org/10.1016/j.micron.2021.103032>
- [199] T. Niewelt, J. Broisch, J. Schon, J. Haunschild, S. Rein, W. Warta, and M. C. Schubert, “Light-induced degradation and regeneration in n-type silicon,” *Energy Procedia*, vol. 77, pp. 626–632, 2015. [Online]. Available: <https://doi.org/10.1016/j.egypro.2015.07.090>
- [200] Y. Li, H. Shen, Z. Hou, Q. Wei, and D. Hu, “Formation of emitter by boron spin-on doping from SiO₂ nanosphere and properties of the related n-PERT solar cells,” *Solar Energy*, vol. 225, pp. 317–322, 2021. [Online]. Available: <https://doi.org/10.1016/j.solener.2021.07.033>
- [201] R. R. King and R. M. Swanson, “Studies of diffused boron emitters: saturation current, bandgap narrowing, and surface recombination velocity,” *IEEE Transactions on Electron Devices*, vol. 38, no. 6, pp. 1399–1409, 1991. [Online]. Available: <https://doi.org/10.1109/16.81632>
- [202] F. W. Chen, T. T. A. Li, and J. E. Cotter, “Passivation of boron emitters on n-type silicon by plasma-enhanced chemical vapor deposited silicon nitride,” *Applied Physics Letters*, vol. 88, no. 26, 2006. [Online]. Available: <https://doi.org/10.1063/1.2217167>
- [203] R. Petres, J. Libal, T. Buck, R. Kopecek, M. Vetter, R. Ferre, I. Martin, D. Borchert, and P. Fath, “Improvements in the Passivation of P⁺-Si Surfaces by PECVD Silicon Carbide Films,” in: *IEEE 4th World Conference on Photovoltaic Energy Conference*, 2006, pp. 1012–1015. [Online]. Available: <https://doi.org/10.1109/WCPEC.2006.279290>
- [204] P. P. Altermatt, H. Plagwitz, R. Bock, J. Schmidt, M. J. Brendel, M. J. Kerr, and A. Cuevas, “The surface recombination velocity at boron-doped emitters: Comparison between various passivation techniques,” in: *21st European Photovoltaic Solar Energy Conference*, 2006, pp. 647–650. [Online]. Available: https://www.researchgate.net/publication/255970110_The_surface_recombination

[_velocity at boron-doped emitters Comparison between various passivation techniques](#)

- [205] S. Shimizu, S. P. Hsu, C. H. Du, A. Orita, T. Sato, and T. Nojiri, “Screen printable boron doping paste and its process for n-type pert solar cells,” *IEEE Journal of Photovoltaics*, vol. 8, no. 2, pp. 483–486, 2018. [Online]. Available: <https://doi.org/10.1109/JPHOTOV.2018.2797973>
- [206] A. Richter, E. Billot, M. Hofmann, J. Benick, J. Rentsch, R. Preu, S.W. Glunz, and P. Saint-Cast, “Very low surface recombination velocity of boron doped emitter passivated with plasma-enhanced chemical-vapor-deposited AlO_x layers,” *Thin Solid Films*, vol. 522, pp. 336–339, 2012. [Online]. Available: <https://doi.org/10.1016/j.tsf.2012.08.050>
- [207] J. Benick, B. Hoex, G. Dingemans, W. M. M. Kessels, A. Richter, M. Hermle, and S. W. Glunz, “High-Efficiency n-Type Silicon Solar Cells with Front Side Boron Emitter,” in: *24th European Photovoltaic Solar Energy Conference*, 2009, pp. 863–870. [Online]. Available: <https://doi.org/10.4229/24thEUPVSEC2009-2BP.1.3>
- [208] G. G. Untila, T. N. Kost, A. B. Chebotareva, A. S. Stepanov, M. B. Zaks, A. M. Sitnikov, and O. I. Solodukha, “Passivation of boron-doped p⁺-Si emitters in the (p⁺nn⁺)Si solar cell structure with AlO_x grown by ultrasonic spray pyrolysis,” *Solar Energy*, vol. 98, pp. 440–447, 2013. [Online]. Available: <https://doi.org/10.1016/j.solener.2013.08.041>
- [209] A. W. Blakers, A. Wang, A. M. Milne, J. Zhao, and M. A. Green, “22.8% efficient silicon solar cell,” *Applied Physics Letters*, vol. 55, no. 13, pp. 1363–1365, 1989. [Online]. Available: <https://doi.org/10.1063/1.101596>
- [210] R. Preu, E. Lohmuller, S. Lohmuller, P. Saint-Cast, and J. M. Greulich, “Passivated emitter and rear cell-Devices, technology, and modeling,” *Applied Physics Reviews*, vol. 7, no. 4, 2020. [Online]. Available: <https://doi.org/10.1063/5.0005090>
- [211] J. Lindroos and H. Savin, “Review of light-induced degradation in crystalline silicon solar cells,” *Solar Energy Materials and Solar Cells*, vol.147, pp. 115–126, 2016. [Online]. Available: <https://doi.org/10.1016/j.solmat.2015.11.047>

- [212] A. Shah (Ed.), *Solar Cells and Modules*, Springer, 2020. [Online]. Available: <https://doi.org/10.1007/978-3-030-46487-5>
- [213] IMEC, “Imec and Jolywood achieve a record of 23.2 percent with bifacial n-PERT solar cells,” 2019. [Online]. Available: <https://www.imec-int.com/en/articles/imec-and-jolywood-achieve-a-record-of-23-2-percent-with-bifacial-n-pert-solar-cells>
- [214] M. H. Norouzi, P. Saint-Cast, E. Lohmüller, S. Lohmüller, B. Steinhauser, A. Wolf, and M. Hofmann, “Inline deposited PassDop layers for rear side passivation and contacting of p-type c-Si PERL solar cells with high bifaciality,” *AIP Conference Proceedings*, vol. 2147, no. 1, 2019. [Online]. Available: <https://doi.org/10.1063/1.5123881>
- [215] E. Lohmuller, S. Lohmuller, M. H. Norouzi, P. Saint-Cast, J. Weber, S. Meier, and A. Wolf, “Towards 90% Bifaciality for p-Type Cz-Si Solar Cells by Adaption of Industrial PERC Processes,” in: *7th World Conference on Photovoltaic Energy Conversion (WCPEC)*, 2018, pp. 3727–3731. [Online]. Available: <https://doi.org/10.1109/PVSC.2018.8548202>
- [216] B. Kafle, B. S. Goraya, S. Mack, F. Feldmann, S. Nold, and J. Rentsch, “TOPCon–Technology options for cost efficient industrial manufacturing,” *Solar Energy Materials and Solar Cells*, vol. 227, 2021. [Online]. Available: <https://doi.org/10.1016/j.solmat.2021.111100>
- [217] J. Gifford, “TOPCon n-type solar cell technology could be a rival to mono PERC,” *pv-magazine*, 2020. [Online]. Available: <https://pv-magazine-usa.com/2020/03/07/topcon-n-type-solar-cell-technology-could-be-a-rival-to-mono-perc/>
- [218] Z. Kiaee, T. Fellmeth, B. Steinhauser, C. Reichel, M. Nazarzadeh, A. C. Nolken, and R. Keding, “TOPCon Silicon Solar Cells With Selectively Doped PECVD Layers Realized by Inkjet-Printing of Phosphorus Dopant Sources,” *IEEE Journal of Photovoltaics*, vol. 12, no. 1, pp. 31–37, 2022. [Online]. Available: <https://doi.org/10.1109/JPHOTOV.2021.3129073>
- [219] Wright M, Chen D, Yang J, Zheng P, Zhang X, Wenham S, Ciesla A, Chen R, “24.58% efficient commercial n-type silicon solar cells with hydrogenation,”

- Progress in Photovoltaics: Research and Applications*, vol. 29, no. 11, pp. 1213–1218, 2021. [Online]. Available: <https://doi.org/10.1002/pip.3464>
- [220] Moldovan, F. Feldmann, G. Krugel, M. Zimmer, J. Rentsch, M. Hermle, A. Roth-Folsch, K. Kaufmann, A. and C. Hagendorf, “Simple cleaning and conditioning of silicon surfaces with UV/ozone sources,” *Energy Procedia* , vol. 55, pp. 834–844, 2014. [Online]. Available: <https://doi.org/10.1016/j.egypro.2014.08.067>
- [221] D. Zhao, “High efficiency n-type cell technology: Development and prospects,” *PV InfoLink*, 2021. [Online]. Available: <https://www.infolink-group.com/en/solar/analysis-trends/n-type-high-efficiency-cell-technology-development-and-prospect>
- [222] S. Shenvekar, “N-Type TOPCon A Sign Of The Times – Jinko Solar,” *Solarquarter*, 2021. [Online]. Available: <https://solarquarter.com/2021/11/26/n-type-topcon-a-sign-of-the-times-jinko-solar/>
- [223] K. Yoshikawa, H. Kawasaki, W. Yoshida, T. Irie, K. Konishi, K. Nakano, T. Uto, D. Adachi, M. Kanematsu, H. Uzu, and K. Yamamoto, “Silicon heterojunction solar cell with interdigitated back contacts for a photoconversion efficiency over 26%,” *Nature Energy*, vol. 2, no. 5, pp. 1–8, 2017. [Online]. Available: <https://doi.org/10.1038/nenergy.2017.32>
- [224] P. J. Ribeyron, “Crystalline silicon solar cells: Better than ever,” *Nature Energy*, vol. 2, no.5, pp. 1–2, 2017. [Online]. Available: <https://doi.org/10.1038/nenergy.2017.67>
- [225] F. Haase, M. Rienacker, V. Barnscheidt, J. Krugener, N. Folchert, R. Brendel, S. Richter, S. Großer, E. Sauter, J. Hubner, and C. Hollemann, “Separating the two polarities of the POLO contacts of an 26.1%-efficient IBC solar cell,” *Scientific Reports*, vol. 10, no.1, pp. 1–5, 2020. [Online]. Available: <https://doi.org/10.1038/s41598-019-57310-0>
- [226] W. Wang, J. He, D. Yan, W. Chen, S. P. Phang, C. Samundsett, S. K. Karuturi, Z. Li, Y. Wan, and W. Shen, “Realization and simulation of interdigitated back contact silicon solar cells with dopant-free asymmetric hetero-contacts,” *Solar Energy*, vol. 231, pp. 203–208, 2020. [Online]. Available: <https://doi.org/10.1016/j.solener.2021.11.044>

- [227] F. Haase, C. Hollemann, S. Schafer, A. Merkle, M. Rienacker, J. Krugener, R. Brendel, and R. Peibst, “Laser contact openings for local poly-Si-metal contacts enabling 26.1%-efficient POLO-IBC solar cells,” *Solar Energy Materials and Solar Cells*, vol. 186, pp. 184–193, 2018. [Online]. Available: <https://doi.org/10.1016/j.solmat.2018.06.020>
- [228] M. Bahr, G. Heinrich, O. Doll, I. Kohler, C. Maier, and A. Lawrenz, “Differences of Rear-Contact Area Formation between Laser Ablation and Etching Paste for PERC Solar Cells,” in: *26th European Photovoltaic Solar Energy Conference and Exhibition*, 2011. pp. 1203–1209. [Online]. Available: <https://www.eupvsec-proceedings.com/proceedings?paper=14517>
- [229] S. H. Lee, “Development of high-efficiency silicon solar cells for commercialization,” *Journal of the Korean Physical Society*, vol. 39, no. 2, pp. 369–373, 2001. [Online]. Available: <https://www.jkps.or.kr/journal/view.html?uid=4513&vmd=Full>
- [230] T. Pu, H. Shen, K. H. Neoh, K. Gao, and F. Ye, “High-efficiency passivated emitter and rear cells with nano honeycomb structure,” *Solar Energy*, vol. 224, pp. 916–922, 2021. [Online]. Available: <https://doi.org/10.1016/j.solener.2021.06.066>
- [231] T. Dullweber, S. Gatz, H. Hannebauer, T. Falcon, R. Hesse, J. Schmidt, and R. Brendel, “19.4% -Efficient Large Area Rear-Passivated Screen-Printed Silicon Solar Cells,” in: *26th European Photovoltaic Solar Energy Conference*, 2011, pp. 811–816. [Online]. Available: <https://www.eupvsec-proceedings.com/proceedings?paper=11205>
- [232] C. Roselund, “Laser ablation of perc solar cells”, *PV magazine*, 2016. [Online]. Available: https://www.pv-magazine.com/magazine-archive/laser-ablation-of-perc-solar-cells_100026168/
- [233] International Technology Roadmap for Photovoltaic, ITRPV-Results 2020 including maturity report 2021, 12th edition, November 2021. [Online]. Available: <https://www.vdma.org/international-technology-roadmap-photovoltaic>
- [234] M. A. Green, “The Passivated Emitter and Rear Cell (PERC): From conception to mass production,” *Solar Energy Materials and Solar Cells*, vol. 143, pp. 190–197, 2015. [Online]. Available: <https://doi.org/10.1016/j.solmat.2015.06.055>

- [235] J. Benick, B. Hoex, M. C. M. van de Sanden, W. M. M. Kessels, O. Schultz, and S. W. Glunz, “High efficiency n-type Si solar cells on Al₂O₃-passivated boron emitters,” *Applied Physics Letters*, vol. 92, no. 25, 2008. [Online]. Available: <https://doi.org/10.1063/1.2945287>
- [236] J. Irikawa, S. Miyajima, T. Watahiki, and M. Konagai, “Development of the Transparent Conductive Oxide Layer for Nanocrystalline Cubic Silicon Carbide/Silicon Heterojunction Solar Cells with Aluminum Oxide Passivation Layers,” *Japanese Journal of Applied Physics*, vol. 51, no. 2S, 2012. [Online]. Available: <https://doi.org/10.1143/JJAP.51.02BP04>
- [237] C. Jin, I. Martin, G. Lopez, S. Harrison, G. Masmitja, P. R. Ortega, and R. Alcubilla, “Silicon solar cells with heterojunction emitters and laser processed base contacts,” *Energy Procedia*, vol. 124, pp. 604–611, 2017. [Online]. Available: <https://doi.org/10.1016/j.egypro.2017.09.084>
- [238] Y. H. Lin, Y. C. Wu, H. C. You, C. H. Chen, P. H. Chen, Y. H. Tsai, Y. Y. Yang, and K. Chang-Liao, “Silicon Heterojunction Solar Cells Using AlO_x and Plasma-Immersion Ion Implantation,” *Energies*, vol. 7, no. 6, pp. 3653–3663, 2014. [Online]. Available: <http://doi.org/10.3390/en7063653>
- [239] J. Bullock, D. Yan, and A. Cuevas, “Passivation of aluminium–n⁺ silicon contacts for solar cells by ultrathin Al₂O₃ and SiO₂ dielectric layers,” *Physica Status Solidi (RRL)– Rapid Research Letters*, vol. 7, no. 11, pp. 946–949, 2013. [Online]. Available: <https://doi.org/10.1002/pssr.201308115>
- [240] T. Dullweber, C. Kranz, B. Beier, B. Veith, J. Schmidt, B. Roos, O. Hohn, T. Dippell, and R. Brendel, “Inductively coupled plasma chemical vapour deposited AlO_x/SiN_y layer stacks for applications in high-efficiency industrial-type silicon solar cells,” *Solar Energy Materials and Solar Cells*, vol. 112, pp. 196–201, 2013. [Online]. Available: <https://doi.org/10.1016/j.solmat.2013.01.036>
- [241] L. E. Black, T. Allen, A. Cuevas, K. R. McIntosh, B. Veith, and J. Schmidt, “Thermal stability of silicon surface passivation by APCVD Al₂O₃,” *Solar Energy Materials and Solar Cells*, vol. 120, pp. 339–345, 2014. [Online]. Available: <https://doi.org/10.1016/j.solmat.2013.05.048>

- [242] M. Bhaisare, S. Sandeep, and A. Kottantharayil, “Thermal stability of single layer pulsed—DC reactive sputtered AlO_x film and stack of ICP-CVD SiN_x on AlO_x for p-type c-Si surface passivation,” in: *IEEE 2nd International Conference on Emerging Electronics (ICEE)*, 2014, pp. 1–4. [Online]. Available: <https://doi.org/10.1109/ICEmElec.2014.7151212>
- [243] P. K. Basu, F. Law, S. Vinodh, A. Kumar, P. Richter, F. Bottari, and B. Hoex, “0.4% absolute efficiency increase for inline-diffused screen-printed multicrystalline silicon wafer solar cells by non-acidic deep emitter etch-back,” *Solar Energy Materials and Solar Cells*, vol. 137, pp. 193–201, 2015. [Online]. Available: <https://doi.org/10.1016/j.solmat.2015.02.004>
- [244] D. S. Kim, M. M. Hilali, A. Rohatgi, K. Nakano, A. Hariharan, and K. Matthei, “Development of a Phosphorus Spray Diffusion System for Low-Cost Silicon Solar Cells,” *Journal of the Electrochemical Society*, vol. 153, no. 7, pp. A1391–A1396, 2006. [Online]. Available: <https://doi.org/10.1149/1.2202088>
- [245] A. Armigliato, D. Nobili, S. Solmi, G. Blendin, B. Schum, A. Lachowicz, and J. Horzel, “Characterization of the PSG/Si interface of H_3PO_4 doping process for solar cells,” *Solar Energy Materials and Solar Cells*, vol. 95, no. 11, pp. 3099–3105, 2011. [Online]. Available: <https://doi.org/10.1016/j.solmat.2011.06.042>
- [246] W. Kern and D. A. Puotinen, “Cleaning solution based on hydrogen peroxide for use in silicon semiconductor technology,” *RCA Review*, vol. 31, pp. 187–205, 1970.
- [247] Indian Institute of Technology Bombay Nanofabrication Facility (IITBNF), Indian Institute of Technology Bombay, Mumbai, India. [Online]. Available: <http://www.iitbnf.iitb.ac.in/iitbnf/>
- [248] F. Wenner, “A Method of Measuring Earth Resistivity,” *Bulletin of the Bureau of Standards*, vol. 12, pp. 469–478, 1916. [Online]. Available: <https://doi.org/10.6028/bulletin.282>
- [249] L. B. Valdes, “Resistivity Measurements on Germanium for Transistors,” in: *Proceedings of the IRE*, 1954, vol. 42, no. 2, pp. 420–427. [Online]. Available: <https://doi.org/10.1109/JRPROC.1954.274680>

- [250] D. K. Schroder, Semiconductor Material and Device Characterization, John Wiley & Sons, 2006. [Online]. Available: <https://doi.org/10.1002/0471749095>
- [251] S. H. Co (ED.), Organic Light Emitting Diode: Material, Process and Devices, IntechOpen, 2011. [Online]. Available: <https://doi.org/10.5772/776>
- [252] H. G. Tompkins, A User's Guide to Ellipsometry, Elsevier, 1993. [Online]. Available: <https://doi.org/10.1016/C2009-0-22336-1>
- [253] A. A. Franco (Ed.), Polymer Electrolyte Fuel Cells: Science, Applications, and Challenges, CRC Press, 2013. [Online]. Available: https://books.google.co.in/books/about/Polymer_Electrolyte_Fuel_Cells.html?id=TN7MBQAAQBAJ&redir_esc=y
- [254] M. Nazarov and D.Y. Noh, New Generation of Europium- and Terbium-Activated Phosphors From Syntheses to Applications, Pan Stanford publishing, 2011. [Online]. Available: https://www.google.co.in/books/edition/New_Generation_of_Europium_and_Terbium_A/kLrNBQAAQBAJ?hl=en&gbpv=0
- [255] M. B. Smith, Organic Chemistry: An Acid-Base Approach, CRC Press, 2011. [Online]. Available: <https://doi.org/10.1201/9781439894620>
- [256] K. Nakamoto, Handbook of Vibrational Spectroscopy Infrared and Raman Spectra of Inorganic and Coordination Compounds, in: Handbook of Vibrational Spectroscopy, John Wiley & Sons, 2006. [Online]. Available: <https://doi.org/10.1002/0470027320.s4104>
- [257] P. Griffiths and J. de Haseth, Fourier transform infrared spectrometry, John Wiley & Sons, 2006. [Online]. Available: <https://doi.org/10.1002/047010631X>
- [258] C. D. Wanger, W. M. Riggs, L. E. Davis, J. F. Moulder and G. E. Muilenberg, Handbook of X-ray Photoelectron Spectroscopy, Perkin-Elmer Corporation, Physical Electronics Division, Eden Prairie, 1979.
- [259] T. A. Carlson, Photoelectron and Auger Spectroscopy, Springer, 1975. [Online]. Available: <https://doi.org/10.1007/978-1-4757-0118-0>
- [260] S. M. Sze and K. K. Ng, Physics of Semiconductor Devices, John Wiley & Sons, 2006. [Online]. Available: <https://doi.org/10.1002/0470068329>

- [261] W. Hill and C. Coleman, "A single-frequency approximation for interface-state density determination," *Solid-State Electronics*, vol. 23, no. 9, pp. 987–993, 1980. [Online]. Available: [https://doi.org/10.1016/0038-1101\(80\)90064-7](https://doi.org/10.1016/0038-1101(80)90064-7)
- [262] R. A. Sinton and A. Cuevas, "Contactless determination of current–voltage characteristics and minority-carrier lifetimes in semiconductors from quasi-steady-state photoconductance data," *Applied Physics Letters*, vol. 69, no. 70, 1996. [Online]. Available: <https://doi.org/10.1063/1.117723>
- [263] B. Lim, Boron-oxygen-related recombination centers in crystalline silicon and the effects of dopant-compensation, Ph.D thesis, University of Hannover, 2012. [Online]. Available: : <https://www.osti.gov/etdeweb/servlets/purl/22000547>
- [264] V. Grivickas, D. Noreika, and J. Tellefsen, "Surface and auger recombination in silicon wafers of high carrier density," *Lithuanian Physics Journal*, vol. 29, pp. 48–53, 1989.
- [265] A. Sproul, "Dimensionless solution of the equation describing the effect of surface recombination on carrier decay in semiconductors," *Journal of Applied Physics*, vol. 76, no. 5, pp. 2851–2854, 1994. [Online]. Available: <https://doi.org/10.1063/1.357521>
- [266] A. Stephens, A. Aberle, and M. Green, "Surface recombination velocity measurements at the silicon–silicon dioxide interface by microwave-detected photoconductance decay," *Journal of Applied Physics*, vol. 76, no. 363, 1994. [Online]. Available: <https://doi.org/10.1063/1.357082>
- [267] H. Takato, I. Sakata, and R. Shimokawa, "Surface passivation of silicon substrates using quinhydrone/methanol treatment," in: *3rd World Conference on Photovoltaic Energy Conversion*, 2003, vol. 2, pp. 1108–1111. [Online]. Available: <https://ieeexplore.ieee.org/abstract/document/1306107>
- [268] B. Chhabra, S. Bowden, R. L. Opila, and C. B. Honsberg, "High effective minority carrier lifetime on silicon substrates using quinhydrone-methanol passivation," *Applied Physics Letters*, vol. 96, no. 6, 2010. [Online]. Available: <https://doi.org/10.1063/1.3309595>

- [269] T. Trupke, B. Mitchell, J. W. Weber, W. McMillan, R. A. Bardos, and R. Kroeze, “Photoluminescence Imaging for Photovoltaic Applications,” *Energy Procedia*, vol. 14, pp. 135–146, 2012. [Online]. Available: <https://doi.org/10.1016/j.egypro.2012.02.016>
- [270] A. H. Kitai (Ed.), *Solid State Luminescence Theory, materials and devices*, Springer, 1993. [Online]. Available: <https://link.springer.com/book/10.1007/978-94-011-1522-3>
- [271] A. K. Sharma, H. Kalasua, S. Kumbhar, K. L. Narasimhan, and B. M. Arora, “Imaging of series resistance and ideality factor in c-Si solar cells,” in: *3rd International Conference on Emerging Electronics (ICEE)*, 2016, pp. 1–3. [Online]. Available: <https://doi.org/10.1109/ICEmElec.2016.8074625>
- [272] K. P. Sreejith, *Advanced texturization processes for industrial crystalline silicon solar cells*, Ph.D thesis, Indian Institute of Technology Bombay, 2021. [Online]. Available: https://www.ee.iitb.ac.in/~anilkg/Sreejith_thesis.pdf
- [273] N. Grant, *Surface passivation and characterisation of crystalline silicon by wet chemical treatments*, Ph.D thesis, The Australian National University, 2012. [Online]. Available: <https://doi.org/10.25911/5d5149c487326>
- [274] D. E. Bornside, C. W. Macosko, and L. E. Scriven, “Spin coating: One-dimensional model,” *Journal of Applied Physics*, vol. 66, no. 11, pp. 5185–5193, 1989. [Online]. Available: <https://doi.org/10.1063/1.343754>
- [275] L. E. Scriven, “Physics and Applications of DIP Coating and Spin Coating,” *MRS Online Proceedings Library*, vol. 121, pp. 717–729, 1988. [Online]. Available: <https://doi.org/10.1557/PROC-121-717>
- [276] K. H. Stern (Ed.), *Metallurgical, and Ceramic Protective Coatings*, Springer, 1996. [Online]. Available: <https://doi.org/10.1007/978-94-009-1501-5>
- [277] M. D. Tyona, “A theoretical study on spin coating technique,” *Advances in Materials Research*, Vol. 2, no. 4, pp. 195–208, 2013. [Online]. Available: <https://doi.org/10.12989/AMR.2013.2.4.195>
- [278] Micro/Nano Technology Center (MNTC), “Standard Operating Procedures - Spin Theory,” University of Louisville. [Online]. Available:

<https://louisville.edu/micronano/files/documents/standard-operating-procedures/SpinTheory.pdf>

- [279] A. Nuermaiti, Studies on the Self-organization of Colloidal Nanoparticles at Interfaces, Diploma thesis, Uppsala University, 2010. [Online]. Available: <https://www.diva-portal.org/smash/get/diva2:351151/FULLTEXT01.pdf>
- [280] N. N. Nikitenkov (Ed.), Modern Technologies for Creating the Thin-film Systems and Coatings, IntechOpen, 2017. [Online]. Available: <https://doi.org/10.5772/63326>
- [281] P. Colson, Nanostructuring induced by self-organization of polystyrene nanospheres as a template for the Controlled growth of functional materials, Ph.D thesis, University of Liege, 2011. [Online]. Available: <https://hdl.handle.net/2268/102356>
- [282] D. Meyerhofer, “Characteristics of resist films produced by spinning,” *Journal of Applied Physics*, vol. 49, no. 7, pp. 3993–3997, 1978. [Online]. Available: <https://doi.org/10.1063/1.325357>
- [283] P. N. Tri, S. Rtimi, and C. M. O. Plamondon (Eds.), Nanomaterials-Based Coatings: Fundamentals and Applications, Elsevier, 2019. [Online]. Available: <https://doi.org/10.1016/C2017-0-03415-8>
- [284] C. Avis and J. Jang, “High-performance solution processed oxide TFT with aluminum oxide gate dielectric fabricated by a sol–gel method,” *Journal of Materials Chemistry*, vol. 21, no. 29, pp. 10649–10652, 2011. [Online]. Available: <https://doi.org/10.1039/C1JM12227D>
- [285] H. Wang, T. Sun, W. Xu, F. Xie, L. Ye, Y. Xiao, Y. Wang, J. Chen, and J. Xu, “Low-temperature facile solution-processed gate dielectric for combustion derived oxide thin film transistors,” *RSC Advances*, vol. 4, no. 97, pp. 54729–54739, 2014. [Online]. Available: <https://doi.org/10.1039/C4RA09077B>
- [286] D. X. Xia and J. B. Xu, “High mobility and low operating voltage ZnGaO and ZnGaLiO transistors with spin-coated Al₂O₃ as gate dielectric,” *Journal of Physics D: Applied Physics*, vol. 43, no. 44, 2010. [Online]. Available: <http://stacks.iop.org/JPhysD/43/442001>

- [287] W. Xu, H. Wang, L. Ye, and J. Xu, “The role of solution-processed high-k gate dielectrics in electrical performance of oxide thin-film transistors”, *Journal of Materials Chemistry C*, vol. 2, no. 27, pp. 5389–5396, 2014. [Online]. Available: <https://doi.org/10.1039/C4TC00334A>
- [288] N. Avci, P. F. Smet, J. Lauwaert, H. Vrielinck, and D. Poelman, “Optical and structural properties of aluminium oxide thin films prepared by a non-aqueous sol–gel technique,” *Journal of Sol-Gel Science and Technology*, vol. 59, pp. 327–333, 2011. [Online]. Available: <https://doi.org/10.1007/s10971-011-2505-9>
- [289] L. Dobrzanski, M. Szindler, A. Drygała, and M. Szindler, “Silicon solar cells with Al₂O₃ antireflection coating,” *Open Physics*, vol. 12, no. 9, pp. 666–670, 2014. [Online]. Available: <https://doi.org/10.2478/s11534-014-0500-9>
- [290] G. Dingemans, M. C. M. van de Sanden, and W. M. M. Kessels, “Excellent Si surface passivation by low temperature SiO₂ using an ultrathin Al₂O₃ capping film,” *Rapid Research Letter*, vol. 5, no. 1, pp. 22–24, 2011. [Online]. Available: <https://doi.org/10.1002/pssr.201004378>
- [291] E. Vermarien, G. Agostinelli, G. Beaucarne, and J. Poortmans, “Progress on the Pseudo-Binary (Al₂O₃)₃(TiO₂)₂-System for Surface Passivation of P-Type Silicon,” in: *IEEE 4th World Conference on Photovoltaic Energy Conference*, 2006, pp. 103–106. [Online]. <https://doi.org/10.1109/WCPEC.2006.279374>
- [292] M. Bhaisare, Pulsed-DC Reactive Sputtered Aluminum Oxide For The Surface Passivation Of Crystalline Silicon Solar Cell, Ph.D thesis, Indian Institute of Technology Bombay, 2019. [Online]. Available: <http://www.ee.iitb.ac.in/~anilk/Meenakshi-Bhaisare-thesis.pdf>
- [293] N. Ozer, J. P. Cronin, Y. J. Yao, and A. P. Tomsia, “Optical properties of sol–gel deposited Al₂O₃ films,” *Solar Energy Materials and Solar Cells*, vol. 59, no. 4, pp. 355–366, 1999. [Online]. Available: [https://doi.org/10.1016/S0927-0248\(99\)00054-9](https://doi.org/10.1016/S0927-0248(99)00054-9)
- [294] B. Yilbas, A. Al-Sharafi, and H. Ali, Self-Cleaning of Surfaces and Water Droplet Mobility, Elsevier, 2019. [Online]. Available: <https://doi.org/10.1016/C2017-0-02187-0>

- [295] E. Cornagliotti, A. Uruena, J. Horzel, J. John, L. Tous, D. Hendrickx, V. Prajapati, S. Singh, R. Hoyer, F. Delahaye, K. Weise, D. Queißer, H. Nussbaumer, and J. Poortmans, “How Much Rear Side Polishing Is Required? A Study on the Impact of Rear Side Polishing in PERC Solar Cells,” in: *27th European Photovoltaic Solar Energy Conference and Exhibition*, 2015, pp. 561–566. [Online]. Available: <http://dx.doi.org/10.4229/27thEUPVSEC2012-2AO.1.6>
- [296] P. Ramm, J. J. Lu, and M. M. V. Taklo (Eds.), *Handbook of Wafer Bonding*, Wiley, 2012. [Online]. Available: <https://doi.org/10.1002/9783527644223>
- [297] H. Singh, M. Kumar, and R. Singh, “An overview of various applications of cold spray coating process,” in: *Materials Today: Proceedings*, 2022, vol. 56, pp. 2826–2830. [Online]. Available: <https://doi.org/10.1016/j.matpr.2021.10.160>
- [298] P. L. Fauchais, J. V. R. Heberlein, and M. I. Boulos, *Thermal Spray Fundamentals: From Powder to Part*, Springer, 2014. [Online]. Available: <https://doi.org/10.1007/978-0-387-68991-3>
- [299] HOLMARK, Operating manual, Spray Pyrolysis Equipment (Model HO-TH-04), Holmarc Opto Mechatronics Pvt. Ltd.
- [300] S. Das, S. Kuma, S. K. Samal, S. Mohanty, and S. K. Nayak, “A review on superhydrophobic polymer nanocoatings: recent development and applications,” *Industrial & Engineering Chemistry Research*, vol. 57, no. 8, pp. 2727–2745, 2018. [Online]. Available: <https://doi.org/10.1021/acs.iecr.7b04887>
- [301] P. Pham, P. Goel, S. Kumar, and K. Yadav (Eds.), *21st Century Surface Science - a Handbook*, IntechOpen, 2020. [Online]. Available: <https://doi.org/10.5772/intechopen.87891>
- [302] M. Grundner and H. Jacob, “Investigations on hydrophilic and hydrophobic silicon (100) wafer surfaces by X-ray photoelectron and high-resolution electron energy loss-spectroscopy,” *Applied Physics A*, vol. 39, pp. 73–82, 1986. [Online]. Available: <https://doi.org/10.1007/BF00616822>
- [303] L. A. Zazzera and J. F. Moulder, “XPS and SIMS Study of Anhydrous HF and UV/Ozone-Modified Silicon (100) Surfaces,” *Journal of The Electrochemical*

- Society*, vol. 136, no. 2, 1989. [Online]. Available: <https://doi.org/10.1149/1.2096659>
- [304] Y. Backlund, K. Hermansson, and L. Smith, “Band-Strength Measurements Related to Silicon Surface Hydrophilicity ,” *Journal of The Electrochemical Society*, vol. 139, no. 8, 1992. [Online]. Available: <https://doi.org/10.1149/1.2221218>
- [305] A. Richter, F. M. M. Souren, D. Schuldis, R. M. W. Gortzen, J. Benick, M. Hermle, and S. W. Glunz, “Thermal Stability of Spatial ALD Deposited Al₂O₃ Capped by PECVD SiN_x for the Passivation of Lowly- and Highly-Doped p-Type Silicon Surfaces,” in: *27th European Photovoltaic Solar Energy Conference and Exhibition*, 2012, pp. 1133–1137. [Online]. Available: <https://doi.org/10.4229/27thEUPVSEC2012-2AV.5.25>
- [306] B. Vermang, H. Goverde, L. Tous, A. Lorenz, P. Choulat, J. Horzel, J. John, J. Poortmans, and R. Mertens, “Approach for Al₂O₃ rear surface passivation of industrial p-type Si PERC above 19%,” *Progress in Photovoltaics: Research and Applications*, vol. 20, no. 3, pp. 269–273, 2012. [Online]. Available: <https://doi.org/10.1002/pip.2196>
- [307] G. Socrates, *Infrared and Raman characteristic group frequencies: tables and charts*, John Wiley & Sons, 2004.
- [308] L. Gong, C. Zhou, J. Zhu, W. Wang, F. Ji, “Passivation Mechanisms of Atomic Layer-deposited AlO_x Films and AlO_x/SiO_x Stack,” in: *IOP Conference Series: Materials Science and Engineering*, 2019. [Online]. Available: <https://doi.org/10.1088/1757-899X/585/1/012026>
- [309] Z. W. Peng, P. T. Hsieh, Y. J. Lin, C. J. Huang, and C. C. Li, “Investigation on Blistering Behavior for n-type Silicon Solar Cells,” *Energy Procedia*, vol. 77, pp. 827–831, 2015. [Online]. Available: <https://doi.org/10.1016/j.egypro.2015.07.117>
- [310] V. Verlaan, L. R. J. G. van den Elzen, G. Dingemans, M. C. M. van de Sanden, W. M. M. Kessels, “Composition and bonding structure of plasma-assisted ALD Al₂O₃ films,” *Physica Status Solidi*, vol. 7, 2010. [Online]. Available: <https://doi.org/10.1002/pssc.200982891>

- [311] H. Goverde, B. Vermang, A. Morato, J. John, J. Horzel, G. Meneghesso, and J. Poortmans, "Al₂O₃ surface passivation characterized on hydrophobic and hydrophilic c-Si by a combination of QSSPC, CV, XPS and FTIR," *Energy Procedia*, vol. 27, pp. 355–360, 2012. [Online]. Available: <https://doi.org/10.1016/j.egypro.2012.07.076>
- [312] S. Kuhnhold, B. Kafle, L. Kroely, P. Saint-Cast, M. Hofmann, J. Rentsch, and R. Preu, "Impact of thermal treatment on PECVD Al₂O₃ passivation layers," *Energy Procedia*, vol. 27, pp. 273–279, 2012. [Online]. Available: <https://doi.org/10.1016/j.egypro.2012.07.063>
- [313] R. E. Sah, R. Driad, F. Bernhardt, L. Kirste, C. C. Leancu, H. Czap, F. Benkhelifa, M. Mikulla, and O. Ambacher, "Mechanical and electrical properties of plasma and thermal atomic layer deposited Al₂O₃ films on GaAs and Si," *Journal of Vacuum Science & Technology A: Vacuum, Surfaces, and Films*, vol. 31, 2013. [Online]. Available: <https://doi.org/10.1116/1.4804175>
- [314] R. Katamreddy, R. Inman, G. Jursich, A. Soulet, and C. Takoudis, "Atomic layer deposition of HfO₂, Al₂O₃, and HfAlO_x using O₃ and metal (diethylamino) precursors," *Journal of Materials Research*, vol. 22, 2007. [Online]. Available: <https://doi.org/10.1557/JMR.2007.0439>
- [315] T. T. A. Li, S. Ruffell, M. Tucci, Y. Mansoulie, C. Samundsett, S. De Iullis, L. Serenelli, and A. Cuevas, "Influence of oxygen on the sputtering of aluminum oxide for the surface passivation of crystalline silicon," *Solar Energy Materials And Solar Cells*, vol. 95, pp. 69–72, 2011. [Online]. Available: <https://doi.org/10.1016/j.solmat.2010.03.034>
- [316] P. Tarte, "Infra-red spectra of inorganic aluminates and characteristic vibrational frequencies of AlO₄ tetrahedra and AlO₆ octahedra," *Spectrochimica Acta Part A: Molecular Spectroscopy*, vol. 23, 1967. [Online]. Available: [https://doi.org/10.1016/0584-8539\(67\)80100-4](https://doi.org/10.1016/0584-8539(67)80100-4)
- [317] J. M. Reyes, B. M. P. Ramos, C. Z. Islas, W. C. Arriaga, P. R. Quintero, and A. T. Jacome, "Chemical and morphological characteristics of ALD Al₂O₃ thin-film surfaces after immersion in pH buffer solutions," *Journal of The Electrochemical Society*, vol. 160, 2013. [Online]. Available: <https://doi.org/10.1149/2.060310jes>

- [318] G. A. Dorsey, "The characterization of anodic aluminas: I. Composition of films from acidic anodizing electrolytes," *Journal of the Electrochemical Society*, vol. 113, 1966. [Online]. Available: <https://doi.org/10.1149/1.2423895>
- [319] Y. C. Kim, H. H. Park, J. S. Chun, and W. J. Lee, "Compositional and structural analysis of aluminum oxide films prepared by plasma-enhanced chemical vapor deposition," *Thin Solid Films*, vol. 237, pp. 57–65, 1994. [Online]. Available: [https://doi.org/10.1016/0040-6090\(94\)90238-0](https://doi.org/10.1016/0040-6090(94)90238-0)
- [320] L. Hennen, Analysis of blister formation in spatial ALD Al₂O₃ for silicon surface passivation in photovoltaics, Master thesis, Eindhoven University of Technology, 2012. [Online]. Available: <https://pure.tue.nl/ws/files/46932414/759012-1.pdf>
- [321] N. Batra, J. Gope, Vandana, J. Panigrahi, R. Singh, and P. Singh, "Influence of deposition temperature of thermal ALD deposited Al₂O₃ films on silicon surface passivation," *AIP Advances*, vol. 5, no. 6, 2015. [Online]. Available: <https://doi.org/10.1063/1.4922267>
- [322] V. Naumann, M. Otto, R. B. Wehrspohn, and C. Hagendorf, "Chemical and structural study of electrically passivating Al₂O₃/Si interfaces prepared by atomic layer deposition," *Journal of Vacuum Science & Technology A*, vol. 30, no. 4, 2012. [Online]. Available: <https://doi.org/10.1116/1.4704601>
- [323] G. D. Wilk, R. M. Wallace, and J. M. Anthony, "High-k gate dielectrics: Current status and materials properties considerations," *Journal of Applied Physics*, vol. 89, no. 10, pp. 5243–5275, 2001. [Online]. Available: <https://doi.org/10.1063/1.1361065>
- [324] R. Muller, C. Reichel, X. Yang, A. Richter, J. Benick, and M. Hermle, "Impact of the homogeneous junction breakdown in IBC solar cells on the passivation quality of Al₂O₃ and SiO₂: degradation and regeneration behavior," *Energy Procedia*, vol. 124, pp. 365–370, 2017. [Online]. Available: <https://doi.org/10.1016/j.egypro.2017.09.311>
- [325] J. Kolodzey, E. A. Chowdhury, T. N. Adam, G. Qui, I. Rau, J. O. Olowolafe, J. S. Suehle, and Y. Chen, "Electrical conduction and dielectric breakdown in aluminum oxide insulators on silicon," *IEEE Transactions on Electron Devices*,

- vol. 47, no. 1, pp. 121–128, 2000. [Online]. Available: <https://doi.org/10.1109/16.817577>
- [326] L. A. Dissado, J. C. Fothergill, S. V. Wolfe, and R. M. Hill, “Weibull Statistics in Dielectric Breakdown; Theoretical Basis, Applications and Implications,” *IEEE Transactions on Electrical Insulation*, vol. EI-19, no. 3, pp. 227–233, 1984. [Online]. Available: <https://doi.org/10.1109/TEI.1984.298753>
- [327] R. Hill and L. Dissado, “Theoretical basis for the statistics of dielectric breakdown,” *Journal of Physics C: Solid State Physics*, vol. 16, no. 11, 1983. [Online]. Available: <https://doi.org/10.1088/0022-3719/16/11/017>
- [328] W. Weibull, “A statistical distribution function of wide applicability,” *Journal of Applied Mechanics*, vol. 18, pp. 290–293, 1951. [Online]. Available: <http://web.cecs.pdx.edu/~cgshirl/Documents/Weibull-ASME-Paper-1951.pdf>
- [329] Y. H. Kim, K. Onishi, C. S. Kang, H. J. Cho, R. Choi, S. Krishnan, M. S. Akbar, and J. C. Lee, “Thickness dependence of Weibull slopes of HfO₂ gate dielectrics,” *IEEE Electron Device Letters*, vol. 24, no. 1, pp. 40–42, 2003. [Online]. Available: <https://doi.org/10.1109/LED.2002.807314>
- [330] A. Benard and E. Bos-Levenbach, “The plotting of observations on probability paper,” *Statistica Neerlandica*, vol. 7, no. 7, pp. 163–173, 1953.
- [331] T. Dullweber, S. Gatz, H. Hannebauer, T. Falcon, R. Hesse, J. Schmidt, and R. Brendel, “Towards 20% efficient large-area screen-printed rear-passivated silicon solar cells,” *Progress in Photovoltaics: Research and Applications*, vol. 20, no. 6, pp. 630–638, 2012. [Online]. Available: <https://doi.org/10.1002/pip.1198>
- [332] G. Dingemans and W. M. M. Kessels, “Recent Progress in the Development and Understanding of Silicon Surface Passivation by Aluminum Oxide for Photovoltaics,” in: *25th European Photovoltaic Solar Energy Conference and Exhibition / 5th World Conference on Photovoltaic Energy Conversion*, 2010, pp. 1083–1090. [Online]. Available: <https://doi.org/10.4229/25theupvsec2010-2dp.2.1>

List of publications and patents

Journal publication

- **Kalaivani S** and Anil Kottantharayil, “Aluminium oxide thin film deposited by spray coating for p-type silicon surface passivation,” *Solar Energy Materials and Solar Cells*, vol. 197, pp. 93–98, 2019.

Patent

- **Kalaivani S** and Anil Kottantharayil, “Method for deposition of metal of oxide over a substrate”, Indian patent number 391027, granted on 2 March 2022.

Conference publications

- **Kalaivani S** and Anil Kottantharayil, “Spray Coated Aluminum Oxide Thin Film For P-type Crystalline Silicon Surface Passivation”, in: 42nd IEEE Photovoltaic Specialist Conference (PVSC), Orleans, USA, 2015 (oral presentation).
- C. Saima, **Kalaivani S** and A. Kottantharayil, “Performance optimization of p⁺ n silicon solar cell with screen-printed boron emitter,” in: 46th IEEE Photovoltaic Specialist Conference (PVSC), Chicago, Illinois, 2019.

Acknowledgements

First and foremost, I express my deepest and sincere gratitude to Lord Sri Sri RadhaKrishna, ultimately for everything. I express my deepest and sincere gratitude to all my Spiritual Masters and all the Vaishnavas for Their blessings, spiritual care, transcendental scriptures and discourses, causeless mercy, transcendental compassion and unconditional love. I would like to express my deep gratitude to my family members for Their blessings, support, love and care throughout my life. I would like to express my gratitude to my friends Smita Sahu and Abhilasha Maheshwari at IITB and Vaishnavas for Their spiritual association and memories to be cherished forever in my life.

I express my sincere gratitude to my thesis supervisor Prof. Anil Kottantharayil for his guidance, insightful comments, help, valuable time, research facilities and resources throughout my research. My sincere gratitude to Prof. Pradeep Nair and Prof. Parag Bhargava for agreeing to be part of my research progress committee, valuable time, insightful feedback and suggestions.

I would like to acknowledge the Ministry of New and Renewable Energy (MNRE) for funding the National Centre for Photovoltaic Education and Research (NCPRE). I would also like to thank Prof. B. G. Fernandes and Prof. C. S. Solanki (the project investigators of NCPRE) for their support. I would like to acknowledge the "IITB Nanofabrication Facility" (IITBNF), Department of Electrical Engineering, IIT Bombay, NCPRE and staff members associated with IITBNF and NCPRE for research facilities and help throughout the research work. I would like to acknowledge the Sophisticated Analytical Instrumentation Facility (SAIF), IIT Bombay, for TEM images. I acknowledge The Industrial Research and Consultancy Centre (IRCC) Facility, IIT Bombay for XPS measurement presented in chapter 4. I acknowledge Mr. Subash Pai, Excel Instruments, Palghar, Maharashtra, India for his technical support and technical drawings for heater and vacuum chuck development. I would like to thank Dr. Ashok for PL images. I would like to thank Saima for p⁺ silicon substrates. I would like to thank Dr. Prabir K. Basu for his help to prepare samples for photolithography and LFC experiments. I would like to thank Swasti Bhatia for her help in LFC experiments. I express my gratitude to all research scholars, project staff and students who helped in my research at IITB with special mention to Sandeep S S and Meenakshi B for their suggestions, comments, help and technical discussions. I also want to thank all my friends at IIT Bombay for their help.

Kalaivani S